UNIVERSITY OF LEEDS

Feedback from Winds and Supernovae in Massive Stellar Clusters

Hazel Claire Rogers

Department of Physics and Astronomy

University of Leeds

Submitted in accordance with
the requirements for the degree of

Doctor of Philosophy

September 2013

The candidate confirms that the work submitted is her own, except where work which has formed part of jointly authored publications has been included. The contribution of the candidate and the other authors of this work has been explicitly indicated. The candidate confirms that appropriate credit has been given within this thesis where reference has been made to the work of others.

For my parents, Phil and Annette Rogers.

Preface

Within this thesis, some chapters have been based on work presented in the following jointly authored publications:

I. "Feedback from Winds and Supernovae in Massive Stellar Clusters. I: Hydrodynamics", **H.Rogers** and J.M.Pittard, 2013, MNRAS, 413,1337.

II. "Feedback from Winds and Supernovae in Massive Stellar Clusters. II: X-Ray Emission", **H.Rogers** and J.M.Pittard, 2013, in prep.

III. "Feedback from Winds and Supernovae in Massive Stellar Clusters. III: Radio Emission", **H.Rogers** and J.M.Pittard, 2013, in prep.

Paper I forms the basis of Chapter 2. The hydrodynamical code used to perform the simulations in this Chapter was written and developed by J.M.Pittard, with the input background conditions for the GMC provided by E.Vasquez-Semadeni. The primary author (H.Rogers) was responsible for small modifications to the code to set up a cluster of stars contained within a GMC clump surrounded by homogeneous material. The primary author wrote the initial draft of the publication, and then incorporated comments from co-authors in the final draft.

Paper II forms the basis of Chapter 3. The simulations and analysis were carried out by the primary author using the radiative transfer X-ray tracing code provided by J.M.Pittard.The primary author wrote the initial draft of the publication, and then incorporated comments from co-authors in the final draft.

Paper III forms the basis of Chapter 4. The simulations and analysis were carried out by the primary author using the radiative transfer radio tracing code provided by J.M.Pittard.The primary author wrote the initial draft of the publication, and then incorporated comments from co-authors in the final draft.

Acknowledgements

I would like to thank Julian Pittard for his supervision and guidance over the past few years. His constant patience and encouragement have been instrumental in this thesis coming together. I have really enjoyed working with you. I would also like to thank Tom Hartquist for his input and wisdom over the years.

My thanks also go to the other PhD students, who over the past four years have put up with me bossing them around. Special thanks must go to John and Mo who had to put up with me in a small confined space for a year. More recently, thank you to Jonny, Luke and Robbie for putting up with my constant monologuing and various states of panic. I would also like to give special thanks to Jim and Jo. You are two of the most generous people I know, and I'll always be grateful for your help when I needed it the most.

I would like to say a huge thank you to Kate, Jess, Josie, Faith and Ingrid. Not only have you helped me out and kept me sane (sort of), you have been a constant source of inspiration and laughter. Sarah, you have been an amazing friend for over four years, and I will always appreciate your generosity, patience and bubbly northern humour. I probably couldn't have done this without you.

I would also like to thank my family for all their support over these years. Sam, Ben, Aunty Lesley, Aunty Helen and Uncle Pete, thank you all so much for inspiring me and keeping me going. You've helped me more than you know.

Finally, I'd like to thank my parents for their unequivocal support and love. Your constant encouragement and belief in me has got me to where I am today.

Abstract

This thesis contains a study of the mechanical feedback from winds and supernovae on inhomogeneous molecular material left over from the formation of a massive stellar cluster. Firstly, the mechanical input from a cluster with three massive O-stars into a giant molecular cloud (GMC) clump containing 3240 $M_\odot$ of molecular material within a 4 pc radius is investigated using a 3D hydrodynamcial model. The cluster wind blows out of the molecular clump along low-density channels, into which denser clump material is entrained. The densest regions are surprisingly resistant to ablation by the cluster wind, in part due to shielding by other dense regions close to the cluster. Nonetheless, molecular material is gradually removed by the cluster wind during which mass-loading factors in excess of several hundred are obtained. Because the clump is very porous, 60-75 % of the injected wind energy escapes the simulation domain. After 4.4 Myrs the massive stars in the simulation start to explode as supernovae. The highly structured environment into which the SN energy is released allows even weaker coupling to the remaining dense material and practically all of the SN energy reaches the wider environment.

Secondly, the X-ray emission from the simulated stellar cluster is presented. The GMC clump causes short–lived attenuation effects on the X-ray emission of the cluster. However, once most of the material has been ablated away by the winds the remaining dense clumps do not have a noticable effect on the attenuation compared with the assumed interstellar medium (ISM) column. The evolution of the X-ray luminosity and spectra are presented, and synthetic images of the emission are generated. The X-ray luminosity is initially high

whilst the winds are "bottled up", but reduce to a near constant value once the GMC clump has been mostly destroyed. The luminosity decreases slighly during the red supergiant phase of the stars due to the depressurization of the hot gas. However, the luminosity dramatically increases during the Wolf-Rayet stage of each star. The X-ray luminosity is enhanced by 2-3 orders of magnitude for at least 466 yrs after each supernova explosion, at which time the blast wave leaves the grid. Comparisons between the simulated cluster and both theoretical models and observations of young stellar clusters are presented.

Thirdly, the radio emission from the simulated cluster is presented. Similar to the X-ray emission, the thermal radio emission is intially high when the winds are confined in the GMC clump and reduce as the material is ablated away. The evolution of the radio flux density and spectra are presented, and synthetic images of the emission are generated. The radio emission is compared with the X-ray results throughout the evolution of the cluster. The flux density increases during the RSG phase, and remains high during the WR phgase of the stars. The radio flux density is enhanced by three orders of magnitude during the first supernova explosion. Comparisons between the simulated cluster and observations of young stellar clusters are made.

Finally, a preliminary investigation of the interaction of stellar winds within a massive cluster are presented. The hydrodynamcial simulations examine the energy and mass input of a stellar cluster into the ISM.

Abbreviations

GMC	Giant Molecular Cloud
IMF	Initial Mass Function
ISM	Interstellar Medium
MS	Main Sequence
MSFR	Massive Star Forming Region
RSG	Red Supergiant
RT	Rayleigh-Taylor
SFR	Star Formation Rate
SN	Supernova
SSC	Super-Star Cluster
WR	Wolf-Rayet

Contents

List of Figures

LIST OF FIGURES

LIST OF FIGURES

List of Tables

LIST OF TABLES

Chapter 1

Introduction

Massive stars have a profound effect on their natal environment creating wind-blown shells, cavities and HII regions. Their winds and supernovae (SNe) chemically enrich the interstellar medium (ISM) and also help to sustain turbulence within it. Massive stars embedded within molecular clouds likely inhibit further star formation as their winds and ionizing radiation disperse and destroy the remaining molecular gas, though in some circumstances massive stars may also trigger new star formation (Koenig *et al.*, 2012) and new cluster formation (Beuther *et al.*, 2008; Gray & Scannapieco, 2011). The removal of molecular material is also crucial to the question of cluster dissolution (Pelupessy & Portegies Zwart, 2011; Pfalzner, 2011; Portegies Zwart *et al.*, 2010).

Stellar feedback is also recognized as having significant influence on galactic and extragalactic scales. For instance, without strong stellar feedback, cosmological models predict around 10 times the stellar mass found in real galaxies (e.g. Cole *et al.*, 2000; Kereš *et al.*, 2009). Feedback from massive stars can also drive galactic winds from starburst galaxies (e.g. Adelberger *et al.*, 2003; Axon &

Taylor, 1978; Bland & Tully, 1988; Heckman *et al.*, 2000), and appears to be responsible for the low star formation efficiency of galaxies with dark matter haloes somewhat less than the halo mass of the Milky Way (Guo *et al.*, 2010). Ionizing radiation from massive stars is also important for the ionization of galaxies (Reynolds, 1984) and the reionization of the early universe (Fan *et al.*, 2006).

In order to understand the effects of massive stars on galactic scales, however, we must first understand their impact on their local (cluster) environment. The extent to which a cloud is affected by stellar feedback is clearly dependent on a number of parameters, including the mass of the cloud and the stellar cluster, the structure of the cloud, the position of the cluster relative to the cloud, and the age of the system. However, the degree to which stellar feedback processes (stellar winds, SNe and ionizing radiation) couple to the clumpy, inhomogeneous molecular clouds which initially surround a massive stellar cluster is exceedingly ill-determined, and the dominant feedback process is still to be settled (e.g. Draine & Woods, 1991; Lopez *et al.*, 2011; Matzner, 2002; Pellegrini *et al.*, 2011; Wang *et al.*, 2010; Yorke *et al.*, 1989).

This thesis examines feedback from massive stellar winds and supernovae in a clumpy environment using state-of-the-art hydrodynamical simulations. This Chapter provides a review of the current understanding of the nature and structure of massive star forming environments and the effect that massive stars have on them.

1.1 Star Formation and GMCs

Within the Milky Way there are approximately 300 Giant Molecular Clouds (GMCs) with masses of the order of $10^{5--6}\,\mathrm{M}_{\odot}$. GMCs have average densities of $\sim\ 100\,\mathrm{cm}^{-3}$, but as they are clumpy and filamentary in structure there are regions of much higher density called clumps, and regions with still higher density known as cores (see Table 1.1). Understanding the properties of these GMCs is important as these are the primary sites for star formation.

The susceptibility of a clump to collapse under its own self gravity can be approximately assessed by examining the Jeans mass (Jeans, 1902), which can be expressed as:

$$M_J = \left(\frac{5k_bT}{G\mu m_p}\right)^{3/2}\left(\frac{3}{4\pi}\right)^{1/2}\rho^{-1/2} \tag{1.1}$$

where T and ρ are the local temperature and density of the clump, k_b is the Boltzmann constant, G is the gravitational constant and μ is the molecular weight of the material in the clump. Clearly, a high density favours collapse whilst a high temperature favours a large Jeans mass. If the mass of any given region exceeds M_J then it is susceptible to gravitational collapse. The Jeans mass is around $50\,\mathrm{M}_{\odot}$ for the typical molecular clump noted in Table 1.1. However, there are many clumps observed in GMCs which are above this mass and haven't undergone gravitational collapse.

The timescales over which cloud collapse occurs can offer insight into the nature of the stars that are formed in these regions. The timescale for gravitational collapse is given by the free-fall time:

Table 1.1: Typical properties of molecular clouds over a multitude of scales.

	GMC	Molecular cloud	Molecular clump	Cloud core
Mean radius (pc)	20	5	2	0.08
Density n(H_2) (cm^{-3})	100	300	10^2-10^3	10^5
Mass ($M_\odot$)	10^5	10^4	10^3	10
Temperature (K)	15	10	10	10

$$t_{ff} = \left(\frac{3}{2\pi G\rho}\right)^{1/2} \tag{1.2}$$

where ρ is the average mass density of the material. Again, using the typical values for a GMC clump noted in Table 1.1, the average free-fall time would be approximately 6.5×10^6 yrs. The collapsing material comes together in the centre of the collapse region and a protostar is formed. The gravitational potential energy of the material is converted into thermal energy. The timescale over which this happens is given by the Kelvin-Helmholtz time.

Within GMCs, the average star formation rate per free-fall time (SFR_{ff}) is only approximately 2% (Kennicutt, 1998), despite the fact that many clumps are observed to exceed the Jeans mass. This implies that something must be preventing the gas contained in GMCs from collapsing, as thermal pressure alone is not sufficient to support these clouds against their self-gravity.

Magnetic fields are a candidate for providing such support. Even relatively weak magnetic fields have been theorized to give support against gravity in dense, massive clouds (Mouschovias, 1991; Shu *et al.*, 1987). However, more recently the role of magnetic fields in supporting GMCs is thought to be more secondary in nature (Krumholz *et al.*, 2006). Crutcher (2010) argues that a significant

population of molecular clouds must have very small magnetic field strengths, which implies that for many molecular clouds magnetic fields do not dominate as a mechanism for support.

Supersonic turbulence may be regarded as another mechanism supporting larger masses (e.g. see the review on supersonic turbulence by Mac Low & Klessen, 2004). However, supersonic turbulence dissipates on such a short time scale compared to cloud lifetimes that it will not be of much significance unless there is something continually driving it. In GMCs where stars have formed, the energy and momentum input from massive stars is a very plausible candidate for support against gravity, and for driving the turbulence in the clouds (McKee & Ostriker, 2007). The main sources of stellar feedback are noted in detail in Section 1.2.

Understanding the extent to which massive stars can affect feedback in small GMC clumps can help to build up a picture of star formation within galaxies. The efficiency with which the gas contained within galaxies is converted to stars, and the extent to which this process can affect further star formation will cause the observed properties of galaxies to evolve over time. A full understanding of the evolution of galaxies therefore requires an understanding of these feedback effects.

1.1.1 Massive Star Formation

The formation of massive stars ($M > 8\,M_{\odot}$) is not as well understood as that of their low mass counterparts, and yet the effect they have on their natal environment is extreme. The high temperatures and luminosities produced by a

massive star results in the injection of large amounts of kinetic energy and ionizing radiation into the ISM. The nucleosynthesis reactions occurring within their core produce heavy elements which are deposited into the surroundings during their lifetimes by continuous mass loss, discrete eruptions and in their inevitable explosion at the end of their lives.

Massive stars form extremely quickly, with a Kelvin-Helmholtz timescale of only $\sim 10^{4-5}$ yrs. For stars with masses above $8\,M_{\odot}$, the Kelvin-Helmholtz timescale is shorter than the free-fall time, which implies that fusion begins in these stars before the gas has finished collapsing, leaving them still embedded in dense material whilst they begin hydrogen burning. This makes observing these stars rather difficult.

Whereas low mass star formation is reasonably well understood, there are problems when trying to scale this process up for massive stars. Low mass star formation results from the gravitational collapse of a clump within a GMC. When the temperature at the core of the collapsing material becomes hot enough fusion begins. Rotation of the protostar becomes important as an accretion disc is formed around it. Winds and outflows from the protostar begin to disperse the surrounding envelope of cloud material. Due to the much shorter Kelvin-Helmholtz timescale for massive stars, however, there is only a short time for the accretion process to occur before the ionization and intense radiation pressure from the protostar halts it (Wolfire & Cassinelli, 1987). This makes it difficult to understand massive star formation as just a scaled up version of low mass star formation.

Early 1D simulations performed to try and understand the physics which could allow a massive star to form agreed that the growing radiation pressure halts and

reverts the accretion flow onto a massive star yielding a theoretical upper mass of approximately $40\,M_\odot$ (Edgar & Clarke, 2004; Kahn, 1974; Larson & Starrfield, 1971; Wolfire & Cassinelli, 1987; Yorke & Kruegel, 1977). However, recent 3D hydrodynamical models indicate that accretion by a disc could circumvent the proposed barrier to massive star formation by shielding the infalling material from the intense radiation field of the central object (Krumholz *et al.*, 2009; Kuiper *et al.*, 2010). Some of these results are summarized in Table 1.2.

The simulations in Krumholz *et al.* (2007, 2009) are simulated for approximately one third and just over one free-fall time of the pre-stellar core, respectively. As these simulations are quite short, the accretion phase has not finished by the time the simulations end (denoted by a "+" in Table 1.2) and there is likely to be further accretion occurring were they to run for longer. The addition of an accretion disc by Kuiper *et al.* (2010) allows stars much more massive than the previous work to be formed. Indeed, for the most massive pre-stellar core in their work, $480\,M_\odot$, the simulation did not last until the end of the accretion phase, and so again further accretion seems to be a natural continuation of the run. The simulation time for the initial core masses of $60\,M_\odot$, $120\,M_\odot$, $240\,M_\odot$ and $480\,M_\odot$ were 14, 10, 7 and 2 free-fall times respectively. These simulations generate the most massive stars to date, and are a promising start at truely understanding the underlying physics in the formation processes of such important astronomical objects.

Table 1.2: Overview of the multi-dimensional radiation hydrodynamic simulations of massive star formation.

Authors	M_{core} ($M_\odot$)	t_{end} (kyr)	M_* ($M_\odot$)
Yorke & Sonnhalter (2002)	30	25	31.6
	60	45	33.6
	120	70	42.9
Krumholz *et al.* (2007)	100 (A)	20^+	5.4 (+3.4)
	100 (B)	20^+	8.9 (+2.4)
	200	20^+	8.6 (+6)
Krumholz *et al.* (2009)	100	75^+	41.5+29.2 (+28.3)
Kuiper *et al.* (2010)	60	939	28.2
	120	489	56.5
	240	226	92.6
	480	41^+	137.2 (+67.8)

Notes: The columns from left to right state the authors, the initial pre-stellar core mass, the evolutionary time simulated and the final star mass. A "+" in the t_{end} column means that the accretion phase is not simulated until the end. Only the formation of the most massive stars are considered here; all other stars formed have masses below $1\,M_\odot$. In the case of Krumholz *et al.* (2007), the "(A)" and "(B)" in the M_{core} column mark the usage of different perturbation fields of the initial state (same labels as in the original paper) and the M_* column gives additionally the remnant disc mass around the primary star. In the case of Krumholz *et al.* (2009) and the $480\,M_\odot$ study from Kuiper *et al.* (2010), the M_* column gives additionally the remnant disc plus envelope mass. Data from this table was compiled by Kuiper *et al.* (2010).

1.1.2 Initial Mass Function and Mass Segregation in Clusters

Stars usually form not individually, but rather in clusters ranging from tens of stars to very dense groups containing thousands of stars. The initial mass function (IMF) is a convenient way of characterizing the relative number of stars as a function of their mass. The IMF for stars above $\sim 1\,M_\odot$ follows a power-law with

a logarithmic slope of -2.35, first found by Salpeter (1955). The exact form of the function is:

$$\xi(M) = \xi_0 M^{-2.35} \tag{1.3}$$

where ξ_0 is a constant which sets the local stellar density. At $1\,M_\odot$ there is a turnover of the IMF, yielding distinct regimes at masses lower than this (Chabrier, 2003). Since the stellar luminosity from galaxies is dominated by high mass stars, the Salpeter IMF is a valuable probe for the field of galaxy evolution as well as for star formation.

Currently, the two favoured theories for the determination of the slope are turbulent fragmentation of the parent cloud (Padoan *et al.*, 2007) or competitive accretion (Bonnell & Bate, 2006). The factors which determine an upper mass limit (m_{up}), should it exist, remains unknown, although some authors argue that a limit close to $150\,M_\odot$ is plausible (Figer, 2005; Koen, 2006). Crowther *et al.* (2010) argue that if massive stars above $150\,M_\odot$ *did* exist then they would be located in very high mass ($\geq\ 10^4\,M_\odot$), very young (≤ 2 Myrs) stellar clusters. They would be incredibly luminous, since $L \propto M^{1.5}$ for zero-age main sequence (ZAMS) stars above $85\,M_\odot$, and they would certainly possess very powerful stellar winds. However, they would be short-lived, with evolution to become a WR star occuring within 1–2 Myrs. Crowther (2012) argue against an upper mass limit, as they have inferred initial masses of 165-320 $M_\odot$ for the massive star forming region R 136, the central ionizing cluster of 30 Dor, which has a total stellar mass of $\sim\ 55,000\,M_\odot$ and an estimated age of 1–2 Myrs. Previous estimates of the stellar masses in this region were 120–155 $M_\odot$ (Massey & Hunter, 1998).

However, statistics of high mass clusters for which accurate stellar masses have been determined remain very poor. Should an upper mass limit actually exist, one viable mechanism for halting accretion onto the protostar is increasingly strong feedback (Zinnecker & Yorke, 2007).

Larson (1998) suggested that the IMF should vary with the pressure and temperature of the star-forming cloud, with regions at higher temperatures producing stars with a higher average mass. Also, fragmentation of a cloud will be easier if the gas can cool, so primordial gas without any metals should form more massive stars. However, so far there is no convincing evidence for a variable IMF, implying that it may well be universal.

Some clusters show mass segregation, where the most massive stars are preferentially found near the centre of the cluster. Mass segregation can be dynamical or primordial in origin. Arguments for dynamical mass segregation include the merging of several subclusters (McMillan *et al.*, 2007), and the dynamical evolution of a cluster whereby the more massive stars gravitate towards the central potential well. Simulations by Yu *et al.* (2011) confirm that mass segregation can arise in an initially cool and clumpy cluster, especially if there is a radially dependent velocity distribution, which would lead to higher velocities towards the centre of the cluster. On the other hand, due to the higher density of gas at the centre of a clump or core than in the outskirts the Jeans mass at the centre will be smaller (see Section 1.1), allowing smaller protostars to be formed. These smaller protostars are then able to accumulate gas and evolve into massive stars more easily than those formed on the outskirts due to competitive accretion. This is an example of primordial mass segregation (Bonnell *et al.*, 1997; Larson, 1982; Murray & Lin, 1996). In addition to the mechanism of competitive accretion, it

is argued that the protostars are so rich in the cluster centre that they can merge into the massive stars (Bonnell & Bate, 2005; Bonnell *et al.*, 1998).

However, Ascenso *et al.* (2009) argue that mass segregation may not be a true phenomenon and may be an observation bias in some cases. Er *et al.* (2009) argue that it may be a temporary effect from the random motions of massive stars.

Mass segregation has been observed in many stellar clusters, including the Trapezium (Hillenbrand, 1997; Hillenbrand & Hartmann, 1998), NGC 6611 (Bonatto *et al.*, 2006), M 17 (Jiang *et al.*, 2002), Westerlund 1 (Lim *et al.*, 2013), NGC 1333 (Lada *et al.*, 1996), NGC 2244 and NGC 6530 (Chen *et al.*, 2007). However, there are some stellar clusters which do not show signs of mass segregation even though they are old enough for dynamic segregation to occur. One example is cited by Wang *et al.* (2008), who find an absence of mass segregation in the Rosette nebula.

1.2 Stellar Feedback

Massive stars deposit a considerable amount of mechanical and thermal energy into the ISM by a variety of processes. On galactic scales the more important feedback mechanism is supernova explosions (e.g. Dekel & Silk, 1986; McKee & Ostriker, 1977). However, the rate of explosions is relatively low compared with the dynamical timescale in star forming regions, and so supernovae are relatively ineffective at regulating star formation on much smaller scales, in the vicinity of the progenitor.

On scales of a few pc, stellar winds and photoionization are likely to play important roles in regulating the formation of stellar clusters (Tenorio-Tagle *et al.*,

1986, 1999, 2003). Whilst the star formation rate may be enhanced by the fragmentation of shells of material swept up by the winds or expanding HII regions (Elmegreen *et al.*, 2002; Whitworth & Francis, 2002) the evacuation of gas away from the immediate region of the OB star will limit the total fraction of the natal cloud that can be converted into stars.

The dominant source of feedback into GMCs is still hotly debated (e.g. Draine & Woods, 1991; Lopez *et al.*, 2011; Matzner, 2002; Pellegrini *et al.*, 2011; Wang *et al.*, 2010; Yorke *et al.*, 1989), and is likely to vary depending on the specific conditions of any individual system. In the following subsections feedback from winds, photoionization and supernovae will be discussed.

1.2.1 Winds

Winds from massive stars clear out cavities in the interstellar medium (ISM). These bubbles impact their surrounding molecular clouds and the star formation occuring within them. Stellar winds can have a significant role in the evolution of starburst galaxies, as they can transfer heavy element enriched gas from the central regions to the outer parts of the galaxy. Within the literature there are two well known models for the structure of a wind-blown bubble.

1.2.1.1 The Castor *et al.* Model

The Castor *et al.* (1975) model has a freely expanding wind, surrounded by a region of shocked wind material. These two regions are separated by a reverse or inner shock (r_a). Outside the shocked wind material is a swept-up shell of shocked ISM material, which will typically collapse into a thin, cold shell as a result of radiative cooling. These two regions of shocked material are separated by

a contact discontinuity (r_b). The outer or forward shock (r_c) propagates into the ISM, sweeping up more material into the shell (this structure is demonstrated in the schematic in the left panel of Fig. 1.3). This model assumes spherical expansion, and therefore that the ISM is homogeneous.

Following the method of Dyson & Williams (1980), an expanding stellar bubble of this structure has radius and expansion speed:

$$R_s \approx \left(\frac{125 L_w t^3}{154 \pi \rho_0}\right)^{\frac{1}{5}} \sim 10 L_{37}^{\frac{1}{5}} n_3^{-\frac{1}{5}} t_M^{\frac{3}{5}} \,\mathrm{pc}, \tag{1.4}$$

and

$$\dot{R}_s \approx \left(\frac{243 L_w}{3850 \pi \rho_0 t^2}\right)^{\frac{1}{5}} \sim 6.2 \times L_{37}^{\frac{1}{5}} n_3^{-\frac{1}{5}} t_M^{-\frac{2}{5}} \,\mathrm{km\,s^{-1}}, \tag{1.5}$$

where L_w is the mechanical luminosity of the stellar wind, ρ_0 is the mass density of the ambient medium and t is the bubble age. L_{37}, n_3 and t_M are normalised values such that L_{37} is the luminosity in units of 10^{37} ergs, n_3 is the density in units of $10^3\,\mathrm{cm^{-3}}$ and t_M is the time elapsed since the wind 'turned on' in units of Myrs.

The radial structure of such a bubble around a massive star in a uniform ambient medium with a constant stellar wind was simulated and is demonstrated in Fig. 1.1. The top panel shows the density and the bottom panel the temperature structure at a time of $t \sim 1.0\,\mathrm{Myrs}$, which represents a time during the main sequence (MS) phase for a massive star with $\dot{M}_w = 5 \times 10^{-7}\,\mathrm{M_\odot\,yr^{-1}}$ and $v_w = 2000\,\mathrm{km\,s^{-1}}$, typical of the mass-loss rates for massive stars presented in Vink *et al.* (2000, 2001). The ambient density of the surrounding ISM is assumed to be $\rho = 10^{-24}\,\mathrm{g\,cm^{-3}}$ and the ambient temperature is $T = 1 \times 10^4\,\mathrm{K}$.

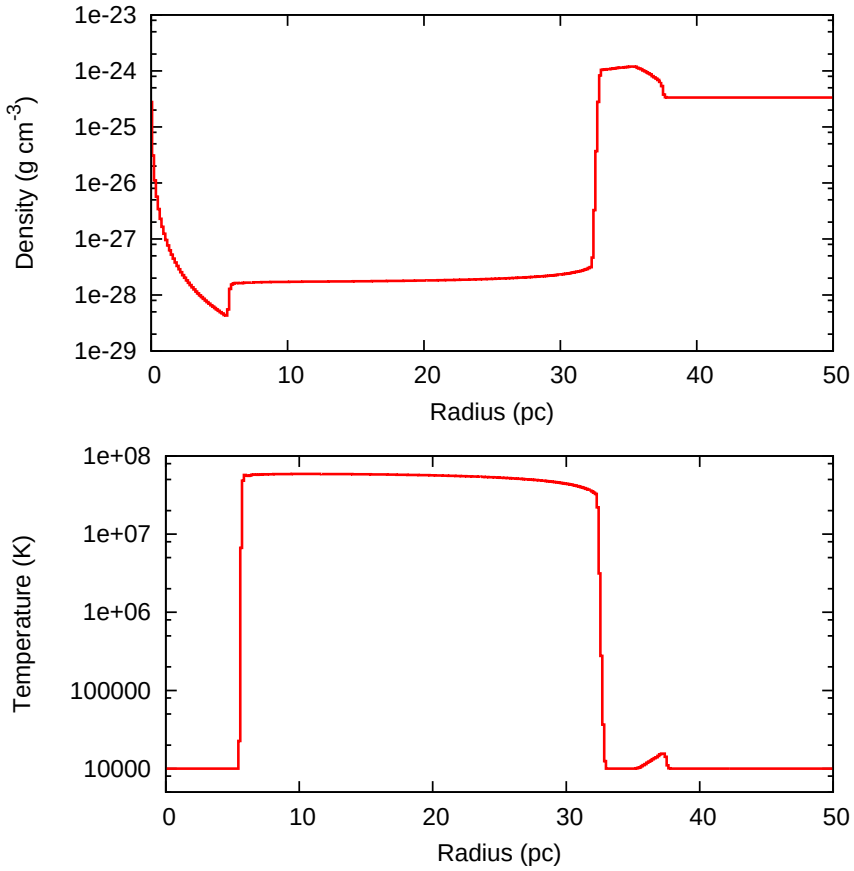

Figure 1.1: Radial density and temperature structure of a stellar wind around a massive MS star calculated by a hydrodynamical code. [Top] shows the density and [Bottom] shows the temperature of the bubble. The stellar wind parameters are $\dot{M}_w = 5 \times 10^{-7}\,\mathrm{M}_\odot\,\mathrm{yr}^{-1}$ and $\mathrm{v}_w = 2000\,\mathrm{km\,s}^{-1}$.

The density of the freely expanding wind region at the centre of the bubble falls off as r^{-2}. The temperature in this region is assumed constant at $\approx 10^4\,\mathrm{K}$. The location of the reverse shock is seen as the jump in density and temperature at $\mathrm{t}_a \approx 6\,\mathrm{pc}$. The region of shocked wind material has approximately constant temperature ($\mathrm{T} \sim 5 \times 10^7\,\mathrm{K}$) and density ($\rho \sim 2 \times 10^{-28}\,\mathrm{g\,cm}^{-3}$). This region occupies by far the largest volume (c.f. the left panel of Fig. 1.3) in the bubble structure. On the other side of contact discontinuity at $\mathrm{r}_b = 32\,\mathrm{pc}$ is the cold,

swept-up shell. The compression of the swept-up gas and the thickness of the shell is determined by the Mach number of the outer shock, which here lies at $r_c = 37\,\mathrm{pc}$. Beyond this point is the ambient medium at $\rho = 10^{-24}\,\mathrm{g\,cm^{-3}}$ and $T = 1\times10^4\,\mathrm{K}$. The bubble has an expansion speed of $\dot{R}_s = 23\,\mathrm{km\,s^{-1}}$, in excellent agreement with Equation. 1.5.

The Castor *et al.* model has been widely applied by many other authors. Weaver *et al.* (1977) included thermal conduction between the hot bubble interior and the cold swept-up shell in their model, as well as modifying the bubble to take radiative losses into account. Harper-Clark & Murray (2009) allowed wind material to leak through holes in the expanding outer shell (see Section 1.2.1.3). More recently, van Marle *et al.* (2012) have performed 2D simulations of the collision of the bubbles around two nearby massive stars, as would be likely for massive stars formed within a cluster. Interestingly, they found that the collective bubble was too large to be sustained purely by the lower mass star once the more massive star had exploded, causing the outer shell to disintegrate.

1.2.1.2 The Chevalier & Clegg Model

Chevalier & Clegg (1985) assume a spherically symmetric wind with steady mass and energy input into the wider ISM. Their work was originally used to describe outflows from starburst galaxies. Stevens & Hartwell (2003) applied the steady state model to super star clusters, where each star contained within the cluster has an individual wind and bubble of the same structure as described by Castor *et al.* (1975). These individual bubbles then combine together to form a global superbubble formed by a spherically symmetric wind driven from a central region of uniform mass and energy deposition. This model has a steady input of energy

and material into the wider ISM, but assumes the ISM has no affect on the wind. A sonic surface exists at the outer radius of the stellar cluster, R_c, with the cluster wind becoming supersonic outside of this.

Cantó *et al.* (2000) carried out hydrodynamic calculations of such a cluster wind assuming a spherical cluster consisting of ∼30 identical stars. These calculations, and those of Stevens & Hartwell (2003), assume a non-uniform stellar distribution, whereas the original Chevalier & Clegg work assumed that mass and energy injection is uniform throughout the region. Cantó *et al.* (2000) showed that their non-uniform distribution generally reproduced the results of the Chevalier & Clegg model despite this difference.

Fig. 1.2 shows the radial structure for the cluster wind simulated by Stevens & Hartwell (2003) based on the Chevalier & Clegg (1985) model. The radius of the cluster is set to $R_c = 1\,\mathrm{pc}$, the central temperature of the cluster is $5.8\times10^7\,\mathrm{K}$, the number density is $0.67\,\mathrm{cm}^{-3}$ and the cumulative X-ray luminosity of the region within a radius R_c is $L_X = 5.1 \times 10^{32}\,\mathrm{ergs\,s}^{-1}$. The vast majority of the X-ray emission originates from the cluster, with the volume outside R_c contributing only 15% of the total X-ray luminosity. The reason for this is the sharp fall-off in both density (bottom left panel in Fig. 1.2) and the temperature (top right panel) outside the cluster radius, which more than compensates for the increasing volume of the emission region.

The solid line in each of the panels represents $\eta = 1$, where η is a prescription for the thermalization efficiency of the cluster, or the fraction of the kinetic energy of stars and supernovae in the cluster which are thermalized. Any energy which is not thermalized is assumed to be lost to the system via radiative losses. Strickland & Stevens (2000) make an argument for a very efficient thermalization of energy

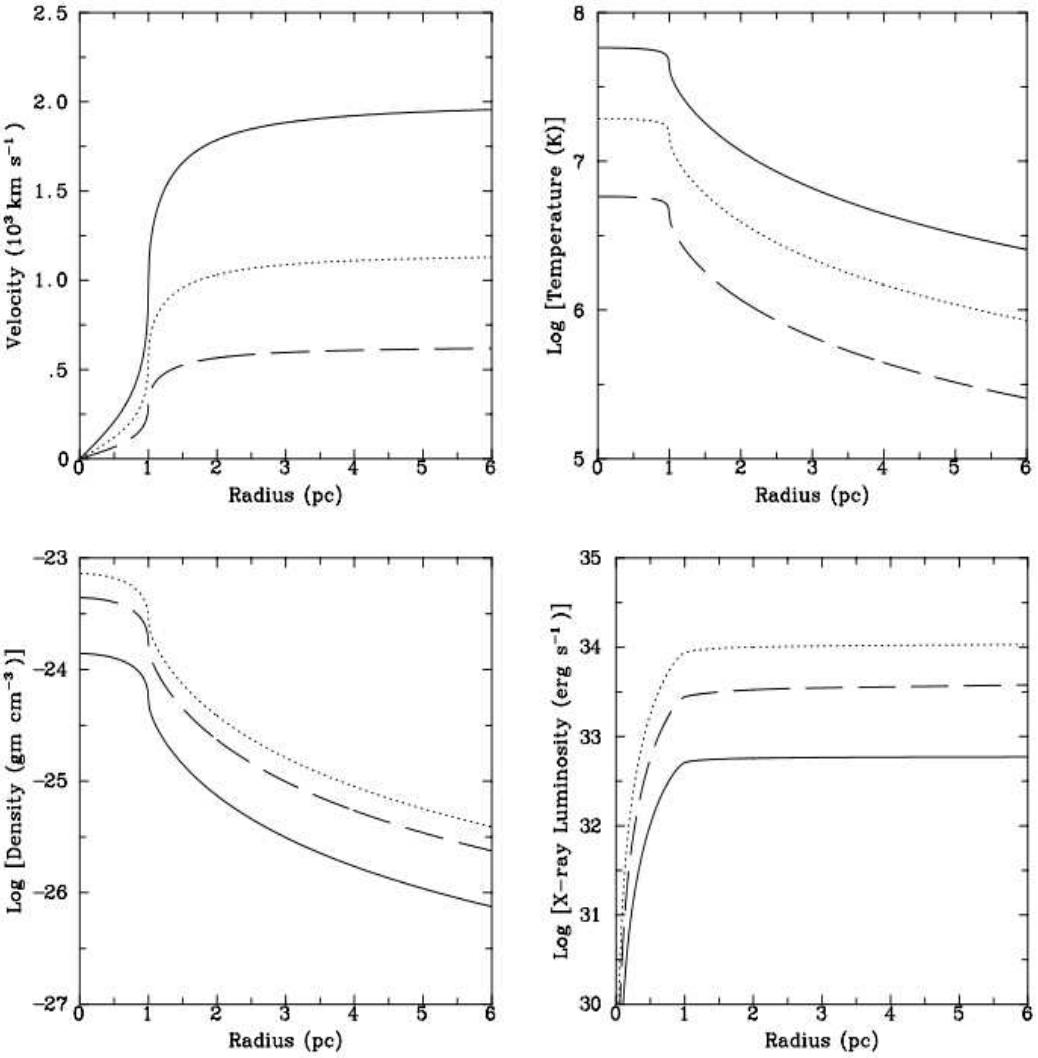

Figure 1.2: The radial structure for the cluster wind, as calculated from the Chevalier & Clegg (1985) model. Shown are the radial profiles for the wind velocity (top left panel), gas temperature (top right), density (bottom left) and the cumulative X-ray luminosity (bottom right). The standard model (solid line) is for a star cluster with a stellar mass injection rate of $\dot{M}_* = 10^{-4}\,\mathrm{M}_\odot\,\mathrm{yr}^{-1}$, $\bar{V}_* = 2000\,\mathrm{km\,s}^{-1}$, $\eta = 1$ and no additional mass loss ($\dot{M}_{cold} = 0$). The second model (dashed line) is identical, except $\eta = 0.1$; and the third model (dotted line) has $\eta = 1$ and $\dot{M}_{cold} = 2\times10^{-4}\,\mathrm{M}_\odot\,\mathrm{yr}^{-1}$. Taken from Stevens & Hartwell (2003).

($\eta = 1$), whereas other authors (e.g. Bradamante *et al.*, 1998) argue for a much lower thermalization efficiency of only a few percent. This model also assumes no additional mass loading from cold material being injected into the cluster wind ($\dot{M}_{cold} = 0$). The mass-loss rate of the cluster is $\dot{M}_* = 10^{-4}\,\mathrm{M}_\odot\,\mathrm{yr}^{-1}$, and the wind velocity is $\bar{V}_* = 2000\,\mathrm{km\,s}^{-1}$. The dashed line is the same model but with $\eta = 0.1$. The dotted line has $\eta = 1$, but has mass-loading with $\dot{M}_{cold} = 2 \times 10^{-4}\,\mathrm{M}_\odot\,\mathrm{yr}^{-1}$, making a combined $\dot{M}_{\mathrm{tot}} = 3 \times 10^{-4}\,\mathrm{M}_\odot\,\mathrm{yr}^{-1}$.

It is interesting to note that both mass loading and a low thermalization efficiency ($\eta < 1$) lead to lower cluster temperatures, but also often higher X-ray luminosities.

In a series of papers, Silich *et al.* has extended the Chevalier & Clegg model to include the effect of radiative losses (e.g. Silich *et al.*, 2004, 2009). They demonstrate that cooling may drastically modify the temperature distribution and the observational appearance of cluster winds if the rate of injected energy approaches a critical value. They also claim that some HII regions can only survive if the majority of the mechanical energy is lost within the star cluster volume due to the effect of radiative cooling.

1.2.1.3 Wind Leakage

Harper-Clark & Murray (2009) have recently modified the Castor *et al.* model to try to describe a more realistic bubble expanding into an inhomogeneous environment, as shown in Fig. 1.3. This causes the shell to expand asymmetrically into the ISM, which causes gaps in the shell through which hot wind material can escape. This "leakage" reduces the expansion speed and therefore the size of the bubble, as well as the interior pressure. As the wind material is not com-

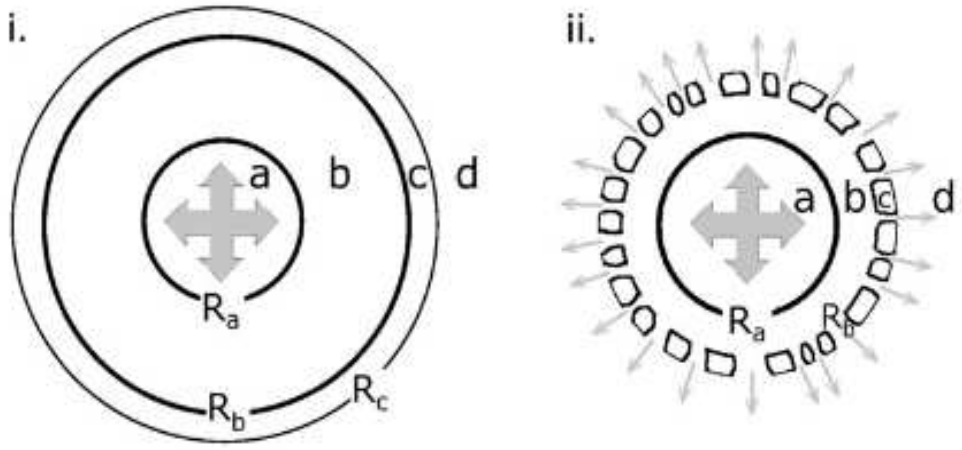

Figure 1.3: Cartoons of the Castor *et al.* bubble (i) and the modified Castor *et al.* bubble (ii). The Castor *et al.* bubbles have a four zone structure. Zone a is a hypersonic stellar wind; zone b is a shocked stellar wind and evaporated material from the shell; zone c is the bubble shell; and zone d is the ambient ISM. ii - The structure of the modified Castor *et al.* bubble, showing the leaking from the shell. Note the larger size of region a, smaller size of region b and material escaping into region d. Taken from Harper-Clark & Murray (2009).

pletely confined the pressure within the bubble is lower than in a completely confined model. This in turn will mean that the region of shocked wind material is proportionally smaller than in the Castor *et al.* (1975) model, whilst the freely expanding wind will be proportionally bigger.

This modified Castor *et al.* bubble fits better to observations of stellar clusters. Harper-Clark & Murray (2009) compared the predicted X-ray luminosity and pressure of the Castor *et al.* (1975) and Chevalier & Clegg (1985) models with observations of Tr 16, a massive stellar cluster in the Carina Nebula, the results of which are presented in Fig. 1.4. The top two black lines represent the X-ray luminosity and pressure within the bubble as a function of radius for the Castor model, whilst the bottom two blue lines represent the X-ray luminosity and bubble pressure as a cumulative function of radius for the Chevalier & Clegg

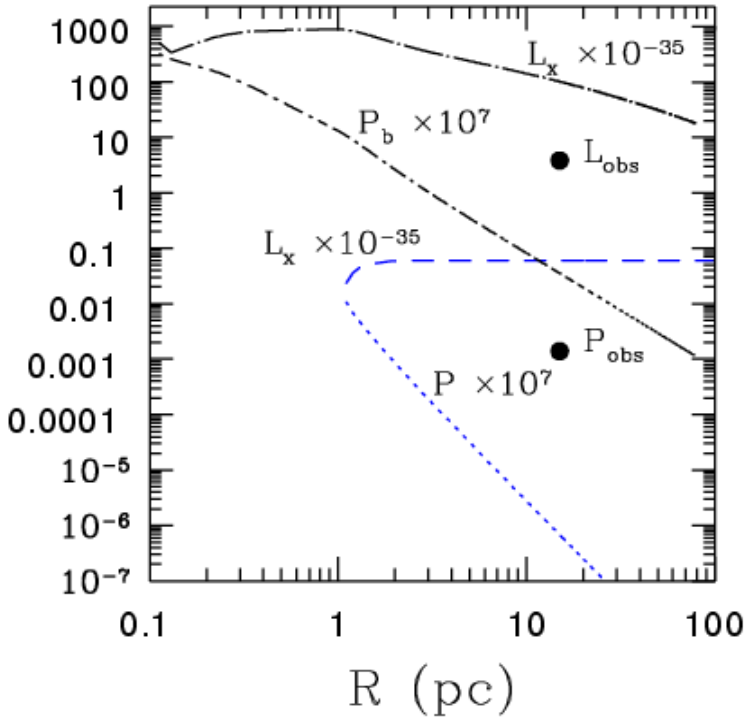

Figure 1.4: Plot of the scaled X-ray luminosity and pressure calculated as a function of radius for the two classes of (unmodified) models for Tr 16. The Castor model is plotted as a function of bubble size whereas the Chevalier model is plotted as a cumulative function of radius (due to its steady state nature). The upper L_X and P lines (black) are for the Castor model and the lower lines (blue) for the Chevalier model. The two dots show the observed pressure (lower) and X-ray luminosity (upper). In the Castor *et al.* model the pressure is roughly constant for $r<R_b$, but this constant pressure is a function of the bubble radius, as shown. In the Chevalier & Clegg model there is no bubble, but pressure decreases with increasing radius. Taken from Harper-Clark & Murray (2009).

model. The higher relative pressure of a confined bubble creates a larger region of hot, shocked gas which leads to greater X-ray emission (see Section **??**). The two labeled dots in Fig. 1.4 show the observed pressure and X-ray luminosity for Tr 16. Clearly both the pressure and X-ray luminosity fall between both models, adding credence to the leaky-bubble model of a partially confined bubble. The

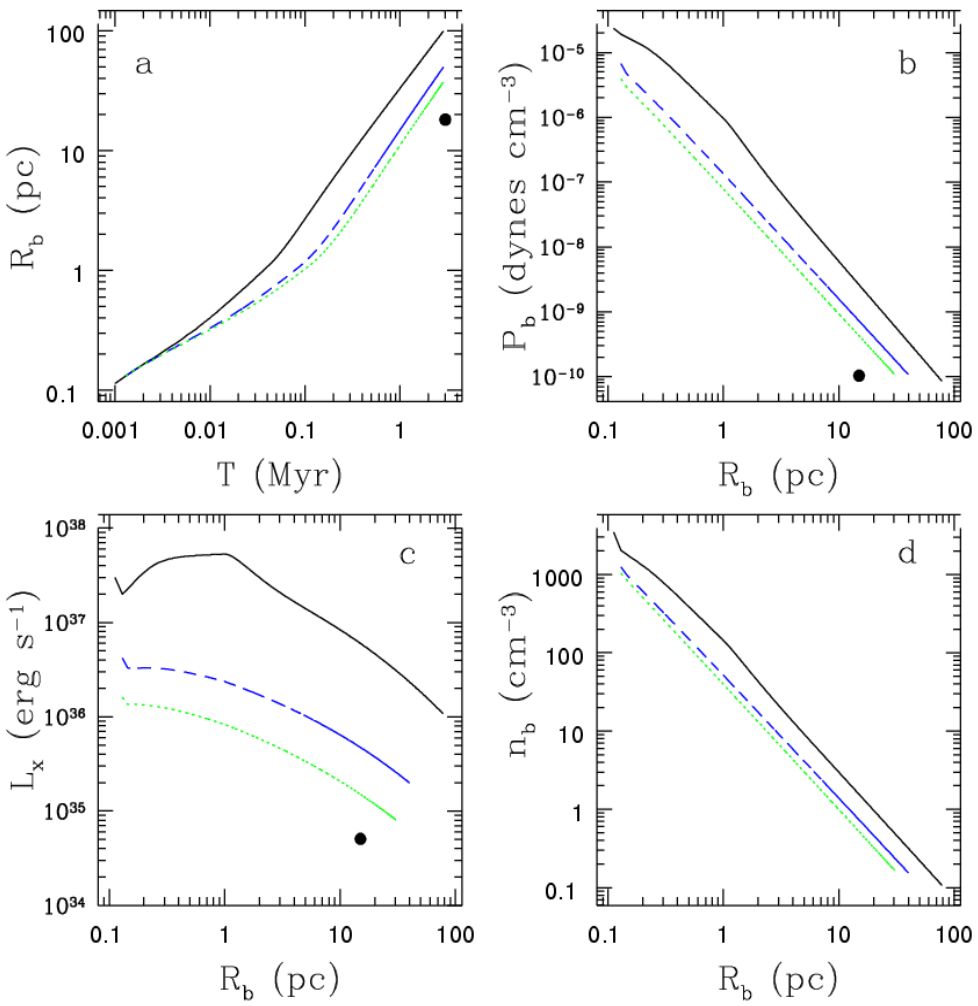

Figure 1.5: Graphs for three modified Castor simulations with $C_f = 1$ (black solid line), $C_f = 0.65$ (blue dashed line) and $C_f = 0.3$ (green dotted line). (a) Radius versus time, (b) pressure versus radius, (c) X-ray luminosity versus radius and (d) number density inside the bubble versus radius. Observed results are shown as a black dot. Taken from Harper-Clark & Murray (2009).

observed X-ray luminosity is $L_X = 6.1 \times 10^{34}\,\mathrm{ergs\,s^{-1}}$ at 2.6 kpc (Seward *et al.*, 1979). This is, in fact, ten times higher than predicted by the Chevalier & Clegg model, but one hundred times lower than predicted by the Castor *et al.* model.

In order to compare their new model against the results from these two models

and observations of Tr 16, Harper-Clark & Murray (2009) considered three porosity values; a completely confined bubble with covering factor $C_f = 1.0$, a mostly confined bubble with $C_f = 0.65$ and a poorly confined bubble with $C_f = 0.3$. The results of their analysis are presented in Fig. 1.5. The observed results are shown as black dots in each panel. Unsurprisingly, as C_f decreases the shell expands more slowly, the bubble interior pressure is lower, as is the predicted X-ray luminosity. It would also appear that the X-ray luminosity is much more sensitive to changes in the covering factor of the bubble than the other measures explored. The degree of porosity of a bubble is therefore important for understanding X-ray observations of stellar clusters.

Many observations of massive clusters support the possibility of hot gas leakage. Most intuitively perhaps, if it is possible to see the stars in a cluster then there must be a gap in the shell along the observers line of sight (Smith & Brooks, 2007). Further support comes from observations of G298-0.34, which is a GMC being affected by the massive star contained within it (see Fig. 1.6). The white solid oval indicates the likely position of the bubble blown by this massive star, whilst the white dotted oval indicates the extent to which radio emission is observed. The fact that the radio emission is observed to much further distances than the bubble indicates that some of the hot wind material is able to leak through holes in the bubble wall. The five red circles show regions where there is further star formation occuring. This is suspected to be triggered by the central star due to the spatial co-incidence with the bubble (see Section **??** for more details on triggered star formation).

Further possible evidence of leakage from bubbles can be seen in RCW 49, which is a giant HII region powered by Westerlund 2, an OB association containing

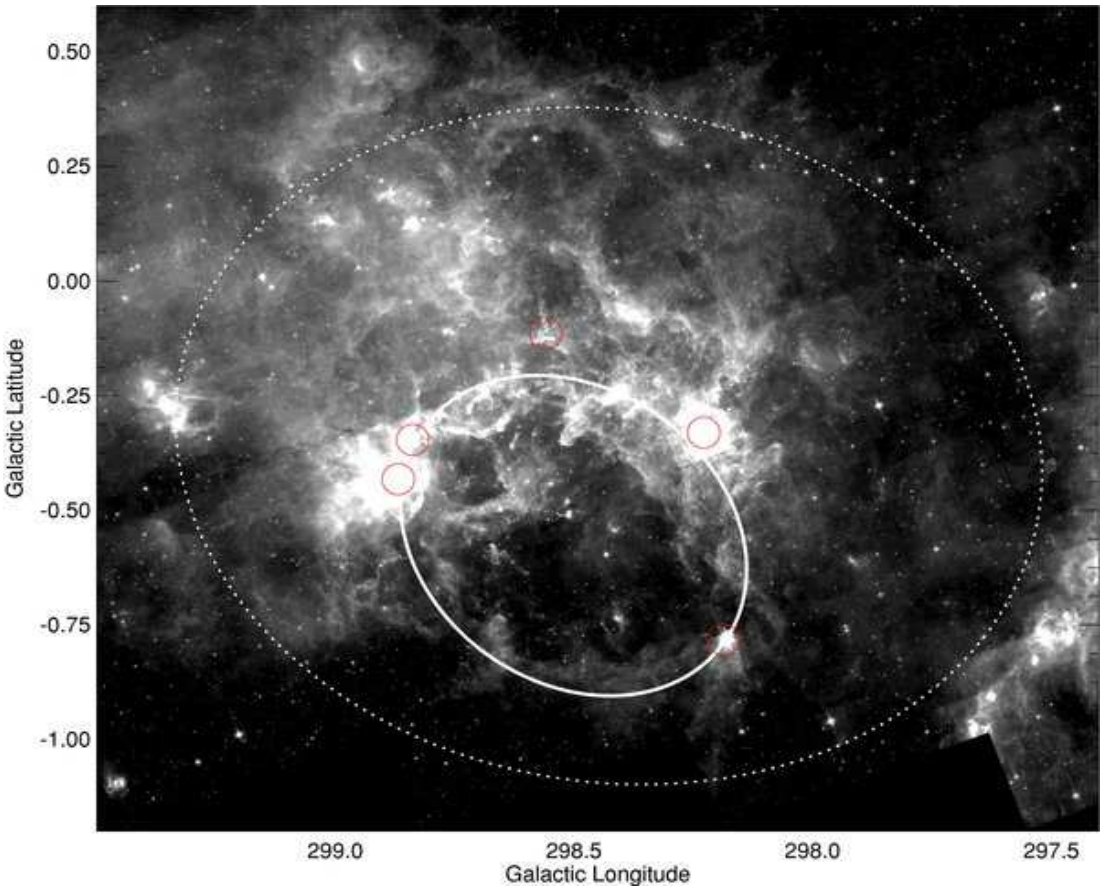

Figure 1.6: A Spitzer Glimpse image of G298-0.34, a GMC in the process of being blown apart by an invisible central massive star cluster (Murray *et al.*, 2010). The small red dashed ellipses show compact HII regions from triggered star formation. The solid oval is the bubble wall and the large dotted oval is the extent of the WMAP source, suggesting the hot gas is leaking from the bubble (Harper-Clark & Murray, 2009). Taken from Harper-Clark & Murray (2011).

at least a dozen OB stars. The earliest is an O6 star, and 5 O7 stars and two Wolf-Rayet stars have also been detected (Moffat *et al.*, 1991). The presence of these massive stars implies a cluster age of 2–3 Myrs (Piatti *et al.*, 1998).

Radio continuum observations by Whiteoak & Uchida (1997) revealed the presence of two wind-blown shells at the centre of RCW 49. One of these is closed and is most likely blown by the WR star WR 20b (see Fig. 1.7). The

other shell is centered on the OB association Westerlund 2, but there is another WR star (WR 20a) in this region as well. Due to the strong wind produced by a WR star, it is likely that WR 20a may govern the dynamics of the shell. This shell shows a large blister extending to the west in the radio data. *Chandra* X-ray observations by Townsley *et al.* (2005) have shown over 100 point sources which are spatially coincident with Westerlund 2. However, there is also a diffuse component centered on the ionizing cluster, implying that RCW 49 is filled with X-ray emitting gas.

Povich *et al.* (2008) have discovered three bowshocks which are associated with RCW 49 from a *Spitzer* GLIMPSE image, shown in Fig. 1.7. Each of the three bowshocks are shown in individual insets in the figure. RCW 49-S2 is oriented away from Westerlund 2, and is therefore likely to be influenced by nearby WR 20b. RCW 49-S3 is oriented broadly towards Westerlund 2 and is therefore likely influenced by the cluster wind. RCW 49-S1 is more difficult to explain. Although it lies relatively far from the HII region, it is still likely that it is associated with RCW 49. The fact that it is far away from any other bright IR sources, and that the bowshock is oriented towards Westerlund 2 are strong indicators of an association. Also, the distance to RCW 49 is consistent with the luminosity of the driving star being an O-star adds weight to this theory. If RCW 49-S1 is indeed associated with Westerlund 2 then this is evidence that the combined winds of the ionizing stars in the cluster have escaped the HII region, creating a flow of hot gas that extends at least 16 pc away from RCW 49.

Despite the continuous input of mass, momentum and energy into the ISM, feedback from stellar winds is clearly less effective if some proportion of their energy can leak out of the bubbles they blow. In cases where there is a great deal

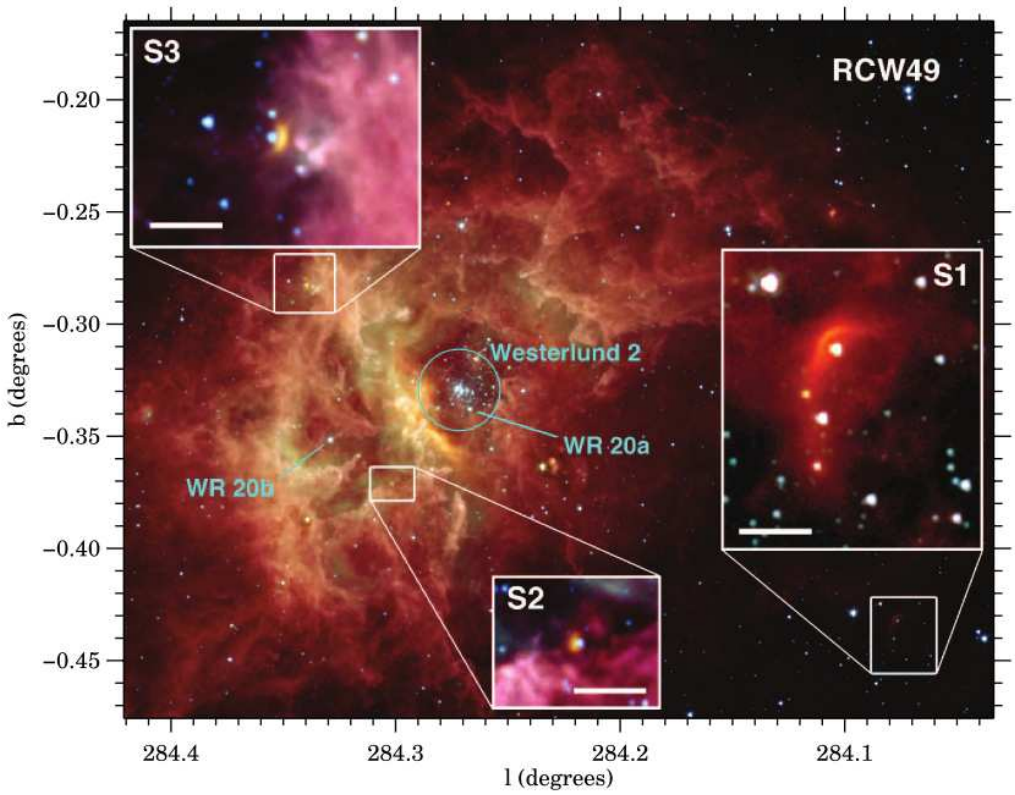

Figure 1.7: GLIMPSE full-colour image of RCW 49 (blue:[3.6]; green:[4.5]; orange:[5.8]; red:[8.0]. The insets show shocks from escaping gas colliding with stellar winds outside the bubble (scale bars are 30" ≈ 0.6 pc at 4.2 kpc). Three energy sources that could drive large-scale interstellar flows are also indicated: the Westerlund 2 cluster (circled), and the Wolf-Rayet stars WR 20a and WR 20b. Taken from Povich *et al.* (2008).

of leakage then it is possible that the effect of the winds is rather weak, and they may provide only an order of unity enhancement to radiation pressure (Krumholz & Matzner, 2009). However, where there is a high degree of confinement the effectiveness of stellar winds will be much higher.

1.2.2 Photoionization

Photoionization is the removal of one or more electrons from an atom or molecule by absorption of a photon of visible or ultraviolet light. On a large scale this can lead to the stripping of material from within a GMC.

In a uniform medium surrounding a star a spherical HII region, or Strömgren sphere will form (Strömgren, 1939). This region will expand if there is an overpressure of the photoionized gas with respect to its surroundings (Kahn, 1954). However, observations have shown neatly spherical HII regions are not the norm (e.g. Kurtz *et al.*, 1994; Wood & Churchwell, 1989). Simulations of photoionization into a uniform medium, such as an HII region, demonstrate that feedback operates preferentially in directions of steeply declining density, which suggests that the net feedback effect in clouds that are realistically clumpy or inhomogeneous may be very different from that in simulated smooth density fields.

If a massive star is formed close to the edge of the natal molecular cloud then the ionization front of the corresponding HII region can break through the surface of the cloud. This is known as a "blister" HII region, as the photoionized gas within the cavity is exposed to view, and can be observed as a blister on the surface of the molecular cloud. The hydrodynamics of blister HII regions was modeled by Tenorio-Tagle and collaborators in a series of papers (Bodenheimer *et al.*, 1979; Tenorio-Tagle, 1979; Yorke *et al.*, 1983), who renamed them "champagne" flows. Subsequently, Comeron (1997) included the effect of adding a stellar wind to this scenario. Such a champagne flow could efficiently disrupt the surrounding molecular cloud (Bodenheimer *et al.*, 1979; Whitworth, 1979). There have been many other numerical photoionization feedback studies performed for

cases of highly idealised cloud structures (e.g. Franco *et al.*, 1990; Garcia-Segura & Franco, 1996; Yorke *et al.*, 1989).

Many more recent hydrodynamical studies have been done to try and elucidate the effect that photoionizing radiation has on actual GMCs with a turbulent density structure (e.g. Dale & Bonnell, 2012; Dale *et al.*, 2012; Mac Low *et al.*, 2007). One of the interesting results from these studies is that photoionization can couple quite weakly to the denser regions of gas in the GMC. In fact, the ionizing radiation preferentially penetrates and ionizes neutral gas along pre-existing low density channels, causing them to expand and start to compress the denser, unionized regions. Similarly, Gritschneder *et al.* (2009) performed hydrodynamic simulations of the effects of photoionizing radiation on a turbulent ISM, and found that the ionized gas reacted to the increased temperature and started to exert pressure on the cold gas in the ISM. The cold gas was compressed and pushed away from the source, leading to peculiar structures such as pillars and fingers. Observations of these features, such as the Pillars of Creation (e.g. Linsky *et al.*, 2007) and the Horsehead nebula (e.g. Bowler *et al.*, 2009) find that there is often star formation occuring within these sculpted pillars.

Photoionized gas can only be considered a dominant feedback mechanism when its pressure exceeds that of radiation throughout most of an HII region. The weak coupling of ionizing radiation to very dense gas also implies that the level of feedback provided will be highly dependent on each individual system/cluster.

1.2.3 Supernovae

Supernovae are an important source of energy and turbulence in the ISM. They are classified into different types according to their spectroscopic characteristics. From the viewpoint of stellar evolution, Type II and Type Ib/c supernovae are explosions of massive stars ($M > 8\,M_\odot$) produced by core collapse following late stages of nuclear burning, whereas a Type Ia supernova results from the thermonuclear runaway burning of an accreting white dwarf in a binary system. Spectroscopically, a Type Ia supernova can be identified as having no observable hydrogen absorption. Because Type II SNe happen on a much shorter timescale than Type Ia, all the ISM and stellar feedback studies focus mostly on their energy deposit and dynamical issues. Each explosion releases of the order of 10^{51} ergs of energy and roughly one to several tens of $M_\odot$ of ejecta, expanding at velocities of up to $\sim 10^4\,km\,s^{-1}$. A supernova explosion synthesizes heavy elements and injects them into the interstellar medium where they can then take part in subsequent star formation. As massive stars do not live long enough to disperse far from their formation site, Type II SNe will often occur within the stellar associations. Understanding these violent cosmic phenomena is crucial to our knowledge of the evolution of the Universe.

A typical massive star of $M_* \sim 35\,M_\odot$ with a mass-loss rate of $\dot{M} = 5 \times 10^{-7}\,M_\odot\,yr^{-1}$ and wind velocity $v_\infty = 2000\,km\,s^{-1}$ would impart a total kinetic energy of $E = 8{\times}10^{49}$ ergs into its surroundings over the course of its main sequence (MS) phase, assuming it lasts $4{\times}10^6$ yrs. The Wolf-Rayet (WR) phase of such a star, assuming a mass-loss rate of $\dot{M} = 2{\times}10^{-5}\,M_\odot\,yr^{-1}$ and wind velocity $v_\infty = 2000\,km\,s^{-1}$ over a period of 300,000 yrs would add a further $2.4{\times}10^{50}$ ergs,

meaning that the course of the lifetime of a massive star, the total integrated energy from the stellar wind would be of the order of 10^{50} ergs. This is an order of magnitude lower than would be expected from the explosion of such a star, making SNe the dominant source of stellar energy input into the ISM.

Although the initial blast wave expands quickly ($\sim 10^4\,\mathrm{km\,s^{-1}}$), over the lifetime of approximately 10^5 yrs it gradually decelerates as it sweeps up the surrounding interstellar gas. During the early evolution the SNR expands freely, with the forward shock effectively being adiabatic due to the high expansion velocity. The swept-up mass becomes concentrated in a thick shell behind the forward shock, and the remnant expands adiabatically, in what is called the Sedov-Taylor (ST) phase (Sedov, 1959; Taylor, 1950). Eventually, the shock wave slows down enough that the post-shock gas begins to lose a significant amount of energy through radiative cooling. The shell collapses into a thin, dense shell of cooled gas, surrounded by a radiative (isothermal) shock on the outside and filled with a low density, high pressure interior in what is known as the pressure-driven snowplough stage (McKee & Ostriker, 1977).

The energy deposited as turbulent energy and consequently as thermal energy by a supernova to an inhomogeneous ISM remains unclear, but it is one of the most important ingredients for our understanding of galaxy formation (e.g. Efstathiou, 2000; Silk, 2003). To date, studies into the efficiency with which a SN couples with a clumpy environment are sparse (see Section 2.3.5).

Although core collapse SN explosions impart a substantial amount of energy and momentum into the ISM, this feedback mechanism only begins after the lifetimes of massive stars, which are a minimum of several 10^6 yrs. Turbulence within a cluster must therefore be maintained by other sources of feedback or

external influences, else stars would form rapidly and consume the material in GMCs in one to two crossing times.

1.2.4 Triggering of Star Formation

Star formation appears to continue throughout the evolution of a rich stellar cluster. Young protostars ($< 10^5$ Myrs) are often seen in HII regions several Myrs old (e.g. Beerer *et al.*, 2010; Bik *et al.*, 2010; Choudhury *et al.*, 2010; Comerón & Schneider, 2011; Hester *et al.*, 1996; Snider *et al.*, 2009). Many of these authors attribute this to feedback from massive O-stars triggering a new stellar generation. However, determining whether any particular group of stars has been triggered is rather complicated. Although clusters may be located spatially nearby the shell of a wind-blown bubble (see Fig. 1.6) or SNR, it is difficult to prove that they formed purely from the affects of stellar feedback, and would not have formed regardless. Whether or not feedback alone has prompted stars to form, the energy and momentum input from massive stars will have been instrumental in hastening the formation processes.

A prime location to look for triggered star formation is in the shell of dense material surrounding the wind-blown bubble and expanding HII region. If this shell becomes gravitationally unstable then theoretically both low and high mass stars could form (see parts 1 and 2 in Fig. 1.8). Small-scale gravitational instabilities, such as the Jeans instability, can lead to low-mass star formation. However, if the gravitational instabilities are on a larger scale then massive fragments can form, from which it is possible that high-mass stars could be born. The process of induced star formation due to gravitational instabilities in a swept-up shell is

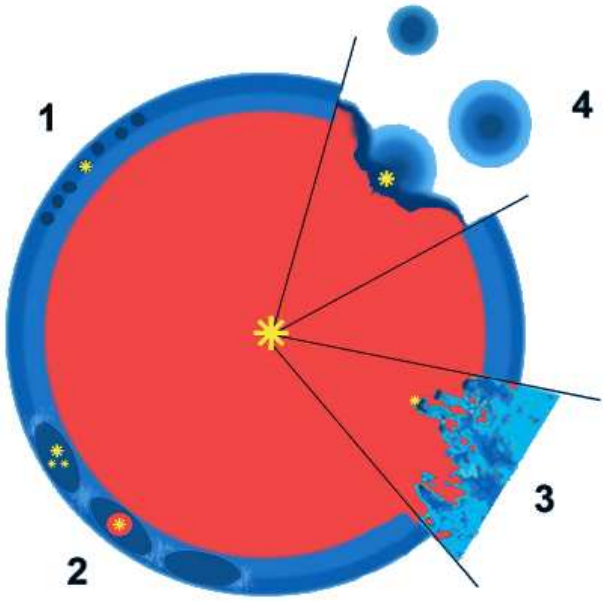

Figure 1.8: Schematic view of a spherical HII region and of its neutral environment. Different processes of triggered star formation are depicted. 1 - small-scale gravitational instabilities; 2 - large-scale gravitational instabilities; 3 - ionizing radiation acting on a turbulent medium; 4 - radiation-driven compression of pre-existing dense clumps. Taken from Deharveng *et al.* (2010).

known as "collect & collapse" (Elmegreen & Lada, 1977). Photoionization can affect a turbulent medium by creating pillars or fingers of material where over-densities in the heads can be sites of star formation (Gritschneder *et al.*, 2009), as discussed in Section 1.2.2 and shown in part 3 of Fig. 1.8.

If the HII region is expanding into an inhomogeneous environment then it is likely that the bubble will expand into regions of pre-existing high density. These condensations can be compressed by the pressure of the ionized gas as an ionization front is driven into the clump. This is illustrated in part 4 of Fig. 1.8, and is also known as radiative-driven implosion. Star formation may also be caused by the expansion of a supernova shockwave into a clumpy medium.

1.3 Multi-Wavelength Analysis of Feedback in Stellar Clusters

In order to build a strong picture of the multiple processes occuring in star forming regions, observations are needed at different wavelengths. Direct optical observations of young stars embedded in dense molecular clouds is extremely difficult. Observations of deeply embedded sources must therefore be carried out at long wavelengths, for example in the infrared, millimeter and radio regions of the spectrum, or a X-ray energies.

1.3.1 X-ray Emission

Many high mass star forming regions are observed to contain diffuse thermal X-ray emission, which requires high temperature plasma. As discussed in Section 1.2.1, the fast winds of individual massive stars create high pressure and high temperature bubbles (e.g. Castor *et al.*, 1975; Weaver *et al.*, 1977). In large clusters containing many early-type stars the individual stellar winds may combine, collectively creating a so-called cluster wind (e.g. Cantó *et al.*, 2000; Chevalier & Clegg, 1985; Stevens & Hartwell, 2003).

X-rays are usually described as either hard or soft based on how energetic the emission is. Soft, low energy X-rays (E$\sim$0.1–0.5 keV) are the least penetrating, and therefore the most sensitive to absorption. Hard X-rays (E$\sim$2.5–10.0 keV) are very penetrating and suffer less from attenuation. Using the equation:

$$I = I_0 e^{(-\mu x)} \tag{1.6}$$

where I is the X-ray beam intensity, I_0 is the initial beam intensity, μ is the linear attenuation coefficient and x is the distance travelled, it can be calculated that a 10 keV photon can penetrate approximately 7.5 times further through hydrogen before the beam intensity drops to half the original strength than a 1 keV photon. The distinction between hard and soft X-rays is not well defined, and therefore a third band referred to as medium energy can be used to describe the overlap.

The X-ray continuum can arise from many processes including bremsstrahlung, black-body radiation, synchrotron radiation, or inverse Compton scattering. In stellar clusters the X-ray continuum is generally dominated by bremsstrahlung emission, where free electrons in the plasma are decelerated when they come in close proximity to atomic nuclei. If the free electrons are high enough in energy then they can also eject electrons from the inner shells of the atoms by colliding, and the quick filling of those vacancies by electrons dropping down from higher energy levels gives rise to sharply defined characteristic X-ray line emission.

In the presence of a strong magnetic field, non-thermal X-rays can also be created by synchrotron radiation. This arises when charged particles, commonly electrons, are accelerated within a magnetic field. Instead of moving across it, the energetic, relativistic electrons will spiral around it. This effective acceleration by the electrons causes synchrotron radiation to be emitted.

In many cases the observed diffuse X-ray emission from massive star forming regions (MSFRs) is relatively soft. For instance, in M17 and the Rosette Nebula the characteristic temperature $kT < 1$ keV (Townsley *et al.*, 2003). The X-ray emitting plasma in the Extended Orion nebula is similarly cool (Güdel *et al.*, 2008). However, in other MSFRs the characteristic temperature is considerably higher. For instance, the diffuse thermal X-ray emission from NGC 3603 (Moffat

et al., 2002), the core of the Arches cluster (Wang *et al.*, 2006) and the Quintuplet cluster (Law & Yusef-Zadeh, 2004) has $kT > 2\,\mathrm{keV}$.

In some clusters the diffuse X-ray emission may be predominantly non-thermal: e.g. NGC 6334 (Ezoe *et al.*, 2006a), RCW 38 (Wolk *et al.*, 2002), the Arches cluster (Wang *et al.*, 2006; Yusef-Zadeh *et al.*, 2002) and ON2 (Oskinova *et al.*, 2010). This requires non-thermal particles, which also occur when high speed flows and strong shocks are present. Townsley *et al.* (2011) argue that the non-thermal emission detected from the NGC 3576 OB association may arise from both a pulsar wind nebula and a cavity supernova. A caveat to some of these works is that the diffuse X-ray emission from clusters which are at larger distances is more likely to suffer contributions from unresolved point sources. A summary of X-ray studies of young stellar clusters is presented by Damiani (2010).

In young MSFRs in which there has not yet been time for any massive star to explode as a supernova, the diffuse X-ray emission must result from the action of stellar winds. However, in older clusters where some of the massive stars have exploded one still might not detect any signature of a SN explosion because the effect of an SNR on the hot cluster gas is likely to be relatively short-lived. This timescale is generally believed to be $\sim 10^4\,\mathrm{yrs}$ (e.g. Kavanagh *et al.*, 2011). For this reason, most studies of stellar clusters prefer a wind based explanation for the diffuse X-ray emission, though Ezoe *et al.* (2009) favour a recent SN explosion in their study of the Eastern Tip of the Carina nebula. A distinction exists between individual stellar clusters, and larger scale regions of star formation which create superbubbles where multiple cavity supernovae are believed to be responsible for the diffuse emission (such as those of 30 Doradus, e.g. Chu & Mac Low, 1990; Townsley *et al.*, 2011).

X-ray surveys of MSFRs are important because they readily discriminate young stars from unrelated objects that often contaminate IR images of such fields. Atmospheric absorption blocks X-ray wavelengths, and therefore any X-ray observations must be taken from satellites rather than ground-based astronomy.

1.3.2 Radio Emission

HII regions are sources of radio emission characterised by the temperature of the gas. As they consist of plasma the electrons can move freely throughout the gas, causing free-free emission or thermal bremsstrahlung. Radio observations of HII regions can therefore provide a diagnostic of their conditions. The emission can either be optically thin or optically thick, connected by a turnover region. In the optically thin regime the flux is a power law:

$$S_\nu \propto \nu^\alpha \tag{1.7}$$

where $\alpha \approx$-0.1 for an optically thin homogeneous plasma (Wright & Barlow, 1975). On a log-log plot, α is the slope of the spectrum. In the optically thick regime, at low frequencies the spectrum rises as ν^2, the same as for blackbody radiation at low frequencies. Wright & Barlow (1975) showed that the spectral flux distribution produced by an ionized, uniform, spherically symmetric mass loss flow leads to an intermediate slope, with a spectrum of the form $S_\nu \propto \nu^{0.6}$.

The emission from a particular part of the sky is often characterised by a brightness temperature. The intensity of radiation from a region of sky, I_ν, has an equivalent brightness temperature, T_b (the temperature a blackbody would have according to the observed intensity), where $I_\nu = 2kT_b/\lambda^2$. At radio wavelengths

the flux S_ν at a frequency ν is given by:

$$S_\nu \approx \frac{2k}{c^2}\nu^2 T_e \tau_\nu \Omega_s, \text{ when emission is optically thin} \tag{1.8}$$

and:

$$S_\nu \approx \frac{2k}{c^2}\nu^2 T_e \Omega_s, \text{ when emission is optically thick} \tag{1.9}$$

where T_e is the electron temperature, τ_ν is the optical depth and Ω_s is the source solid angle in steradians. The shape of the free-free portion of the spectrum is determined for the most part by the optical depth, τ_ν, derived using the expression given by Mezger & Henderson (1967):

$$\tau_\nu \; = \; 8.235 \times 10^2 a_\nu \left(\frac{T_e}{K}\right)^{-1.35} \left(\frac{\nu}{GHz}\right)^{-2.1} \left(\frac{EM}{pc\, cm^{-6}}\right)^{-2.1} \tag{1.10}$$

where a_ν is a frequency dependent correction factor approximately equal to unity and EM $= \int n_e^2 \mathrm{dl}$ is the emission measure.

Relatively little radio emission is in the form of discrete lines. The most important line is the hydrogen 21 cm line, which refers to the electromagnetic radiation spectral line that is created by a change in the energy state of neutral hydrogen atoms. This electromagnetic radiation is at the precise frequency of 1.420 GHz. A spontaneous spin-flip from one state to another is highly forbidden, with an extremely small probability. The time for a single isolated atom of neutral hydrogen to undergo such a transition would be around 11 million years. However, when collisions between hydrogen atoms occur, an exchange of electrons can take place and this can lead to a random spin-flip transition with one (or both) atoms

being excited to the higher energy state. Due to the density of neutral hydrogen, the mean time between collisions is only around 200 years. The 21 cm emission is therefore collisionally enduced. Although the transition itself is rare, there is so much hydrogen distributed throughout the ISM that the 21 cm line emission is fairly ubiquitous throughout the galaxy. As ISM absorption is insignificant at the 21 cm wavelength, the line emission is also easily observable throughout the galaxy.

By studying the 21 cm line we can determine the velocity of neutral hydrogen clouds, the distribution of neutral hydrogen and the amount of gas in the ISM from the strength of the lines observed. The detection of this emission line and measurement of its Doppler shift have allowed mapping of the distribution of galactic neutral hydrogen (HI regions) and of galactic rotation. The matter distribution so measured shows a spiral arm structure within our galaxy, as is seen in optical images of other galaxies.

Hydrogen recombination lines at low transitions are normally seen in the optical/UV. However, if the levels are higher they show in the radio. This process can occur in HII regions i.e. regions of the ISM in which hydrogen is mostly ionized (e.g. due to UV photons produced by young star clusters in star forming regions). For example, some fraction of electrons will make the transition from the 110^{th} energy level to the 109^{th}, and emit a 5 GHz photon. Although the density of the interstellar medium is low, the path length is long through an HII region (~ 0.5 pc) so the emission can be observed as a weak radio line. Studying these recombination lines allows the temperature and density (from the thermal width of lines and line ratios), and velocities and motions (from Doppler shifts) of HII regions to be determined. The composition can also be determined from

measurements of He and C lines, for example.

Radio emission can also be caused by non-thermal processes, of which synchrotron emission is the most common. The relativistic electrons required for this emission are thought to have been accelerated either in strong shocks within the stellar wind for single stars (White, 1985), or in a wind-collision region between stellar components for binary systems (WR+O-star, Eichler & Usov, 1993; Usov, 1992). Massive stars often have both a thermal and non-thermal component to their spectrum. About a quarter of the brightest O-stars have a radio spectrum which is dominated by non-thermal emission at cm wavelengths (Bieging *et al.*, 1989).

Radio waves can penetrate the large clouds of interstellar cosmic dust that are opaque to visible light, and unlike X-rays they can penetrate the atmosphere, making ground-based observations feasible.

1.3.3 Multi-Wavelength Observations of Feedback in Stellar Clusters

In this Section, multi-wavelength observations of three star forming regions of various ages and sizes will be examined to see whether there are similarities in the structures observed.

1.3.3.1 Orion Nebula

The Orion Nebula, or M 42, is part of the Orion Molecular Cloud and is a region of massive star formation a distance of 414±7 pc (Menten *et al.*, 2007), and therefore has been studied extensively at multiple wavelengths (e.g. see the review on M42

by O'dell, 2001, and references therein). This region is therefore a great place to look to try and understand star formation processes. M 42 is a component of the ridge of GMCs in the constellation Orion, which are part of the Eridanus superbubble of material (Heiles, 1998). The long ridge of molecular material extending N-S through the belt of Orion and its sword region is home to several star associations of various young ages, with M 42 probably being the youngest of these. The Huygens region of this nebula is centered around a group of massive stars known as the Trapezium group, which are bounded by the molecular cloud. Infrared studies have revealed a large cavity which has formed to the south-west of the Trapezium group. This is known as the Extended Orion Nebula (EON).

Güdel *et al.* (2008) undertook a study of the region using XMM-Newton to perform deep X-ray observations that extend across the entire region. They found diffuse X-rays were present in the cavity of the EON, and that they appeared to be confined by the dense, warm dust. A comparison of the X-ray emission with the emission at other wavelengths is shown in Fig. 1.9.

The top left panel plots the diffuse 0.3–1.0 keV emission in blue, against an infrared image of the region from Spitzer, with 4.5 μm emission in green and 5.8 μm emission in red. All of the X-ray point sources have been removed. The white contour shows the field of view of the detector for the X-ray observations. The top right panel shows just the infrared image with the 3.6 μm emission added, with the overlaid dotted contour being the boundary of the location of the majority of the diffuse X-ray emission. The diffuse emission is clearly confined by the warm dust surrounding the EON. Güdel *et al.* (2008) estimate that the absorption-corrected intrinsic luminosity of the X-ray emission in the range of 0.1–10.0 keV is $L_X = 5.5 \times 10^{31}\,\mathrm{ergs\,s^{-1}}$, and estimate the temperature of the X-ray emitting

plasma to be 1.7–2.1$\times10^6$ K. They find it most likely that the high velocity winds produced by the Trapezium group are the source of the hot plasma.

The bottom left panel shows an optical image of the region taken by the UK Schmidt telescope. There are multiple shocks along the right of the cavity, coinciding with areas where the diffuse X-ray emission looks to be in contact with the cavity wall. There are bright lanes to the bottom.

The bottom right panel again shows the optical image, but with 330 MHz radio contours overlaid. The radio emission is dominated by thermal bremsstrahlung from hot gas ionized by the central stars of the nebula, and therefore the majority of this emission originates from the Trapezium group in the top left of the image. However, radio emission is observed throughout the cavity, indicating the presence of hot winds originating from the stellar cluster in the Trapezium group which is blowing into the surrounding material and creating this cavity.

The wind-shocked gas leaking from the Orion Nebula is likely to impact the Eridanus superbubble, which is thought to have been produced by multiple supernovae from previous generations of OB stars in the Orion Nebula. The hot gas leaking from the Orion Nebula could be capable of continuously replenishing this superbubble.

1.3.3.2 M17

M 17, also known as the Omega Nebula, is a young, massive star formation region located on the northeast edge of one of the largest GMCs in the Galaxy, approximately 1.55 kpc away. M 17 is very young, with an estimated age of only $\sim$0.5 Myrs (Chini & Hoffmeister, 2008; Hoffmeister *et al.*, 2008), and so none of the massive stars should have undergone supernova explosions. The nebula is

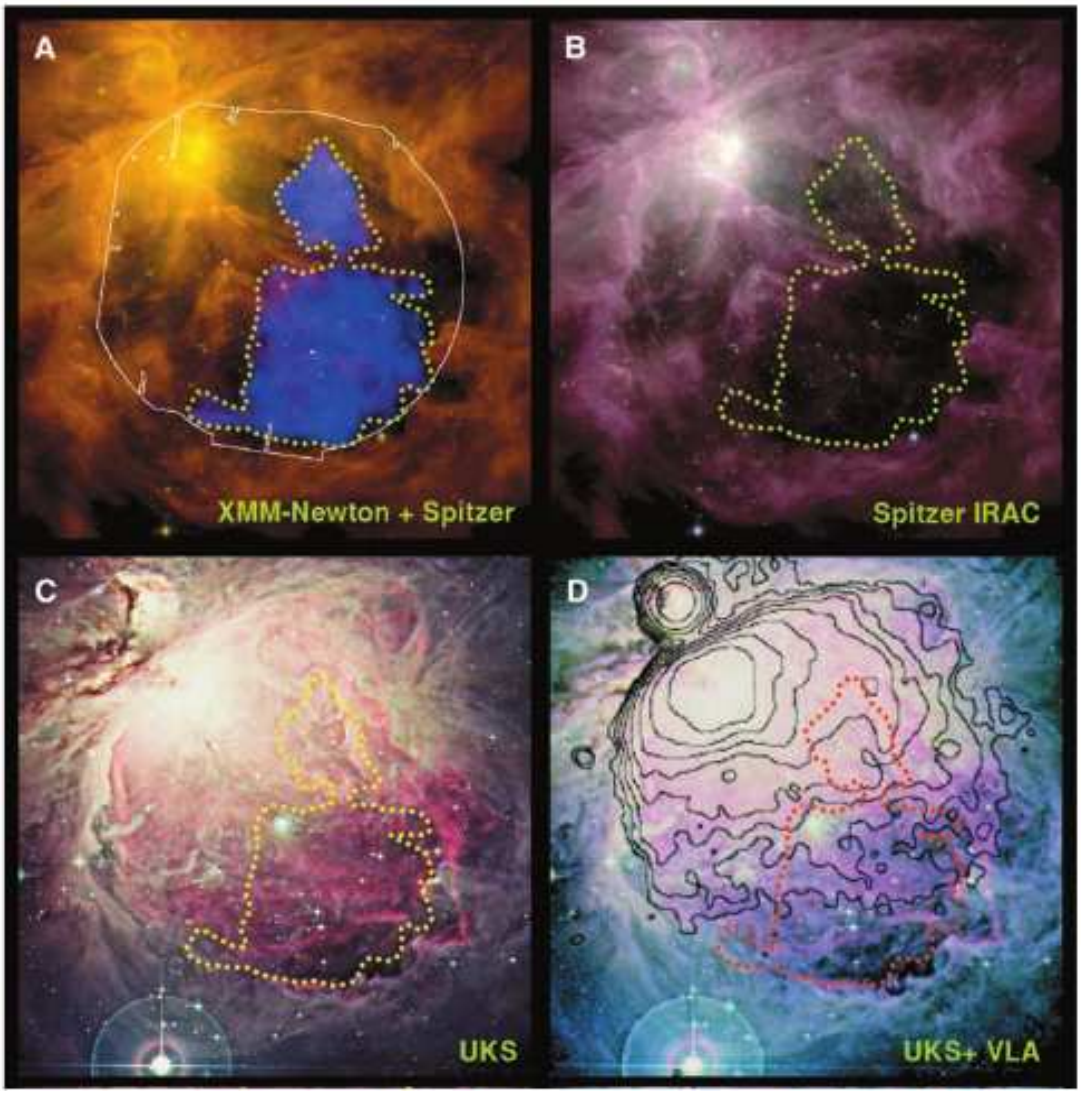

Figure 1.9: Multi-wavelength images of the Orion nebula. The four panels show identical regions. The width of each panel is approximately 42 arcmin, corresponding to 4.9 pc at a distance of 400 pc. Top left (A): Diffuse X-rays (in blue) superimposed on a Spitzer infrared image. Top right (B): An infrared image (3.6+4.5+5.8 μm composite) from the Spitzer Space Telescope. Bottom left (C): An optical image (from the UK Schmidt telescope). Bottom right (D): Same, with radio contours overlays (from the VLA, observed at 330 MHz). The dotted contour outlines the area where most of the detected diffuse soft X-ray emission is located. Taken from Güdel *et al.* (2008).

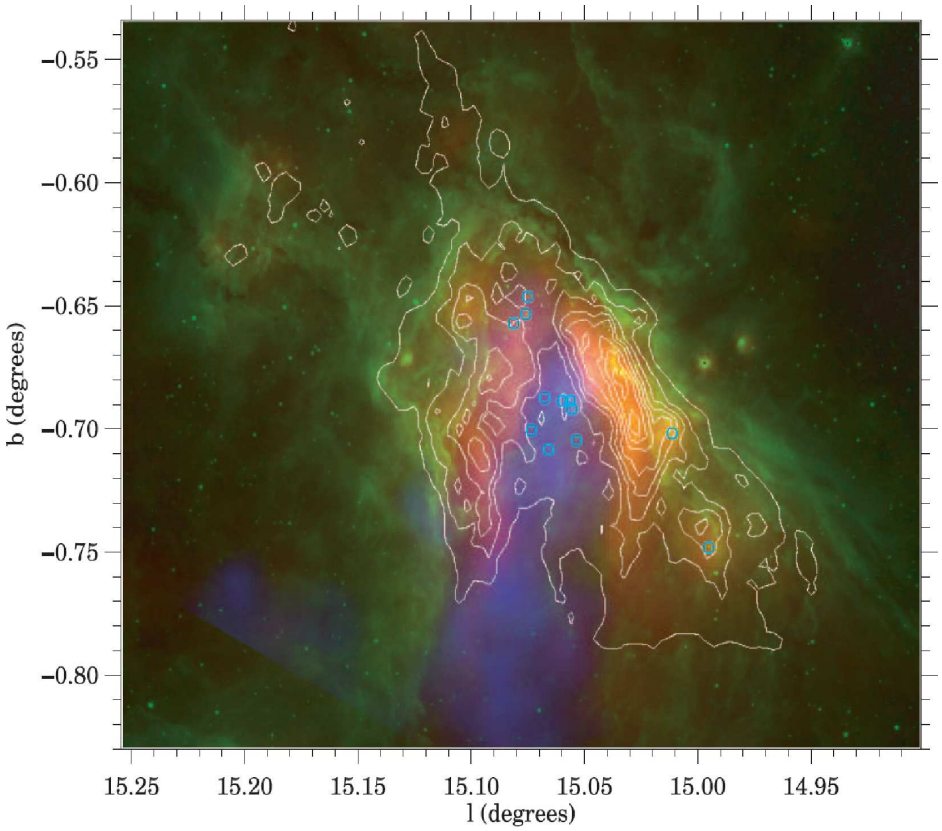

Figure 1.10: Multi-wavelength image of M17. A river of MK plasma glows in soft X-rays (0.5–2.0 keV *Chandra* diffuse emission map; blue) as it flows outward from the central cavity surrounding the O-stars of NGC 6618 (light blue circles). The radio HII region (20 cm continuum; white contours) defines the cavity walls, and warm dust permeates the ionized gas, as shown by the 21.3 μm continuum emission (*MSXE*; red). The entire M17 complex is surrounded by a dusty wrapper (GLIMPSE [5.8]; green) that traces the PDR in emission from PAHs. Taken from Povich *et al.* (2007).

photoionized by the massive stellar cluster NGC 6618, within which Broos *et al.* (2007) have identified 14 O-stars.

Povich *et al.* (2007) combined multi-wavelength observations of M 17, the result of which is shown in Fig. 1.10. The O-stars contained within the central ionizing cluster, NGC 6618, are shown individually as the light blue circles. The cluster is contained on three sides by warm dust (21.3 μm emission, shown in red).

The radio 20 cm continuum (white contours) shows the HII region bounding the cavity. To the south of the image, hot X-ray (0.5–2.0 keV) gas fills, and is flowing out of, the central cavity (shown in blue). The most likely explanation is that the hot cluster wind from the O-stars has carved a cavity in the surrounding medium, through which the hot gas is escaping in one direction.

1.3.3.3 30 Doradus

30 Doradus (30 Dor) is a massive star-forming region in the Large Magellanic Cloud (LMC). There are an abundance of massive stars in the centre of 30 Dor (Melnick, 1985; Parker, 1993; Schild & Testor, 1992; Walborn & Blades, 1997), also known as the Tarantula nebula. It hosts the massive compact star cluster R 136 (Feast *et al.*, 1960), believed to contain stars with masses $> 150\,M_{\odot}$ (Crowther *et al.*, 2010). R 136 has a mass of $\sim 6 \times 10^4\,M_{\odot}$ (Brandl, 2005), and has more than 50 times the ionizing radiation of the Orion Nebula. The stellar population of 30 Dor spans multiple ages, with areas of ongoing star formation (Brandner *et al.*, 2001; Walborn *et al.*, 2013) and older (∼20–25 Myrs) supergiants in the Hodge 301 cluster (Grebel & Chu, 2000). Roughly a third of the LMC WR stars compiled by Breysacher *et al.* (1999) are contained within the 30 Dor nebular region of N 157 (Henize, 1956), with several found within R 136 itself. 30 Dor is the most massive and the largest HII region in the Local Group. Due to its proximity and size it is an excellent target for studying the effects of massive stars on the evolution of an HII region.

Townsley *et al.* (2006a) performed a study of the diffuse X-ray emission in 30 Dor using *Chandra*. Fig. 1.11 shows an image of 30 Dor in X-rays (green and blue) with infrared 6.5–9.4 μm *Spitzer* data overlaid (red). The hot X-ray plasma

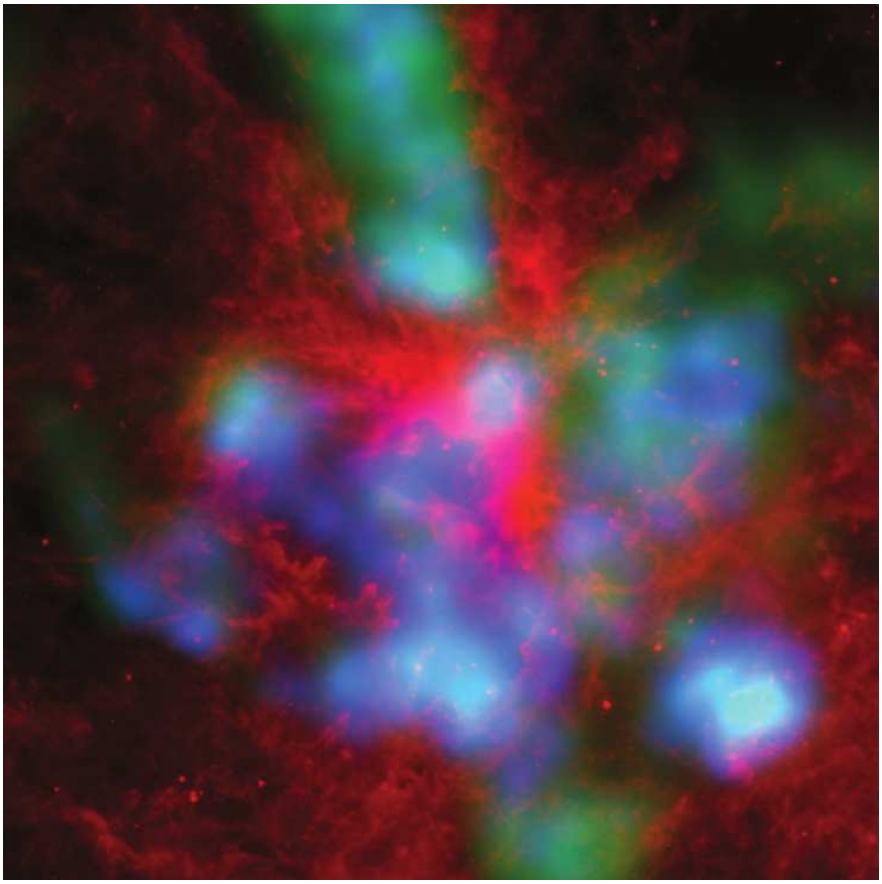

Figure 1.11: Composite of the mid-infrared (6.5–9.4 μm) *Spitzer* IRAC image of 30 Dor (red) with the 0.35–0.9 and 0.9–2.3 keV adaptively smoothed *Chandra* ACIS images (green and blue respectively). The point sources have been removed from the X-ray images. Taken from Townsley *et al.* (2006a).

fills the interiors of superbubbles that are outlined by warm dust. The X-ray point sources have been removed from this figure so that it is clearer to distinguish the bright diffuse emission from the R 136 cluster and from nearby WR stars.

Although 30 Dor is much larger than the Orion Nebula, Figs. 1.9 and 1.11 both show the same feature of diffuse X-ray emission being anti-correlated with and bounded by the warm dust and gas. The effect of the winds and SNe from the massive stars can be scaled up from smaller clusters to larger systems. Un-

derstanding how the winds affect their natal environments can therefore also shed light on the processes occuring on much larger scales.

1.4 An Introduction to this Thesis

This thesis contains a study of simulations of the mechanical effects of winds and supernovae from a massive stellar cluster on their surrounding natal cloud. Chapter 2 presents a hydrodynamical model of a cluster wind blowing into an inhomogeneous GMC clump. It is found that the winds carve out channels through the low density material, whilst the high density clumps prove resilient to the ablation by the winds and that SNe couple very weakly to the dense gas.

Chapter 3 explores the X-ray emission produced by the cluster as outlined in Chapter 2. Only gas above 10^5 K is considered to be hot enough to produce X-rays. The synthetic emission is compared to one dimensional models and to observations. The simulated emission is fainter than predicted by simpler models, but is mostly comparable with observations of young stellar clusters. Chapter 4 explores the thermal radio emission produced by the cluster as outlined in Chapter 2 and compares this with the X-ray emission discussed in Chapter 3. Looking at the emission in the radio and X-ray regimes builds a strong picture of the processes occuring within such a system.

Chapter 5 takes a closer look at the central cluster, using a Salpeter IMF to generate a cluster of a size comparable with that assumed in Chapter 2. The X-ray and radio emission of the cluster is also simulated. Finally, the thesis is summarized in Chapter 6 where possible extensions and future work are discussed.

Chapter 2

Mechanical Feedback from Winds and Supernovae in a Massive Young Stellar Cluster

2.1 Introduction

That stellar winds play a significant role in stellar cluster feedback is apparent from the fact that many young (pre-supernova) massive star forming regions contain diffuse X-ray emission - the hot gas responsible can only have been created by winds. Observations reveal that the surrounding cold molecular material can sometimes confine this hot gas (e.g. Townsley *et al.*, 2006b), but around other clusters the cold clouds appear to be shaped and removed by the hot gas. In fact, there are now several lines of evidence that indicate that the hot X-ray emitting gas often escapes or leaks out of the local cluster environment, instead of being bottled up inside a swept-up shell. Firstly, the diffuse X-ray emission in M17 and

the Rosette nebula reveals that only a small proportion of the cluster wind energy is radiated in the X-ray, and Townsley *et al.* (2003) conclude that most of the hot gas must flow without cooling into the wider ISM. This picture is supported by analysis of the Omega nebula, the Arches cluster, and NGC 3603, all of which contain an amount of hot gas equal to only 1 per cent of the wind material from the O-stars over the age of the cluster. Secondly, direct evidence for outflowing gas comes from observations of M17 and particularly RCW 49 which show stellar bow shocks around O-stars outside of the central clusters. These indicate large scale gas outflows away from the stellar cluster with velocities of at least a few hundred $\mathrm{km\,s^{-1}}$ (Povich *et al.*, 2008).

Stellar wind feedback into an inhomogeneous environment has been considered by Tan & McKee (2001) and more recently by Harper-Clark & Murray (2009). The latter postulate that the non-uniform surrounding medium causes gaps in the swept-up shell surrounding the wind-blown bubble where some of the high-pressure gas in the bubble interior can leak out. This scenario has received backing from Lopez *et al.* (2011) who conclude that such leakage may be occuring within 30 Doradus. Lopez *et al.* (2011) also conclude that direct stellar radiation pressure dominates the interior dynamics, but this claim has proved far more controversial, and other works argue in favour of the thermal pressure of hot X-ray emitting plasma shaping the large-scale structure and dynamics in 30 Doradus (Pellegrini *et al.*, 2011; Povich, 2012). One must recognize that there are significant uncertainties in determining the hot gas pressure in regions like 30 Doradus, where it is unclear whether the X-ray emitting gas should be treated as a single large bubble or as multiple smaller bubbles with distinct identities.

The possibility that the pressure exerted by stellar radiation may be dynam-

ically important in massive young stellar clusters has received much attention in recent years, with Krumholz & Matzner (2009), Fall *et al.* (2010) and Murray *et al.* (2010) all arguing that radiation pressure is the dominant feedback mechanism. However, these works disagree on the net momentum coupling between the radiation field and the gas, partially because this depends on the degree of inhomogeneity of the gas and the effect that this has on the radiation field (e.g. Krumholz & Thompson, 2012). Complementary work on the ionized gas pressure has shown that ionization feedback into a highly inhomogeneous medium is not very effective at high cluster masses (Dale & Bonnell, 2011), but becomes more so at lower masses (Dale *et al.*, 2012; Walch *et al.*, 2012).

Given these competing processes, our aim in this Chapter is to examine the extent to which the mechanical energy input from a cluster of massive stars is confined by and shapes the local environment. The focus in this initial Chapter is solely on feedback due to stellar winds and supernovae, and investigations of other forms of feedback (radiation pressure, photoionization etc.) is deferred to future works (see Section 6.2). This investigation is conducted through 3D hydrodynamic simulations of this interaction. In Section 2.2 the numerical models and initial conditions used in this Chapter are outlined. The results from the simulations are presented and discussed in Section 2.3. Section 2.4 summarizes and concludes this Chapter.

2.2 Simulations of Stellar Feedback

2.2.1 Numerical Setup

The simulations were performed using the hydrodynamic code ARWEN (Astrophysical Research with Enhanced Numerics). This is a uniform grid code written in C++. The hydrodynamic update is performed using sweeps over each direction separately. The hydrodynamic algorithm is similar to that in the vh-1 code (Blondin *et al.*, 1990). We use an MPI-parallelized numerical scheme to solve the Euler equations of hydrodynamics using a Lagrangian formulation and a remap onto the original grid. A piecewise parabolic interpolation and characteristic tracing is used to obtain the time-averaged fluid variables at each zone interface. The code then solves a Riemann problem to determine the time-averaged fluxes, and then solves the equations of hydrodynamics:

$$\frac{\partial \rho}{\partial t} + \nabla \cdot (\rho \mathbf{u}) = 0, \tag{2.1}$$

$$\frac{\partial \rho \mathbf{u}}{\partial t} + \nabla \cdot (\rho \mathbf{u} u + P) = 0, \tag{2.2}$$

$$\frac{\partial \rho \varepsilon}{\partial t} + \nabla \cdot [(\rho \varepsilon + P)\mathbf{u}] = n\Gamma - n^2\Lambda, \tag{2.3}$$

where $\varepsilon = \mathbf{u}^2/2 + e/\rho$ is the total specific energy, ρ is the mass density, e is the internal energy density, P is the pressure, and T is the temperature. An ideal gas equation of state, $e = P/(\gamma - 1)$, and solar abundances are adopted throughout.

The simulations were run on the ARC1 supercomputer located at the University of Leeds, running on 128 cores continuously over 2 months. Other hydrodynamic codes were trialled before finally settling on ARWEN, including MG, vh-1

and FLASH. However, the codes utilising adaptive mesh refinement (AMR) did not significantly speed up the run-time of the simulations due to the refinement needed in the majority of the computational volume. Furthermore, using a Lagrangian update with a remap was found to be more robust with the large density and temperature contrast in the simulations than using a direct Eulerian solver, such as is used in FLASH and MG.

The net heating/cooling rate per unit volume is parameterized as $\dot{e} = n\Gamma - n^2\Lambda$, where $n = \rho/m_{\rm H}$, and Γ and Λ are heating and cooling coefficients which are assumed to depend only on temperature. In the ISM, Γ decreases with increasing density as the starlight, soft X-ray, and cosmic ray flux are attenuated by the high column densities associated with dense clouds. Because the exact form of the attenuation depends on details which remain uncertain (for instance the size and abundance of PAHs), the heating rate at $\mathrm{T} \lesssim 10^4$ K is similarly uncertain. In this work we assume that $\Gamma = 10^{-26}\,\mathrm{ergs\,s^{-1}}$ (independent of ρ or T). The low-temperature ($\mathrm{T} \lesssim 10^4$ K) cooling was then adjusted to give 3 thermally stable phases at thermal pressures between $2000 - 6000$ cm^{-3} K, as required by observations. These stable phases, at temperatures $\sim 10\,\mathrm{K}$, $\sim 150\,\mathrm{K}$ and $\sim 8500\,\mathrm{K}$, correspond to the molecular, atomic and warm neutral/ionized phases, respectively. The cooling curve and phase diagram are shown in Pittard (2011).

The simulation uses a temperature-dependent average particle mass, μ. In the molecular phase $\mu = 2.36$, reducing to 0.61 in ionized gas. The value of μ is determined from a look-up table of values of p/ρ (Sutherland, 2010), as shown in the top panel of Fig. 2.1. The values of pressure and density in a given cell can therefore be used to calculate a temperature value, from which the ionization fraction and temperature dependent average particle mass can be determined. A

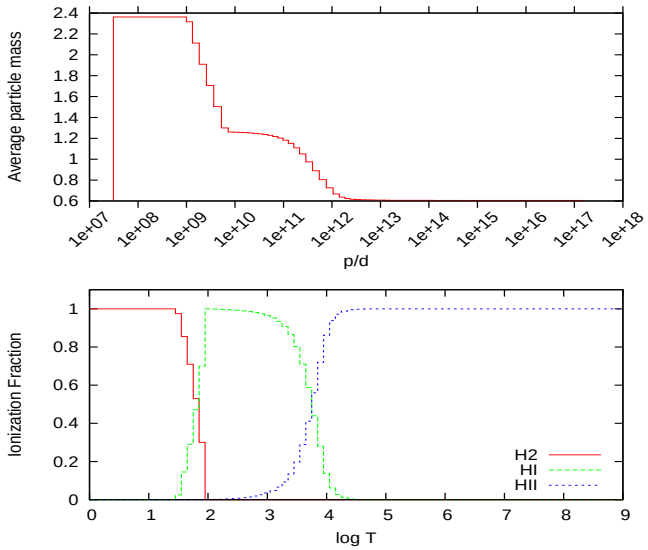

Figure 2.1: Plot to show the ionization fraction of the hydrogen in the simulation. [Top] Shows the temperature dependent average particle mass, μ as a function of the density and pressure. [Bottom] Shows the ionization fraction of the atomic, molecular and ionized hydrogen at different temperatures.

temperature independent value of γ, the ratio of specific heats, is used, and we set $\gamma = 5/3$.

Simulations are performed on a grid with 512^3 cells with free outflow boundary conditions. A number of advected scalars are included to trace the different origins of the gas - stellar wind/SN, GMC clump, and surrounding ambient ISM.

2.2.2 Stellar Evolution

In this Chapter it is assumed that the stellar wind feedback into the surrounding GMC clump is dominated by 3 O-stars with initial masses $35\,M_\odot$, $32\,M_\odot$ and $28\,M_\odot$, and Main Sequence (MS) mass-loss rates of 5, 2.5 and $1.5\times10^{-7}\,M_\odot\,yr^{-1}$ respectively. For each star the MS wind terminal velocity is assumed to be $2000\,km\,s^{-1}$. Three evolutionary phases are considered for each star. The MS

phase of the $35\,M_\odot$ star lasts for 4 Myrs, after which the star becomes a Red Supergiant (RSG) and blows a dense, very slow wind characterized by $\dot{M} = 10^{-4}\,M_\odot\,\mathrm{yr}^{-1}$ and $v_\infty = 50\,\mathrm{km\,s}^{-1}$. This phase lasts for 0.1 Myrs after which the star enters the Wolf-Rayet (WR) stage, and a fast, high momentum wind is blown ($\dot{M} = 2 \times 10^{-5}\,M_\odot\,\mathrm{yr}^{-1}$ and $v_\infty = 2000\,\mathrm{km\,s}^{-1}$). The WR phase lasts for a further 0.3 Myrs, after which the star undergoes a supernova explosion. At this point the star's wind is switched off, and 10^{51} ergs of thermal energy is imparted to the simulation along with $10\,M_\odot$ of ejecta. The other two stars remain on the MS throughout this entire evolutionary period. The $32\,M_\odot$ star evolves onto the RSG branch 0.1 Myrs after the $35\,M_\odot$ star explodes. The wind values and lifetimes used are summarized in Table 2.1 and are intended to be representative of stars of these masses. The mass-loss rates compare well to the formulas in Vink *et al.* (2000, 2001) and are also similar to those used by Freyer *et al.* (2006).

2.2.3 Initial Conditions

The cluster wind blows into a turbulent and inhomogeneous GMC clump, whose structure is based on the work of Vázquez-Semadeni *et al.* (2008) of turbulent and clumpy molecular clouds (specifically model Ms24J6). This model has a nominal Mach number of 15, is isothermal, and has no magnetic field. These results are scaled to create a GMC clump of radius 4 pc and mass $3240\,M_\odot$ (SimA). This gives an average density of $\approx 8 \times 10^{-22}\,\mathrm{g\,cm}^{-3}$, or a molecular hydrogen number density $n_{\mathrm{H}_2} \approx 250\,\mathrm{cm}^{-3}$. The clump initially has a uniform temperature of about 10 K, and is in rough pressure equilibrium with a surrounding uniform medium of density $3.33 \times 10^{-25}\,\mathrm{g\,cm}^{-3}$ ($n_{\mathrm{H}} \approx n_{\mathrm{e}} \approx 0.2\,\mathrm{cm}^{-3}$) and temperature 8000 K (see

Table 2.1: Wind properties of the three stars in the cluster as they evolve.

Stellar			MS stage		
Mass	$\dot{M}$	v_∞	Duration	Mtm	Energy
($M_\odot$)	($M_\odot\,yr^{-1}$)	(km s^{-1})	(Myrs)	(kg m s^{-1})	(ergs)
35	5.0×10^{-7}	2000	4.0	8.0×10^{36}	8.0×10^{49}
32	2.5×10^{-7}	2000	4.5	4.5×10^{36}	4.5×10^{49}
28	1.5×10^{-7}	2000	5.0	3.0×10^{36}	3.0×10^{49}
Stellar			RSG stage		
Mass	$\dot{M}$	v_∞	Duration	Mtm	Energy
($M_\odot$)	($M_\odot\,yr^{-1}$)	(km s^{-1})	(Myrs)	(kg m s^{-1})	(ergs)
35	1.0×10^{-4}	50	0.1	1.0×10^{36}	2.5×10^{47}
32	1.0×10^{-4}	50	0.1	1.0×10^{36}	2.5×10^{47}
28	1.0×10^{-4}	50	0.1	1.0×10^{36}	2.5×10^{47}
Stellar			WR stage		
Mass	$\dot{M}$	v_∞	Duration	Mtm	Energy
($M_\odot$)	($M_\odot\,yr^{-1}$)	(km s^{-1})	(Myrs)	(kg m s^{-1})	(ergs)
35	2.0×10^{-5}	2000	0.3	2.4×10^{37}	2.4×10^{50}
32	2.0×10^{-5}	2000	0.3	2.4×10^{37}	2.4×10^{50}
28	2.0×10^{-5}	2000	0.3	2.4×10^{37}	2.4×10^{50}

Table 1.1 for typical values of GMC clumps).

The hydrodynamic grid covers a cubic region of ±16 pc extent centered on the GMC clump. The cluster wind is injected as purely thermal energy within a radius of 0.375 pc (6 cells). The densest regions cool to ≈ 3.3 K, and a temperature floor of 1 K is imposed.

Another model is also explored where the GMC clump radius is 5 pc and where the density and pressure of the GMC clump and its surroundings are twice as great (SimB). This produces a clump mass of 10,500 $M_\odot$ (due to the inhomogeneity of the clump it is not quite 3.9× as massive as the clump in SimA). Unless otherwise

noted, all results are for SimA.

Using a Saltpeter initial mass function, one would expect the total stellar mass of a cluster containing three massive OB stars, such as those noted above, to be $\sim 0.5 - 1.0 \times 10^4\,\mathrm{M}_\odot$. Given that there is $3240\,\mathrm{M}_\odot$ of clump material in SimA, this implies a star formation efficiency of $\approx 50\,\%$. In SimB the mass of the stellar cluster is unchanged whilst there is $10{,}500\,\mathrm{M}_\odot$ of clump material, which implies a star formation efficiency of $\approx 30\,\%$.

2.2.4 Neglected Processes and Simplifications

This work is the first step in examining the feedback from a stellar cluster into surrounding molecular material left over from its formation. As such, many simplifications and approximations have been made.

These simulations do not include gravity, thermal conduction, magnetic fields, radiation pressure, photoionization, dust, cosmic rays or radiative losses *within* the stellar cluster. It is reasonable to estimate from the parameters noted in Table 2.1 that the winds have comparable momentum to the radiation fields of the stars (both emit momentum of roughly $10^{43}\,\mathrm{g\,cm\,s^{-1}}$ over the lifetime of the cluster[1]). The key factor in determining the relative importance of the winds and radiation fields to the dynamics of the gas is the strength of the coupling of the radiation field to the gas. If the degree of wind and photon leakage out of the cluster is comparable, then radiation pressure will provide just an order-unity enhancement to the wind pressure (Krumholz & Matzner, 2009). It should be noted that the neglect of direct radiation pressure and gravity in these simulations

[1]Note that in an optically thick medium where each photon is absorbed and reemitted multiple times, the momentum deposited is limited by the energy rather than by the momentum of the radiation field.

offset each other to some degree. However, the self-gravity of some of the densest structures in our cluster may be important on the timescales that we consider. The freefall time for the whole clump is about 3 Myrs. For the densest clumps in the simulation ($\rho \approx 10^{-19}\,\mathrm{g\,cm^{-3}}$) the freefall time is about 0.3 Myrs.

Inclusion of thermal conduction and photoevaporation should speed up the destruction of molecular material. These simulations reveal that the densest cloud fragments have $\rho \sim 10^{-19}\,\mathrm{g\,cm^{-3}}$ and radii of about 0.1 pc. At a distance of 3 pc from a stellar cluster emitting 10^{50} ionizing photons per second, we estimate that the mass-loss rate from photoevaporation (see, e.g., Pittard, 2007, for the relevant equations) is $\sim 4 \times 10^{20}\,\mathrm{g\,s^{-1}}$, giving a lifetime of about 1.5 Myrs. This is comparable to the mass-loss rate and lifetime due to hydrodynamic ablation. So it should be expected that the destruction of molecular material should be slightly quicker than occurs in these simulations through ablation alone. Having said this, photoevaporation may be suppressed in regions where the ram or thermal pressure of the surrounding medium is greater than the pressure of the evaporating flow (Dyson, 1994). Given these considerations, it is reasonable to assert that the simulations presented in this Chapter should be fairly representative even with the neglect of photoevaporation. Neglecting thermal conduction may also make little difference to the results given that it will be confined to regions where there is a temperature gradient parallel to the magnetic field.

It should further be noted that dust can dramatically affect the cooling within hot bubbles if it can be continuously replenished, perhaps by the evaporation/destruction of dense clumps (Everett & Churchwell, 2010) which will also mass-load the bubble (see, e.g., Pittard *et al.*, 2001a,b). The presence of dust will also affect the photoionization rate throughout the cluster. Clearly the effects of dust warrant

study in future work.

Radiative losses within the cluster can significantly change the energy flux into the surrounding environment (Silich *et al.*, 2004). However, this is not a significant effect for the cluster parameters considered in this work, and is likely important only for the most massive clusters and super star clusters.

2.3 Results

In this section the results of the simulations detailed above are presented. The initial blowout (Sec. 2.3.1) is examined, then the evolution up to $t = 4\,\mathrm{Myrs}$ (Sec. 2.3.2). Sec. 2.3.3 focuses on the feedback during the evolution of the stars through their various evolved stages (RSG and WR) and their subsequent explosions as SNe. The mass and energy fluxes into the wider surroundings are examined in Sec. 2.3.5 and the evolution of the column density in Sec. 2.3.6. A comparison between SimA and SimB, plus the evolution of the molecular mass is made in Sec. 2.3.7.

2.3.1 Initial Blowout

The cluster wind creates a high pressure and high temperature bubble within the GMC clump which expands most rapidly into regions of lower density. The initial blowout of this bubble into the lower density medium surrounding the GMC clump occurs at $t \sim 0.03\,\mathrm{Myrs}$, and is very aspherical due to inhomogeneity of the GMC clump (Fig. 2.2). This blowout occurs much faster than for a GMC clump with an equivalent uniform density - in such a case a 1D spherical bubble expands to a radius of $4\,\mathrm{pc}$ in $0.29\,\mathrm{Myrs}$, which is ~ 10 times slower than for the

inhomogeneous GMC clump used in the models presented in this work. Isolated blowouts at a number of distinct positions around the surface of the GMC clump rapidly grow and merge so that the entire clump is quickly surrounded by hot, expanding wind material. As this wind material streams out through low density channels, clump material is ablated into the flow and the clump gradually loses mass. Fig. 2.3 shows snapshots of the temperature evolution during this initial phase at $t = 0.03$, 0.13 and 0.22 Myrs. Here the hot wind is clearly visible streaming through the cold GMC. It is noticeable that dense parts of the clump can shield and protect less dense material in their "shadow", though the ability of the hot, high pressure gas to flow around denser objects mitigates this effect to some extent. This behaviour is apparent in Fig. 2.2 where material towards the bottom right of the clump is protected against ablation from the cluster wind by intervening dense material.

A swept-up shell around the outer edge of the bubble is visible in both Figs. 2.2 and 2.3. In this simulation the shell is reasonably thick and confines the hotter gas in the bubble interior, but for bubbles expanding into a higher density medium the shell is thinner and less stable. In such situations the shell fragments, and mini blowouts occur. These expand for a certain distance, before stalling, and merging back into the "global" shell (see also Meaburn *et al.*, 1988).

At this early stage by far the strongest shock in the simulation is the reverse shock near the central stellar cluster. The reverse shock is not spherical - instead its position is largely defined by the presence and location of the dense molecular material nearest to the stellar cluster. The shock heated cluster wind experiences a large range of densities, temperatures and velocities as it flows out of the GMC clump. At times it interacts subsonically with its environment, and at other times

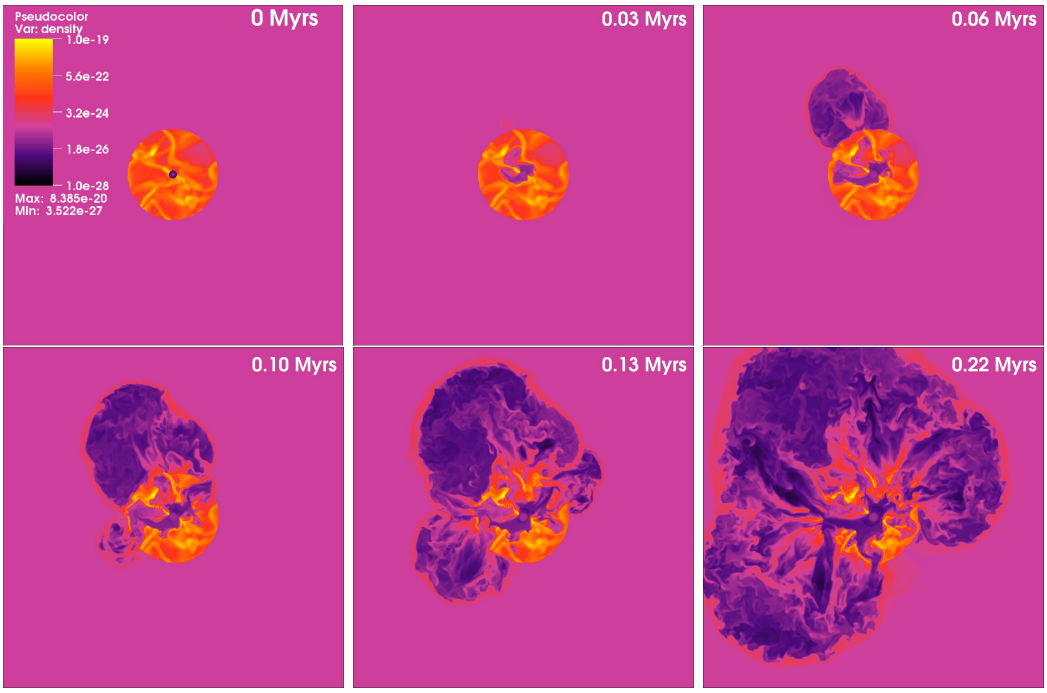

Figure 2.2: Density slices through the 3D simulation (SimA) in the xy-plane during the initial interaction of the cluster wind with the GMC clump. The density scale is shown in the top left panel. All such plots are produced using the VisIt Visualisation package.

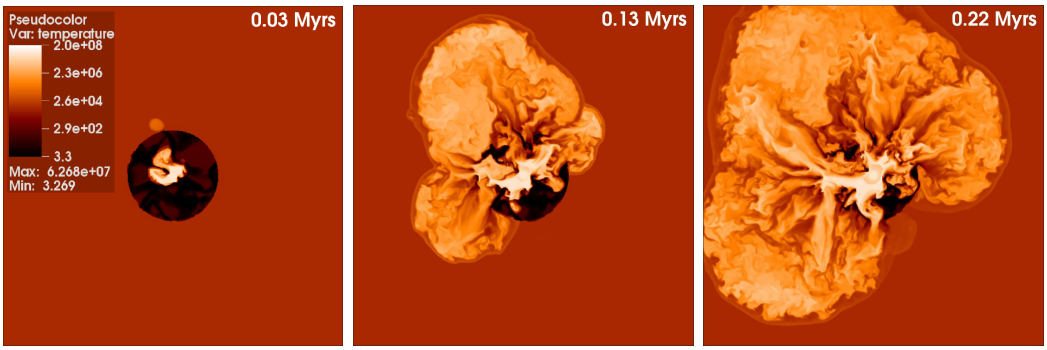

Figure 2.3: Temperature slices through the 3D simulation (SimA) in the xy-plane during the initial interaction of the cluster wind with the GMC clump. The temperature scale is shown in the left panel.

this interaction is supersonic. Relatively weaker shocks occur within the shock heated wind as it flows into and past the densest molecular gas. The outflow is generally quite turbulent in nature. This can affect the rate at which material is stripped from clouds (Pittard, 2009). The rate at which clouds lose mass through hydrodynamic ablation has been investigated in detail by Pittard *et al.* (2010).

2.3.2 Evolution during the star's MS stage

Fig. 2.4 shows the early evolution of the cluster environment after the initial blow out has occured but while all three stars remain on the MS. The low density channels through the GMC clump have left their imprint on the outflowing cluster wind as similarly low density channels. These channels contain hot ($\sim 10^7\,\mathrm{K}$), fast flowing gas which is relatively unimpeded by dense gas along its route, with a typical velocity of around 1000 $\mathrm{km\,s^{-1}}$. The flows are mass-loaded as denser material along their edges is mixed in. The orientation of the channels alters slightly as the simulation progresses due to the small velocity dispersion ($\approx$ few $\mathrm{km\,s^{-1}}$) of the dense molecular material in the GMC clump causing its structure to change with time. By about $t = 3\,\mathrm{Myrs}$ the position of the channels seems to have settled and they are reasonably stable.

Fig. 2.6 shows the situation at $t = 3.41\,\mathrm{Myrs}$ in three different planes. The channels carved by the cluster wind are evident in the panels in this figure, and the changes in orientation of the channels is apparent between Figs. 2.4 and 2.6. The left panel of Fig. 2.6 corresponds to the xy-plane, which is the default used for the other 2D slices within this Chapter. However, the center and right panels in Fig. 2.6 show that dense clump material remains closer, for longer, to the central

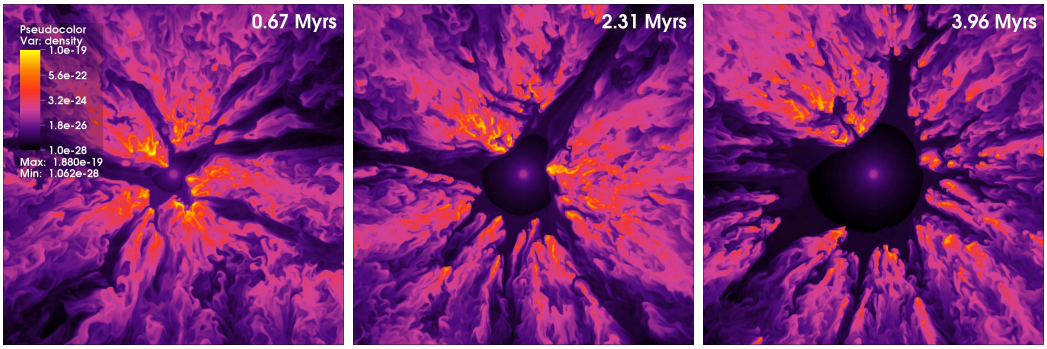

Figure 2.4: Density slices during the MS phase of the simulation (SimA) in the xy-plane. The last panel shows the density of gas in the cluster environment shortly before the most massive star transitions to a RSG. The channels carved by the cluster wind in the GMC clump structure slowly evolve over this period. The density scale is shown in the left panel.

star cluster in the xz and yz-planes. This is further shown in Fig. 2.5, which shows a cut-out of the 3D simulation at t = 2 Myrs. The cut-away octant allows a view into the centre of the cube where the cluster of stars is positioned and the reverse shock of the expanding winds can be seen. In the bottom left of Fig. 2.5 is an indication of the orientation of the axes of the cube. The presence of very dense clumps close to the reverse shock in the yz-plane is extremely apparent, but there are also some observable clumps in the xz-plane.

Together, Figs. 2.4-2.6 reveal that the reverse shock expands and becomes gradually more spherical with time as the cluster wind drives out more material and high density material continues to ablate away. By $t = 4$ Myrs the average radius of the reverse shock has increased to ~ 5 pc, though its radius is ≈ 3 pc at the position of the closest dense cloud to the centre of the cluster.

Fig. 2.7 shows the pressure at the reverse shock as a function of time. The pressure steadily declines throughout the main sequence phase of the most massive star, reaching a value of $P_{RS} \simeq 3 \times 10^{-12}\,\mathrm{dyn\,cm^{-2}}$ at $t = 4$ Myrs. It is

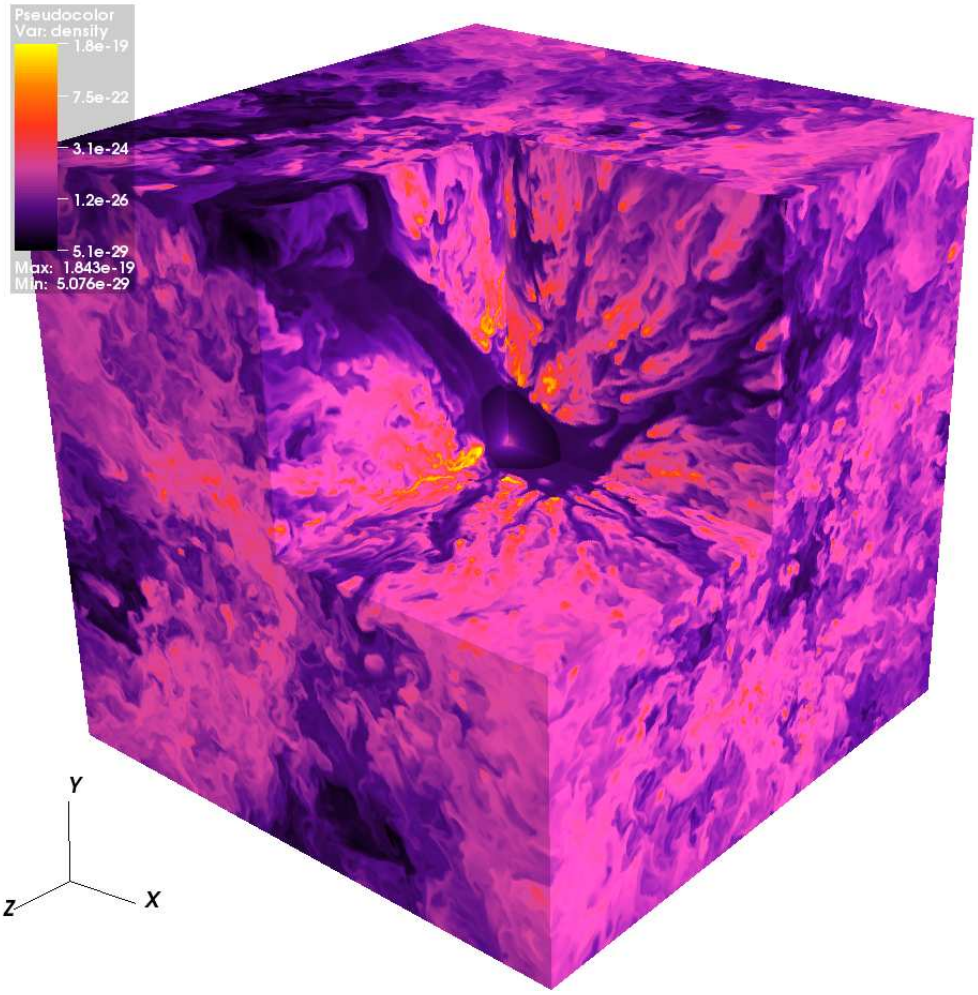

Figure 2.5: 3D density plot at 2 Myrs. The cut-away octant allows a view to the centre of the cube where the cluster of stars is positioned. The position of the reverse shock and the dense remnants of the GMC clump are evident.

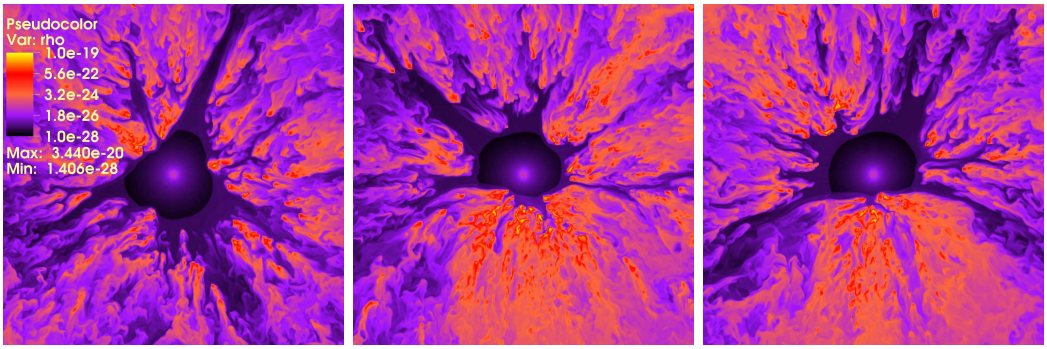

Figure 2.6: Density slices in three planes from SimA at $t = 3.41\,\mathrm{Myrs}$. [Left]: xy [Middle]: xz and [Right]: yz.

difficult to know a priori what value to expect for the reverse shock pressure. At $t = 1\,\mathrm{Myrs}$, Eq. 22 of Weaver *et al.* (1977) gives $P_{bub} = 1.6 \times 10^{-10}\,\mathrm{dyn\,cm^{-2}}$ assuming an ambient density of $9 \times 10^{-22}\,\mathrm{g\,cm^{-3}}$ (roughly the average density of our GMC clump), and $P_{bub} = 1.4 \times 10^{-12}\,\mathrm{dyn\,cm^{-2}}$ assuming an ambient density of $3.33 \times 10^{-25}\,\mathrm{g\,cm^{-3}}$ (the density of the medium outside of our GMC clump). Compared to the measured pressure of $\approx 10^{-11}\,\mathrm{dyn\,cm^{-2}}$ at this time, the former estimate is too high, while the latter is too low. Fig. 5 of Harper-Clark & Murray (2009) reveals that P_{bub} is about a factor of $4-5$ lower, when the covering fraction $C_f \sim 0.3 - 0.6$, than the Weaver *et al.* (1977) estimate. This implies that the finite-sized and porous clump used in these simulations has an effective covering fraction $C_f < 0.3$.

The way that P_{bub} is set is fundamental to the 0evolution of the flow and its affect on the GMC clump. Harper-Clark & Murray (2009) claim that the dynamics of a leaky bubble is set by P_{HII}, the pressure of the ionized gas component. Their argument is that when P_{RS} drops to $\approx P_{\mathrm{HII}}$, the escape of hot gas through gaps in the bubble shell slows as the hot gas is impeded by the cooler gas. However, it seems more likely that it is simply determined by the covering fraction of the

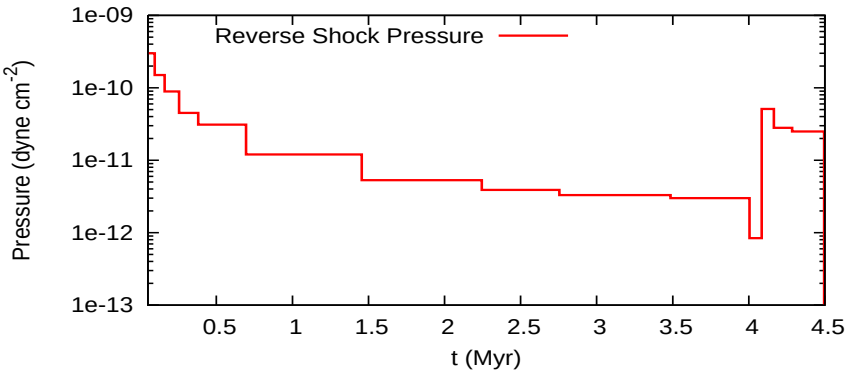

Figure 2.7: Pressure at the reverse shock as a function of time.

shell C_f and the ram pressure of the wind at the shell. If C_f is reasonably high, then individual bow shocks around the shell fragments/dense clumps merge to create a single reverse shock. The reverse shock will have an increasingly large stand-off distance (and thus smaller distance from the cluster) as C_f approaches unity. On the other hand, if C_f is reasonably low, then the bow shocks around individual clumps maintain their identity for longer, only merging downstream to create a global reverse shock at larger radii from the cluster. Such behaviour can be identified in the simulations presented in Pittard *et al.* (2005) and Alūzas *et al.* (2012).

2.3.3 Later evolutionary stages

2.3.3.1 Response due to the evolution of the 35 $M_\odot$ star

The most massive star evolves to a RSG after 4 Myrs. At this point its wind speed decreases to $v_\infty = 50\,\mathrm{km\,s^{-1}}$ and its mass loss rate increases to $\dot{M} = 10^{-4}\,M_\odot\,\mathrm{yr}^{-1}$ (see Table 2.1). This change results in a slower and denser cluster wind. The total kinetic power of the cluster wind reduces by about a half, from 1.14 $\times$

$10^{36}\,\mathrm{ergs\,s^{-1}}$ to $5.87\times10^{35}\,\mathrm{ergs\,s^{-1}}$, while the cluster wind becomes dominated by RSG material. This transition is shown in the top and middle rows of Fig. 2.8 and Fig. 2.9. The reverse shock moves inward to reestablish pressure equilibrium with the weaker cluster wind. This depressurises the previously shocked gas and leads to a rapid fall in temperature of the hottest gas in the simulation.

The RSG-enhanced cluster wind is much denser than the wind blown when all three stars were on the MS. As it interacts with the surrounding gas it is compressed into a thin shell which is Rayleigh-Taylor (RT) unstable. RT fingers are visible at t = 4.02 and 4.07 Myrs in Fig. 2.8 and at t =4.02 and t =4.06 Myrs in Fig. 2.9. These are short lived, lasting approximately 0.04 Myrs. The most massive star remains in the RSG phase for 0.1 Myrs, at which point the RSG-enhanced cluster wind has expanded to a typical radius of $\sim 5\,\mathrm{pc}$.

The most massive star then evolves into a Wolf Rayet star, with a mass-loss rate of $2\times10^{-5}\,\mathrm{M_\odot\,yr^{-1}}$ and a wind speed of $2000\mathrm{km\,s^{-1}}$. This change results in a much faster and more powerful cluster wind. The total kinetic power of the cluster wind increases by nearly two orders of magnitude to $2.59\times10^{37}\,\mathrm{ergs\,s^{-1}}$. This transition occurs at $t = 4.1\,\mathrm{Myrs}$ and can be seen in the middle rows of Fig. 2.8 and Fig. 2.9. The more powerful cluster wind forcefully pushes back the dense RSG material to beyond the position of the reverse shock during the previous MS phase. The typical radius of the reverse shock increases from about 5 pc at $t = 4.14\,\mathrm{Myrs}$ to $\approx 8\,\mathrm{pc}$ at $t = 4.4\,\mathrm{Myrs}$ (see third row of Fig. 2.8). The shocked cluster wind is $\approx 10^3$ times hotter than was the case when the cluster wind was "RSG-enhanced". Hot gas pervades almost completely the computational volume by $t = 4.15\,\mathrm{Myrs}$ (see Fig. 2.9).

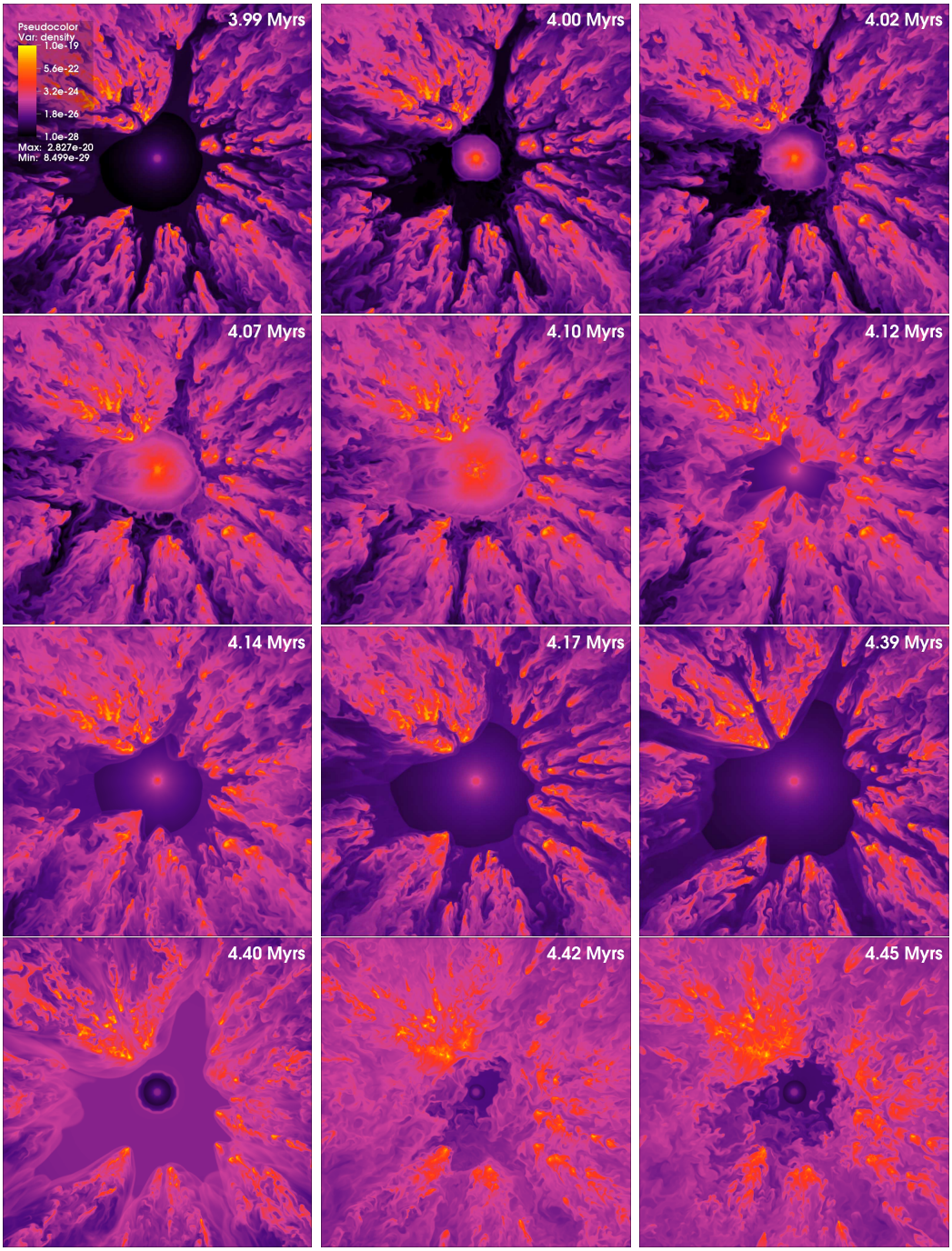

Figure 2.8: Density slices from SimA in the xy-plane during the RSG, WR and SN stages of the highest mass star. This star transitions from the MS to the RSG stage at $t = 4.0\,\mathrm{Myrs}$ (top middle panel), from the RSG to the WR stage at $t = 4.1\,\mathrm{Myrs}$ (second middle panel), and explodes at $t = 4.4\,\mathrm{Myrs}$ (bottom left panel). The other two stars remain on the MS during this time. The density scale is shown in the top left panel.

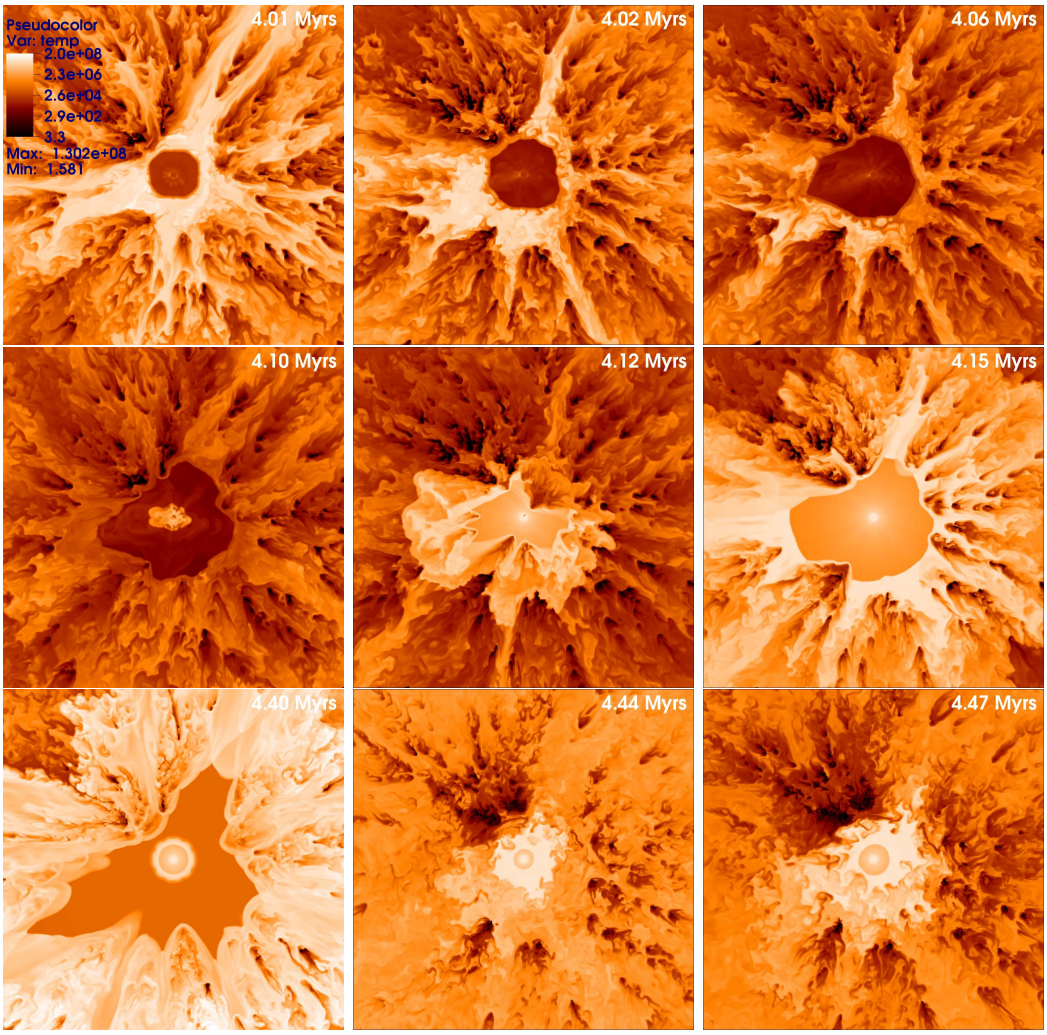

Figure 2.9: Temperature slices from SimA in the xy-plane during the RSG, WR and SN stages for the highest mass star. The first panel corresponds to just after this star has become a RSG. The star transitions to a WR star at $t = 4.1\,\mathrm{Myrs}$ (left panel middle row) and explodes as a SN at $t = 4.4\,\mathrm{Myrs}$ (left panel bottom row). The other stars remain on the MS during this time. The temperature scale is shown in the left panels.

2.3.3.2 Impact of the first supernova explosion

After 4.4 Myrs of evolution the most massive star explodes as a supernova (see the bottom rows of Figs. 2.8 and 2.9), adding $10\,M_\odot$ of ejecta and 10^{51} ergs of energy into the surroundings. The SN ejecta sweeps up the WR-dominated cluster wind into a thick shell, which propagates at high speed through the lower density regions surrounding the explosion, heating the gas to very high temperatures. The forward shock has already propagated off the grid by the time of the snapshot in the bottom left panel of Fig. 2.8. The highly aspherical reverse shock seen in this panel is caused by the forward shock reflecting off dense clumps of gas in the simulation. The reverse shock then moves inwards towards the central cluster and nearly overwhelms the MS-dominated cluster wind from the remaining two stars (bottom middle panel of Fig. 2.8), which is seen sweeping up the cold SN ejecta in the bottom left panel. The reverse shock of the cluster wind is forced back to a radius of $\approx 0.9\,$pc by $t = 4.42\,$Myrs, but slowly begins to expand to $\approx 1.5\,$pc by $t = 4.47\,$Myrs as the pressure within the supernova remnant diminishes. One of the main effects of the SN is to fill the low-density wind-carved channels through the GMC clump with denser material which the cluster wind must again clear. The very densest fragments left over from the original GMC clump are not only resistant to ablation from the cluster wind, but also are affected very little by the propagation of the SN shockwave.

The top panel of Fig. 2.10 shows the temperature of the gas in the simulation during the 5000 years after the most massive star goes supernova. The green dashed line shows the state just before the supernova explosion, and the thick, red, solid line corresponds to just afterwards. The maximum temperature on the

grid jumps by a factor of 4 in the first 100 years (from $\sim 10^8$ to $\sim 4 \times 10^8$ K) and the amount of material between $10^7 - 10^8$ K increases from about 1 $M_\odot$ to 10 $M_\odot$. The maximum temperature continues to increase up to 10^9 K as the shockwave propagates through the cloud. Gas with $T \lesssim 100$ K responds more slowly to the SN explosion, but it is clear that some of it is heated to $T \approx 10^4$ K by the passage of the shock wave. A significant proportion of the coldest gas with $T \lesssim 10$ K is hardly affected, however. This very cold gas is situated in the very densest regions of the remaining GMC clump. As the shockwave passes through the simulation, the less dense material surrounding these regions is heated and ionized, but the densest parts are relatively untouched. This is because the transmitted shock speed through the densest clumps is as low as a few 10's of km s^{-1}, and the gas cools back to its original pre-shock temperature on timescales as short as a few 10's of yrs. More typical cooling times are 10^3 yrs or so, but it is clear that the transmitted shocks into the densest clumps are highly radiative (the crossing time of the transmitted shocks through these fragments is $\sim 10^4$ yrs). The strong cooling of this gas is responsible for the rapid rise in the H_2 mass following its initial drop after each SN explosion (see Sec. 2.3.7). The SN ejecta first begins to leave the grid approximately 4000 years after the explosion.

The middle panel of Fig. 2.10 shows the pressure (p/k) during this time. After the SN explosion the pressure increases by four orders of magnitude from $10^8 - 10^{12}$ K cm^{-3}. The maximum pressure then slowly decreases as the remnant expands adiabatically. By $t = 4.4046$ Myrs (black double-dashed line) the maximum pressure on the grid is back to $\approx 10^8$ K cm^{-3}, but now there is ≈ 860 $M_\odot$ of material at $10^7 \leq$ p/k $\leq 10^8$ K cm^{-3}, compared to the 0.02 $M_\odot$ of gas in this pressure range prior to the SN. 50,000 yrs after the SN explosion the net effect is a shift

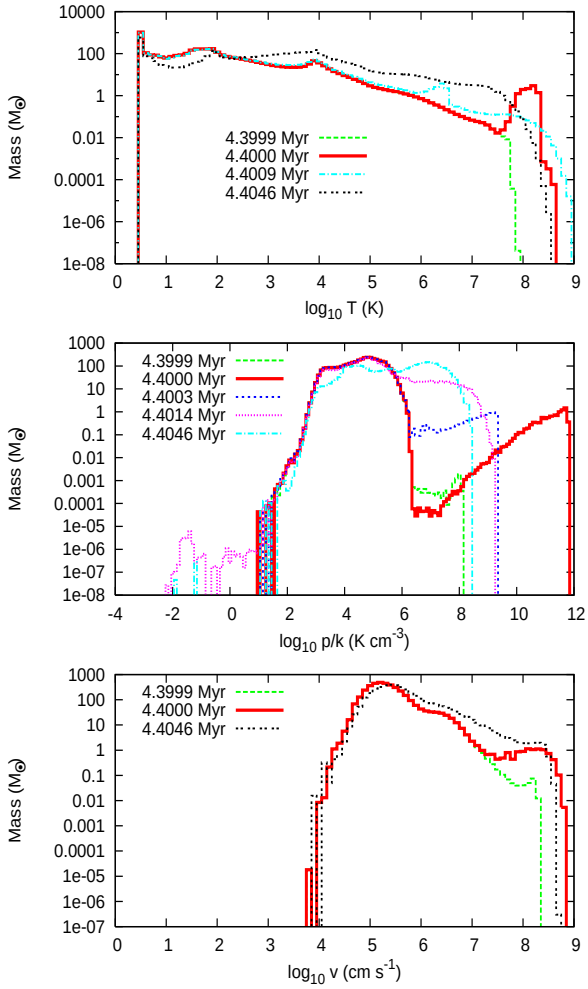

Figure 2.10: Histogram of the gas temperature (top), pressure (middle), and velocity (bottom) during the first supernova explosion. In each panel the solid red line corresponds to a time just after the explosion occurs.

in gas from lower ($10^3 \lesssim \mathrm{p/k} \lesssim 10^6\,\mathrm{K\,cm^{-3}}$) to higher ($10^6 \lesssim \mathrm{p/k} \lesssim 10^8\,\mathrm{K\,cm^{-3}}$) pressure.

The maximum gas velocity also increases rapidly in the first 100 years after the supernova explosion, as shown in the bottom panel of Fig. 2.10. The maximum gas velocity increases from $2000\,\mathrm{km\,s^{-1}}$ to $10,000\,\mathrm{km\,s^{-1}}$ as the hot, high pressure ejecta starts its expansion. Over the next 5000 yrs the maximum velocity drops

to $\approx 5000\,\mathrm{km\,s^{-1}}$ and there is significantly more mass with $v \geq 100\,\mathrm{km\,s^{-1}}$ than was the case pre-SN. The majority of the gas continues to have a velocity of $\sim 1-10\,\mathrm{km\,s^{-1}}$, however, which highlights the weak coupling of the SN explosion to the densest parts of the surrounding gas.

2.3.3.3 Response due to the evolution of the 32 $\mathrm{M_\odot}$ and 28 $\mathrm{M_\odot}$ stars

0.1 Myrs after the explosion of the most massive star, the $32\,\mathrm{M_\odot}$ star evolves off the MS and onto the RSG branch (see Table 2.1), decreasing the kinetic power of the cluster wind still further to $2.7 \times 10^{35}\,\mathrm{ergs\,s^{-1}}$. This star follows the same post-MS evolution as the most massive star, and blows a dense slow moving RSG wind followed by a high momentum WR wind before finally exploding. The SN explosion again imparts $10\,\mathrm{M_\odot}$ of material and $10^{51}\,\mathrm{ergs\,s^{-1}}$ of energy into the surroundings. After a further 0.1 Myrs the lowest mass (and only remaining) star considered in our model evolves onto the RSG branch, reducing the kinetic power of the cluster wind to $7.9 \times 10^{34}\,\mathrm{ergs\,s^{-1}}$. This star explodes as a supernova at $t = 5.4\,\mathrm{Myrs}$. At this moment there are no wind-blowing stars remaining in our model, and the ambient and enriched gas gradually disperses and flows off the grid boundaries.

2.3.4 Wind Velocity

Fig. 2.11 shows four density snapshots during the various evolutionary phases of the cluster overlaid with velocity vectors. The top two panels are both from the MS phase - the former during the initial blowout and the latter shortly before the most massive star transitions to its RSG phase. At $\mathrm{t} = 0.32\,\mathrm{Myrs}$ (top left panel in Fig. 2.11) there is relatively fast moving gas streaming through the low density

channels, with much slower, denser gas elsewhere, most of which is relatively undisturbed and almost stationary. Gas at intermediate densities which is slowly moving away from the stellar cluster is likely material which has been ablated from the denser parts of the GMC clump. At t = 3.99 Myrs (top right panel) the winds have evacuated a large region in the centre of the original GMC clump and the freely expanding wind is now approximately spherical. Wind material is still clearly flowing fastest through the existing channels. The t =4.09 Myrs snapshot (bottom left panel) corresponds to a time shortly before the most massive star evolves from a RSG to a WR star. The RSG wind is a lot slower, and the panel shows a favourable expansion towards the left side of the cluster where confinement by dense surrounding clouds is a minimum. The bottom right panel of Fig. 2.11 shows the cluster once the most massive star has evolved to become a WR star and shortly before the first supernova. The high momentum WR wind has evacuated a large region of gas around the star and the reverse shock has expanded out to a large radius. This panel nicely illustrates how the fastest moving material is confined to the pre-shock wind and the low density channels.

2.3.5 Mass and energy fluxes into the wider environment

The top left panel in Fig. 2.12 shows the total mass flux off the grid as a function of time. The mass flux is zero until the first blowouts reach the edge of the grid and then steadily increases up until $t \approx 0.4$ Myrs as various shells of swept up material reach the outer boundary of the simulation. The material behind the shells is less dense, and therefore the mass flux declines as the shells leave the

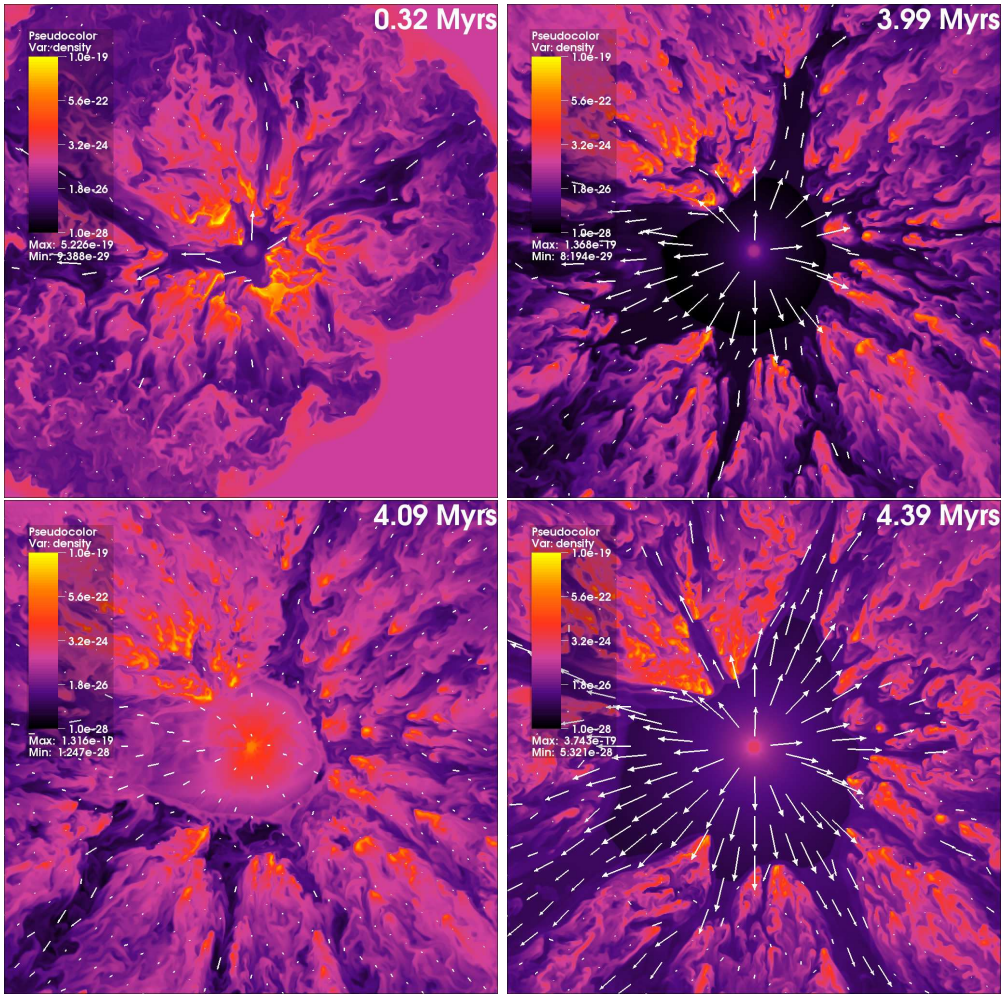

Figure 2.11: Density in the xy plane at t = 0.32, 3.99, 4.09 and 4.39 Myrs with velocity vectors overlaid. The largest arrows correspond to a velocity of 2000 km s^{-1}.

grid. The mass flux stabilizes at $t \approx 1.15$ Myrs and then begins a slow, almost linear, increase from $1.6 \times 10^{-4}\,\mathrm{M}_\odot\,\mathrm{yr}^{-1}$, reaching nearly $3 \times 10^{-4}\,\mathrm{M}_\odot\,\mathrm{yr}^{-1}$ at $t = 4.0$ Myrs. In comparison, the mass-loss rates of the three stars during the MS is $5 \times 10^{-7}, 2.5 \times 10^{-7}$ and $1.5 \times 10^{-7}\,\mathrm{M}_\odot\,\mathrm{yr}^{-1}$ for the $35\,\mathrm{M}_\odot$, $32\,\mathrm{M}_\odot$ and $28\,\mathrm{M}_\odot$ stars, respectively, giving a cluster mass-loss rate of $9 \times 10^{-7}\,\mathrm{M}_\odot\,\mathrm{yr}^{-1}$.

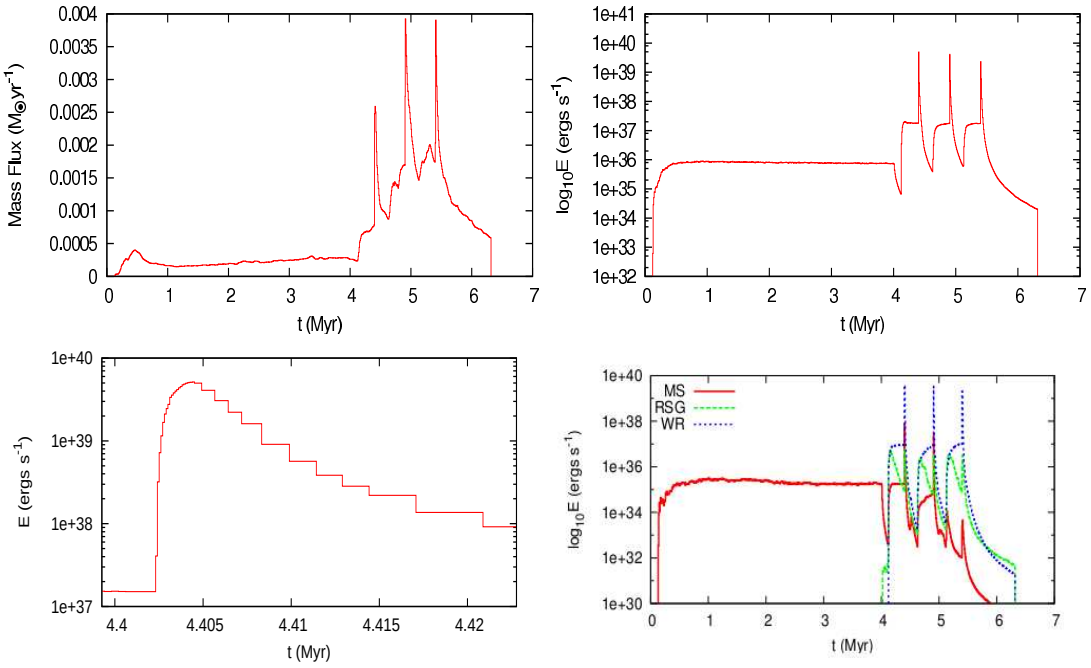

Figure 2.12: Total mass and energy fluxes off the grid as a function of time. [Top left]: Total mass flux off the grid as a function of time. [Top right]: Energy flux off the grid as a function of time across the entire simulation. [Bottom left]: Energy flux off the grid focused on the first SN explosion. The different step sizes are caused by a change in the cadence of the dump files analyzed, and do not reflect the simulation timestep which is much smaller. [Bottom right]: Energy flux off the grid split into the components from MS (red solid line), RSG (green dashed line) and WR (dotted blue line) material.

This indicates that the cluster wind is "mass-loaded"[1] by factors of $200 - 300$ as it streams through the molecular material in the GMC clump, and that less than 1 per cent of the material leaving the grid during this period originated in the stellar winds.

There is a slight decrease in the mass flux off the grid between $t = 4.0$ and 4.1 Myrs, during the RSG stage of the highest mass star in which the flow depressurizes. This is followed by an increase in the mass flux to $\approx 7 \times 10^{-4}\,\mathrm{M_\odot\,yr^{-1}}$

[1] Although the term "mass-loaded" is used here, the molecular material ablated by the cluster wind is not fully mixed into the flow by the time that it leaves the grid. Since distinct phases are still identifiable, "mass entrainment" may be a more appropriate term.

during the subsequent WR stage. This represents a "mass-loading" factor 35× the mass-loss rate of the cluster wind during this period ($2.04 \times 10^{-5}\,\mathrm{M_\odot\,yr^{-1}}$). Therefore, only 3 per cent of the material leaving the grid is from the stellar winds. The mass flux jumps to $2.5 \times 10^{-3}\,\mathrm{M_\odot\,yr^{-1}}$ following the first SN explosion, and peaks at $3.9 \times 10^{-3}\,\mathrm{M_\odot\,yr^{-1}}$ following each of the second and third explosions. In between the SN explosions, the mass flux peaks at $2.0 \times 10^{-3}\,\mathrm{M_\odot\,yr^{-1}}$ at $t = 5.31\,\mathrm{Myrs}$. Clearly the WR winds and SN explosions act to speed up the rate at which molecular material is cleared from the cluster surroundings.

The top right panel of Fig. 2.12 shows the total energy flux off the grid as a function of time. The energy flux increases from zero at the time when the shell first encounters the grid boundary, to $\approx 8.5 \times 10^{35}\,\mathrm{ergs\,s^{-1}}$ at $t = 1\,\mathrm{Myrs}$, with a gradual and linear decline to $7.5 \times 10^{35}\,\mathrm{ergs\,s^{-1}}$ at $t = 4\,\mathrm{Myrs}$. The linear decline correlates with the gradual increase in the ablation rate during this period. These values for the energy flux compare to the total kinetic power of the cluster wind of $1.14 \times 10^{36}\,\mathrm{ergs\,s^{-1}}$. It is clear, therefore, that the shocked cluster wind is largely adiabatic, but that nevertheless about one quarter to one third of the injected wind power is lost to radiative processes. It is interesting to note that Bruhweiler *et al.* (2010) invoke substantial radiative losses due to the turbulent interaction of stellar winds with inhomogeneous surroundings in order to explain their observations of the Rosette Nebula.

The combined energy input by the 3 O-stars during the first 4 Myrs is $1.44 \times 10^{50}\,\mathrm{ergs}$. When the most massive star evolves to the RSG phase there is a decrease in the kinetic power of the cluster wind to $5.87 \times 10^{35}\,\mathrm{ergs\,s^{-1}}$, and this is reflected in a corresponding decrease in the energy flux off the grid, which, however, drops below this value. This "overshoot" is likely due to some combination

of enhanced cooling in the denser cluster wind and possible overstable behaviour of the flow. The energy flux off the grid increases by two orders of magnitude to $1.8 \times 10^{37}\,\mathrm{ergs\,s^{-1}}$ when the most massive star has evolved to a WR star. Comparing to the kinetic power of the cluster wind at this time ($2.59 \times 10^{37}\,\mathrm{ergs\,s^{-1}}$), we find that radiative losses are again about 30 per cent. The combined energy input by the WR star and the 2 remaining O-stars during the period $4.1 - 4.4\,\mathrm{Myrs}$ is $2.46 \times 10^{50}\,\mathrm{ergs}$. Altogether, the most massive star injects $\approx 3.9 \times 10^{50}\,\mathrm{ergs}$ of energy via its wind during its lifetime, and about 70 per cent of this escapes to large distances.

The bottom left panel of Fig. 2.12 shows the total energy flux off the grid around the time of the first SN explosion which occurs at $t = 4.4\,\mathrm{Myrs}$. The energy flux rises steeply as the blast shock propagates off the grid, and peaks at $\approx 5 \times 10^{39}\,\mathrm{ergs\,s^{-1}}$ about $5000\,\mathrm{yr}$ after the explosion. Thereafter the energy flux steadily decreases. The integrated energy off the grid during this time reveals that greater than 99 per cent of the SN energy flows off the grid, and less than 0.5 per cent is radiated. Clearly the SN energy propagates through the environment relatively unimpeded by the dense clumps.

The subsequent energy flux from the grid is dominated by the WR stages from the two lower mass stars and their subsequent explosions, and drops below $10^{35}\,\mathrm{ergs\,s^{-1}}$ as relic hot gas expands and dissipates.

The bottom right panel of Fig. 2.12 shows the proportion of the energy flux off the grid from each of the three evolutionary stellar phases. The solid red line shows the contribution from the MS wind, the green dashed line shows the RSG contribution and the blue dotted line represents the energy flowing off the grid contained in the WR wind. For the first 4 Myrs all three of the stars are on the MS,

and therefore all of the energy leaving the grid is contained within MS material. When the most massive star evolves to a RSG at $t = 4.0$ Myrs the MS contribution dips. However, although there is a small amount of energy leaving the grid from RSG material, this is very limited at approximately 5×10^{31} ergs s^{-1}. When the star evolves further to the WR phase, the energy flux off the grid contains components from all three phases as remnant MS and RSG material is swept from the grid. The energy contained within the WR material dominates after this initial expulsion. The first SN has a similar effect, expelling a material from all three phases, with energy contained within the WR material dominating. These same trends are observed throughout the evolution of the other two stars. At $t = 5.0$ Myrs the only remaining star evolves onto the RSG branch, and therefore there is no longer any MS material being generated. From this point there is still energy leaving the grid which is contained in remnant MS material, but the quantity declines rapidly. The same is true for RSG material after $t = 5.1$ Myrs and WR material after $t = 5.4$ Myrs. By $t = 5.8$ Myrs there is negligible energy leaving the grid contained within MS material, and although the energy contained within RSG and WR material is declining, the simulation ends before it is all expelled completely.

2.3.6 Evolution of column densities

Fig. 2.13 shows the time evolution of the average column density, $\bar{N}_{\rm H}$, from the centre of the cluster. This is calculated over 10^4 individual sight lines spaced equally in solid angle and traced out to the edge of the grid. The column density is greatest at $t = 0$, but diminishes with time as the stellar winds push the clump

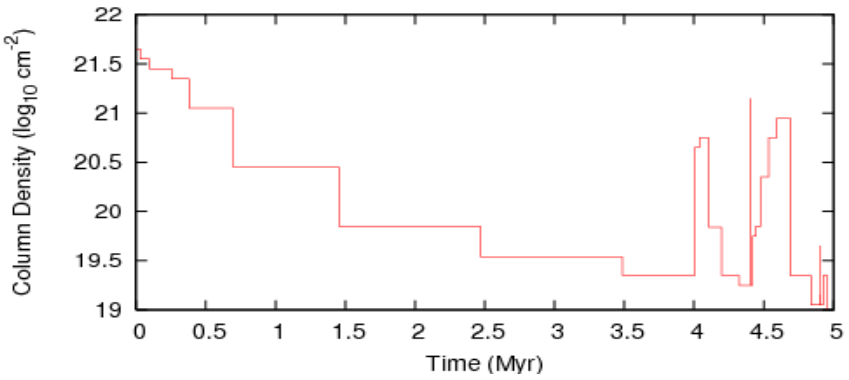

Figure 2.13: The evolution of the average column density from the centre of the cluster throughout the simulation.

material away from the cluster (some of this decrease is also due to material leaving the grid). A factor of 100 reduction from an initial value of $\approx 4 \times 10^{21}\,\mathrm{cm}^{-2}$ occurs by 4 Myrs. Then, as the most massive star enters its RSG stage, $\bar{N}_{\mathrm{H}}$ increases by over 1 dex to nearly $10^{21}\,\mathrm{cm}^{-2}$. This increase is short-lived however, because the density of the cluster wind drops significantly once the most massive star enters its WR stage. Immediately prior to the first SN explosion, $\bar{N}_{\mathrm{H}} \approx 2 \times 10^{19}\,\mathrm{cm}^{-2}$. The $10\,\mathrm{M}_{\odot}$ of ejecta from the explosion momentarily increases the average column density to more than $10^{21}\,\mathrm{cm}^{-2}$, but this rise is extremely short-lived and less than a few hundred years in duration. $\bar{N}_{\mathrm{H}}$ then gradually increases as the cluster wind again begins to fill the nearby environment with mass, especially once the second most massive star enters its RSG stage. Similar behaviour in the evolution of $\bar{N}_{\mathrm{H}}$ then occurs as the remaining massive stars evolve in turn through their various wind and SN stages.

Fig. 2.14 shows histograms of the column density distribution at specific times in the simulation. At $t = 0\,\mathrm{yr}$, columns up to $\approx 10^{23}\,\mathrm{cm}^{-2}$ exist for sightlines through the densest parts of the initial GMC clump, but a very small fraction of

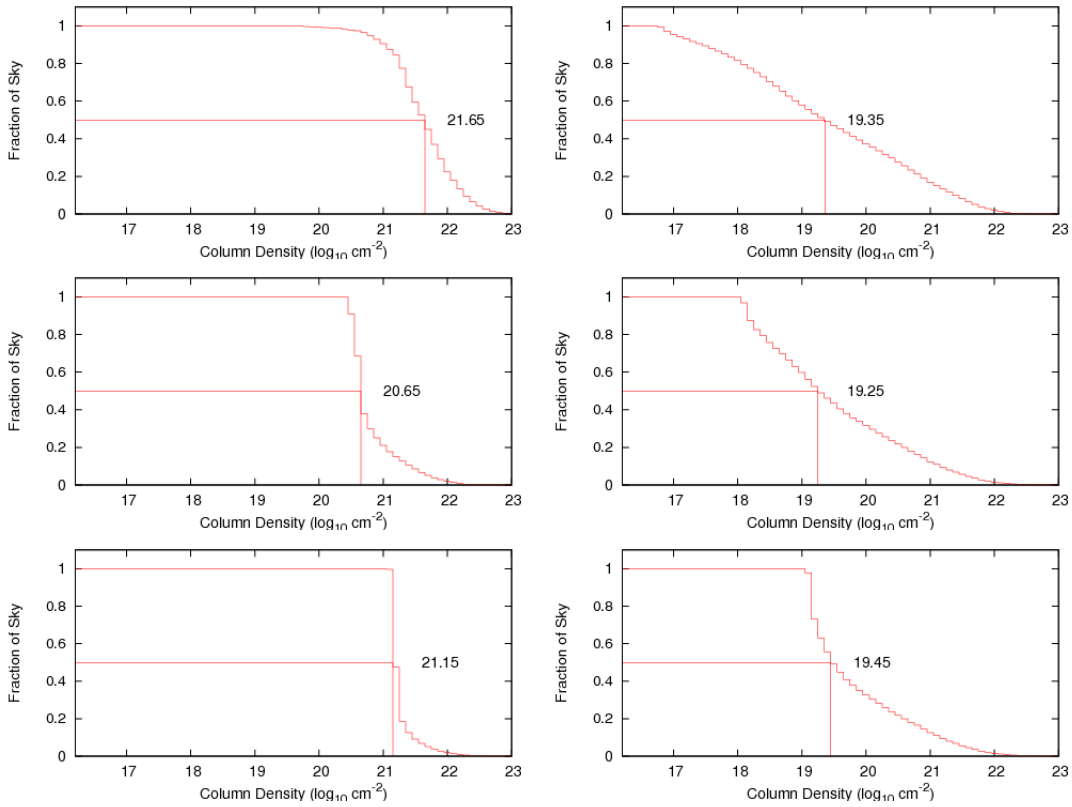

Figure 2.14: The evolution of the average column density from the centre of the cluster. From left to right and top to bottom the plots are at times $t = 0$, $t = 3.99$, $t = 4.02$, $t = 4.39$, $t = 4.40000$ and $t = 4.40110$ Myrs. The numerical value in each panel notes the value of $\log_{10} \mathrm{N_H}$ at which 50 per cent of the sky has a smaller or larger column.

sightlines from the cluster experience column densities as low as $10^{20}\,\mathrm{cm}^{-2}$. At $t = 3.99$ Myrs (see top right panel in Fig. 2.14 and middle left panel in Fig. 2.15), the distribution of column densities is much broader, with those passing through dense and relatively nearby regions having column densities up to $10^{22}\,\mathrm{cm}^{-2}$ and those passing through the lowest density material having $N_\mathrm{H} \approx 10^{17}\,\mathrm{cm}^{-2}$. It is interesting to see how the distribution has changed shape by $t = 4.02$ Myrs, once the most massive star has entered its RSG stage (see middle left panel in Fig. 2.14 and middle right panel in Fig. 2.15). The RSG-enhanced cluster wind

"fills in" all of the low column density sightlines so that the minimum value is now $N_{\rm H} \approx 3 \times 10^{20}\,{\rm cm}^{-2}$. The impact of the WR-enhanced cluster wind is seen at $t = 4.39\,{\rm Myrs}$ (see middle right panel in Fig. 2.14 and bottom left panel in Fig. 2.15). The higher speed and reduced density of the cluster wind now reduces the low column density sightlines to $\approx 10^{18}\,{\rm cm}^{-2}$. The column density distribution at a time just after the first SN explosion is shown at $t = 4.40000\,{\rm Myrs}$ (bottom left panel in Fig. 2.14). The relatively dense ejecta causes the minimum value of $N_{\rm H}$ to rise to $\approx 10^{21}\,{\rm cm}^{-2}$, yet this drops to just $10^{19}\,{\rm cm}^{-2}$ 1100 yrs later (bottom right panel in Fig. 2.14).

Fig. 2.15 shows Hammer projections of the column density at specific times. The directions with the highest (lowest) initial column density maintain their positions throughout the simulation. It is clear that the regions of highest column density become increasingly "porous" and "shredded" by the action of the cluster wind and supernovae. The "filling in" of the column density during the time of the RSG-enhanced cluster wind ($t = 4.02\,{\rm Myrs}$ in Fig. 2.15) is readily apparent.

Though photoionization is not included in this work, it is interesting to estimate the fraction of ionizing photons which could escape to large distances. The integral of $4\pi r^2 \alpha_{\rm B} n_{\rm e}^2 dr$, where r is the radial distance to the stellar cluster, $n_{\rm e}$ is the electron number density, $\alpha_{\rm B}$ is the case B recombination coefficient, is evaluated along each sightline. Where it exceeds $\dot{S}_{\rm cl}$, the rate of ionizing photons from the stellar cluster, the ionization front is trapped on the grid in that direction. Fig. 2.16 shows the result of this calculation. Initially the ionization front is almost completely trapped within the GMC clump surrounding the stellar cluster, with less than 1 per cent of ionizing photons escaping (as indicated by the red colour). However, by $t = 0.95\,{\rm Myrs}$, the stellar winds have sufficiently

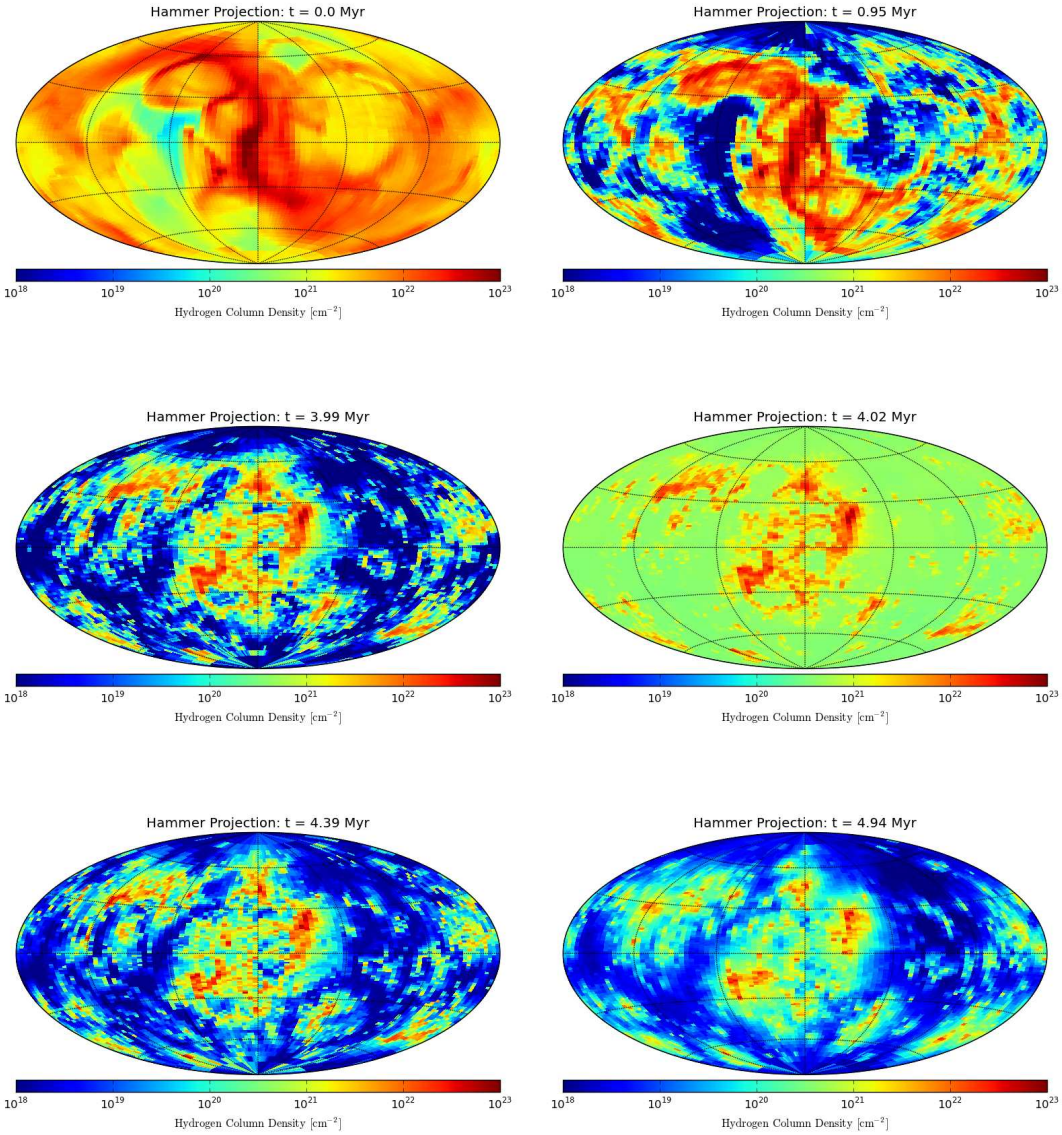

Figure 2.15: Hammer projections of the column density at specific times.

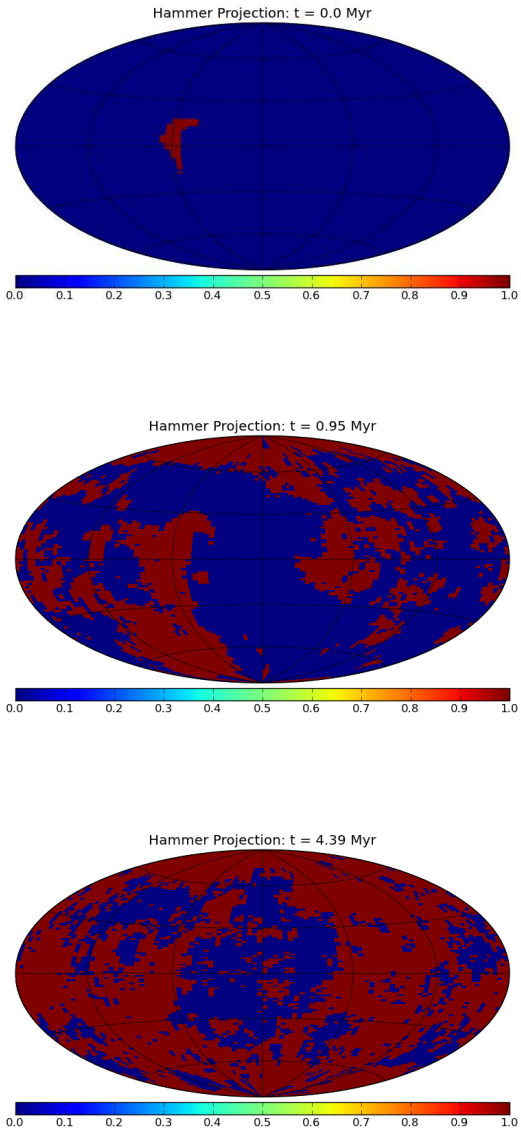

Figure 2.16: Hammer projections of the position of the ionization front at specific times. Red (blue) corresponds to the ionization front being outside (within) the grid in that direction, and identifies the directions where ionizing photons escape to large distances.

cleared away dense molecular and atomic material that about 40 per cent of the ionizing radiation escapes. This increases to nearly 60 per cent by $t = 3.99\,\mathrm{Myrs}$. The RSG-enhanced cluster wind is then sufficiently dense to completely prevent any ionizing radiation escaping to large distances. Once the lower density WR-enhanced cluster wind clears the RSG dominated material off the grid the escape fraction increases once more, reaching nearly 65 per cent just prior to the first SN explosion and 75 per cent at $t = 4.94\,\mathrm{Myrs}$.

Recently, Pellegrini *et al.* (2012) determined that the mean, luminosity weighted, escape fraction of ionizing photons from the HII region population in the LMC and SMC is $\gtrsim 0.42$ and $\gtrsim 0.40$, respectively. The results in this Chapter are consistent with these values, and similar values from Reines *et al.* (2008), but a more rigorous and detailed analysis of the photoionization beyond this work is necessary.

2.3.7 Comparison of SimA and SimB and evolution of the molecular mass

Fig. 2.17 shows the initial destruction of the GMC clump for SimA and SimB. The higher density clump and increased clump radius in SimB inevitably delays the blowout and subsequent expansion of the cluster wind. However, the nature of the interaction is broadly similar, and the same general features are seen as the cluster wind percolates through the "porous" molecular environment, including the formation of fast-flowing low-density channels.

The mass flux off the grid from SimB behaves qualitatively similarly to that from SimA, although the exact values are a little higher. There is again a broad

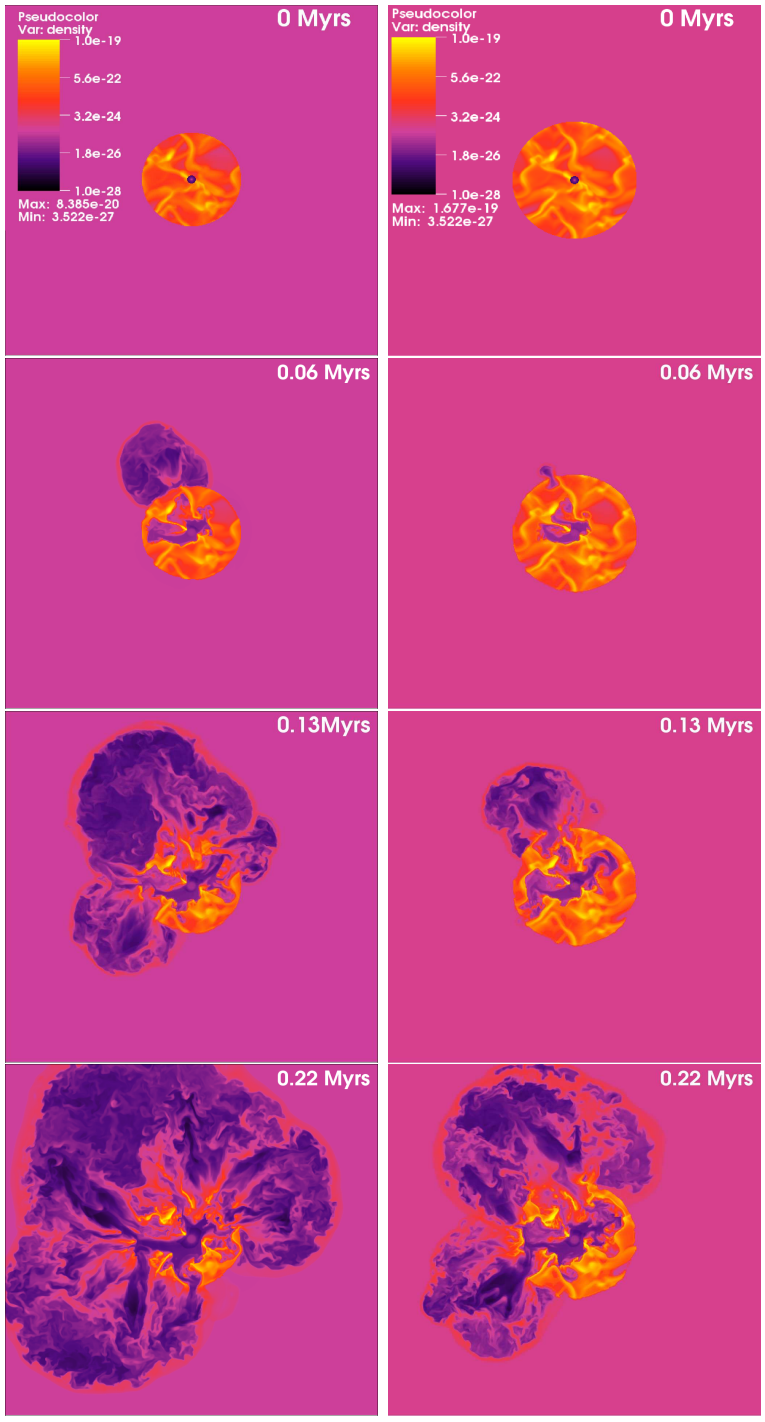

Figure 2.17: Comparison of the initial expansion of the cluster wind in the xy-plane. [Left]: Sim A and [Right]: Sim B. Sim B has a higher ambient density and a larger clump radius than Sim A. The density scales for each simulation are shown in the top panels.

peak caused by the initial encounter of the shell with the boundaries, in which the mass flux off the grid peaks at a rate of $4.6 \times 10^{-4}\,\mathrm{M_\odot\,yr^{-1}}$ at $t = 0.67\,\mathrm{Myrs}$. The mass flux declines to a minimum of $2.9 \times 10^{-4}\,\mathrm{M_\odot\,yr^{-1}}$ at $t \approx 1.6\,\mathrm{Myrs}$, and then increases roughly linearly with time to reach a value of $7 \times 10^{-4}\,\mathrm{M_\odot\,yr^{-1}}$ at $t = 4\,\mathrm{Myrs}$. The latter indicates a "mass-loading" factor of nearly 1000. The mass flux increases to $1.6 \times 10^{-3}\,\mathrm{M_\odot\,yr^{-1}}$ during the first WR stage, a mass-loading factor of nearly 80. A peak mass flux of $4.3 \times 10^{-3}\,\mathrm{M_\odot\,yr^{-1}}$ is attained following the first SN explosion, with peaks at 7 and $8 \times 10^{-3}\,\mathrm{M_\odot\,yr^{-1}}$ following the second and third explosions respectively.

The energy flux off the grid from SimB peaks at $\approx 7.4 \times 10^{35}\,\mathrm{ergs\,s^{-1}}$ at $t = 1.5\,\mathrm{Myrs}$, followed by a gradual decline to a roughly constant rate of $\approx 6.4 \times 10^{35}\,\mathrm{ergs\,s^{-1}}$ between $t = 2.5 - 4\,\mathrm{Myrs}$. During this latter period, nearly half of the cluster wind power is radiated. The energy flux plateau's at about $1.45 \times 10^{37}\,\mathrm{ergs\,s^{-1}}$ during the first WR stage (indicating that again nearly half of the input energy is being radiated), but similar values are reached only towards the very end of the other two WR stages.

The evolution of the total H_2 mass throughout the simulation volume for both SimA and SimB is shown in Fig. 2.18 (see the bottom panel of Fig. 2.1 for the ionization fraction of hydrogen with respect to the temperature). Due to the larger clump radius and higher density, SimB has approximately three times the initial H_2 mass as SimA. At very early times during the initial blowout the H_2 mass decreases by $\approx 10\%$ as molecular gas at relatively low densities is cleared out of the GMC clump. Both simulations then show the same general trend of steady H_2 depletion during the MS phase of the cluster wind. SimA loses H_2 mass at a rate of $1.74 \times 10^{-4}\,\mathrm{M_\odot\,yr^{-1}}$ between $t = 1 - 4\,\mathrm{Myrs}$. Since this is comparable

to the mass flux off the grid during this time it further reinforces the point that most of the mass streaming into the wider environment was originally molecular material.

The evolution of the H_2 mass becomes more exciting when the stars undergo evolutionary transitions. There are slight rises during periods when the cluster wind is dominated by RSG mass-loss, and more significant decreases during WR dominated periods when the molecular material is ablated at a much faster rate. But most dramatic of all is the response of the H_2 gas to a supernova explosion. Immediately after an explosion, the H_2 mass undergoes a rapid and steep decline which is quickly followed by a recovery to a similar or higher value than the pre-SN H_2 mass. The depletion of H_2 at this time is caused by its conversion to neutral and ionized hydrogen as it is heated by the SN shockwave which propagates relatively slowly through such dense molecular material. Note that it is not due to the H_2 gas being expelled from the grid. Once the shockwave has passed the densest shocked (neutral and atomic) gas cools and reverts quickly to its previous molecular state, resulting in the replenishment of the H_2 mass seen in Fig. 2.18. The overshoot of the H_2 mass relative to its pre-SN value is likely a result of the higher gas pressure which now exists within the cluster environment, and which allows some of the originally atomic hydrogen to become molecular. There are clear implications here for triggered star formation, such as might occur in the pillar in NGC 6357 (Cappa *et al.*, 2011). The mass of molecular gas resumes its decline once the next most massive star in the cluster enters its WR stage.

Since most of each SN's energy escapes along the low density channels through the remains of the GMC clump (see Sec. 2.3.5), the SNe couple very weakly to the densest, low volume filling factor, gas. Hence the very densest regions are

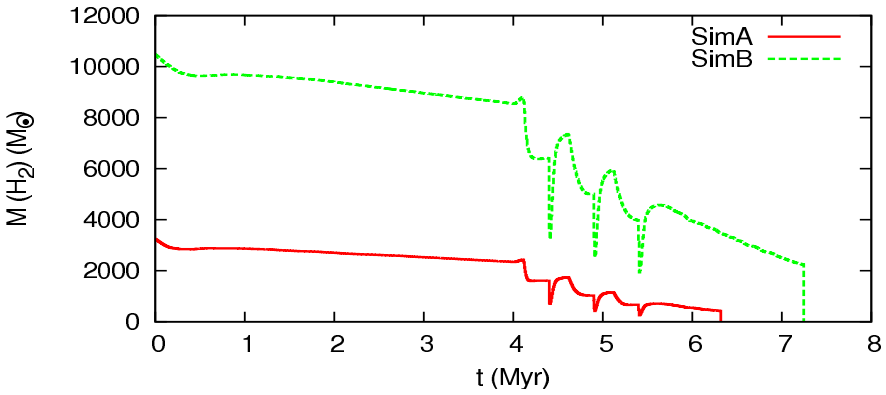

Figure 2.18: Mass of H_2 contained within the full computational volume of SimA (solid red line) and SimB (dotted green line).

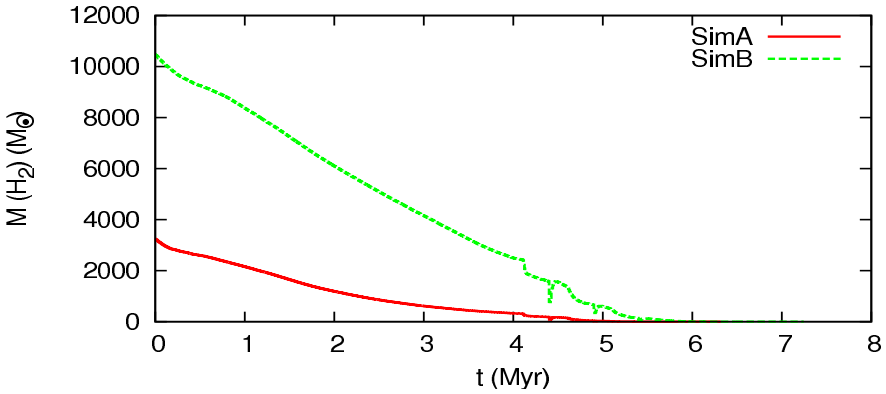

Figure 2.19: Mass of H_2 contained within the initial GMC clump radius of SimA (4 pc, solid red line) and SimB (5 pc, dotted green line).

relatively immune to the effects of the supernovae (see also Figs. 2.8 and 2.9). Indeed, Fig. 2.18 shows that overall, the supernova shocks actually *increase* the amount of molecular material in the cluster environment. This rather unexpected result demonstrates that the inhomogeneity of the environment, the density range of the gas, and its effective porosity, are key considerations in understanding massive star feedback. This picture also differs substantially from the many models of mass-loaded supernova remnants in the literature which envisage the complete mixing of material injected into the remant from embedded clumps (e.g.

Dyson *et al.*, 2002; Pittard *et al.*, 2003; White & Long, 1991).

The last supernova occurs at $t = 5.4\,\mathrm{Myrs}$, after which there is $\approx 470\,\mathrm{M}_\odot$ (14.4% of the original mass) of H_2 remaining in SimA and $\approx 3100\,\mathrm{M}_\odot$ (29.8% of the original mass) in SimB.

Fig. 2.19 shows the mass of H_2 contained within the initial clump radius (4 and 5 pc for SimA and SimB respectively). The depletion of H_2 is much more rapid within this radius as the cluster wind not only ablates but also pushes molecular material away from the stars. By the time the lowest mass star explodes there is very little H_2 present within the original volume of the GMC clump in either simulation (< 0.1 per cent of the original mass for SimA). The features due to the evolution of the stars shown in Fig. 2.18 are apparent here also, although to a lesser degree.

2.4 Conclusion

This paper investigates the effects of massive star feedback, via stellar winds and supernovae, on the inhomogeneous molecular environment left over from the formation of a stellar cluster from a GMC clump. The remains of the GMC clump confines and shapes the initial structure of the expanding wind-blown bubble, which breaks out of the clump along paths of least resistance. Hot, high speed gas flows away from the cluster through low-density channels opened up by these blow-outs. Mass is loaded into these flows from the ablation of dense clumps embedded within them and from material stripped from the dense gas which confines and directs the flows. This complex interaction of the cluster wind with its environment is far removed from the results of simple spherically

symmetric models. Increasing the density (by a factor of two) and the radius (by 25 per cent) of the cluster-forming GMC clump does not significantly affect this qualitative picture.

The density, temperature, pressure and velocity of gas in the cluster environment all span many orders of magnitude. The hottest gas typically occurs at the reverse shock of the cluster wind, and cools as it expands away from the cluster and mixes in with denser surrounding material. A multitude of weaker shocks exist around dense inhomogeneities entrained into gas flowing at mildly supersonic speeds. In addition, gas within the cluster environment is subject to changes of several orders of magnitude in the dynamic pressure as the stars in the cluster evolve through their MS, RSG and WR stages, and explode as supernovae.

The simulations presented in this Chapter show how molecular material is gradually ablated by the cluster wind and pushed away from the stellar cluster. Despite mass-loading or entrainment factors of several hundreds during the MS phase of the cluster wind, and several tens during the later WR-dominated phase, the destruction and sweeping up of molecular material is a relatively slow process, and a substantial amount of molecular mass remains when the first star explodes as a SN. These simulations imply that the shocks resulting from SN explosions couple very weakly to the molecular gas, due to its small volume filling fraction, and the ease with which the energy from the SN can "by-pass" it. The high porosity of the GMC clump at this stage allows the SN blast to rip through the cluster in a largely unimpeded fashion, with the forward shock refracting around dense inhomogeneities. The early evolution of the remnant is markedly different from the standard spherically symmetric picture. Although the SN shock destroys molecular material which it overruns, the cooling times of the densest regions are

very short and allow molecular material to quickly reform. At least in these simulations, the stellar winds appear to be a more effective agent at removing molecular material from the cluster environment, despite injecting less energy than the SNe.

Examination of the energy flux off the hydrodynamic grid reveals that between one quarter and one half of the energy injected by the stellar winds is radiated away, with the remaining energy available to do work on the immediate surroundings. In comparison, more than 99 per cent of the energy from each SN explosion escapes into the wider environment. These fractions are clearly dependent on the initial conditions of the model. In particular, the limited study performed suggests that the fractions of energy radiated away will increase for denser cluster environments, and vice-versa.

The fraction of ionizing photons which escape the cluster environment is also investigated. This increases from less than 1 per cent at the start of the simulation, to 40 per cent when the cluster is 1 Myrs old, and to 60 per cent after 4 Myrs. The escape fraction momentarily reduces when the cluster wind is RSG dominated, but the overall trend is of an increasing escape fraction as dense material is pushed away from the cluster.

Chapter 3

X-ray Emission from a Massive Young Stellar Cluster

3.1 Introduction

Early studies indicated that the detection of diffuse X-ray emission in stellar clusters required the presence of stars earlier than O6 (Townsley *et al.*, 2003), although an exception, the O7-powered Hourglass nebula (Rauw *et al.*, 2002), was known. Ezoe *et al.* (2006b) have since discovered diffuse X-ray emission from NGC 2024 (the Flame nebula), which contains only late O- to early B-type stars. On the other hand, it is curious that diffuse X-ray emission has yet to be detected from some very massive stellar clusters where very early O-type stars are present, such as Trumpler 16 (Wolk *et al.*, 2011).

Other work has indicated that the temperature of the diffuse plasma may be correlated with how embedded it is, as measured by the column density (Ezoe *et al.*, 2006a). Clusters with high temperature plasma appear to have $N_{\rm H} >$

$5 \times 10^{21}\,\mathrm{cm}^{-2}$, while clusters with cooler plasma have less absorption. Wolk *et al.* (2008) suggest that while the stellar winds are bottled up the shocked gas remains maximally heated, but leakage and the resulting adiabatic cooling of the gas causes the gas temperature to drop.

Unfortunately, past comparisons of X-ray observations with theory have had mixed success. Many works on MSFRs simply compare the observed X-ray luminosity against the mechanical wind power of the stars, or the thermal energy of the plasma against an estimate of the time-integrated energy input of the winds (e.g. Ezoe *et al.*, 2006b; Güdel *et al.*, 2008; Townsley *et al.*, 2003). The efficiency of the conversion of mechanical energy to radiation is then found to range from 10^{-4} to 0.1. This, and the estimated mass of the X-ray emitting gas, indicates that in many cases the winds are not completely confined and that hot plasma must flow into the wider environment. This conclusion is reinforced by the fact that the application of completely confined wind-blown-bubble models often leads to a significant overprediction of the X-ray luminosity (e.g. Dunne *et al.*, 2003; Harper-Clark & Murray, 2009; Rauw *et al.*, 2002).

Other works have compared the X-ray luminosity and the surface brightness profile of the diffuse emission to the predictions of cluster-wind models. In their analysis of the Arches and Quintuplet clusters, Wang *et al.* (2006) found that the radial intensity profiles of the diffuse emission were more extended than theoretical predictions. Muno *et al.* (2006) found that the observed surface brightness profile of the diffuse X-ray emission from Westerlund 1 was approximately constant between radii of 2-5 arcmin (3-7 pc). This "broad halo" is also inconsistent with theory.

The Harper-Clark & Murray (2009) model discussed in Section 1.2.1.3, which

incorporated breaks in the bubble shell through which some of the high-pressure gas in the bubble interior can leak is more consistent with observations. The model predicts a lower pressure within the bubble interior than the Castor *et al.* model, as the wind material is not completely confined, and also a lower X-ray luminosity. However, since the covering fraction of the shell is a free parameter this model suffers from a lack of predictive power.

It has also become clear that the diffuse emission from MSFRs often contains emission lines that are not well matched by standard thermal plasma models. These lines may instead result from the process of charge exchange at the interfaces between cold, dense material and the hot, tenuous, X-ray emitting plasma (Townsley *et al.*, 2011). Such interfaces occur at large-scale boundaries between hot and cold structures, and also at the boundaries of much smaller scale clouds which may be the remains of the natal molecular cloud. These latter clouds may often occur throughout much of the core volumes of clusters and their immediate surroundings. As well as affecting the emission of such regions, their presence may also affect the dynamics of the region, for instance by "mass-loading" diffuse flows (see the review in Pittard, 2007).

Given the challenges of interpreting such complex environments as MSFRs, and the highly idealized models of most theoretical and modelling work, in this Chapter the hydrodynamical models of stellar wind and supernova feedback in an inhomogeneous environment outlined in Chapter 2 and in (Rogers & Pittard, 2013) are used as a basis to simulate the resulting X-ray emission from such regions. Of great interest are the X-ray luminosity and spectrum, and their temporal variation as the stars in the simulation cycle through various evolutionary stages, including main sequence, red supergiant, Wolf-Rayet and supernova. In

Section. 3.2 the details of the model and the method of calculating the X-ray emission and absorption are discussed. The results are presented in Section. 3.3. Comparisons to numerical models and observations are made in Sections. 3.4 and 3.5 respectively. Section. 3.6 summarises and concludes this Chapter.

3.2 Simulations

3.2.1 The Numerical Model

The X-ray calculations in this Chapter are based on the 3D hydrodynamical model described in Rogers & Pittard (2013) and discussed in detail in Chapter 2. The simulations consist of three massive O stars which represent the main sources of mechanical feedback in a massive star forming region contained within an inhomogeneous GMC clump. The evolution of the three stars is treated simplistically as three distinct phases - the Main Sequence (MS), Red Supergiant (RSG) and Wolf-Rayet (WR) phases. The details of the stellar cluster are summarized in Table 2.1. At the end of the Wolf-Rayet phase the stars explode imparting $10\,\mathrm{M}_{\odot}$ of material and 10^{51} ergs of thermal energy into the environment. The lifespans of the stars are designed in such a way so that there are three distinct supernova explosions over the course of the simulation.

The simulation utilizes a temperature dependent average particle mass, and molecular, atomic and ionized phases are tracked separately. The net heating/cooling rate per unit volume is parameterized as $\dot{e} = n\Gamma - n^2\Lambda$, where $\mathrm{n} = \rho/\mathrm{m_H}$, and Γ and Λ are heating and cooling coefficients which are assumed to depend only on temperature. Photoevaporation is not treated in these simula-

tions. However, as the photoevaporation time for a clump of these characteristics is comparable to the lifetime from ablation this should not significantly affect the results.

The simulations in Chapter 2 showed that the inhomogeneous structure of the natal GMC cloud surrounding the cluster had an important effect on the initial expansion of the cluster wind, which cut channels through the low density material to escape the clump. The regions of high density within the initial clump proved to be surprisingly resistant to ablation from the cluster wind, and at later times the shockwaves of the SNRs.

3.2.2 Modelling the X-ray Emission and Absorption

To calculate the X-ray emission the results from the hydrodynamical model are read into a radiative transfer ray-tracing code, and the appropriate emission and absorption coefficients are calculated for each cell using the temperature and density values. A synthetic image on the plane of the sky is then generated by solving the radiative transfer equation along suitable lines of sight through the grid. Solar abundances and collisional ionization equilibrium are assumed throughout this Chapter. The emissivity is stored in look-up tables containing 200 logarithmic energy bins between 0.1 and 10 keV, and 91 logarithmic temperature bins between 10^4 and 10^9 K. Line emission dominates the emissivity at temperatures below 10^7 K, with thermal bremsstrahlung dominating at higher temperatures. The present calculations also have an interstellar absorption column ($N_H = 10^{21}\,cm^{-2}$) added to them, and each model is assumed to be at a distance of 1 kpc from an observer.

The energy bins are split into three energy bands which represent the soft, medium and hard X-ray components of the spectra. The soft X-ray regime runs from 0.1–0.5 keV, the medium runs from 0.5–2.5 keV and the hard X-rays run from 2.5–10.0 keV. These regions will be referred to as BB1, BB2 and BB3 respectively throughout this Chapter.

3.3 Results

3.3.1 The Main Sequence Phase

The X-ray lightcurve for the cluster throughout the simulation is shown in the top panel of Fig. 3.1. The initial observable luminosity of the cluster is $L_X \sim 7\times10^{31}\,\mathrm{ergs\,s^{-1}}$. Over the next 0.7 Myrs this luminosity decreases by a factor of 10 to approximately $L_X \sim 9\times10^{30}\,\mathrm{ergs\,s^{-1}}$, at which point it remains fairly constant for the duration of the MS of the cluster. Initially the X-ray luminosity is high as the cluster wind blown bubble is confined within the GMC clump. However, as the wind blows out of the low density regions of the clump, hot gas escapes from the centre, as described by the "leaky bubble" model of Harper-Clark & Murray (2009) and Chapter 2. The reduced pressure within the bubble caused by this leakage results in a lower X-ray luminosity.

Fig. 3.2 shows simulated X-ray images of the cluster at time $t = 0.13$ Myrs, where extended bubbles to either side indicate that some of the hot wind material is leaking from the GMC clump. However, it is clear that there is still partial confinement by the inhomogeneous GMC clump since the images are not spherically symmetric. At this time all three stars are on the MS (see Table 2.1

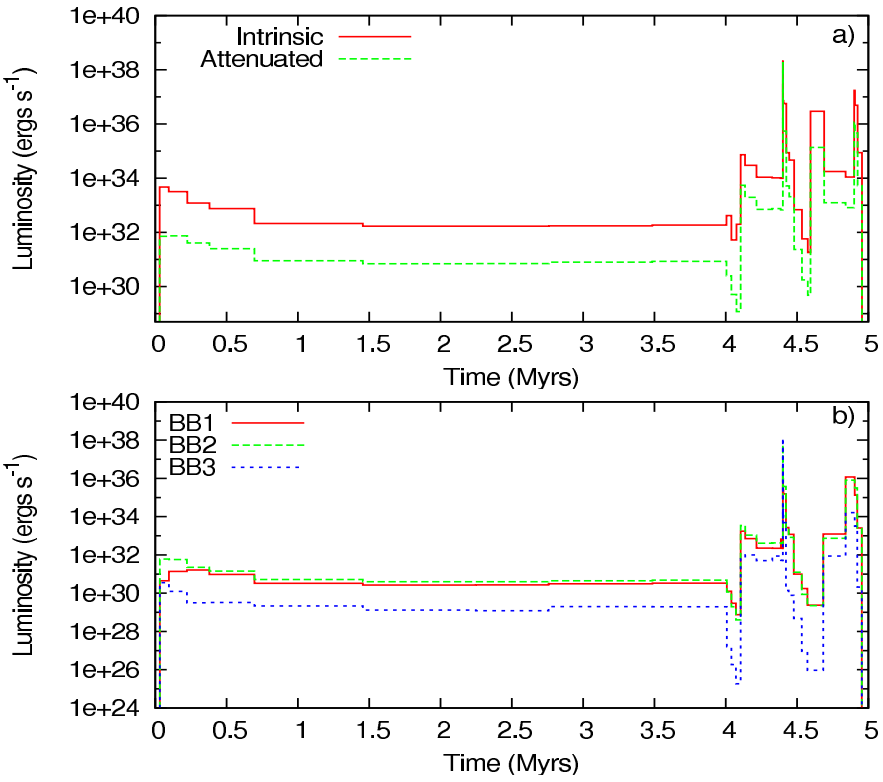

Figure 3.1: The X-ray lightcurve for the cluster over the course of the simulation. a) Shows the total intrinsic luminosity produced by the cluster (solid red line) compared with the observable luminosity after attenuation (dotted green line). b) Shows the attenuated luminosity in all three energy bands defined in Sec 3.2.2. The solid red line shows the soft X-rays in BB1, the green dashed line shows the medium X-rays in BB2 and the blue dotted line shows the hard X-rays in BB3.

for the stellar properties). The left and middle panels show images of the soft and medium energy X-rays produced at this time, whilst the right panel shows the hard X-rays. The emission is brightest at the centre in all three images, but particularly so in the medium and hard images. At this early time there is strong absorption of the soft X-rays within the GMC clump, as revealed by the low surface brightness of regions which are more clearly emitting at higher energies (compare the left and middle panels). This behaviour is not so prominent in the

medium energy X-ray image, although there is some absorption occuring.

The most striking feature in the images is the extended emission to the top right of the cluster, which results from the hot gas that has already broken out of the clump in this direction. It is also interesting to observe that the hot fluid adiabatically cools as it accelerates to supersonic speeds through the 'nozzles' from which it leaves the confining clump. This is visible as a reduction in the X-ray surface brightness in the hard band. The surface brightness of this gas increases at larger distances from the clump as it passes through a termination shock. At this point it runs up against previously shocked gas which is inflating the bubble and sweeping up a shell of the ambient medium which surrounds the GMC clump. The hardest X-rays are produced by the hot gas in the cluster centre, where the cluster wind is partially confined. The bottom panel of Fig. 3.1 shows that the luminosities in the BB1 and BB2 energy bands are almost equal during the period when all three stars are on the MS. However, at $t < 0.25\,\mathrm{Myrs}$ the luminosity in the BB2 energy band is dominant due to the greater attenuation of the lower energy X-rays by the remnant GMC clump. The hard X-ray luminosity in the BB3 energy band is about an order of magnitude lower than the luminosities in the soft and medium energy bands throughout the MS-dominated phase of the cluster evolution.

At $t = 0.13\,\mathrm{Myrs}$, approximately 90% of the total (0.1-10 keV) intrinsic X-ray luminosity originates from the inner 4 pc radius of the simulation, which is the original radius of the GMC clump containing the cluster. This is not unexpected as the cluster wind is young and hot plasma vents out of only a few open channels at this time. Since the GMC clump is mostly intact, significant attenuation of low energy X-rays occurs within the clump radius. This is reflected by the fact

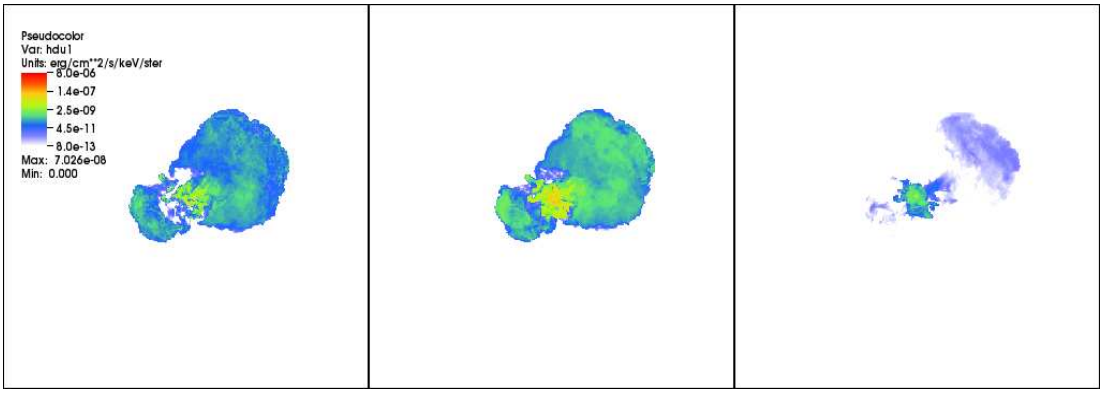

Figure 3.2: X-ray emission for the cluster at time t = 0.13 Myrs. Each panel has sides of length 55.4 pc. [Left] shows soft X-rays 0.1–0.5 keV, [Middle] shows medium X-rays at 0.5–2.5 keV and [Right] shows hard X-rays at 2.5–10.0 keV. The stellar cluster is at the centre of each panel.

that only $\sim 2/3$ of the total attenuated luminosity originates from the inner 4 pc radius, indicating that the dense material within that radius has absorbed a substantial amount of the intrinsic emission.

The low density regions of the clump are rapidly blown out by the cluster wind but afterwards the remaining high density regions are much longer-lived. The effective covering fraction of the densest regions, the gross properties of the cluster wind and the X-ray luminosity evolve only slowly. However, the characteristic size of the emitting region continues to increase. Although much of the hot gas leaves the grid through the outflow boundaries, we can nevertheless examine how the emission from hot gas on the grid evolves with time. At t = 0.44 Myrs approximately 50% of both the intrinsic and attenuated luminosity originates from within the original clump radius. By t = 1.96 Myrs this value has decreased to 20% for both luminosities and by t = 2.53 Myrs, approximately midway through the MS, only 12% of the luminosity originating on the numerical grid comes from the central 4 pc radius. This decline is driven by two factors. First, the cluster

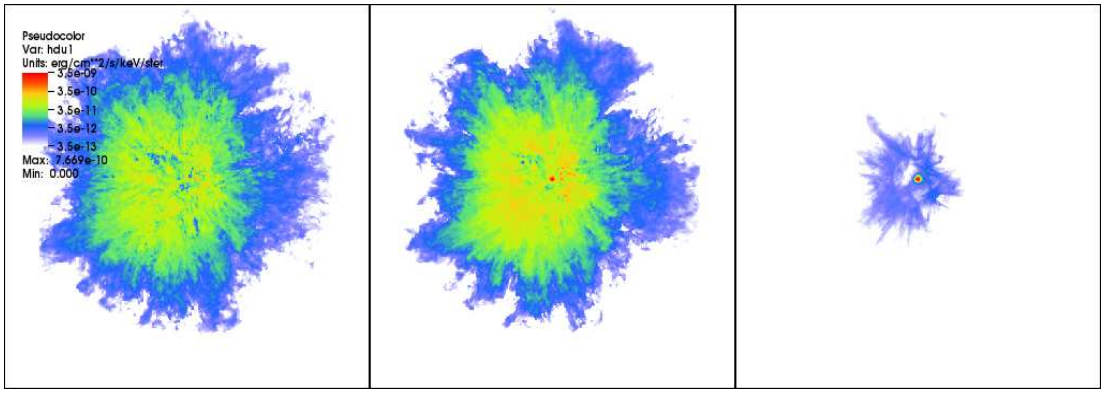

Figure 3.3: X-ray emission for the cluster at time t = 2.53 Myrs. Each panel has sides of length 55.4 pc. [Left] shows soft X-rays 0.1–0.5 keV, [Middle] shows medium X-rays at 0.5–2.5 keV and [Right] shows hard X-rays at 2.5–10.0 keV.

wind increasingly clears out dense molecular gas within the original GMC clump as time goes on. The dense gas is both ablated into the hot gas streaming past and also pushed away. The bowshocks which form around the nearest dense clouds, and which merge to produce the reverse/termination shock of the cluster wind, thus form at greater and greater distances. Hence there is simply less hot gas in this central region as time increases. Secondly, the ablated material is entrained into the outflows away from the GMC clump. Indeed, mass entrainment/loading factors may exceed ∼100 (see Chapter 2). This entrainment increases the density of the flow and its emissivity, while also creating slow moving obstacles which faster moving parts of the flow shock against. The flow outside of the GMC clump thus contains a multitude of shocks, and a wide range of densities and temperatures.

X-ray images of the cluster at t = 2.53 Myrs are shown in Fig. 3.3. There is considerable diffuse emission in the soft and medium X-ray bands (left and middle panels of Fig. 3.3). In contrast, the spatial extent of the hard X-rays is much smaller, and these instead primarily trace the stellar cluster and the hot,

shocked gas immediately downstream of the reverse shock of the cluster wind. The gas responsible for this emission reduces in temperature as colder material from the remains of the GMC clump mixes in with it, which limits the extent of the emission in this image. The extent of the diffuse emission reaches well beyond the original cluster radius, with more than 88% of the overall luminosity originating from outside that radius. Although the images for the soft and medium regimes are similar in structure, with strong emission in the centre and a filamentary diffuse structure towards the edges, there is a higher intensity in the BB2 image, and the stellar cluster is clearly discernible at the centre of the clump.

3.3.2 ISM Absorption Effects

The attenuated X-ray luminosity is dependent on both the ISM column density and the density and size of the GMC clump in which the cluster forms. However, as the molecular material in the clump is ablated by the winds it will have less of an effect on the observable luminosity of the cluster. Fig. 3.4 gives an indication of the degree of attenuation caused by the ISM and by dense clump material. The red solid line shows the intrinsic X-ray spectrum from the cluster, with the green dashed line showing the total attenuated spectrum taking all absorption effects into account. As discussed previously, the vast majority of the absorption occurs at soft X-ray energies, with very little occuring above $\mathrm{E} = 1.0\,\mathrm{keV}$. The blue dotted line shows the attenuation effects caused only by absorption from the ISM. Close inspection of Fig. 3.4 reveals that the ISM absorption has little effect above $0.5\,\mathrm{keV}$, whereas the circumcluster absorption affects the spectrum up to energies around $1\,\mathrm{keV}$. Therefore it is clear that these two distinct absorption

components affect the spectrum in slightly different ways. It is consistent with the hottest gas (and therefore the hardest emission) being buried more deeply within the GMC clump. We note that the average column density from the centre of the cluster through the GMC clump to an observer at $t = 0.06$ Myrs is, at $\approx 3 \times 10^{21}\,\mathrm{cm}^{-2}$ (see Fig. 2.13), about 3 times the assumed ISM column.

At $t = 2.53$ Myrs (bottom panel) the two attenuated spectra are practically identical. This is because the X-ray emitting gas is no longer confined by the dense absorbing material of the GMC clump as it is in the early stages of the bubble's expansion, but now suffuses through the entire volume of the simulation. This is again consistent with the average column density from the centre of the cluster through the GMC clump to an observer at this time, which Fig. 2.13 shows to be about $10^{19.6}\,\mathrm{cm}^{-2}$, or only about 4% of the assumed ISM column.

Changing the viewing angle to the cluster at late times leads to only very small differences ($\approx$ 5–10 %) in the attenuated luminosity, reinforcing the conclusion that the destruction of the clumpy environment results in very minimal column densities and thus attenuation by this gas. Even at earlier times when the hot wind gas is still breaking out of the clump the difference in the attenuated luminosity as the viewing angle to the cluster changes is only around 15–20 %. This likely reflects the relatively low initial column density of the clump. Larger variations can be expected from models with higher initial column densities.

3.3.3 RSG and WR Phases for the 35 $M_\odot$ Star

At $t = 4.0$ Myrs the most massive star evolves into a RSG. Its mass loss rate increases, and its wind velocity decreases. The averaged mass-loss rate and

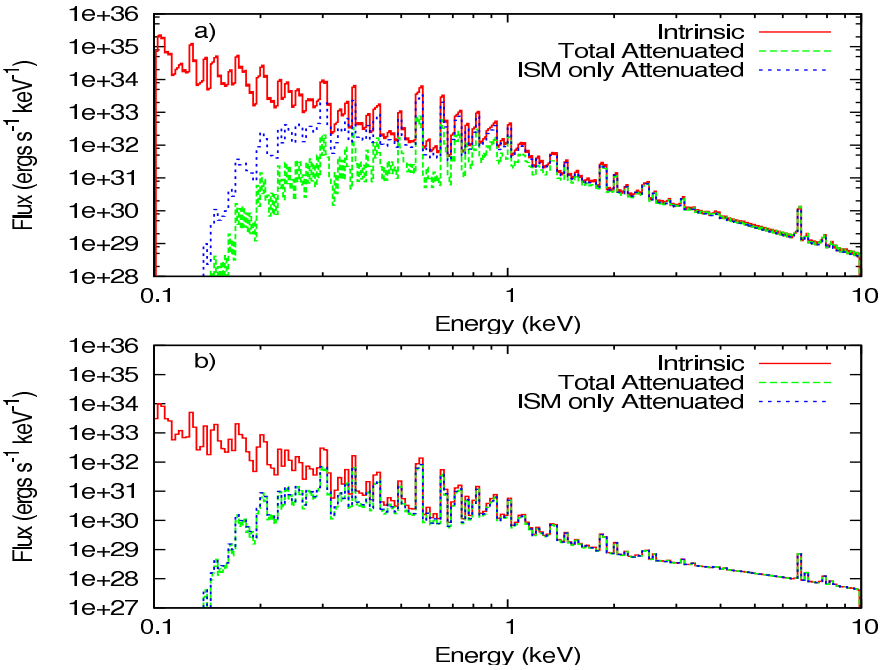

Figure 3.4: X-ray spectra of the cluster at two times during the MS dominated phase. The red solid line shows the total intrinsic emission produced by the cluster. The green dashed line shows the total observable emission after all attenuation effects are considered, whilst the blue dotted line shows the effect of just the ISM absorption on the emission. a) Shows the spectra at $t = 0.06$ Myrs, when there is a notable difference between the ISM only and total attenuated emission. b) Shows the spectra at $t = 2.53$ Myrs when absorption by dense material from the GMC clump has little effect on the overall attenuated emission.

.

speed of the cluster wind then changes from $9{\times}10^{-7}\,M_{\odot}\,yr^{-1}$ and $2000\,km\,s^{-1}$ to $\approx 10^{-4}\,M_{\odot}\,yr^{-1}$ and $136\,km\,s^{-1}$. The cluster wind therefore becomes slow and dense. The central cluster is no longer a source of hard X-rays, and there is no replenishment of the highest temperature gas in the surrounding environment as it flows away from the cluster through the remains of the porous GMC clump (see Fig. 2.9). Together these changes lead to a substantial reduction in the amount of hard X-rays being produced. In fact, the BB3 luminosity decreases 4 orders of magnitude from $L_X \sim 2 \times 10^{29}\,ergs\,s^{-1}$ just before the evolutionary transition to

$L_X \sim 2 \times 10^{25}\,\mathrm{ergs\,s^{-1}}$ by the end of the RSG phase (see Fig. 3.1). In contrast, the intrinsic luminosity briefly increases following this transition, due to an increase in luminosity in the BB1 band.

Whilst the reason for this is not completely understood, it is possible that the sudden drop in pressure during the transition causes material stripped from the dense clouds to mix more rapidly with the hotter gas. Overall however, because the soft X-rays suffer from attenuation from the dense RSG-enhanced wind material close to the centre of the cluster, the attenuated emission actually drops.

The dense material deposited during the cluster wind's first RSG phase is subsequently blown from the simulation volume once the most massive star further evolves to its WR phase at $t = 4.1\,\mathrm{Myrs}$. The combined average speed of the cluster wind increases back to $2000\,\mathrm{km\,s^{-1}}$ while the combined mass-loss rate becomes $2.04 \times 10^{-5}\,\mathrm{M_\odot\,yr^{-1}}$. The very high momentum that the cluster wind now has efficiently clears out the RSG dominated cluster wind filling the lower density channels and dramatically increases the ablation rate of the remaining dense clouds. This causes increased emission in all three X-ray bands. The intrinsic luminosity increases by over 2 dex above that reached in the MS phase, with an initial peak that then declines quickly to a steady value. This phase is relatively short-lived, lasting only 0.3 Myrs.

3.3.4 The First Supernova

The most massive star explodes as a supernova at $t = 4.4\,\mathrm{Myrs}$, imparting $10\,\mathrm{M_\odot}$ of material and $10^{51}\,\mathrm{ergs}$ of energy into the centre of the GMC clump. At this

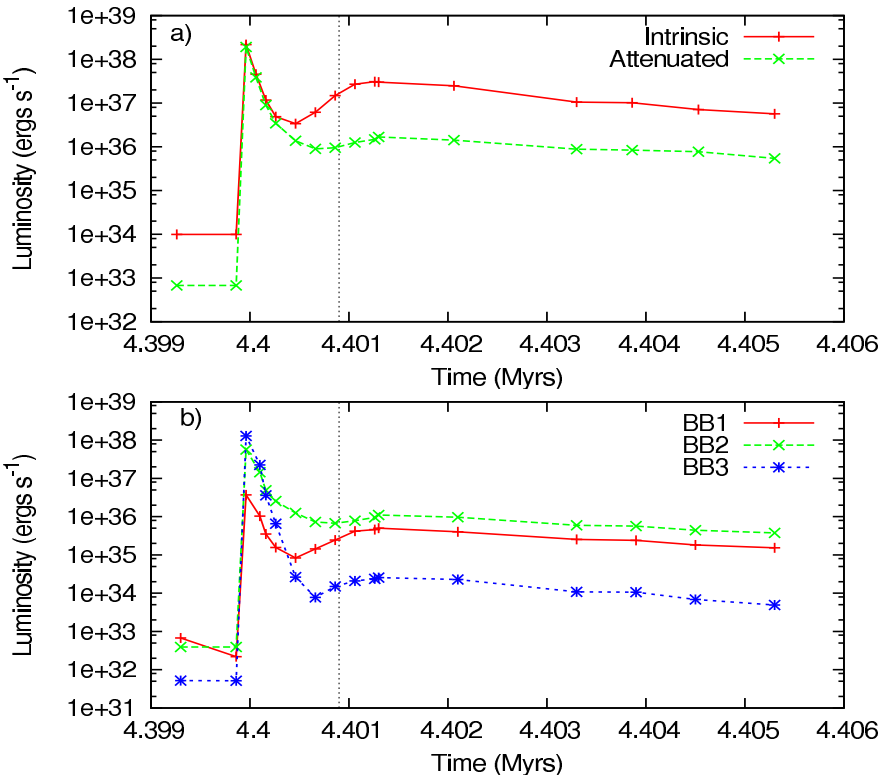

Figure 3.5: The X-ray light curve for the cluster at the time of the first SN explosion. The black dashed line indicates 900 years after the explosion, at which point emission from interactions with the surrounding clump material is dominant in all three energy bands. a) Shows the total intrinsic luminosity produced by the cluster (solid red line) compared with the observable luminosity after attenuation (green dashed line). b) Shows the attenuated luminosity in all three of the broadband energy bands. The solid red line shows the soft X-rays in BB1, the green dashed line shows the medium energy X-rays in BB2 and the blue dotted line shows the hard X-rays in BB3.

point both of the other stars remain in their MS phases.

The X-ray lightcurve immediately following the supernova explosion is shown in Fig. 3.5. To model the SN explosion 10^{51} ergs of thermal energy and $10\,M_{\odot}$ of ejecta are placed at the position of the stellar cluster. This gas is highly overpressured and rapidly expands into the surrounding medium. Although this approach leads to the desired response on the surrounding medium, in actual SN explosions

the ejecta rapidly cools through adiabatic expansion, and is considerably cooler than the simulated ejecta at comparable times. Therefore the bright peak in the X-rays seen in Fig. 3.5 immediately after the explosion should be ignored as it is an artifact of the utilized approach. The X-ray luminosity of the hot ejecta drops rapidly from its peak as the ejecta starts to expand and its density decreases. However, Fig. 3.5 shows that the rate of decline of the X-ray luminosity decreases, and a minimum is reached after which the X-ray luminosity increases again. This behaviour is caused by ejecta running into the remaining dense clouds near the cluster. The kinetic energy that this ejecta has acquired at this time is then re-thermalized and subsequently radiates more strongly. The dashed line 900 yrs after the explosion indicates when the luminosity is dominated by the interactions of the ejecta with surrounding gas, and thus no longer affected by the explosion setup.

Synthetic X-ray images in all three energy bands during the explosion are shown in Figs. 3.6-3.8. When the star first explodes there is high intensity emission at the centre of the cluster, as seen in all three figures, which is a consequence of the implementation of the explosion with thermal rather than kinetic energy. As the hot ejecta expands outwards the intensity at the centre decreases, although it is still much higher than the pre-explosion levels.

Once the shockwave has expanded out far enough it begins to interact with the high density remains of the GMC clump. This is apparent from around $t = 4.4005$ Myrs onwards (see for example the right panel in the second row of Fig. 3.8). Prior to this, absorption by dense clumps projected in front of the blast wave is visible (see for example the 3^{rd}, 4^{th} and 5^{th} panels in Fig. 3.6). As the shockwave sweeps through the inhomogeneous environment successive bow-

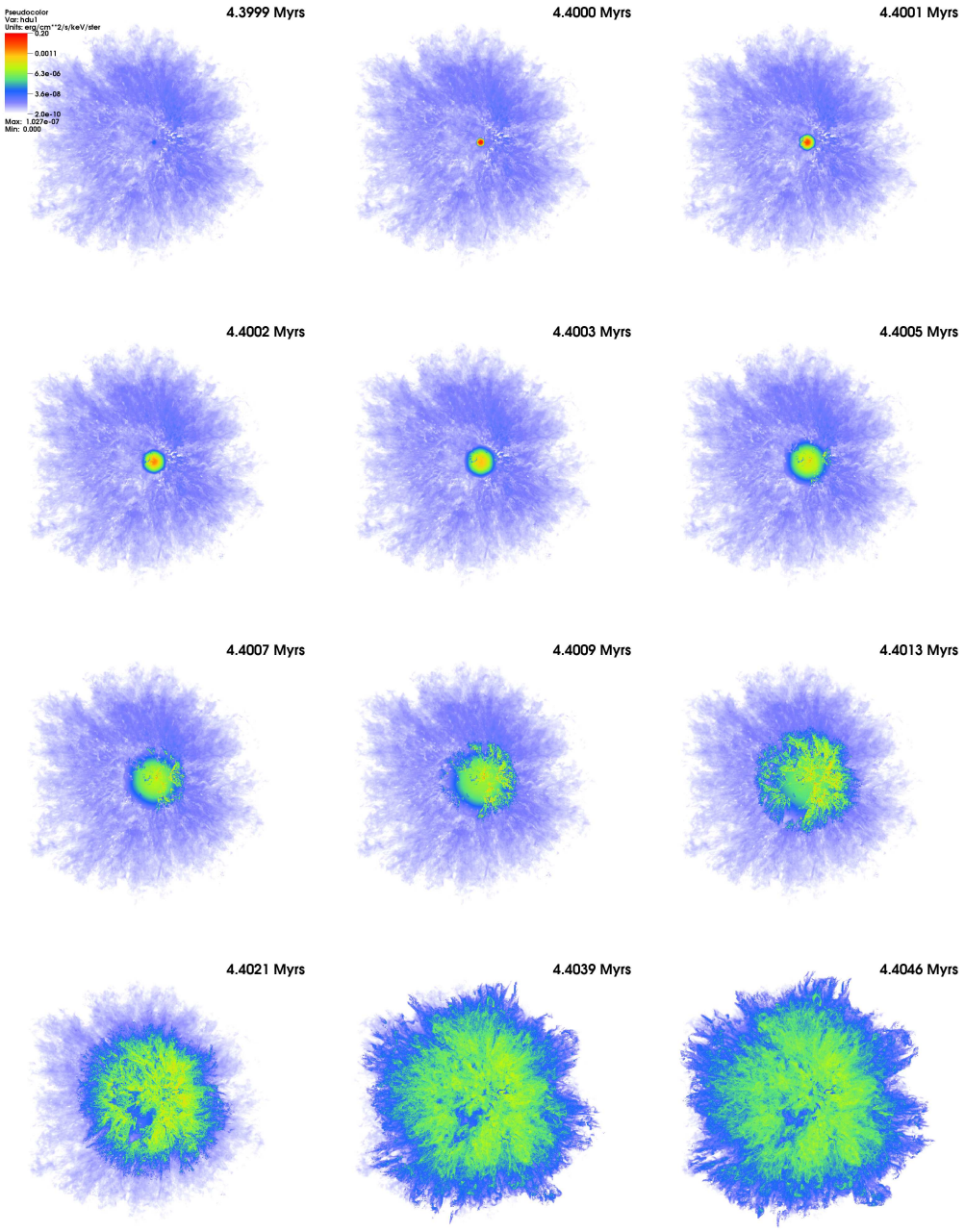

Figure 3.6: Synthetic X-ray image in the BB1 (0.1–0.5 keV) energy band during the first 4600 years after the most massive star explodes. The explosion occurs at t=4.4000 Myrs (middle panel, top row). Absorption is visible from 100 years after the explosion (t=4.4001 Myrs). Bow shock emission dominates from 900 years.

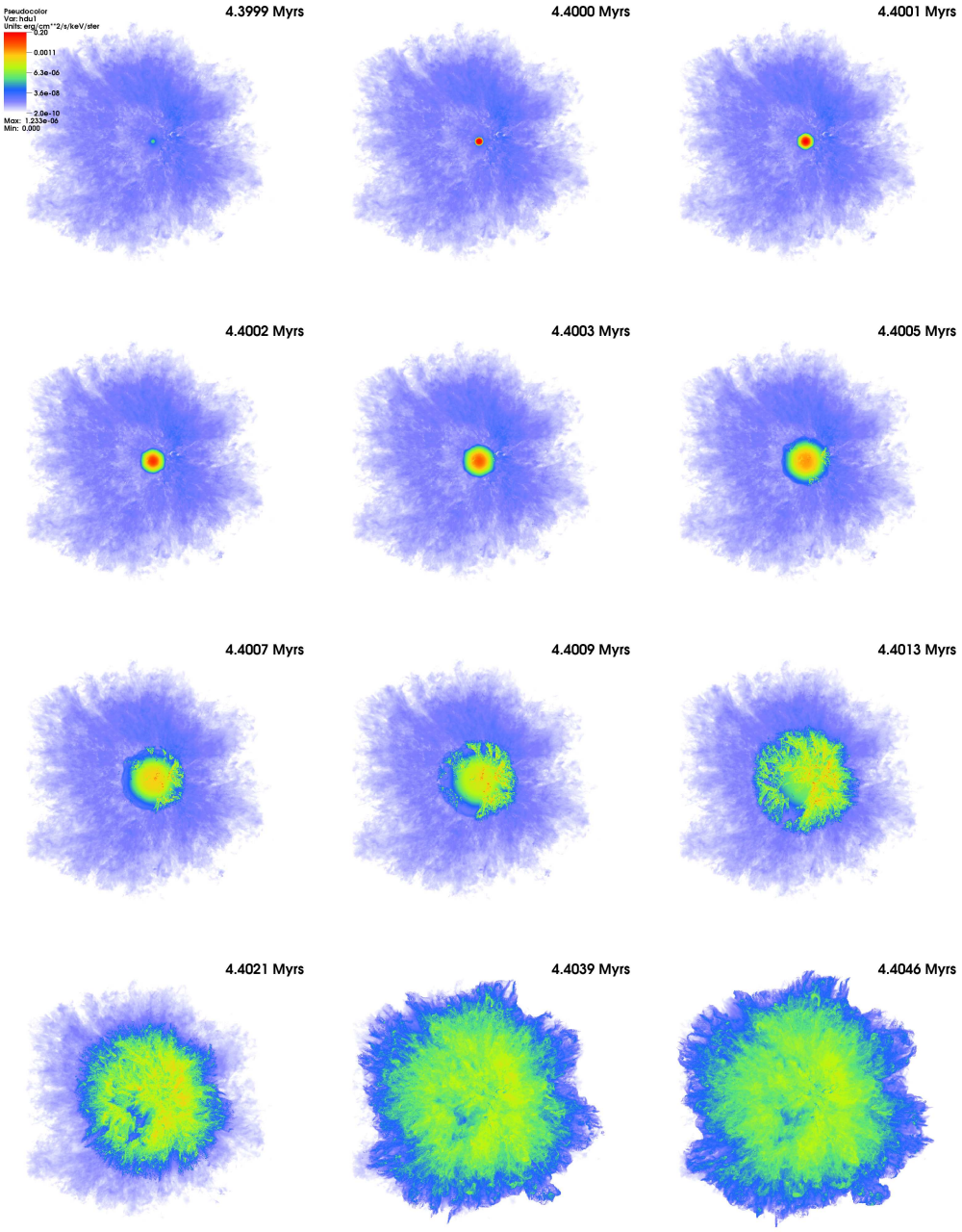

Figure 3.7: Same as Fig. 3.6, but for the BB2 (0.5–2.5 keV) energy band.

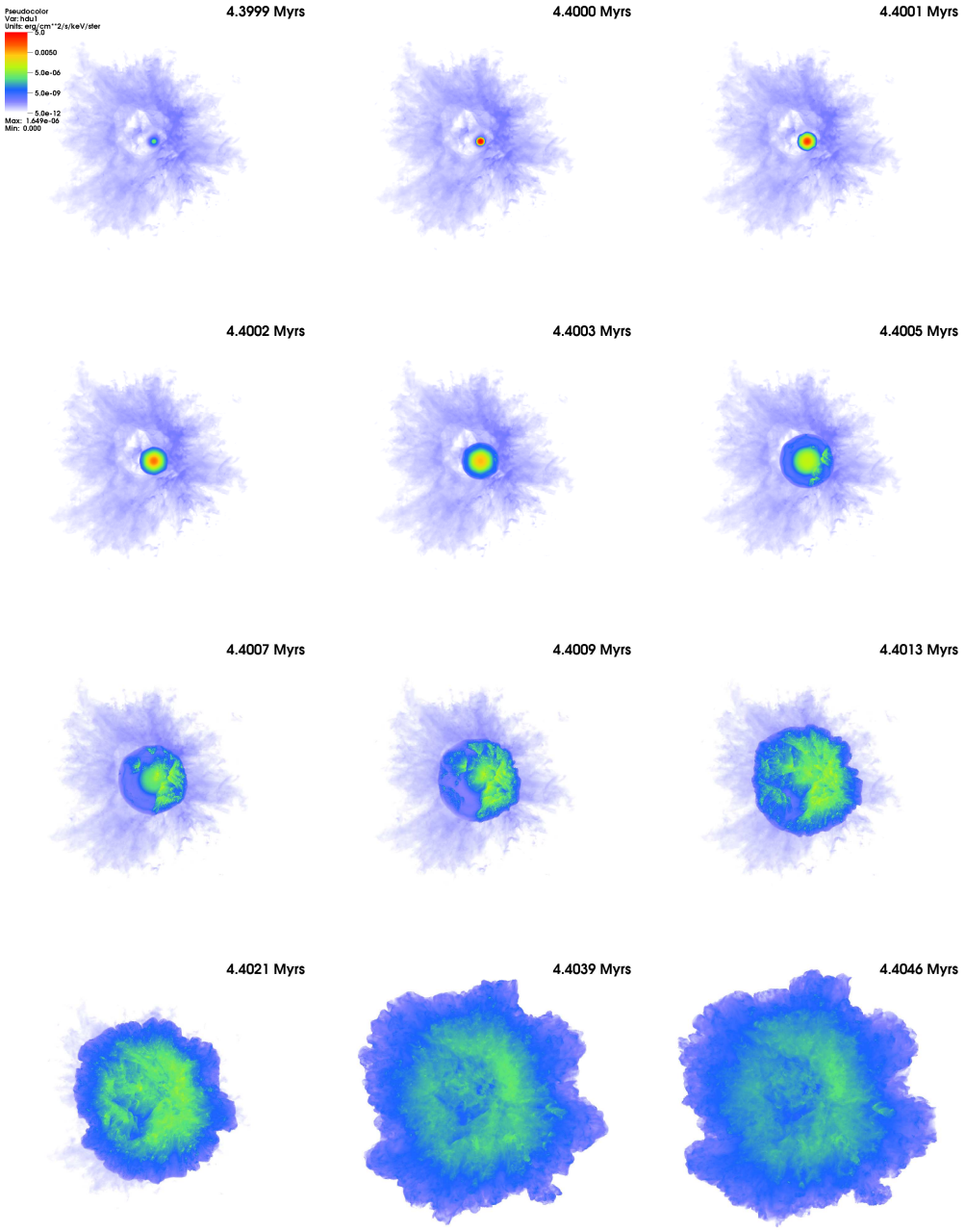

Figure 3.8: Same as Fig. 3.6, but for the BB3 (2.5–10.0 keV) energy band.

shocks form around each dense cloud that it encounters. Individual bowshocks can be identified during the first 900 yrs after the explosion, but at later times these merge to create a single, though highly structured, region of emission with variable surface brightness. The simulated X-ray emission should be largely unaffected by the explosion setup once the emission from the bow shocks becomes dominant, which as is apparent from the previous discussion of the light curve occurs approximately 900 yrs after the explosion.

The X-ray image is broadly spherical overall, though there is substantial curvature to the main shock front on local scales. Ejecta begins to leave the grid approximately 4000 yrs after the explosion. By 2000 yrs after the explosion the most intense emission is observed someway behind the main shock front and the remnant takes on a "shell-like" morphology. This is likely due to the fact that at the time of the SN explosion the densest clouds surrounding the cluster tend to occur in a shell with inner and outer radii of $\approx$ 5-10 pc. Virtually all of the dense gas previously within 5 pc has been cleared out by the cluster wind, being either ablated and entrained into the cluster wind or pushed away from the cluster by the ram pressure of the cluster wind up to a typical distance of 10 pc (see Fig. 2.8). The brightest X-ray emission seems to occur where the SN ejecta interacts with the remaining dense clouds in this shell. In contrast, the position of the forward shock indicates where the SN ejecta has traversed relatively unimpeded through the surrounding medium.

The X-ray image appears to be smoother at the higher energies of BB3, and much more filamentary in the lower energies of BB1 and BB2, even near the edge of the forward shock front. The emission in BB1 and BB2 is likely picking up gas at relatively low and intermediate temperatures associated with material

from dense clouds which is entrained into and partially mixed with the SN ejecta. Thus the resulting emission traces to some extent the interfaces associated with this process. However, this gas will be too cool to radiate strongly at the higher energies of the BB3 image, and instead the BB3 image shows the location of hot, but relatively unmixed ejecta.

The forward shock front also shows structures which could be interpreted as "blow-outs" (see for example the protrusion to the lower right of the SNR in the final two panels of Fig. 3.8). While these protrusions may indicate that the remnant is expanding into a region with a lower pre-shock density in this direction, it may also be affected by the structure of the surrounding medium that the shock front has encountered at distances considerably prior to this.

The X-ray emission from the environment external (and prior) to the SNR is also of interest. The emission at $t = 0.13\,\mathrm{Myrs}$ and at $t = 2.53\,\mathrm{Myrs}$ has already been displayed in Figs. 3.2 and 3.3, and discussed earlier. However, Figs. 3.6– 3.8 further illuminate the filamentary emission and absorption which occurs in the BB1 and BB2 energy bands, and the smoother emission which occurs in BB3. The volume within the reverse shock surrounding the stellar cluster is devoid of any hot gas and is visible as a deficit of emission in the central regions of Figs. 3.6 and 3.7. The highly structured nature of the reverse shock is directly visible in the top row of panels in Fig. 3.8. It is the X-ray bright parts of the top left panel in Fig. 3.8 which first "light-up" as the ejecta expands outwards, as seen in the sequence of panels in the second and third rows of Fig. 3.8. Bowshocks around the closest dense clouds to the cluster are responsible in both instances.

The time evolution of the attenuated spectra during the period of the first SN explosion is shown in Fig. 3.9. The solid red line is at a time just before

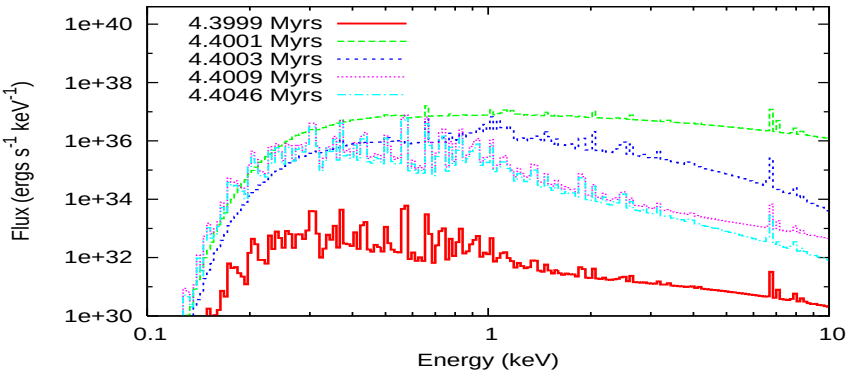

Figure 3.9: The time evolution of the attenuated X-ray spectra of the cluster as the most massive star undergoes a SN explosion. The solid red line is at a time just before the star explodes and the green dashed line is at t^{-} 4.4001 Myrs, shortly after the explosion. The dark blue short-dashed line is $\sim$300 yrs after the explosion, the purple dotted line is $\sim$900 yrs after the explosion and the light blue dot-dashed line is $\sim$4,600 yrs after the explosion.

the star explodes whilst the light blue dot-dashed line is t = 4600 yrs after the explosion, which is the approximate time at which the shockwave begins to leave the grid. During the first few hundred years after the explosion the spectrum is fairly flat, indicating a brightening of the hard X-rays relative to the rest of the spectrum. However, as discussed earlier this is an effect caused by the way the SN is initialised. The attenuated spectrum for the cluster at t = 4.4009 Myrs, when bowshock emission begins to dominate, is shown as the purple dotted line in Fig. 3.9. The spectrum is the same shape, albeit considerably more luminous, as that of the pre-SN cluster. However, whilst the intensity of the soft and medium X-ray energies change little, by the time the ejecta reaches the edge of the grid (light blue dot-dashed line) there is a considerable decrease in the hard X-ray ($E \gtrsim 3$ keV) emission of the cluster.

3.3.5 Further Evolutionary Stages

After the $35\,M_\odot$ star has exploded the remaining two stars continue in their MS phases for a further 0.1 Myrs, at which point the $32\,M_\odot$ star begins to follow the same evolutionary path as its predecessor. At $t = 4.5$ Myrs it evolves to a RSG and at $t = 4.6$ Myrs it becomes a WR star. The X-ray lightcurve shown in Fig. 3.1 shows a similar pattern to the previous evolution, in that the X-ray luminosity decreases once the less powerful RSG wind contributes to the cluster wind, while it increases once the star becomes a WR. However, as the evolution of the $32\,M_\odot$ star occurs so shortly after the first supernova, the luminosity is still declining from the aftermath of that event, partially as a consequence of the blast wave leaving the grid, and so it is hard to distinguish this from the natural decline during the RSG phase. In fact, the luminosity at this stage is comparable to that of the previous RSG phase despite the loss of one wind source and the commensurate reduction in the momentum and energy flux of the cluster wind. The $32\,M_\odot$ star explodes at $t = 4.9$ Myrs, imparting a further $10\,M_\odot$ of ejecta material and 10^{51} ergs of energy into the simulation. 0.1 Myrs after this explosion the final remaining star begins the evolutionary sequence already performed by its brethren.

3.3.6 Properties of the X-ray Emitting Gas

The mass, volume and density of the X-ray emitting gas are shown in Table 3.1. The mass of gas with a temperature in excess of 10^5 K increases until $t \approx 0.3$ Myrs when it stands at nearly $7\,M_\odot$. The mass then drops slightly and stays around 3-4 $M_\odot$ during the remaining MS phase of the cluster wind. During this time

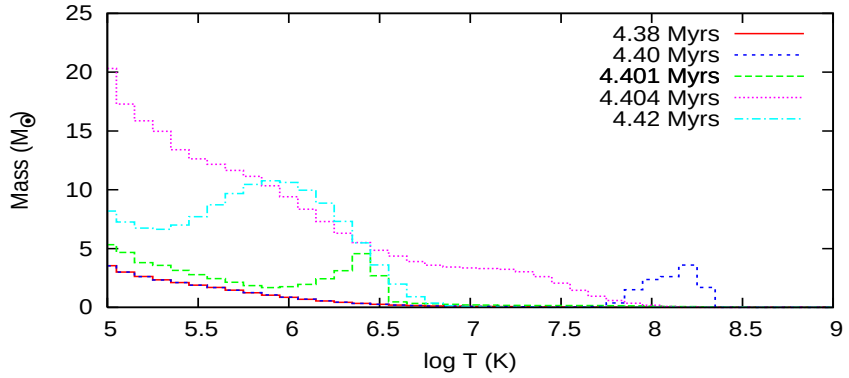

Figure 3.10: Mass of X-ray emitting material above $T = 10^5$ K at five times during the simulation. The red solid line is at t = 4.38 Myrs, shortly before the most massive star explodes. The blue short-dashed line is at t = 4.40 Myrs immediately after the supernova explosion (this reflects the conditions used to simulate the explosion) and the green long-dashed line is at t = 4.401 Myrs, 1000 yrs after the explosion when the emission is dominated by bowshock interaction. The purple dotted line is at t = 4.402 Myrs when the ejecta begins to leave the grid. The light blue dot-dashed line is at t = 4.42 Myrs, 20,000 yrs after the explosion.

the X-ray emitting volume is just over 50% of the total simulation volume, since the shocked cluster wind has spread throughout most of the grid. The average temperature of the X-ray emitting gas is 2.5×10^6 K, whilst the mass-weighted average is 2.3×10^5 K, implying that most of the X-ray emitting gas is closer to the 10^5 K mark. After the first star evolves to the RSG branch the mass of material which is hot enough to produce X-rays decreases along with both the average and the mass-weighted average temperature of the gas. Once the star evolves further to the WR phase the mass of X-ray producing gas increases by a factor of 10 and the volume of the material at $T > 10^5$ K almost doubles. The average temperature of the X-ray emitting gas increases to 2.8×10^6 K and the mass-weighted average to 3.2×10^5 K.

The mass distribution of the simulation before, during and after the first supernova explosion is shown in Fig. 3.10, and the amount of material which

Table 3.1: The mass, density and volume of the X-ray emitting gas, and the average and mass-weighted average temperature of that gas at various times throughout the simulation.

Time (Myrs)	Phase of each star ($35,32,28\,M_\odot$)	Mass at $T > 10^5$ K ($M_\odot$)	Density at $T > 10^5$ K ($\times 10^{-26}\,g\,cm^{-3}$)	Volume at $T > 10^5$ K ($\times 10^4\,pc^3$)	% of Volume at $T > 10^5$ K	$\log[T_{av}]$ at $T > 10^5$ (K)	Mass-weighted $\log[T_{av}]$ at $T > 10^5$ K (K)
0.00	MS,MS,MS	0.00	0.00	0.00	0.00 %	0.00	0.00
0.13	MS,MS,MS	1.89	5.17	0.25	7.63 %	6.40	5.58
0.32	MS,MS,MS	6.75	3.22	1.43	43.53 %	6.40	5.44
0.63	MS,MS,MS	4.26	1.60	1.81	55.28 %	6.40	5.36
0.95	MS,MS,MS	3.25	1.20	1.83	55.92 %	6.40	5.36
1.95	MS,MS,MS	3.43	1.33	1.75	53.32 %	6.40	5.37
2.53	MS,MS,MS	3.84	1.41	1.85	56.46 %	6.40	5.37
3.61	MS,MS,MS	4.06	1.42	1.95	59.40 %	6.40	5.39
4.06	RSG,MS,MS	2.13	1.08	1.34	40.89 %	6.30	5.28
4.31	WR,MS,MS	24.87	6.64	2.55	77.82 %	6.45	5.51
4.38	WR,MS,MS	24.99	6.69	2.54	77.54 %	6.40	5.51
4.40	SN,MS,MS	37.24	9.87	2.57	78.43 %	6.80	6.36
4.4009	SN,MS,MS	51.29	13.64	2.56	78.09 %	6.95	5.77
4.404	SN,MS,MS	217.97	52.67	2.82	85.95 %	6.80	5.83
4.41	MS,MS	231.57	53.04	2.97	90.64 %	6.65	5.86
4.42	MS,MS	132.53	29.94	3.01	91.92 %	6.45	5.77
4.56	RSG,MS	1.69	2.51	0.46	14.04 %	6.20	5.29
4.78	WR,MS	28.53	9.07	2.14	65.31 %	6.40	5.52
4.90	SN,MS	37.61	10.66	2.40	73.24 %	7.00	5.86
4.94	MS	81.54	21.05	2.64	80.57 %	6.35	5.58

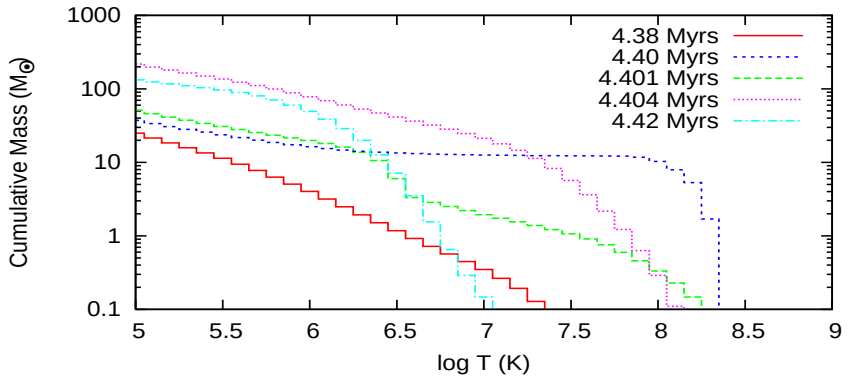

Figure 3.11: Shows the cumulative mass of X-ray emitting material above $T = 10^5$ K at five times throughout the simulation. The red solid line is at t = 4.38 Myrs, shortly before the most massive star explodes, the blue short-dashed line is at t = 4.40 Myrs immediately after the SN explosion. The green long-dashed line is at t = 4.401 Myrs at which point bowshock emission becomes dominant and the purple dotted line is at t = 4.404 Myrs, when SN ejecta begins to leave the grid. The light blue dot-dashed line is at t = 4.42 Myrs, 20,000 yrs after the explosion.

is at each temperature above 10^5 K is shown in Fig. 3.11. The red line shows the temperature distribution of the 25 $M_\odot$ of material above 10^5 K shortly before the explosion at t = 4.38 Myrs. There is virtually no gas at temperatures greater than 10^7 K (0.35 M⊙, see the red line in Fig. 3.11), and the mass-weighted average temperature is $T_{av} = 3.2 \times 10^5$ K. The SN occurs at t = 4.40 Myrs, and its hot ejecta is visible as the short-dashed blue line in Figs. 3.10 and 3.11. As discussed previously, bowshock emission from the SN becomes dominant approximately 900 yrs after the explosion. The temperature distribution of the 51 $M_\odot$ of material above 10^5 K is shown by the green long-dashed line in Figs. 3.10 and 3.11. There is a small amount of material above 10^7 K ($\sim$ 2 $M_\odot$), but the majority of the material is between $10^5 - 10^{6.5}$ K, after which there is an obvious decrease in X-ray emitting material. The mass-weighted average temperature is $T_{av} = 5.9 \times 10^5$ K at this time.

The SN ejecta begins to leave the grid at t = 4.404 Myrs, shown as the purple dotted line in Figs. 3.10 and 3.11. There is approximately 218 $M_\odot$ of material above 10^5 K at this time (see Table 3.1), with $\sim$ 10% (21 $M_\odot$) of that material above 10^7 K. 20,000 yrs after the explosion there is again virtually no gas at $T > 10^7$ K as the shock heated gas slowly cools (shown by the dotted purple line in Fig. 3.10). However, there is approximately 5 times more material between $10^5 - 10^7$ K than before the supernova, with a peak at about $T = 10^6$ K. Fig. 3.11 also reveals that the maximum temperature of gas at t = 4.42 Myrs is actually lower than that at t = 4.38 Myrs, at $T_{max} = 10^{7.4}$ K and $T_{max} = 10^{7.7}$ K respectively.

3.4 Comparison to 1D Bubble Models

3.4.1 Wind-Blown Bubble Models

Chu *et al.* (1995) derived an analytical expression for the X-ray emission from a Weaver *et al.* (1977) wind-blown bubble, in terms of various physical parameters which are observable, such as the density and size of the bubble. The predicted X-ray luminosity in the 0.1–2.4 keV band is:

$$L_X = \left(1.1 \times 10^{35}\,\mathrm{ergs\,s^{-1}}\right) \xi I(\tau) L_{37}^{33/35} n_0^{17/35} t_6^{19/35} \tag{3.1}$$

where ξ is the metalicity relative to the solar value, L_{37} is the mechanical luminosity of the stellar wind(s) in units of 10^{37} ergs s^{-1}, n_0 is the number density of the ambient medium in cm^{-3} and t_6 is the age of the bubble in 10^6 yr. The above equation contains a dimensionless temperature τ, where the dimensionless integral $I(\tau) = (125/33) - 5\tau^{1/2} + (5/3)\tau^3 - (5/11)\tau^{11/2}$ and $\tau = 0.16 L_{37}^{-8/35} n_0^{-2/35} t_6^{6/35}$.

At $t = 0.3\,\mathrm{Myrs}$ the expected luminosity in the 0.1–2.4 keV energy band as predicted using Equation 3.1 is $L_X \approx 2.06 \times 10^{35}\,\mathrm{ergs\,s^{-1}}$ using the average ambient density of the mostly intact GMC clump of $n_0 \approx 250\,\mathrm{cm^{-3}}$. This compares to the combined luminosity from our BB1 and BB2 energy bands, which at $L_X = 3.9 \times 10^{31}\,\mathrm{ergs\,s^{-1}}$ is roughly 5000 times lower than the prediction from the standard Weaver *et al.* (1977) bubble. Because the edge of the bubble expands off the grid at $t \sim 0.2\,\mathrm{Myrs}$, we will have somewhat underestimated the true luminosity in our simulation, but it is clear that a large discrepancy nevertheless remains.

By $t = 2.53\,\mathrm{Myrs}$ the destruction of the GMC clump is well advanced and we should clearly reduce our estimate of the value of the ambient density, n_0. Using an estimate of the density as $n_0 \approx 0.3\,\mathrm{cm^{-3}}$ (which is just 50% greater than the low density medium which surrounds the GMC clump in the simulations), the predicted X-ray luminosity from Equation 3.1 would be $L_X \approx 1.4 \times 10^{34}\,\mathrm{ergs\,s^{-1}}$. Although our simulation only "captures" a small proportion of the X-ray luminosity at this time since a lot of the hot gas has flowed through the grid boundaries, the estimate from Equation 3.1 is approximately 2000 times larger than the luminosity from our simulations at this time. Since this factor is likely to be many times greater than the "true" X-ray luminosity from our simulation (i.e. the luminosity we would infer if our grid were big enough to contain the expanding bubble), we conclude that Equation 3.1 consistently overestimates the X-ray luminosity produced from our simulations by a large margin.

Harper-Clark & Murray (2009) also provide an analytical expression for the expected X-ray luminosity of a Weaver wind-blown-bubble:

$$L_X \sim 3 \times 10^{38} \xi \left(\frac{L_w}{4 \times 10^{38} \mathrm{ergs\,s^{-1}}} \right)^2 \left(\frac{20pc}{r} \right)^3 \left(\frac{6 \times 10^6\, K}{T} \right)^2 \left(\frac{3.6 \times 10^6\, \mathrm{yr}}{t} \right)^2 \tag{3.2}$$

where they have assumed an X-ray cooling rate $\Lambda_X \approx 3 \times 10^{-23} \xi\, \mathrm{ergs\,s^{-1}\,cm^3}$, ξ is the metalicity relative to solar, and t is the age of the cluster/wind source. Applying this expression to the Carina nebula overestimates the observed luminosity by a factor of 10^4 (Harper-Clark & Murray, 2009). In the following we apply Equation 3.2 to our simulated cluster at a time when the stars are on their MS phases and the mechanical luminosity of the cluster wind is $\mathrm{L}_w = 1.16 \times 10^{36}\,\mathrm{ergs\,s^{-1}}$. The average temperature of the X-ray emitting gas at $\mathrm{t} = 2.53\,\mathrm{Myrs}$ is $2.5 \times 10^6\,\mathrm{K}$ (see Table 3.1). We only capture a small part of the bubble volume at this time. However, we can be guided by what an observer may choose as the bubble radius. If the ISM column to the cluster was substantially higher than our assumed value of $10^{21}\,\mathrm{cm^{-2}}$, the emission below 2.5 keV may be almost completely absorbed, in which case Fig. 3.3 shows that only the harder emission might be detected. The radius that an observer might then infer for the "bubble" in the BB3 image in Fig. 3.3 could then be approximated to 6 pc. This leads to a predicted X-ray luminosity of $\mathrm{L}_X \approx 10^{36}\,\mathrm{ergs\,s^{-1}}$ using Equation 3.2, and an overestimate of the intrinsic emission "captured" in our simulation by roughly 4 orders of magnitude. To bring the values from Equation. 3.2 in line with the simulated results would require a bubble radius of 130 pc.

Clearly some of the underlying assumptions made in these equations are incompatible with the simulated results. The two main assumptions in the Weaver *et al.* bubble model which differ from our simulations are that the energy de-

posited by the stellar winds is confined within the bubble and that the surrounding ISM is homogeneous. As discussed in both Harper-Clark & Murray (2009) and Chapter 2, leakage of hot gas from the bubble interior leads to a significant reduction in the pressure. This in turn reduces the X-ray luminosity so that it is well below that from a confined bubble (c.f. Harper-Clark & Murray, 2009). It is interesting that the calculated X-ray luminosity from our simulations is roughly 3–4 dex lower than the predictions from the confined bubble model, which is of order of the same difference between observations of real clusters and the confined bubble model.

3.5 Comparisons to Observations

3.5.1 Young Massive Stellar Clusters

It is widely observed that there is a deficit of X-ray emission from stellar clusters compared with predictions (Dorland & Montmerle, 1987; Dorland *et al.*, 1986; Dunne *et al.*, 2003; Harper-Clark & Murray, 2009; Oey, 1996; Rauw *et al.*, 2002; Smith *et al.*, 2005). Many explanations of this effect have been suggested, for example lower stellar luminosities, mass or energy loss from the bubble, or highly efficient mass loading which reduces the temperature of the cluster below X-ray temperatures. However, this latter effect may also produce higher X-ray luminosities (Stevens & Hartwell, 2003). Section **??** demonstrated that the X-ray luminosities produced by the model in Chapter 2 also exhibit a lower luminosity than predicted by models. A comparison will now be made between the model and observations of M17 and the Rosette Nebula. For a full literature review of

young massive stellar clusters from which diffuse X-ray emission has been detected see Table. 3.2 and Appendix A.

3.5.1.1 M17

M17 is a young blister HII region located on the northeast edge of one of the largest GMCs in the Galaxy, at an approximate distance of 1.55 kpc. It is estimated to be only ~ 0.5 Myrs old (Chini & Hoffmeister, 2008; Hoffmeister *et al.*, 2008). M17 is photoionized by the massive stellar cluster NGC 6618, within which Broos *et al.* (2007) have identified 14 O-stars. An earlier study by Hanson *et al.* (1997) identified at least 9 O-stars and a few late-O/early-B stars.

The diffuse X-ray emission from M17 has previously been analyzed by Dunne *et al.* (2003),Townsley *et al.* (2003), Hyodo *et al.* (2008), and most recently by Townsley *et al.* (2011). The total X-ray luminosity is thought to be $L_X = 2 \times 10^{34}\,\mathrm{ergs\,s^{-1}}$. At t = 0.44 Myrs, the simulated cluster has an intrinsic 0.1–10 keV luminosity (BB1+BB2+BB3) of $L_X = 7.48 \times 10^{32}\,\mathrm{ergs\,s^{-1}}$, approximately 25 times lower than in M17. However, considering the number of O-stars in M17, the emission from the simulated cluster is of the same order of magnitude, and thus is perfectly acceptable given the differences in environment. For more information on M17 see Appendix A.

3.5.1.2 Rosette Nebula

The Rosette Nebula is a blister HII region at the tip of the giant Rosette molecular cloud. It is estimated to be ~ 2 Myrs old (Hensberge *et al.*, 2000). A study carried out by Martins *et al.* (2012) has identified 7 O-stars in the cluster NGC 2244 contained within the Rosette Nebula. The earliest spectral type so far detected

Table 3.2: The properties of young massive stellar clusters from which diffuse X-ray emission has been detected. The clusters are ordered roughly by age. Further details and references for values in this table can be found in Appendix A.

Cluster/Region Name	Age (Myrs)	Distance (kpc)	X-ray Morphology	Thermal/NT	L_X (ergs s^{-1})	kT (keV)	N_H (cm^{-2})
RCW 38	$\lesssim 1$	1.7	CF/blowouts	NT	3×10^{32}	0.2	9.5×10^{21}
Omega (M 17)	~ 0.5	2.0	CF/blowout	T	2×10^{34}	0.28+0.29+0.57	$1.6,5,10\times10^{21}$
Westerlund 2	$\lesssim 2$	2.85±0.43	CF	T	4.6×10^{33}	0.1+0.8+3.1	$4,12,12\times10^{21}$
Rosette	2	1.55	CF	T	7×10^{32}	0.06,0.8	2×10^{21}
Hourglass	1–2.5	1.3	CF	T	$\lesssim 6.6\times10^{32}$	0.63	1.1×10^{22}
Arches	2–2.5	8	CF	T (+NT)	3.8×10^{33}	2.56	1.1×10^{23}
NGC 2024 (Flame)	0.3–3	0.415	CF	T	2×10^{31}	11	$0.21,3.3\times10^{22}$
Orion (M 42)	3	0.49	Champagne	T	5.5×10^{31}	0.17	$4.1(<1.0)\times10^{2}$
Quintuplet	3.5–4	8	CF	T	3×10^{33}	$10^{+4.6}_{2.7}$	3.8×10^{22}
NGC 3603	1–4	7±1	CF	T	2.6×10^{35}	0.53	2×10^{22}
Westerlund 1	4–5	4–5	CF	T (+NT?)	$1.7\text{–}30\times10^{33}$	0.7+3.0	2×10^{22}
NGC 3576N		2.8±0.3	CF	T (+NT)	5.9×10^{33}	0.11,0.5,0.67	$0.3,1.3\times10^{22}$
NGC 3576S		2.8±0.3	Blowout	T	1.1×10^{34}	0.31,0.53	$1.3,0.3\times10^{22}$

is O4V((f)).

Townsley *et al.* (2003) find that soft diffuse X-ray plasma surround the OB association and fills the nebula cavity completely. This plasma likely originates from the O star winds and is later brought to thermalization by wind-wind interactions or by shocking against surrounding molecular material. The intrinsic 0.5–2 keV luminosity is $\approx 7 \times 10^{32}\,\mathrm{ergs\,s^{-1}}$, with no significant emission detected above 2 keV. At t = 1.96 Myrs, the simulated cluster has an intrinsic 0.5–2.5 keV luminosity (BB2) of $L_X = 6.46 \times 10^{30}\,\mathrm{ergs\,s^{-1}}$. Given the higher mass-loss rate of the Rosette cluster ($\dot{M}_* = 2.5 \times 10^{-6}\,\mathrm{M_\odot\,yr^{-1}}$ Stevens & Hartwell, 2003) and the higher number of O-stars present, this is a reasonably close match to the simulations. For more information on the Rosette Nebula see Appendix A.

3.5.2 Young SNRs from Core-Collapse SNe

When the stars in the simulation explode they input $10\,\mathrm{M_\odot}$ of material and 10^{51} ergs of energy into the surroundings. As seen in Fig. 3.5 the results of this explosion should only be trusted after 900 yrs when the dominant source of X-ray emission is from interactions between the blast wave and the surrounding clumpy medium. The ejecta begins to leave the grid after 4600 years, at which point hot gas and its corresponding emission begins to be lost. A comparison will now be made between the model and observations of young SNRs which are of age $900 < t < 4600$ years.

3.5.2.1 1E0102.2-7219

1E0102.2-7219 (hereafter 1E0102) is a SNR in the Small Magellanic Cloud (SMC) with an inferred kinematic age of $\sim$2100 yrs (Eriksen *et al.*, 2001) at a distance of

Table 3.3: Young SNRs from core-collapse SNe compared with the simulated results. The SNRs are ordered roughly by age.

SNR Name	Alternative Name	L_x (ergs/s)	Diameter (pc)	Age (yr)	V_{exp} (km/s)	Temperature (keV)	Distance (kpc)	Prog. Mass ($M_\odot$)
1E0102.2-7219		$\sim 8.8 \times 10^{35}$	~ 12	~ 1000–2100	1000	2.5–4.5,0.4–1	60	32
MSH 11-54	G292.0+1.8	$> 7.2 \times 10^{32}$	15	2700–3200	$\lesssim 1200$	1.05,0.37	< 6	20-40
N 132D	SNR 0525-69.6	$4.5\text{-}7.5 \times 10^{37}$	~ 20–25	3150	2250–3700	0.6–0.7	55	30-35
Puppis A		1.2×10^{37}	~ 32	3700–4450	> 1500	0.6	1.3-2.2	> 25
Simulation		2.71×10^{37}	~ 18	1060	~ 5900	0.68	1	35
Simulation		2.49×10^{37}	~ 27	2060	~ 5200	0.68	1	35
Simulation		1.67×10^{37}	~ 29	2630	~ 1600	0.68	1	35
Simulation		1.05×10^{37}	~ 30	3300	~ 1000	0.54	1	35
Simulation		1.02×10^{37}	~ 31	3860	~ 1000	0.54	1	35

$\sim 60\,\mathrm{kpc}$ (Wada *et al.*, 2013). The progenitor is thought to have been a Wolf-Rayet star with a zero-age MS (ZAMS) mass of $\sim 32\,\mathrm{M}_{\odot}$ that underwent significant mass loss prior to exploding as a Type Ib/c or IIL/b supernova. Gaetz *et al.* (2000) used *Chandra* to image the SNR, finding it to be almost "textbook", with a hotter outer ring surrounding a cooler, denser inner ring which is likely the reverse-shocked stellar ejecta. The diameter of the SNR was estimated to be 40" by Hughes (1988) (approximately 12 pc at 60 kpc distance), which is in good agreement with Hughes *et al.* (2000) who estimated the radius of the blast wave to be 6.4 pc. Hughes *et al.* (2000) estimated an expansion age of $\sim 1000\,\mathrm{yrs}$, in contrast to the estimate by Eriksen *et al.* (2001). However, recently Wada *et al.* (2013) have proposed the source is a B*e*/NS binary. There is little interstellar extinction along the line of sight to 1E0102.2-7219 which allows a comprehensive, multi-wavelength analysis from the X-ray to the radio domain.

Hughes *et al.* (2000) estimated the expansion velocity of the blast wave to be $6000\,\mathrm{km\,s^{-1}}$ based on a radius of 6 pc and an age of 1000 yrs, although Flanagan *et al.* (2004) find from Doppler shifts in the SNR that the majority of the bulk matter is moving at a lower $1000\,\mathrm{km\,s^{-1}}$. Hughes *et al.* (2000) also estimate the temperature in the postshock region to be 0.4–1.0 keV. Gaetz *et al.* (2000) estimated the upper limit on X-ray emission of the central source to be $< 9 \times 10^{33}\,\mathrm{ergs\,s^{-1}}$, whilst Wada *et al.* (2013) estimate the 0.5–10 keV luminosity of the SNR to be $\sim\ 8.8 \times 10^{35}\,\mathrm{ergs\,s^{-1}}$. This is considerably lower than the intrinsic 0.5–10 keV X-ray emission from the simulated cluster, which is $\mathrm{L}_X = 1.53 \times 10^{36}\,\mathrm{ergs\,s^{-1}}$ and $\mathrm{L}_X = 1.69 \times 10^{36}\,\mathrm{ergs\,s^{-1}}$ for 1000 and 2000 yrs after the first SN explosion respectively. As the simulation assumes collisional ionization equilibrium (CIE), which is unlikely to be the case in 1E0102, it is

not surprising that higher luminosities are obtained from the simulation. The clumpy environment in the simulated cluster may also be partially responsible, if the environment of 1E0102 is lower density and/or more homogeneous. The expansion velocity of the simulated blastwave is between $\sim$6000–8000 km s^{-1} (see Table. 3.3), which although high is similar to the estimate of the blast wave by Hughes *et al.* (2000).

3.5.2.2 MSH 11-54

Also known as G292.0+1.8, this is a core-collapse SN with an estimated age of 2700 - 3200 years (Chevalier, 2005; Tanaka & Takahara, 2013; Winkler *et al.*, 2009), a distance of 6 kpc (Gaensler & Wallace, 2003) and is one of only a handfull of O-rich SNRs known today (Ghavamian *et al.*, 2012; Park *et al.*, 2007). The X-ray emission from such O-rich SNRs is thought to arise from faster, non-radiative shocks in lower density ejecta and interstellar gas. The central source is thought to be a pulsar wind nebula. The SNR has a radius of approximately 15 pc assuming a distance of 6.2 kpc (Gaensler & Wallace, 2003).

Gonzalez & Safi-Harb (2003) derived an average temperature for the SNR using two components - a high temperature plasma associated with the supernova blast wave and a low temperature plasma from the reverse shock. These two components were estimated to be 1.05 $\pm$ 0.34 and 0.37 $\pm$ 0.18 keV respectively. They also make an estimate of the progenitor mass to be 30-40 $M_{\odot}$, compared with the estimate by Hughes & Singh (1994), who predicted a star of 20-25 $M_{\odot}$ to be a reasonable candidate for the progenitor. However, a more recent estimate of the temperature by Park *et al.* (2007) using *Chandra* data found a highly non-uniform distribution of hot, X-ray emitting gas in the remnant ranging from

kT$\sim$5 keV in the NW regions to around kT$\sim$0.7 keV in the SE. These results are a promising match with the simulated results of the 35 $M_\odot$ progenitor star at an average temperature of 0.54–0.68 keV at around 2000–3300 years after the explosion. The SN explosion is thought to have been asymmetric, which would explain the distribution of temperatures and the greater expansion of the remnant towards the NW. Hughes *et al.* (2003) found the unabsorbed 0.3–10 keV X-ray luminosity of the central pulsar to be $L_X = 7.2 \times 10^{32}$ ergs s^{-1}, but made no estimate for the entire remnant. The simulated cluster at around this time has a total 0.1–10 keV intrinsic luminosity of $L_X \sim 1 \times 10^{37}$ ergs s^{-1}.

3.5.2.3 N132D

N132D is one of the brightest SNRs in the Large Magellanic Cloud (LMC) with an estimated age of 3150 years (Morse *et al.*, 1995) and an inferred progenitor mass of 30-35 $M_\odot$ (Blair *et al.*, 2000). With a diameter of 80", the distance to the SNR of approximately 55 kpc (Hughes, 1987) implies a real diameter of $\sim$21 pc. This is a similar estimate to the extent of the X-ray shell, which has an estimated radius of 12 pc (Morse *et al.*, 1995). The expansion velocity of the SNR has been estimated by several authors (e.g. Hwang *et al.*, 1992; Morse *et al.*, 1995), with values ranging from 2250–3700 km s^{-1}. The radius of the simulated SNR at around 3300 yrs after the explosion is $\sim$ 15 pc, with an inferred expansion velocity of $\sim$4400 km s^{-1}.

The X-ray luminosity in the 0.2–4 keV energy band was estimated by Hughes (1987) to be 4.5–7.5$\times 10^{37}$ ergs s^{-1}, based on thermal plasma temperatures of $10^{6.8} - 10^{7.1}$ K and a hydrogen column density of $10^{21} - 10^{21.5}$ cm^{-2} (Raymond & Smith, 1977). The estimated luminosity is actually slightly higher than the

simulated results ($L_X = 1.05 \times 10^{37}\,\mathrm{ergs\,s^{-1}}$ at 3300 yrs), despite the fact that the simulations assume CIE. Given the inherent differences in the simulated and actual environments these results can be considered a reasonable match. The plasma temperature is very similar to that found in the other SNRs mentioned, at approximately 0.6-0.7 keV, compared with an average of 0.54 keV from the simulated remnant (see Table 3.1). There is patchy X-ray absorption around the remnant thought to be caused by gas just outside the molecular cloud towards the northern tip of N132D (Kim *et al.*, 2003).

3.5.2.4 Puppis A

Puppis A is a nearby Galactic SNR with age estimates ranging from 3700 yr (Winkler & Kirshner, 1985) to 4450 yr (Becker *et al.*, 2012), making it most comparable to the simulation 3,900 yrs after the explosion (see Table. 3.3). A distance of 2.2 kpc was estimated based on HI and CO studies (Reynoso *et al.*, 2003), although a closer distance of 1.3 kpc has been proposed by Woermann *et al.* (2000) based on OH line detections. This remnant is embedded in a complex region composed of large atomic and molecular clouds and an interstellar density gradient. The remnant is about 50′ in diameter (approximately 32 pc at a distance of 2.2 kpc), with a progenitor mass of 25 $M_\odot$ inferred from Canizares & Winkler (1981).

Optical knots detected from Puppis A are evident only in the northeast, implying the ejection of the matter during the explosion was asymmetric (Katsuda *et al.*, 2008). Oxygen-rich filaments are detected to have radial velocities higher than $\sim 1500\,\mathrm{km\,s^{-1}}$. These filaments are interpreted as SN ejecta which have remained mostly uncontaminated by the ISM (Winkler & Kirshner, 1985).

Recently, Dubner *et al.* (2013) studied Puppis A using *Chandra* and XMM-Newton. They estimated the X-ray luminosity between 0.3 and 8.0 keV to be $L_X = 1.2 \times 10^{37}\,\mathrm{ergs\,s^{-1}}$ assuming a distance of 2.2 kpc. The X-ray emission from Puppis A appears to be dominated by the swept-up ISM due to very low metal abundances (Hwang *et al.*, 2008). The total intrinsic X-ray luminosity of the simulated remnant 3860 yrs after the explosion is $L_X = 1.02 \times 10^{37}\,\mathrm{ergs\,s^{-1}}$, which is a reasonable match to Puppis A.

The average temperature in the remnant is 0.6 keV, very similar to the average temperature of 0.54 keV seen in the simulated remnant at 3860 years after the explosion (see Table 3.1).

3.6 Conclusion

This Chapter investigates the X-ray emission from a massive young stellar cluster embedded in an inhomogeneous GMC clump treating only the mechanical effects from winds and supernovae. The hydrodynamical input model was previously simulated in Chapter 2, and this Chapter explores the emission arising from that model. Initially the dense parts of the clump decrease the observed X-ray emission due to attenuation, but once the cluster wind has destroyed and ablated a large portion of this material the attenuation from the ISM material is dominant.

At very early times, when the wind material is still confined by the inhomogeneous GMC material the X-ray luminosity is reasonably bright, at $L_X \approx 5 \times 10^{33}\,\mathrm{ergs\,s^{-1}}$. However, as the cluster wind erodes and destroys the surrounding clump it is no longer completely confined and therefore hot gas is able to leak through the gaps in the shell. This causes a reduction in the X-ray luminosity

as the pressure within the bubble decreases. Once the low density gas from the clump has been ablated away the covering factor of the cluster remains more or less constant, leading to an approximately constant intrinsic X-ray luminosity of $1.7\times10^{32}\,\mathrm{ergs\,s^{-1}}$ and an attenuated X-ray luminosity of $7\times10^{30}\,\mathrm{ergs\,s^{-1}}$.

The most massive star becomes a RSG at $\mathrm{t}=4.0\,\mathrm{Myrs}$, resulting in a large drop in the X-ray luminosity in all three of the broadband regions studied. The most dramatic decrease is seen in the BB3 emission, where the attenuated X-ray luminosity drops four orders of magnitude, from $\mathrm{L}_X \sim 2 \times 10^{29}\,\mathrm{ergs\,s^{-1}}$ to $\mathrm{L}_X \sim 2\times10^{25}\,\mathrm{ergs\,s^{-1}}$ by the end of the RSG phase. The drop in X-ray luminosity in the other two broadbands over this period is around a factor of 50 and 100 for BB1 and BB2 respectively. Although a lot of material is deposited in the RSG-enhanced cluster wind, the amount of material at X-ray emitting temperatures is very low, contributing to the lack of X-ray emission observed at this time.

100,000 years later the most massive star further evolves to become a WR, with a corresponding increase in X-ray emission in all three broadband regions studied. The amount of material at a temperature greater than $10^5\,\mathrm{K}$ increases by an order of magnitude over that seen in the RSG stage, and a total of 78% of the computational volume contains X-ray emitting material. The high momentum wind sweeps up the material deposited in the previous phase and heats it to high temperatures, with the average temperature at this time being around $\bar{\mathrm{T}} = 2.5 \times 10^6\,\mathrm{K}$. The total attenuated X-ray emission increases to $\mathrm{L}_X \sim 5 \times 10^{33}\,\mathrm{ergs\,s^{-1}}$, which is about 30 times greater than that observed when all three stars were on the MS.

At $\mathrm{t}=4.4\,\mathrm{Myrs}$ the star explodes as a SN, ejecting $10\,\mathrm{M}_\odot$ of material 10^{51} ergs of energy into the simulation. Due to the way in which the explosion was ini-

tialised, the emission from the SN should only be analysed from the time at which the interaction of the blastwave with the surrounding material becomes dominant. In this work this occurs approximately 900 years after the explosion of the most massive star. The ejecta begins to leave the grid 4600 years after the explosion, and therefore the results of the SN can be compared with results only between the ages of $900 < t < 4600$ years.

The supernova of the $35\,M_{\odot}$ star was compared with four young core-collapse SNe with ages ranging from $\sim$1000–4450 yrs. Although the simulated SNR assumed collisional ionization equilibrium, which is unlikely to be true for such young remnants, the X-ray luminosity and electron temperatures are reasonable matches. Unfortunately, as the ejecta begins to leave the grid 4,600 yrs after the initial explosion no comparisons can be made with older remnants.

The simulated emission from the cluster during the wind-dominated phases is substantially lower than predicted by 1D spherically symmetric bubble calculations, but matches reasonably well to actual observations of several massive young stellar clusters. This is likely due to two of the assumptions made in these calculations being overly simplified compared to the model used in this thesis. Firstly, the assumption that the hot wind material is confined within a bubble is very much not the case, and therefore a reduction in the pressure in the simulated cluster leads to a reduction in the X-ray luminosity. Secondly, the surrounding density is not homogeneous as described in these models, which will lead to local areas of confinement and leakage. Clearly the highly complex environment of young massive star forming regions requires similar complexity in simulations in order to better understand their properties.

Chapter 4

Thermal Radio Emission from a Massive Young Stellar Cluster

4.1 Introduction

Radio continuum emission from star forming regions is a useful probe of the physical conditions present therein. Radio observations are one of the only extinction-free measures of recent ($\lesssim 30$ Myrs) star formation.

There are two major components that make up radio continuum emission from a typical star forming region (see Condon, 1992, and references therein for a comprehensive review). First, the fast, dense, ionized winds from OB and WR stars emit free-free radiation over a wide range of wavelengths, from cm emission in the radio band to μm emission in the near-infrared. With a radio spectrum characterized by $S_\nu \sim \nu^\alpha$, pure optically thin thermal bremsstrahlung emission will show a nearly flat slope ($\alpha \sim -0.1$). An early study by Wright & Barlow (1975) found that the thermal radio emission of an ionized, spherically symmetric,

uniform wind with an electron density profile $n_e \propto r^{-2}$ (where r is the distance from the central star), has a positive spectral index of $\alpha \approx 0.6$. Reynolds (1986) showed that $\alpha < 0.6$ occurs for an unresolved, partially opaque flow whose cross section grows more slowly than its length. The index can vary from $\alpha = 2$ for totally opaque emission to $\alpha = -0.1$ for totally transparent emission.

Second, there is a non-thermal component attributed to synchrotron emission produced by relativistic electrons accelerated by diffusive shock acceleration in the winds of massive stars (White, 1985), or accelerated in recent supernova explosions and remnants. There remains some uncertainty as to whether non-thermal radio emission can be observed from the wind of a single massive star (see Dougherty & Williams, 2000; van Loo, 2010; van Loo *et al.*, 2005). This non-thermal emission will show a more negative spectral index ($-1.2 \lesssim \alpha \lesssim -0.4$). About a quarter of the brightest O-stars have a radio spectrum which is dominated by non-thermal emission at cm wavelengths (Bieging *et al.*, 1989).

If the radio continuum emission is observed at multiple frequencies then it is possible to identify which of these physical processes dominate within individual star forming regions.

At wavelengths where the wind is optically thick, the thermal radio emission can be used to determine stellar mass-loss rates (e.g. Abbott *et al.*, 1980, 1981; Bieging *et al.*, 1989; Leitherer *et al.*, 1995; Schnerr *et al.*, 2007; Scuderi *et al.*, 1998). Even if the wind expands aspherically, the radio derived mass-loss rates do not typically change by more than a factor of two (Schmid-Burgk, 1982). However, part of the emission may be of non-thermal origin, which must be accounted for in any calculations. Bieging *et al.* (1982) used radio continuum observations of WR stars to estimate the mass-loss rates, based on the formula

of Wright & Barlow (1975):

$$\frac{\dot{M}}{10^{-5}\,\mathrm{M_\odot\,yr^{-1}}} = C_1 \left(\frac{S_\nu}{\mathrm{mJy}}\right)^{3/4} \left(\frac{v_\infty}{10^3\,\mathrm{km\,s^{-1}}}\right) \left(\frac{d}{1\,\mathrm{kpc}}\right)^{3/2} \tag{4.1}$$

where

$$C_1 = \frac{0.095\mu}{Z(\gamma g_{ff}\nu)^{1/2}} \tag{4.2}$$

with S_ν the flux density of the source, v_∞ the terminal velocity of the wind and d the distance to the source. The quantities μ, Z and γ are the mean molecular weight per ion, the rms charge per ion and the mean number of electrons per ion. g_{ff} is the free-free gaunt factor, which can be approximated following Leitherer & Robert (1991) as:

$$g_{ff} = 9.77\left(1 + 0.13\log\left[\frac{\mathrm{T_e^{3/2}}}{\mathrm{Z}\nu}\right]\right) \tag{4.3}$$

where T_e is the electron temperature of the wind in K. Lang *et al.* (2001) adopt $C_1 = 0.34$ for 22.5 GHz and Lang *et al.* (2005) adopt $C_1 = 0.52$ for 8.5 GHz.

Equation. 4.1 is based on a spherically symmetric, stationary, isothermal wind flowing at constant velocity. Any non-thermal components may contaminate the radio flux density at lower frequencies. Therefore, high frequency observations may be a better tracer of the thermal component and give more reliable mass-loss rates (Contreras *et al.*, 1996).

The radio emission produced by the stellar winds themselves will be on relatively small scales. The optical depth unity surface for this emission is typically of the order of 1000 $\mathrm{R_\odot}$ for early type stars (Pittard *et al.*, 2005). The collisionally

ionized emission, on the other hand, will be much more extended and observable on much larger scales.

In this Chapter the hydrodynamical model of stellar wind and supernova feedback into an inhomogeneous environment outlined in Chapter 2 is used as a basis to simulate the resulting thermal radio emission from massive star-forming regions. It is worth pointing out that the total flux will be dominated by photoionization. However, the results in this Chapter will be useful in quantifying the collisonal contribution to the total radio flux. In Section 4.2 the details of the model and the method of calculating the radio emission and absorption are discussed. The results are presented in Section 4.3, including comparisons between the X-ray and radio emission originating from the cluster throughout the lifetime of the most massive star. Comparisons to observations of young stellar clusters and young core-collapse SNe are made in Section 4.4. Section 4.5 summarises and concludes this Chapter.

4.2 Simulations

4.2.1 The Numerical Model

The radio calculations in this Chapter are based on the 3D hydrodynamical model described in Rogers & Pittard (2013) and discussed in detail in Chapter 2. The simulations consist of three massive O stars which represent the main sources of mechanical feedback in a massive star forming region contained within an inhomogeneous GMC clump. The evolution of these stars is treated simplistically as three distinct phases - MS, RSG and WR. The details of the stellar cluster

are summarized in Table 2.1 in Chapter 2. At the end of their lifespan the stars explode imparting $10\,M_\odot$ of material and 10^{51} ergs of thermal energy into the environment. The lifespans of the stars are designed in such a way so that there are three distinct supernova explosions over the course of the simulation.

The simulation tracks the molecular, atomic and ionized phases separately, and uses a temperature dependent average particle mass for the calculations. The net heating/cooling rate per unit volume is parameterized as $\dot{e} = n\Gamma - n^2\Lambda$, where $n = \rho/m_H$ and Γ and Λ are heating and cooling coefficients which are assumed to depend only on temperature. Photoionization is not treated in this work. Hence the dense clumps in direct view of the stellar cluster will lack a "skin" of photoionized material on their surface. This means that the simulated radio emission will be underestimated since radio photons should not be absorbed by the cold neutral clump material.

The simulations in Chapter 2 showed that the inhomogeneous structure of the natal GMC cloud surrounding the cluster had an important effect on the initial expansion of the cluster wind, which carved channels through the low density material to escape the clump. The regions of high density within the initial clump proved to be surprisingly resistant to ablation from the cluster wind, and at later times to the shockwaves of the SNRs.

4.2.2 Modelling the Radio Emission and Absorption

To calculate the radio emission the results of the hydrodynamic model are read into a radiative transfer ray-tracing code. A synthetic image on the plane of the sky is then generated by solving the radiative transfer equation along suitable

lines of sight through the grid. The thermal emission ($\epsilon_\nu^{\rm ff}$) and absorption ($\alpha_\nu^{\rm ff}$) at frequency ν are given by Rybicki & Lightman (1979) as:

$$\epsilon_\nu^{\rm ff} = 6.8 \times 10^{-38} Z^2 n_e n_i T^{-\frac{1}{2}} e^{\frac{-h\nu}{kT}} g_{\rm ff} \tag{4.4}$$

and

$$\alpha_\nu^{\rm ff} = 3.7 \times 10^{8} T^{-\frac{1}{2}} Z^2 n_e n_i \nu^{-3} (1 - e^{\frac{-h\nu}{kT}}) g_{\rm ff} \tag{4.5}$$

where Z is the mean ionic charge, n_e and n_i are the electron and ion number densities, T is the temperature of the gas and g_{ff} is a velocity averaged Gaunt factor (Hummer, 1988). All quantities are in cgs units. The densities n_e and n_i are determined from the cell density, composition and ionization, where the ionization is specified as a function of cell temperature. The appropriate ionization for a particular temperature regime is determined, as shown in Table 4.1, and the absorption and emission coefficients are then evaluated. The unshocked winds are assumed to be isothermal at $T = 10\,000\,K$. It is assumed that there is no ionization at temperatures below $T < 10^4\,K$. This will underestimate the actual emission. The free-free emission from the gas with $T < 10^4\,K$ will most likely be dominated by material which is photoionized. Line emission dominates the cooling at temperatures below $10^7\,K$, with thermal bremsstrahlung dominating at higher temperatures. The cluster is assumed to be at a distance of 1 kpc from an observer. Solar abundances are assumed throughout this work.

In this Chapter it is only the thermal emission which is examined. This emission originates from the stellar winds and the regions of hot, shocked gas where they collide. To generate the spectrum over the radio regime the emission is

Table 4.1: Ionization structure for H, He and CNO at various temperatures.

	H	He	CNO
	1+2+3+6+	1+2+3+6+	1+2+3+6+
$T < 10^4$ K	- - - -	- - - -	- - - -
$1 \times 10^4 < T < 2 \times 10^4$ K	1 - - -	1 0 - -	0 1 0 0
$2 \times 10^4 < T < 3 \times 10^4$ K	1 - - -	1 0 - -	0 1 0 0
$3 \times 10^4 < T < 1 \times 10^6$ K	1 - - -	0 1 - -	0 0 1 0
$T > 1 \times 10^6$ K	1 - - -	0 1 - -	0 0 0 1

calculated at 40 frequencies ranging from 0.23–46.59 GHz. The three frequencies analyzed in this chapter are 1.4 GHz, 5 GHz and 15 GHz, which are in the radio recombination bands L, C and U respectively.

4.3 Results

4.3.1 Main Sequence

The collisionally ionized free-free radio lightcurve for the cluster throughout the simulation is shown in Fig. 4.1. The solid red line, dashed green line and blue dotted line tracks the flux density at 1.4 GHz, 5 GHz and 15 GHz respectively. The initial radio flux density of the cluster is $S_{1.4} = 1262$ mJy, $S_5 = 1113$ mJy and $S_{15} = 980$ mJy at 1.4, 5 and 15 GHz respectively, and steadily decreases over the next Myr to $S_{1.4} = 49$ mJy, $S_5 = 43$ mJy and $S_{15} = 38$ mJ as the cluster wind clears out the low density regions of the remnant GMC.

After $t \approx 1$ Myrs the cluster wind has effectively destroyed the majority of the GMC clump, with only a few high density regions resisting the ablation of the wind (see, e.g. Fig. 2.4 in Chapter 2). Once the GMC clump is no longer confining

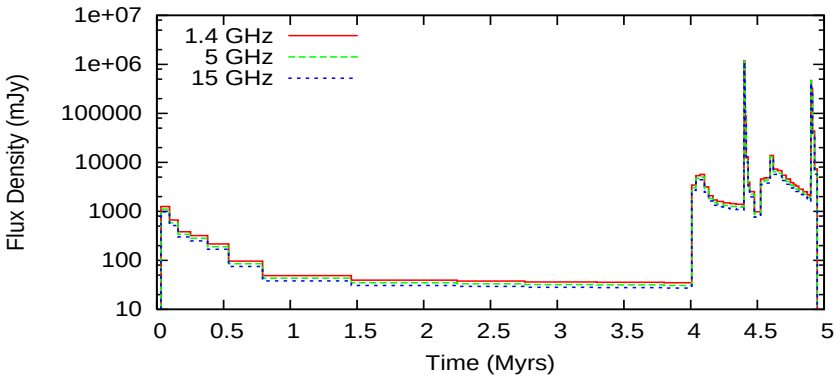

Figure 4.1: The radio lightcurve for the cluster over the course of the simulation. The red solid line, green dashed line and blue dotted line tracks the 1.4 GHz, 5 GHz and 15 GHz radio emission respectively.

the cluster wind the covering fraction will be fairly constant, and therefore the flux density remains fairly constant for the duration of the MS of the cluster.

Synthetic images at three radio frequencies during this clearout at t = 0.13 Myrs are shown in Fig. 4.2, where extended lobes to either side indicate that some of the hot wind material must be leaking out of the GMC clump. The lobes are approximately spherical and trace the bubbles inflated by the venting gas. At this time all three stars are on the MS (see Table 2.1 for the stellar properties). The left panel shows the 1.4 GHz radio emission, the middle panel shows the 5 GHz radio emission and the right panel shows the 15 GHz emission. As can be seen in both the lightcurve and the synthetic images, all three of the frequencies tracked are very similar in magnitude, with the 1.4 GHz emission slightly greater ($S_{1.4}$ = 663 mJy) and the 15 GHz emission marginally fainter (S_{15} = 517 mJy) than the 5 GHz emission (S_5 = 586 mJy). The structure of the thermal radio emission at all three frequencies analyzed is the same, with the brightest emission at the centre where a lot of shocked gas is present. Also visible is a slight brightening in the region of the shell around the asymmetrically expanding gas,

Figure 4.2: Collisionally ionized free-free radio emission for the cluster at time $t = 0.13\,\mathrm{Myrs}$. Each panel is $55.4\,\mathrm{pc}^2$. [Left] shows the emission at 1.4 GHz, [Middle] shows the emission at 5 GHz and [Right] shows the emission at 15 GHz. The stellar cluster is located at the centre of each panel.

and multiple filamentary structures within the hot bubble interior. The optical depth unity surface at these frequencies is of the order of $10^3\,\mathrm{R}_\odot$, which is much too small to be resolved in these images. Therefore, the small scale radio emission from the winds themselves will not be picked up in these images. The emission originates from the shocked, collisionally ionized plasma.

However, the telescope sensitivity required to pick up the lobes and the greater structure shown in Fig. 4.2 is far beyond what is currently available (the lowest scale of the legend is $1.5\times10^{-25}\,\mathrm{ergs\,cm^{-2}\,s^{-1}\,Hz^{-1}\,ster^{-1}}$, which is the equivalent of $5.6\times10^{-7}\,\mathrm{mJy\,beam^{-1}}$). Fig. 4.3 shows a comparison between the total 1.4 GHz thermal radio emission from our simulated cluster as shown in the left panel of Fig. 4.2 and the emission which could feasibly be detected using current radio telescopes. The only emission which would actually be detected is from the vicinity close to the cluster centre. The majority of the thermal radio emission originates in this region, containing approximately 590 mJy of the total 663.25 mJy generated. If the sensitivity is increased by a further order of magnitude then the radio active shell surrounding the larger of the two lobes begins to

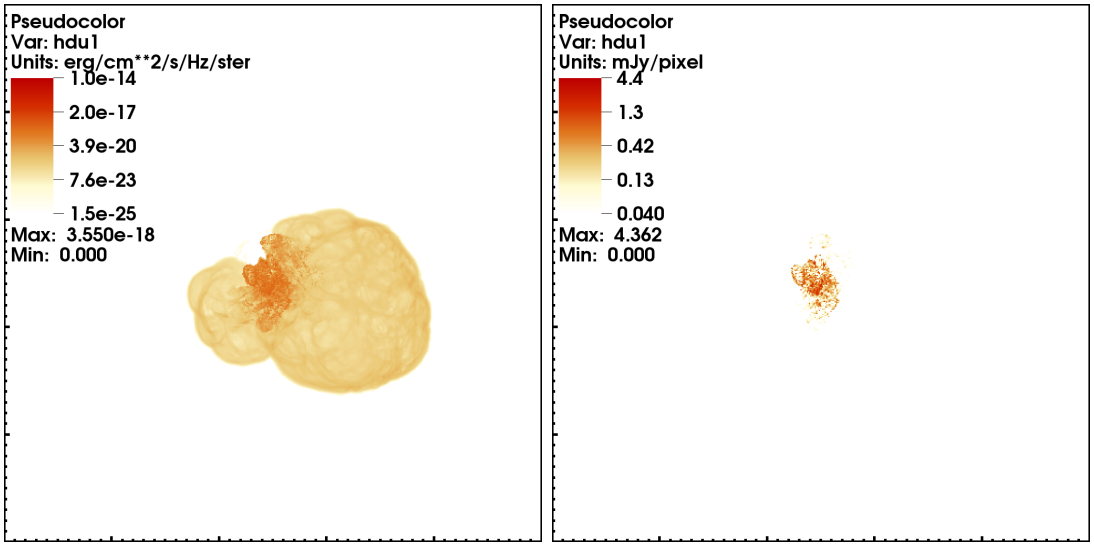

Figure 4.3: Radio emission for the cluster at time t = 0.13 Myrs. [Left] shows the simulated emission at 1.4 GHz. [Right] shows emission at detectable levels at 1.4 GHz. The panels are 500×500 pixels and each side is 55.4 pc long.

be apparent, although at this level it would be completely indistinguishable from any noise.

As discussed in the introduction, this emission would be overwhelmed by the contribution from photoionzation. However, given that the escape fraction of ionizing photons is low at early times (see Fig. 2.16), photoionization may not play as important a role for regions outside the GMC clump whilst a large proportion of the ionizing photons are trapped within the clump. Fig 4.3 may therefore be a reasonable approximation for the large scale extended radio emission at this time. This will not be true for the radio emission at later times once the GMC clump has been ablated by the cluster wind and most of the ionizing photons escape to large distances.

Despite the fact that a large portion of the simulated free-free radio emission will not be detected with current radio telescopes, for the remainder of this Chap-

ter the results will be presented in this manner, and the actual sensitivity and the potential for detections should be considered with Fig. 4.3 in mind.

After $t = 1\,\mathrm{Myr}$ the covering factor of the cluster is approximately constant after the low density regions of the clump have been rapidly blown out by the cluster wind and therefore the flux density also remains mostly constant until $t = 4.0\,\mathrm{Myrs}$, at which point the most massive star evolves onto the RSG branch.

At $t = 2.53\,\mathrm{Myrs}$, a point at which all three of the stars are on the MS, the cluster wind velocity is $2000\,\mathrm{km\,s^{-1}}$ and the cluster mass-loss rate is $\dot{M}_{cl} = 9 \times 10^{-7}\,\mathrm{M_\odot\,yr^{-1}}$ (see Table 2.1 for the individual stellar parameters). Using Equations 4.2 and 4.3 and assuming $Z = 1$ and $\mu = 2$ (Lang *et al.*, 2001, 2005) and $T_e = 1 \times 10^4\,\mathrm{K}$, the values of C_1 can be calculated as ~ 1.16, 0.66 and 0.40 at 1.41, 4.98 and 15.23 GHz. From Equation 4.1, the individual flux density of each of the stars can be calculated, and combined make a cluster flux density of $S_{1.4} = 0.013\,\mathrm{mJy}$, $S_5 = 0.028\,\mathrm{mJy}$ and $S_{15} = 0.054\,\mathrm{mJy}$ at 1.4, 5 and 15 GHz respectively. The simulated flux densities at this time are $S_{1.4} = 37.7\,\mathrm{mJy}$, $S_5 = 33.3\,\mathrm{mJy}$ and $S_{15} = 29.4\,\mathrm{mJy}$ at 1.4, 5 and 15 GHz respectively. The calculated results are obviously much smaller than the simulated results. This is because the cluster wind is interacting with the surrounding material, ablating and mass-loading material from the denser clumps. To make the calculated results match the simulated results, the cluster mass-loss rate would need to be of the order of $10^{-4}\,\mathrm{M_\odot\,yr^{-1}}$. This is over 100 times greater than simulated. However, as can be seen from the top left panel in Fig. 2.12 and the discussion in Section 2.3.5, a mass-loss rate of $10^{-4}\,\mathrm{M_\odot\,yr^{-1}}$ is in excellent agreement with the "mass-loading" factor due to the ablation of the dense clumps.

Throughout the first 4 Myrs whilst all three of the stars are on the MS the

radio spectrum of the cluster remains optically thin, with $\alpha \approx -0.100 \pm 0.002$, which is consistent with a thermal source (see the red line in Fig. 4.6 for the spectrum during the cluster MS).

4.3.1.1 Comparisons between Radio and X-ray Emission

Figs. 4.4 and 4.5 show the soft (0.1–0.5 keV) and hard (2.5–10.0 keV) X-ray emission respectively for the cluster and compare it to the 1.4 GHz radio emission during the initial breakout phase.

The top left panel of Fig. 4.4 shows a synthetic image of the 1.4 GHz emission from the cluster at $t = 0.06$ Myrs. The asymmetrical expansion is immediately apparent, as gas is only leaking from the right of the cluster. However, the edge of the GMC clump is illuminated as hot wind material is carving out of the clump. This feature is not seen in the 0.1–0.5 keV (top right panel in Fig. 4.4) or the 2.5–10.0 keV (top right panel in Fig. 4.5) X-ray emission. Both the X-ray and radio emission are brightest at the cluster centre, where the cluster wind is partially confined. There is a high degree of spatial coincidence between both types of emission. However, there appears to be a thin shell of radio emission surrounding the regions of soft X-ray emission at all points throughout the early cluster MS. This traces the ambient gas which has been swept-up by the cluster wind after its blowout of the GMC clump.

An interesting feature is a small knot of emission which is apparent at the top of the X-ray lobe (see the top right panel in Fig. 4.4, and slightly fainter in the top right panel in Fig. 4.5), which is seen in the radio as a small blister on the surface of the expanding lobe of leaking gas. This feature is coincident with the radius of the GMC clump, which is also seen in the radio, and it is therefore

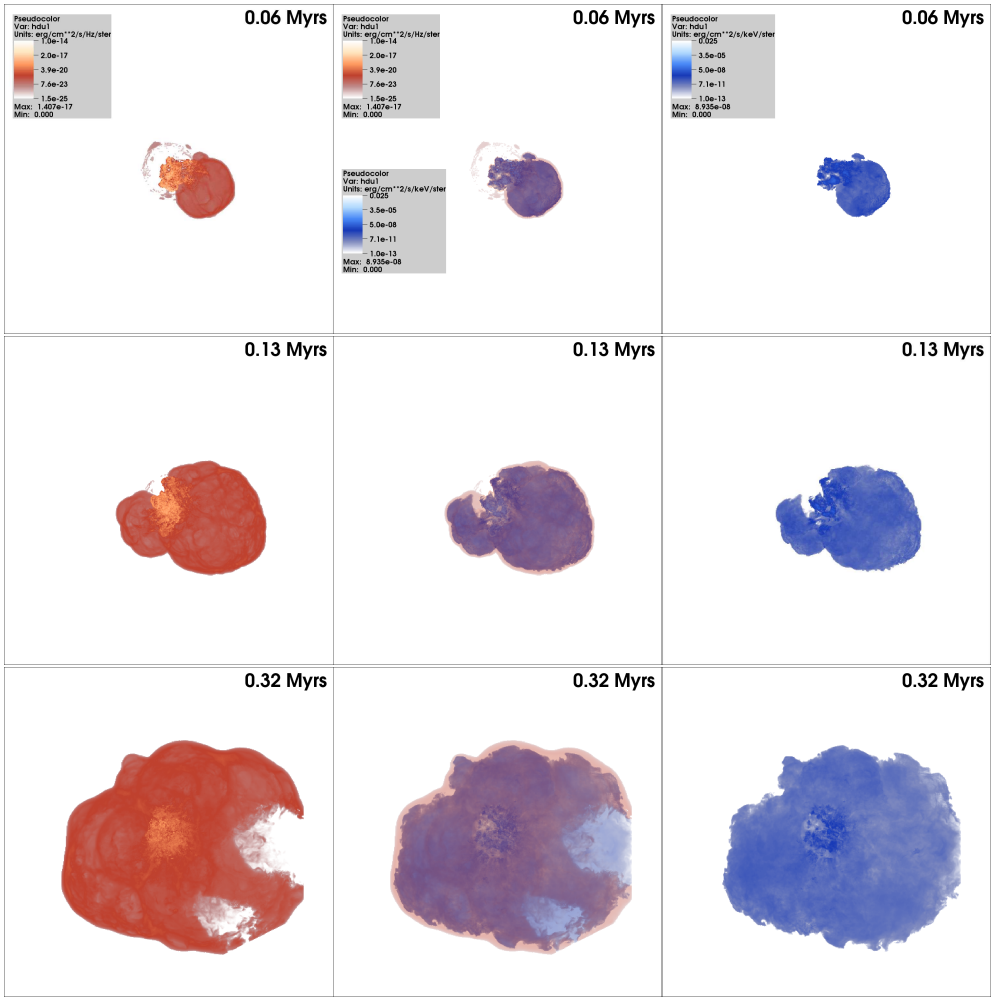

Figure 4.4: Synthetic radio and X-ray images for the cluster during the initial breakout at t = 0.06, 0.13 and 0.32 Myrs. [Left] shows the radio 1.4 GHz emission, [Right] shows the soft X-ray 0.1–0.5 keV emission and [Middle] shows the two overlaid.

possible that this could be an area where hot gas is breaking free of the clump into the surrounding homogeneous ISM.

The 1.4 GHz emission at t = 0.13 Myrs, as discussed earlier and shown in Fig. 4.2 is compared with the X-ray emission at this time in the middle rows of Figs. 4.4 and 4.5. The central cluster is still bright in both X-rays and radio, and the two types of emission are again spatially coincident, with a thin shell of

radio emission surrounding the soft X-rays. The GMC clump radius is also still visible in the radio, although the hot cluster wind has breached this radius in all but one small region. The hard X-rays do not fill the entirety of the bubble interior: rather they are evident where the wind material undergoes shocks (see Section 3.3.1).

At $t = 0.32$ Myrs the cluster wind has escaped the GMC clump in all directions, and the expansion of the bubble is more spherical. An odd feature is evident in the radio emission where there are two visible gaps to the bottom right of the bubble which isn't seen in X-rays (see the bottom row of Fig. 4.4). This is likely due to that part of the shell leaving the grid. Once the shell has left the grid in all directions this feature disappears and the morphology becomes more filamentary, reflecting the interactions of the cluster wind with the densest clumps (see the top row of Fig. 4.7).

4.3.2 RSG and WR Phases for the 35 $M_\odot$ star

At $t = 4.0$ Myrs the most massive star becomes a RSG. At this time the mass-loss rate of the star increases, but the wind velocity decreases, such that the cluster mass-loss rate and average wind velocity change from $9\times10^{-7}\,M_\odot\,yr^{-1}$ and $2000\,km\,s^{-1}$ to $\sim\ 10^{-4}\,M_\odot\,yr^{-1}$ and $136\,km\,s^{-1}$. The resulting slow and dense cluster wind causes the radio flux density to increase by approximately two orders of magnitude, from around $S_{1.4} = 34.9$ mJy at $t = 3.99$ Myrs to $S_{1.4} = 3435.9$ mJy at $t = 4.02$ Myrs. The radio flux density then continues to increase throughout the 100,000 year duration of the RSG phase, rising to a maximum of $S_{1.4} = 5687.1$ mJy at $t = 4.09$ Myrs.

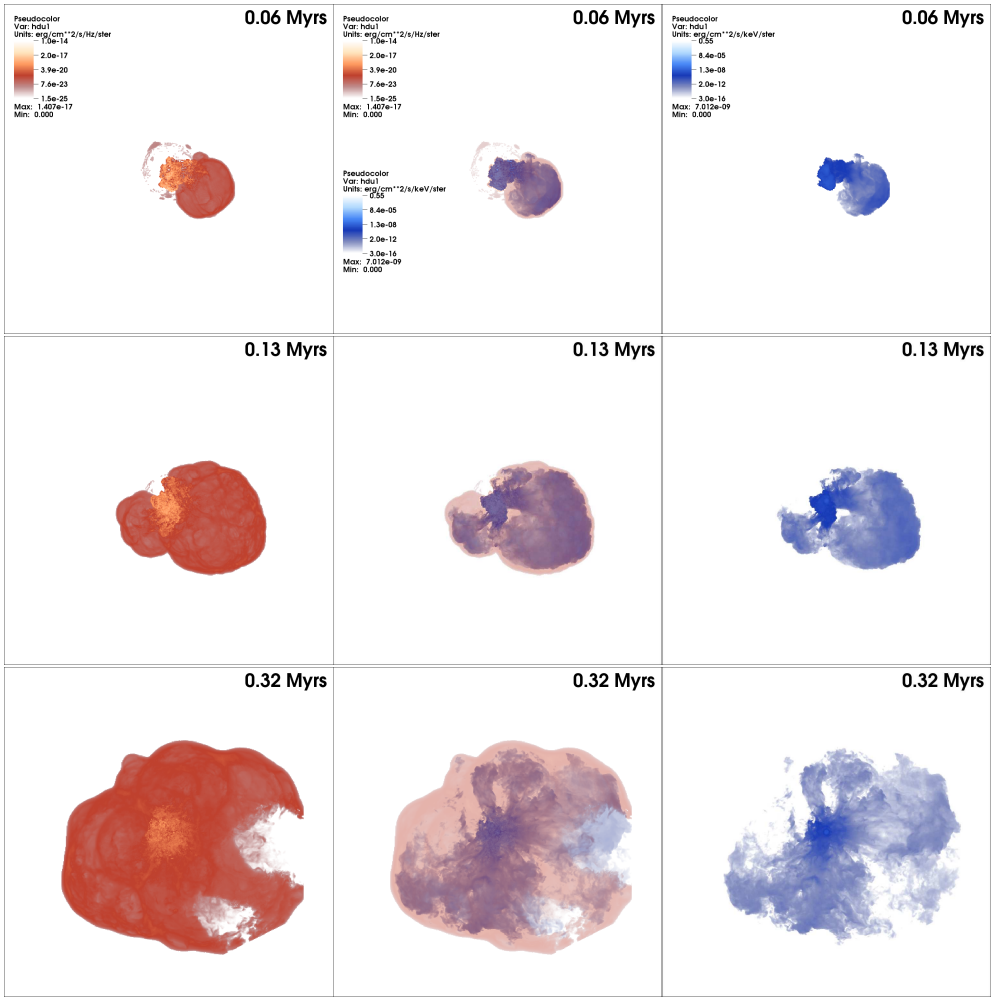

Figure 4.5: Synthetic radio and X-ray images for the cluster during the initial breakout. [Left] shows the radio 1.4 GHz emission, [Right] shows the hard X-ray 2.5–10.0 keV emission and [Middle] shows the two overlaid.

The evolving radio spectra of the cluster during the RSG is shown in Fig. 4.6. The spectrum shortly before (solid red line) the most massive star evolves off the MS branch and shortly after it becomes a WR (pink dotted line) are also shown for comparison. The figure shows a clear jump in flux density from the MS dominated cluster wind to the RSG enhanced wind. The spectrum also gains an optically thick component during this RSG-enhanced phase, with the

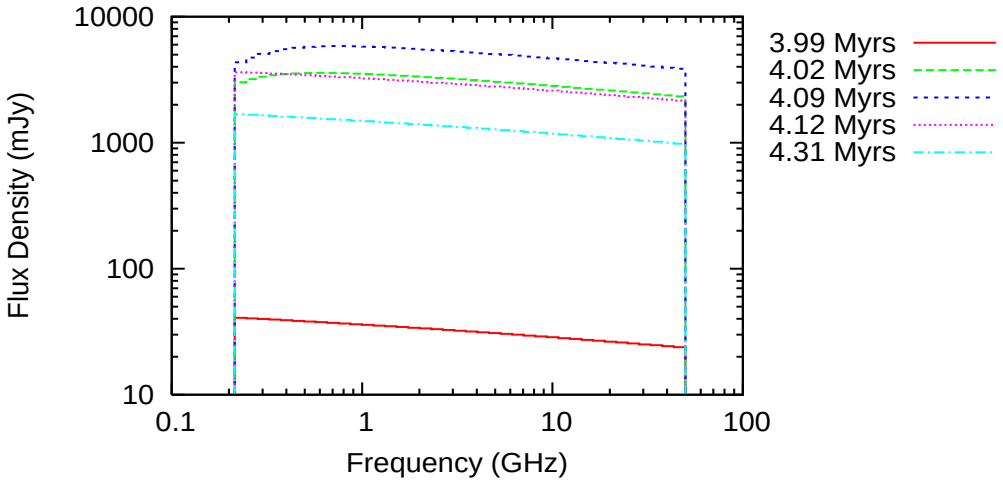

Figure 4.6: The evolving radio spectra of the cluster as the most massive star undergoes the transition from the MS (red solid line) to the RSG phase (green long-dashed and blue short-dashed lines) and then to the WR phase (pink dotted and light blue dot-dashed lines).

turnover at around 0.7 GHz. The optically thin component of the spectra has $\alpha \approx$-0.106 $\pm$ 0.002, which remains consistent with a thermal source.

At t = 4.06 Myrs the cluster wind velocity is 136 km s^{-1} and the cluster mass-loss rate is $\dot{M}_{cl} = 1 \times 10^{-4}$ M$_{\odot}$ yr^{-1} due to the contribution of the dense, slow RSG wind (see Table 2.1). Using C$_1$ = 1.16, 0.66 and 0.40, as discussed earlier, the flux density of the cluster is calculated to be S$_{1.4}$ = 254.2 mJy, S$_5$ = 541.2 mJy and S$_{15}$ = 1045.8 mJy at 1.4, 5 and 15 GHz respectively. The simulated flux densities at this time are S$_{1.4}$ = 5368.8 mJy, S$_5$ = 4765.3 mJy and S$_{15}$ = 4183.4 mJy at 1.4, 5 and 15 GHz respectively. The cluster mass-loss rate required to match the calculated results to the simulated results is 3×10^{-4}–1×10^{-3} M$_{\odot}$ yr^{-1}. This is 3–10 times greater than the actual mass-loss rate, and can be attributed to the ongoing mass-loading of the cluster wind and its inhomogeneous (clumpy) nature.

At t = 4.1 Myrs the 35 M$_{\odot}$ star evolves further to become a WR star. At this

time, the radio flux density begins to decrease from the maximum attained during the RSG phase, although it remains considerably higher than that observed during the MS (see the purple dotted and light-blue dot-dashed lines in Fig. 4.6). The radio spectrum returns to being optically thin over the whole spectrum during this phase, and the radio flux density evens off at $S_{1.4} = 1373.0\,\mathrm{mJy}$.

At $t = 4.31\,\mathrm{Myrs}$, whilst the most massive star is still a WR and the two lower mass stars are on the MS, the cluster wind velocity is $2000\,\mathrm{km\,s^{-1}}$ and the cluster mass-loss rate is $\dot{M}_{cl} = 2.04 \times 10^{-5}\,\mathrm{M_{\odot}\,yr^{-1}}$ (see Table 2.1 for the individual stellar parameters). Using $C_1 = 1.16$, 0.66 and 0.40, as discussed earlier, the flux density of the cluster is calculated to be $S_{1.4} = 0.84\,\mathrm{mJy}$, $S_5 = 1.79\,\mathrm{mJy}$ and $S_{15} = 3.47\,\mathrm{mJy}$ at 1.4, 5 and 15 GHz respectively. The simulated flux densities at this time are $S_{1.4} = 1443\,\mathrm{mJy}$, $S_5 = 1274\,\mathrm{mJy}$ and $S_{15} = 1124\,\mathrm{mJy}$ at 1.4, 5 and 15 GHz respectively. The cluster mass-loss rate required to match the calculated results to the simulated results is 1.6×10^{-3}–$5.4 \times 10^{-3}\,\mathrm{M_{\odot}\,yr^{-1}}$. This is ∼75–260 times greater than the cluster mass-loss rate at this time. Interestingly, the mass-loading occurring at this time is found to be only ∼35 times the mass-loss rate of the cluster (see Fig. 2.12 and the discussion in Section 2.3.5). However, Equation 4.1 assumes that the stellar wind is smooth, spherically symmetric and expanding at a constant velocity, which is not the case for the simulated cluster wind. This may be especially true for the WR phase of the most massive star, as the high momentum wind begins to sweep up the material deposited during the RSG-enhanced phase. Thus the clumpy nature of the WR-enhanced cluster wind will increase the flux density above what would be expected from Equation 4.1.

4.3.2.1 Comparisons between Radio and X-ray Emission

Figs. 4.7 and 4.8 show the soft (0.1–0.5 keV) and hard (2.5–10.0 keV) X-ray emission respectively for the cluster, with comparable 1.4 GHz radio emission, during the three evolutionary stages of the most massive star.

The top row of Figs. 4.7 and 4.8 shows the cluster at $t = 2.53$ Myrs, at which point all three of the stars are on the MS. The radio flux density at this time is $S_{1.4} = 37.7$ mJy, $S_5 = 33.3$ mJy and $S_{15} = 29.2$ mJy at 1.4 GHz, 5 GHz and 15 GHz emission respectively. Spatially, the radio and soft X-ray emission are well matched (Fig. 4.7). The hard X-ray emission traces the reverse shock of the bubble, and some of the channels carved by the hot cluster wind are evident (Fig. 4.8, see Chapter 3 for more details). The central cluster is now only obvious in hard X-rays. The structure of the emission is now much more filamentary and diffuse than in the early evolution of the cluster, as the cluster wind has filled the computational volume.

At $t = 4.06$ Myrs (second row in Figs. 4.7 and 4.8) the most massive star is approximately midway through its RSG phase. At this time, the X-ray luminosity in all of the bands studied massively decreases, to the point where there is virtually no emission evident in the hard regime, and only faint emission in the soft regime. However, the radio emission at this time actually increases due to the much higher wind density, and as already mentioned the spectrum gains an optically thick component (c.f. Fig. 4.1 for the radio lightcurve and Fig. 4.6 for the spectra during the RSG). The radio flux density at this time is $S_{1.4} = 5363.8$ mJy, $S_5 = 4765.3$ mJy and $S_{15} = 4183.4$ mJy for 1.4 GHz, 5 GHz and 15 GHz emission respectively. The synthetic images indicate that the increase in emission is lim-

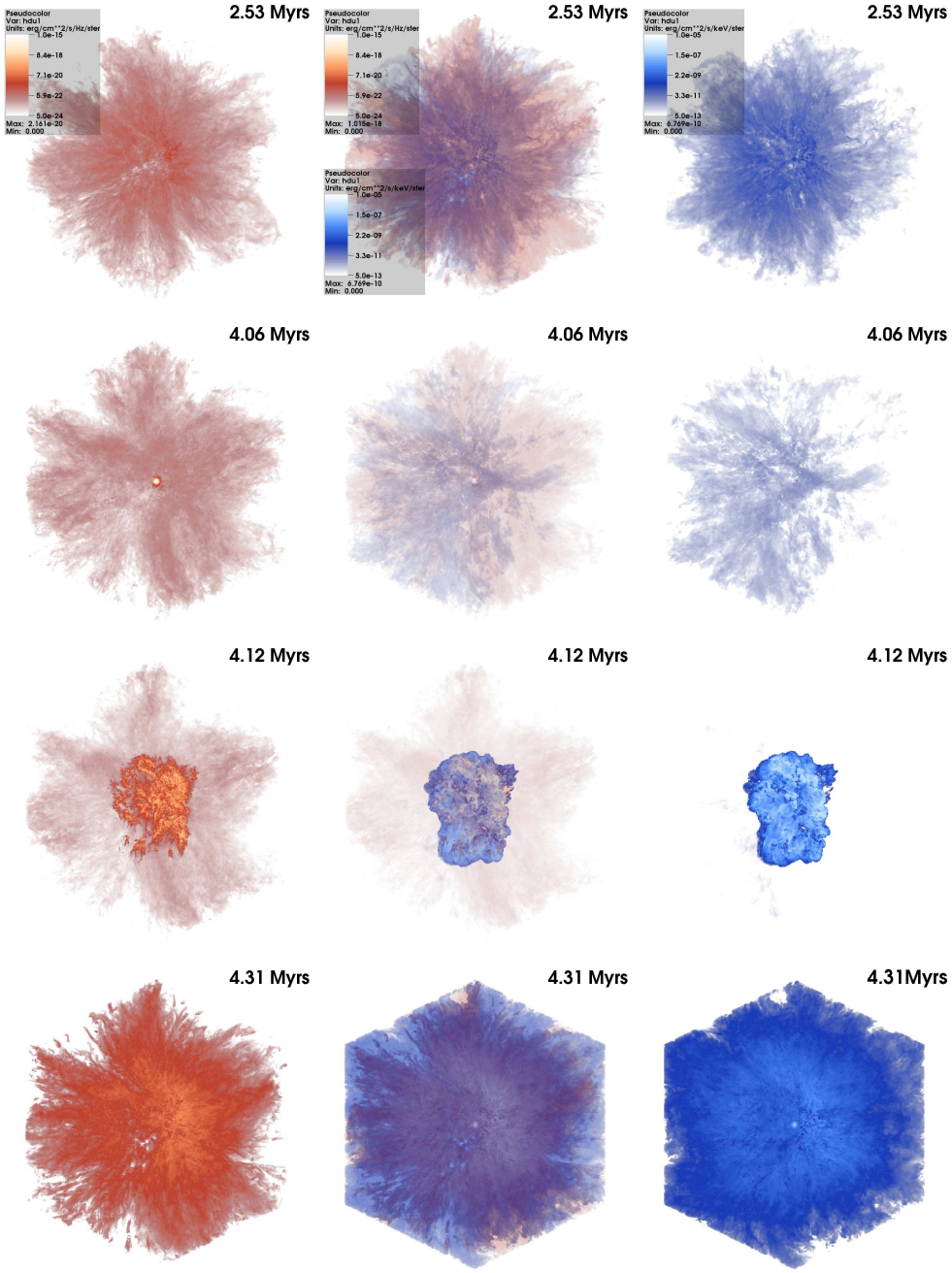

Figure 4.7: Synthetic radio and X-ray images for the cluster throughout the simulation at t = 2.53, 4.06, 4.12 and 4.31 Myrs. [Left] shows the radio 1.4 GHz emission, [Right] shows the soft X-ray 0.1–0.5 keV emission and [Middle] shows the two overlaid.

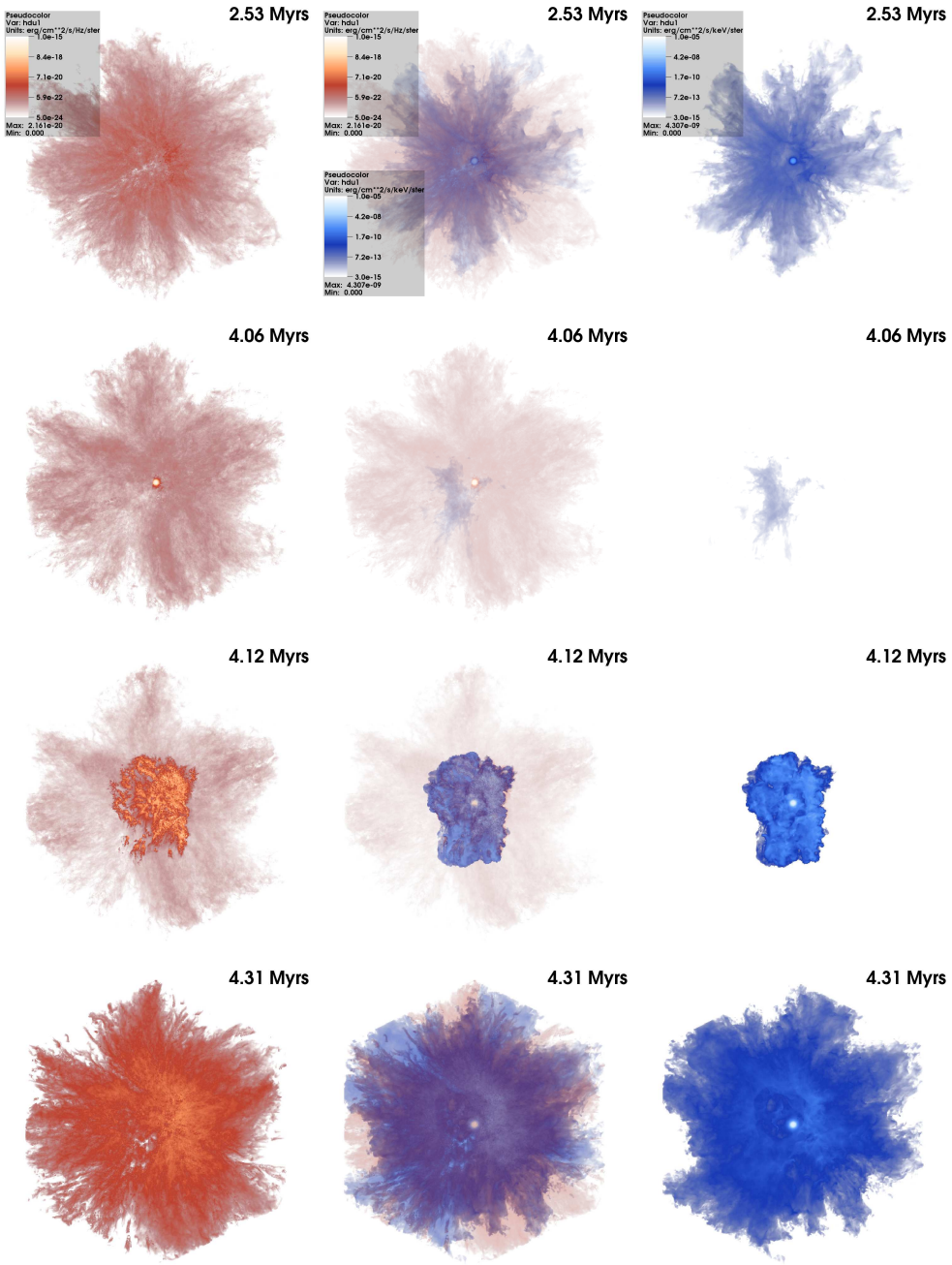

Figure 4.8: Synthetic radio and X-ray images for the cluster throughout the simulation at t = 2.53, 4.06, 4.12 and 4.31 Myrs. [Left] shows the radio 1.4 GHz emission, [Right] shows the hard X-ray 2.5–10.0 keV emission and [Middle] shows the two overlaid.

ited to an intense brightening in the cluster centre, and that the more diffuse emission filling the simulation volume actually becomes fainter. This highlights the extent of the RSG-dominated cluster wind at this time.

At $t = 4.12\,\mathrm{Myrs}$ (third row in Figs. 4.7 and 4.8) the most massive star has evolved further to become a WR. At this time the X-ray emission in both the hard and soft bands increases dramatically as the powerful WR-enriched wind creates further shocks in the hot gas and increases its density. The radio emission decreases slightly from the bright RSG-enriched phase, but is still more luminous than the emission observed whilst all three stars are on the MS, with $S_{1.4} = 3152.7\,\mathrm{mJy}$, $S_5 = 2788.1\,\mathrm{mJy}$ and $S_{15} = 2463.1\,\mathrm{mJy}$ for $1.4\,\mathrm{GHz}$, $5\,\mathrm{GHz}$ and $15\,\mathrm{GHz}$ emission respectively. The brightest emission still comes from the centre of the cluster at this time, as the high-momentum WR-enriched wind expands into the cluster environs. The radio emission is spatially coincident with both the soft and hard X-ray emission. The third row nicely illustrates the formation and early growth of a WR nebula. It is clear that the nebula is lightly structured, reflecting the inhomogeneous nature of the environment into which it expands.

By $t = 4.31\,\mathrm{Myrs}$ the most massive star is almost at the end of its WR phase (bottom row in Figs. 4.7 and 4.8). As shown in Fig. 4.1, the radio flux density decreases over the course of the WR phase, with $S_{1.4} = 1442.6\,\mathrm{mJy}$, $S_5 = 1273.7\,\mathrm{mJy}$ and $S_{15} = 1123.6\,\mathrm{mJy}$ for $1.4\,\mathrm{GHz}$, $5\,\mathrm{GHz}$ and $15\,\mathrm{GHz}$ emission respectively at this time. The soft X-ray emission now completely fills the simulation volume (its cube is clearly evident), whilst the extent of the hard X-ray emission is approximately the same as the radio emission. The cluster centre is very bright in hard X-rays, and the position of the reverse shock is again visible in this energy band. The radio emission is brightest in the centre, with the flux density trailing

off towards the edges.

4.3.3 The First Supernova

At t = 4.40 Myrs the most massive star explodes, inputting $10\,M_{\odot}$ of material and 10^{51} ergs of energy into the centre of the GMC clump. At this time both of the other stars remain in their MS phases. The collisionally ionized free-free radio emission following the SN explosion is calculated from our simulation. WE assume that the electrons and ions in the shock heated gas are in temperature equilibrium (i.e. $T_e = T_i$). We do not calculate synchrotron emission because our simulation does not model particle acceleration. This component may be dominant, although the free-free emission is enhanced by the clumpy nature of the surrounding gas.

The radio lightcurve immediately following the supernova explosion and subsequent expansion of the shockwave is shown in Fig. 4.9. As discussed in Section 3.3.4, to model the SN explosion 10^{51} ergs of thermal energy and $10\,M_{\odot}$ of material are placed at the centre of the simulation at the position of the stellar cluster. This gas is overpressured compared with the wind material, and so rapidly expands into the surrounding medium. Whilst this creates the required response on the surrounding medium, it is not typical of actual SN explosions where the ejecta rapidly cools through adiabatic expansion which would make it considerably cooler than the simulated ejecta at comparable times. For this reason, the small peak in the radio seen in Fig. 4.9 at t = 4.40 Myrs should be ignored as it is an artifact of the initial conditions used. This peak is short-lived, with the radio flux density of the hot ejecta dropping rapidly to just above pre-SN levels

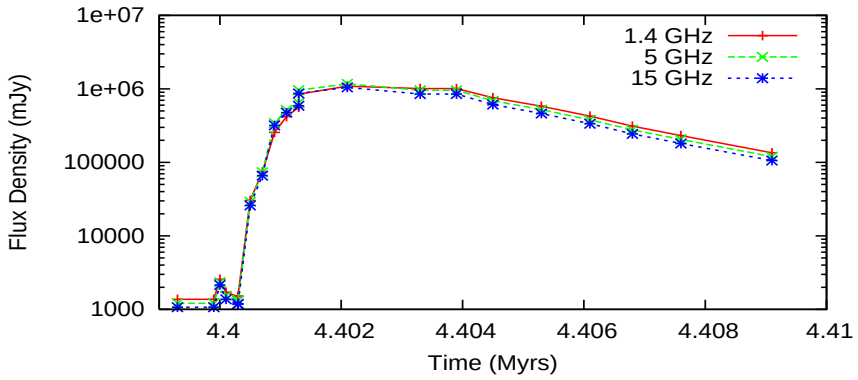

Figure 4.9: The radio lightcurve for the cluster during the SN of the most massive star. The black dotted line indicates 900 yrs after the explosion, at which point X-ray emission from interactions with the surrounding clump material is dominant. The red solid line, green dashed line and blue dotted line tracks the 1.4 GHz, 5 GHz and 15 GHz radio emission respectively.

as it starts to expand and its density decreases. Fig. 4.9 shows that t ∼300 yrs after the explosion the radio flux density begins to increase again. This increase is caused by the SN ejecta running into the dense clouds near the cluster which have so far avoided destruction by the cluster wind. The dotted line indicates 900 yrs after the explosion, which is the time identified in Chapter 3 when the X-ray luminosity is dominated by interactions of the ejecta with the surrounding gas, and thus no longer affected by the explosion setup (see the middle panel, third row of Figs. 3.6– 3.8).

It is interesting to note that the 5 GHz and 15 GHz emission briefly increases above the 1.4 GHz emission from 900 to 1300 years after the explosion, with $S_{1.4} = 2.6\times10^5$ mJy, $S_5 = 3.4\times10^5$ mJy and $S_{15} = 3.2\times10^5$ mJy for 1.4 GHz, 5 GHz and 15 GHz emission respectively at t = 4.4009 Myrs (see the dotted line in Fig. 4.9). After this time, the 1.4 GHz emission increases above the 15 GHz emission, but remains marginally lower than the 5 GHz emission until t = 4.4021 Myrs. This indicates that the spectrum of the cluster begins to flatten approximately 1300 yrs

after the explosion, and that the emission is transitting from optically thick to optically thin (see Fig. 4.13).

Synthetic radio images at 1.4 GHz during the explosion are shown in Fig. 4.10. The initial peak seen in the lightcurve is visible as a bright central spot of emission when the star first explodes. This is a consequence of the way the explosion is implemented, as discussed earlier. As the hot ejecta expands outwards the bright emission at the centre of the cluster begins to fade, although it is still noticeably higher than the pre-SN levels. The interaction of the expanding shockwave with the surrounding material is visible from $t = 4.4005$ Myrs (see right panel, second row of Fig. 4.10), slightly earlier than observed in X-rays. Fig. 4.11 compares both the soft 0.1–0.5 keV X-ray emission (top row) and the hard 2.5–10.0 keV X-ray emission (bottom row) with the 1.4 GHz radio emission at $t = 4.4009$ Myrs, when bowshock interaction dominates both the radio and X-ray emission. The two regimes are again spatially coincident, especially between the 1.4 GHz and 0.1–0.5 keV emission. The hard X-ray emission appears to be slightly more extended than the emission seen at the other energies, although this may be due to the smoothed nature of the emission. Unlike with the evolution of the SNR seen in X-rays shown in Figs. 3.6– 3.8, the structure of the shockwave is not observed in radio emission. Instead, the expansion of the blastwave is seen as a brightening of the pre-existing filamentary structure. As such, there is a region towards the south of the image which is faint in radio emission pre-SN and which also shows relatively little brightening as the shockwave expands outwards (see for example the bottom row of Fig. 4.10). There is a similar region of relatively faint emission seen in the X-ray (see for example the bottom row of Fig. 3.6).

The time evolution of the radio spectrum during the period of the first SN

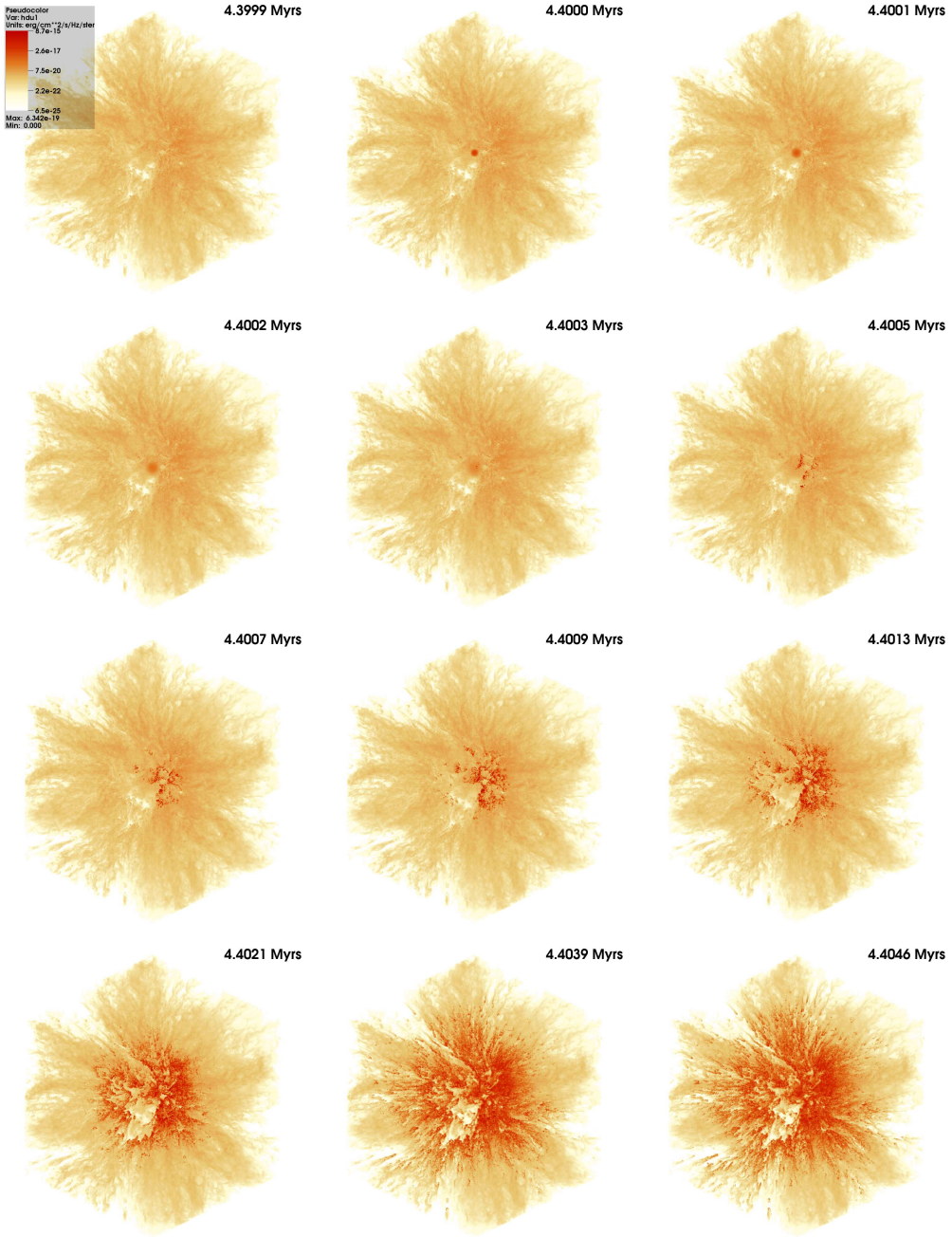

Figure 4.10: Synthetic radio images at 1.4 GHz during the first 4600 years after the most massive star explodes. The explosion occurs at t = 4.4000 Myrs (middle panel, top row).

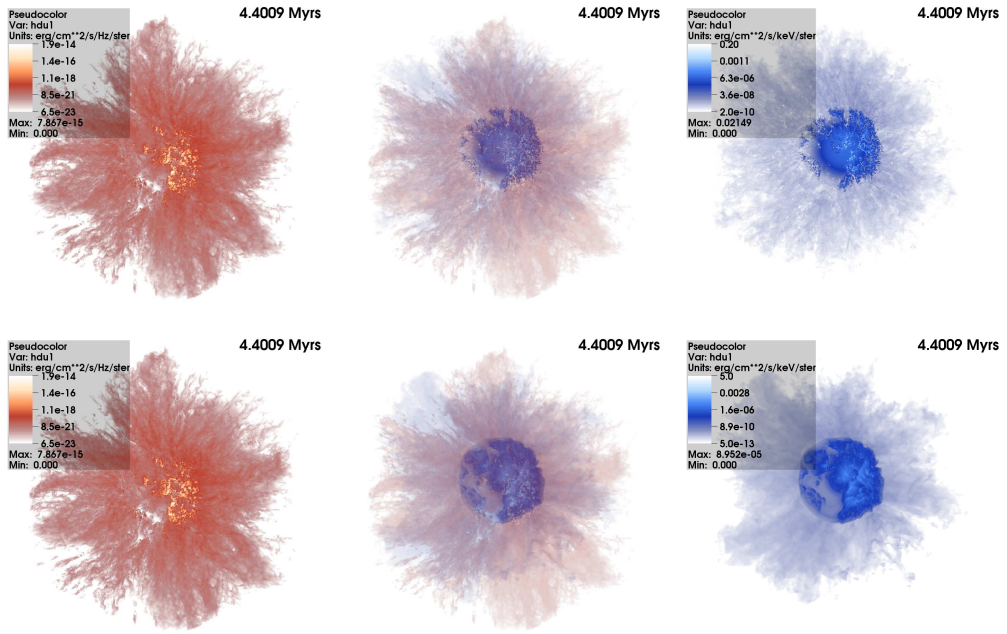

Figure 4.11: Synthetic radio and X-ray images for the cluster at t = 4.4009 Myrs when bowshock emission begins to dominate. The top row shows the soft 0.1–0.5 keV X-ray emission. The bottom row shows the hard 2.5–10.0 keV X-ray emission. [Left]: shows the 1.4 GHz radio emission, [Right]: shows the X-ray emission and [Middle]: shows the two overlaid.

explosion is shown in Fig. 4.12. The solid red line represents the time immediately after the most massive star explodes, and corresponds to the small peak seen in the lightcurve in Fig. 4.9. The subsequent green long-dashed line shows the dip in radio flux density ∼300 yrs after the initial explosion. At both these times the radio spectrum is optically thin. The blue short-dashed and purple dotted lines show the radio emission from 900–1300 years after the explosion, revealing the massive increase in flux density caused by the shockwave interacting with the surrounding material. As discussed earlier, during this time period the 5 and 15 GHz emission is higher than the 1.4 GHz emission. This is caused by the spectrum becoming optically thick. The light-blue dot-dashed line shows the

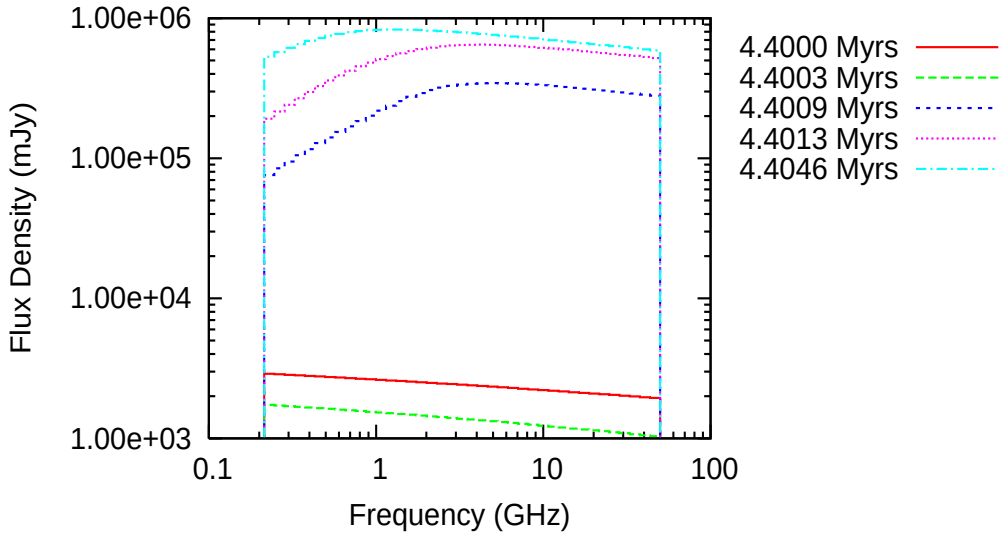

Figure 4.12: The evolving radio spectra of the cluster as the most massive star undergoes a SN explosion. The star explodes at t = 4.4000 Myrs (solid red line). The blue short-dashed line is ∼900 yrs after the explosion when bowshock emission becomes dominant and the light blue dot-dashed line is ∼4600 yrs after the explosion when the ejecta begins to leave the grid.

radio spectrum 4600 yrs after the explosion, at which point the hot ejecta begins to leave the grid. The spectrum begins to flatten around this time, although there is still an optically thick turnover at low frequencies. The turnover point varies with time, and the frequency at which the turnover occurs can be seen in Fig. 4.13. The radio spectrum first exhibits an optically thick component at t = 4.4005 Myrs. The turnover frequency reaches a peak value of $\nu \sim 5$ GHz at t = 4.4009 Myrs, before slowly declining below $\nu \sim 1$ GHz.

4.3.4 Further Evolutionary Stages

After the explosion of the 35 $M_\odot$ star, the remaining two stars continue in their MS phase for a further 0.1 Myrs, at which point the most massive remaining star (32 $M_\odot$) begins to follow the same evolutionary path as its predecessor. At

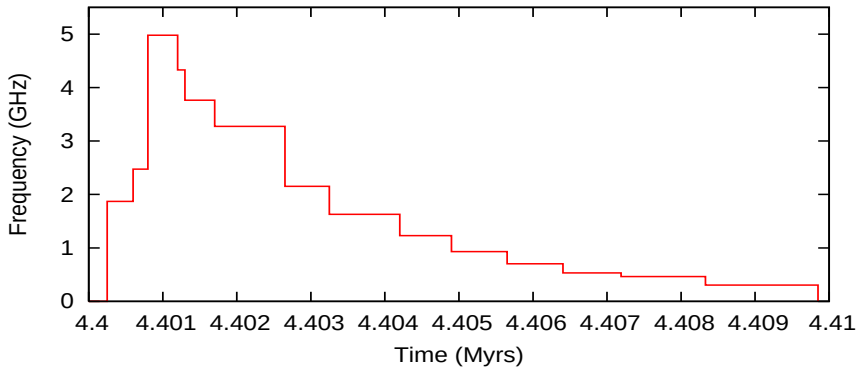

Figure 4.13: The turnover frequency between optically thin and optically thick gas during the first SN explosion.

$t = 4.5\,\mathrm{Myrs}$ it evolves to a RSG and at $t = 4.6\,\mathrm{Myrs}$ it becomes a WR star. The radio lightcurve shown in Fig. 4.1 shows a similar pattern to the evolution of the $35\,M_\odot$ star discussed previously, in that the radio flux density increases once the slow and dense RSG wind contributes to the cluster wind, then increases further once the star becomes a WR, before undergoing a slow decline throughout that phase. However, as the $32\,M_\odot$ star evolves off the MS so shortly after the first supernova, it is difficult to determine exactly to what extent the flux density during this RSG-enhanced phase is affected by the decrease caused by the SN blastwave leaving the grid. The flux density in this phase is comparable to that seen in the previous RSG phase, despite the loss of one wind source, and the associated reduction in the momentum and energy flux of the cluster wind. The $32\,M_\odot$ star explodes at $t = 4.9\,\mathrm{Myrs}$, imparting a further $10\,M_\odot$ of ejecta material and 10^{51} ergs of energy into the simulation. $0.1\,\mathrm{Myrs}$ after this explosion the final remaining star ($28\,M_\odot$) begins the post-MS evolutionary behaviour outlined previously.

4.4 Comparisons to Observations

4.4.1 Young Massive Stellar Clusters

A comparison will now be made between the model and observations of M 17 and Westerlund 1. For a fuller literature review of young massive stellar clusters from which thermal radio emission has been detected see Table 4.2 and Appendix A.

4.4.1.1 M 17

An introduction is made to M 17 in Sections 1.3.3.2 and 3.5.1.1. A fuller review of this cluster is made in Appendix A, and it will be briefly summarized here. M 17 is a young (∼0.5 Myrs, Chini & Hoffmeister, 2008; Hoffmeister *et al.*, 2008) blister HII region ionized by the stellar cluster NGC 6618, thought to contain approximately 14 O-stars (Broos *et al.*, 2007). It is located approximately 1.55 kpc away.

Rodríguez *et al.* (2012) observed M 17 at 4.96, 8.46 and 22.46 GHz using the *JVLA* (Jansky Very Large Array) in the highest angular resolution A configuration. They revealed the presence of 38 compact radio sources, 19 of which have stellar counterparts detected in infrared, optical or X-rays, in addition to the hyper-compact (HC) cometary HII region, M 17 UC1. This HC HII region was first discussed by Felli *et al.* (1980), who estimated a density $n_e > 10^6\,\mathrm{cm}^{-3}$ and an electron temperature $T_e > 25{,}000\,\mathrm{K}$. It is approximately spherical, with a diamter of $\sim 0.006\,\mathrm{pc}$, and is embedded in the molecular cloud adjacent to the SW of the M 17 region (Johnson *et al.*, 1998). There is widespread evidence of massive star formation occuring within ∼0.4 pc of UC1 (Genzel & Downes, 1977; Harper *et al.*, 1976; Knowles *et al.*, 1976). This region is much more compact,

Table 4.2: The properties of young massive stellar clusters from which thermal radio emission has been detected. The clusters are ordered roughly by age. Further details and references for values in this table can be found in Appendix A.

Cluster/Region Name	Age (Myrs)	Distance (kpc)	Thermal/ NT	Frequency of Obs. (GHz)	Flux Density (mJy)	No. of sources	Spectral Index (α)
Omega (M 17)	$\sim$0.5	2.0	T	4.96, 8.46, 22.46	0.04, 0.12, 0.19	38 (19)	0.8±0.2
Westerlund 2	$\lesssim$2	2.85±0.43	T	5.5, 9.0	146±12, 103±30	6 (1)	$\sim$0
Rosette	2	1.55	T	1.41, 4.75	420±70, 350±30		-0.15±0.11
Hourglass	1–2.5	1.3	T + NT	5.0	4.03	10	
Arches	2–2.5	8	T + NT	4.9, 8.5	$>(0.003, 0.003)^{(+)}$	8 (7)	0.3–0.6
NGC 2024 (Flame)	0.3–3	0.415	T	1.41, 2.7, 5.0, 15.35	64.9, 65.9, 63.0, 58.6	25 (21)	
Orion (M 42)	3	0.49	T	23	400	21 (20)	1.19±0.12
Quintuplet	3.5–4	8	T (+NT?)	4.9, 8.5, 22.5, 43.4	$>0.01^{(+)}$	10 (7)	$\sim$-0.1–+2.0
NGC 3603	1–4	7±1	T + NT	8.8	25	10–20	-0.2±0.2
Westerlund 1	4–5	4–5	T + NT	1.4, 2.2, 4.8, 8.6	0.67, 0.52, 0.46, 0.42	18	-0.26±0.07
NGC 3576		2.8±0.3	T	8.8	71±1		

Notes: The frequencies at which these observations were taken are quoted from smallest to largest, as shown in column 5. The flux densities in column 6 are ordered to match the corresponding frequency at which they were observed. The value in brackets in column 7 are the number of compact sources detected which have stellar counterparts. Values in column 6 marked with a (+) represent stellar clusters where the total integrated flux over the entire region is not given, and are therefore the summation of the individual fluxes of the radio sources detected.

and therefore denser, than the region simulated.

Rodríguez *et al.* (2012) measure the flux density of this HII region to be 44, 107 and 194 mJy at 4.96, 8.46 and 22.46 GHz respectively. At t = 0.44 Myrs the simulated flux densities are $S_{4.98} = 191.1$ mJy, $S_{8.71} = 179.75$ mJy and $S_{23.16} = 160.51$ mJy. These results are surprisingly similar, given the greater number of O-stars detected in M 17. However, as it is such a young cluster it is unlikely that any of the stars have yet exploded as a SN, and the winds will not yet have had much of an opportunity to expel all of the gas from the surroundings. The free-free emission may therefore be comparable to that simulated.

Rodríguez *et al.* (2012) also estimate the spectral index of the M 17 UC1, to range from values of ∼2 (optically thick emission) near the head of the cometary nebula to values of ∼-0.1 (optically thin emission) near the tail. This result suggests that at least in this HC HII region the intermediate values of ∼1 for the spectral index comes from a gradient in optical depth across the face of the nebula.

4.4.1.2 Westerlund 1

Westerlund 1 (hereafter W 1) is the most massive stellar cluster known in the Galaxy (Brandner *et al.*, 2008; Clark *et al.*, 2005). It contains a rich population of massive stars which include more than 20 WR stars (Crowther *et al.*, 2006), more than 80 OB stars, and short-lived transitional objects including luminous blue variables (LBVs) and red supergiants (RSGs). Estimates for its age range from 3.6±0.7 Myrs (Brandner *et al.*, 2008) to 5±1 Myrs (Lim *et al.*, 2013). Its distance remains somewhat uncertain, but estimates appear to be converging on the range 4–5 kpc (see Brandner *et al.*, 2008, and references therein). It is

therefore much bigger than M 17 and the simulated cluster.

Dougherty *et al.* (2010) find 18 radio-emitting cluster members in W1, with spectra containing both thermal and non-thermal components using *ATCA*. The brightest source in the cluster is W 9, which has a radio flux density of 55.4 mJy at 8.6 GHz, making it one of the most luminous radio stars. They also found the total radio flux from W1 to be 699, 523, 461 and 422 mJy at 1.4, 2.2, 4.8 and 8.6 GHz respectively. The resulting images of W1 at these frequencies is shown in Fig. 4.14. The extended emission (with the fluxes of the radio stars subtracted from the total emission) is 426, 351 and 307 mJy at 2.2, 4.8 and 8.6 GHz respectively. At t = 4 Myrs, the most massive star in the simulation evolves to become a RSG. At this time the flux density drastically increases due to the high density, reaching 3436, 3313, 3046 and 2862 mJy at 1.4, 2.2, 5.0 and 8.7 GHz respectively. This is approximately 5–6 times higher than observed interferometrically in W1. However, if W1 is at a distance of 5 kpc its flux density will be reduced by a factor of 25 compared to the simulation. Thus W1 is intrinsically brighter than the simulated cluster, as expected given its greater size and mass.

Using the total fluxes quoted, the spectral index of W1 is -0.26±0.07, which is consistent with optically thin, thermal emission. For more information on W1 see Appendix A.

4.4.2 Young Core-Collapse SNRs

When the stars in the simulation explode they input 10 $M_{\odot}$ of material and 10^{51} ergs of energy into the surroundings. As discussed previously, the timeframe from which comparisons between simulations and observations can be made is

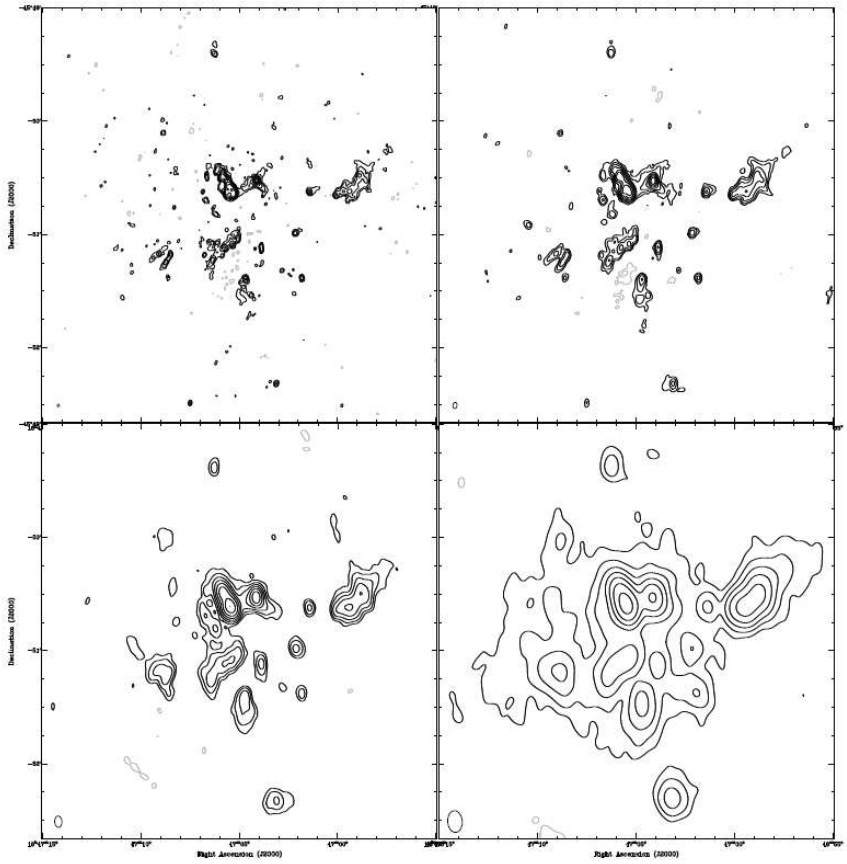

Figure 4.14: *ATCA* observations of W1 at 8.6 GHz (upper left), 4.8 GHz (upper right), 2.5 GHz (lower left) and 1.4 GHz (lower right). In each image, contour levels are -3, 3, 6, 12, 24, 48, 96, 192σ, where 1σ rms uncertainty is 0.006, 0.1, 0.2, 0.4 mJy beam^{-1} respectively at the four frequencies. These images were reconstructed using the nominal FWHM of the synthesized beam at each frequency, shown in the lower left-hand corner of each image. Note that these images are not corrected for the primary beam pattern. Taken from Dougherty *et al.* (2010).

narrow, with only SNRs which are of age 900<t<4600 being suitable.

In Section 3.5.2, comparisons were made with four young SNRs: 1E0102.2-7219, MSH 11-54, N132D and Puppis A. However, only the latter two SNRs have been studied in any detail in the radio regime. A comparison between these two SNe and the simulated results of the first SN explosion will now be made.

4.4.2.1 N132D

The SNR N 132D was previously introduced and discussed in Section 3.5.2.3 and will be briefly summarized here. N132D is located in the LMC, with an estimated age of 3150 yrs (Morse *et al.*, 1995) and an inferred progenitor mass of 30–35 $M_{\odot}$ (Blair *et al.*, 2000). The distance to the SNR is approximately 55 kpc (Hughes, 1987).

Despite being well studied at X-ray wavelengths, there are fewer studies in the radio. Dickel & Milne (1991) conducted observations of the remnant using the Australia Telescope and found the integrated flux density at 6 cm to be 1.6 Jy.

4.4.2.2 Puppis A

The SNR Puppis A was previously introduced and discussed in Section 3.5.2.4 and will be briefly summarized here. Puppis A is a nearby Galactic SNR with age estimates ranging from 3700–4450 yrs (Becker *et al.*, 2012; Winkler & Kirshner, 1985). It is estimated to be 1.3–2.2 kpc away (Reynoso *et al.*, 2003; Woermann *et al.*, 2000). Canizares & Winkler (1981) propose a progenitor mass of 25 $M_{\odot}$.

The integrated flux densities measured for Puppis A over a range of frequencies are shown in Table 4.3. The values range from 38±4 Jy at 8.4 GHz to 166±17 Jy at 1.44 GHz. This is substantially lower than the flux density from the simulated cluster, which is approximately 1000 Jy at a similar age of 4000 yrs. The spectral index over the remnant, based on the observations of Milne *et al.* (1993), is $\alpha = -0.6$ (Castelletti *et al.*, 2006), indicating that the emission is dominated by synchrotron and arises from a population of non-thermal particles.

Only moderate agreement between radio and X-ray emission has been ob-

Table 4.3: Integrated flux densities for Puppis A.

Frequency (GHz)	Flux Density (Jy)	Reference
8.4	38±4 Jy	Milne *et al.* (1993)
5.0	61±7 Jy	Milne (1971)
5.0	67±7 Jy	Milne & Hill (1969)
4.75	59±5 Jy	Milne *et al.* (1993)
2.7	78±12 Jy	Milne (1971)
2.65	92±14 Jy	Milne & Hill (1969)
1.52	118±10 Jy	Dubner *et al.* (1991)
1.44	166±17 Jy	Mathewson *et al.* (1962)
1.43	114±8 Jy	Castelletti *et al.* (2006)
1.41	129±20 Jy	Milne & Hill (1969)

served at a detailed level (Castelletti *et al.*, 2006). Small scale structures, such as filaments and knots, are poorly correlated with the observable radio features (see Fig. 7 in Castelletti *et al.*, 2006). This conclusion is not necessarily surprising since the X-rays have been associated with thermal radiation from the hot plasma, while the radio continuum is thought to arise from synchrotron emission from relativistic electrons. There is also little correlation between the optical and radio emission (Milne *et al.*, 1983).

4.5 Conclusion

This Chapter investigates the thermal radio emission from collisionally ionized gas in a massive young stellar cluster embedded in an inhomogeneous GMC clump, treating only the mechanical effects from winds and supernovae. The hydrodynamical model was previously simulated, with the results discussed in Chapter 2.

The X-ray emission produced by the cluster was discussed in Chapter 3. This Chapter explores the radio emission arising from that model and compares it with the simulated X-ray emission, and also with radio observations of actual clusters.

At very early times, when the wind material is still confined by the inhomogeneous GMC material the radio flux density is reasonably bright, at $S_{1.4} = 1261.5\,\mathrm{mJy}$. However, as the cluster wind begins to erode and ablate the surrounding GMC clump material it is no longer completely confined, and therefore hot gas is able to leak through the gaps in the expanding shell. This leads to a reduction in the radio flux density as the pressure within the bubble decreases. Once all of the low density material in the clump has been ablated away by the cluster wind the covering factor is mostly constant. The mass ablation rate is approximately constant too (see the top left panel of Fig. 2.12). Taken together these result in an approximately constant radio flux density of $S_{1.4} \sim 35\,\mathrm{mJy}$, $S_5 \sim 31\,\mathrm{mJy}$ and $S_{15} \sim 28\,\mathrm{mJy}$ at 1.4, 5 and 15 GHz respectively for the rest of the cluster MS phase.

At $t = 4.0\,\mathrm{Myrs}$ the most massive star becomes a RSG, resulting in a large increase in the radio flux density at all three of the frequencies studied. The flux density reaches $S_{1.4} \sim 5690\,\mathrm{mJy}$, $S_5 \sim 5050\,\mathrm{mJy}$ and $S_{15} \sim 4440\,\mathrm{mJy}$ at 1.4, 5 and 15 GHz respectively by the end of the RSG phase. The RSG-enhanced cluster wind deposits a lot of material into the simulation, with the increase in the radio flux density coming from a bright peak at the cluster centre. There is only $\sim 2\,\mathrm{M}_\odot$ of material above $10^5\,\mathrm{K}$ at this time (see Table 3.1). The spectrum of the cluster also gains an optically thick component during this phase, with the turnover occuring at about 0.7 GHz.

After a further 0.1 Myrs the most massive star evolves to become a WR. The

flux density decreases slightly during this phase, although it remains approximately 2 orders of magnitude higher than during the MS cluster wind. The amount of material above 10^5 K increases by an order of magnitude over that seen in the RSG-enriched phase. The high momentum WR-enhanced cluster wind sweeps up all the material which was deposited in the previous phase and heats it to high temperatures. The radio flux density by the end of the phase is $S_{1.4} \sim 1400$ mJy, $S_5 \sim 1235$ mJy and $S_{15} \sim 1100$ mJy at 1.4, 5 and 15 GHz respectively, which is about 40 times greater than when all three of the stars were on the MS. The spectrum of the cluster returns to being completely optically thin during this phase.

The predicted radio flux density for the cluster using the simulated variables is much lower than the results presented in the Chapter. This is attributed to the mass-loading, or entrainment, which is occurring throughout the simulation. Not only does this increase the effective mass-loss rate of the cluster, but it also makes the cluster wind very inhomogeneous and clumpy, which increases the emissivity. The degree to which this mass entrainment occurs was quantified in Section 2.3.5 and Fig. 2.12 in Chapter 2. The entrainment of this material into the wind effectively increases the mass-loss rate, and therefore increases the thermal radio emission. During the MS phase, once the covering factor of the cluster is mostly constant, the inferred mass-loss rate is ∼100–300 times greater than the cluster mass-loss rate, which is in excellent agreement with the MS mass-loading factor of 200-300. During the RSG phase of the most massive star this factor reduces to ∼3-10 times the cluster mass-loss rate, and during the WR phase of this star it is a factor of ∼75-260. However, the underlying assumptions for this formula require the stellar wind to be spherically symmetric, smooth, isothermal

and expanding at constant velocity. These assumptions are clearly not met by the simulation due to the inhomogeneous environment used.

The most massive star explodes as a core-collapse SN at $t = 4.40$ Myrs, ejecting $10\,M_\odot$ of material and 10^{51} ergs of thermal energy into the simulation. Again, we compare only the collisionally ionized free-free emission. Synchrotron emission is not calculated. Equal electron and ion temperatures in the shocked gas are supposed. Due to the way in which the explosion was initialised, the emission from the SN should only be trusted from the time at which the interaction of the blastwave with the surrounding medium dominates the emission. For the X-rays this was determined to be approximately 900 yrs after the explosion in Chapter 3, but radio emission from bowshocks first dominates at approximately 500 yrs after the explosion. The ejecta begins to leave the grid 4600 yrs after the explosion.

The simulated emission from the cluster during the wind-dominated phases matches reasonably well to observations of M 17. However, observations of various young massive stellar clusters are widely varied. The presence of evolved stars and SNRs has a notable effect on the flux densities, and therefore the age of the cluster must be considered.

The simulated emission from the cluster during the SNe is considerably higher than that found in Puppis A, despite the fact that non-thermal emission has not been considered in this work. It is possible that, if Puppis A is not the first remnant in the cluster or region, much of the surrounding material has already been cleared. This would result in less thermal emission than simulated due to the remnant expanding into a lower density environment. If the flux density shortly after the second SN explosion is considered, this is approximately 400 Jy, which is much closer to the values observed for Puppis A.

Clearly these young massive star forming regions are very complex, and more simulations need to be undertaken in order to ellucidate the physical processes occurring within them.

Chapter 5

Energy and Mass Input from a Massive Stellar Cluster

5.1 Introduction

In order to understand the role of stellar feedback in the formation and evolution of galaxies, an understanding of the how massive stars interact with their environments on smaller scales is required.

Freyer *et al.* have investigated the impact of a single massive star on its circumstellar environment in a series of papers (Freyer *et al.*, 2003, 2006). They determined that by the end of the lifetime of a $35\,M_{\odot}$ star only 1% of the total energy released by that star had been transferred to the circumstellar gas. From this 1%, 10% is kinetic energy of bulk motion, 36% is thermal energy, and the remaining 54% is ionization energy. Distinct emission features are produced as the fast WR wind expands into and sweeps up the material deposited by the slow RSG wind. They determined that almost all of the X-ray emission in the WR

stage comes from the swept-up shell of RSG wind swept up by the shocked WR wind rather than from the shocked WR wind itself.

Several authors have expanded on this by producing models of the mass and energy input from a cluster of stars into the ISM (e.g. Leitherer *et al.*, 1992; Smith, 2004; van Buren, 1985). Leitherer *et al.* (1992) compared the effects of both stellar winds and SNe in a starburst galaxy, and found that in general the winds were more important at higher metal content and during early phases of the starburst. However, Smith (2004) determined mass and energy input rates from young massive clusters which were significantly different to those found by Leitherer *et al.*, particularly during the WR phase of the massive stars. The results of these simulations will be heavily dependent on the input paramenters used, such as the mass-loss rates and wind velocities of the cluster constituents.

Mass segregation has been observed in many massive, young stellar clusters, including the Trapezium (Hillenbrand, 1997; Hillenbrand & Hartmann, 1998), NGC 6611 (Bonatto *et al.*, 2006), M17 (Jiang *et al.*, 2002), Westerlund 1 (Lim *et al.*, 2013), NGC 1333 (Lada *et al.*, 1996), NGC 2244 and NGC 6530 (Chen *et al.*, 2007). However, not all young clusters show signs of segreagtion. Er *et al.* (2013) performed a study of 18 embedded clusters in the galaxy using 2MASS to attempt to distinguish the degree of mass segregation, if any, present in each. They found that eleven of their sample of eighteen clusters were mass segregated and seven were not, and that the richer clusters tended to present mass segregation.

Understanding the physics of massive stars and how they interact with their environment will help to quantify the rate of energy and mass input into the ISM. In this Chapter hydrodynamical simulations of the interaction of stellar winds within a massive cluster are discussed. This extends the work presented

in the previous Chapters to smaller scales and allows an investigation of the development of a cluster wind. In Section 5.2 the details of the model and the method of calculating the cluster masses and positions are discussed. The results are presented in Section 5.3. Comparisons between the X-ray and radio emission originating from the cluster are made in Section 5.4. Section 5.5 summarizes and concludes this Chapter.

5.2 Simulations

5.2.1 The Numerical Model

The simulations in this Chapter detail a stellar cluster blowing into a homogeneous environment. The cluster is designed to be similar to the one used in Chapter 2, where the feedback is dominated by three O-stars and the total cluster mass is $M_{cl} = 0.5 \times 10^4\,M_{\odot}$. As will be discussed, the stellar masses of the most massive stars in the cluster are slightly higher than the stars assumed in the earlier Chapters, and their mass-loss rates are greater too. The code uses a random number generator and a Saltpeter IMF to determine suitable masses of individual stars within a cluster, and uses the prescriptions of Vink *et al.* (2000, 2001) to calculate the mass-loss rates and wind velocities for each star. These stars are then given an x-, y- and z-position based on another random number generator. Checks are then performed to ensure that there is sufficient space between each star to enable a "balanced" wind-wind collision to occur between any two stars. Only stars with masses in the range $20\,M_{\odot} \leq M_{*} \leq 40\,M_{\odot}$ are positioned in this way, as the contribution to the cluster wind by lower mass stars is assumed to be

Table 5.1: Initial properties of the 25 most massive stars in a cluster of 5000 $M_\odot$.

Star ID	Mass ($M_\odot$)	x-pos (pc)	y-pos (pc)	z-pos (pc)	$\dot{M}$ ($M_\odot\,yr^{-1}$)	v_∞ ($km\,s^{-1}$)
01	27.3	0.011	0.015	0.023	5.37×10^{-7}	2430
02	26.0	-0.004	0.029	0.011	3.25×10^{-7}	2462
03	36.0	0.013	-0.002	0.000	1.19×10^{-6}	2629
04	23.0	0.019	-0.005	0.030	2.15×10^{-7}	2390
05	26.3	0.008	0.022	-0.020	3.21×10^{-7}	2476
06	39.5	0.002	0.002	-0.001	1.78×10^{-6}	2628
07	21.4	0.034	-0.016	-0.007	1.33×10^{-7}	2388
08	21.3	-0.016	0.033	-0.010	1.34×10^{-7}	2382
09	22.1	0.010	-0.015	-0.032	2.26×10^{-7}	2339
10	31.0	-0.023	0.002	-0.003	8.38×10^{-7}	2503
11	21.2	0.022	0.027	0.017	1.34×10^{-7}	2378
12	20.6	-0.001	0.029	0.026	8.21×10^{-8}	2423
13	32.9	0.001	-0.013	0.013	7.77×10^{-7}	2593
14	33.1	0.006	0.014	0.012	7.72×10^{-7}	2601
15	27.4	0.017	0.003	-0.023	5.35×10^{-7}	2434
16	39.0	-0.003	-0.001	0.004	1.07×10^{-6}	2763
17	31.1	0.005	0.016	0.015	8.31×10^{-7}	2514
18	22.4	-0.029	-0.006	-0.021	2.23×10^{-7}	2354
19	22.8	-0.004	-0.032	-0.016	2.18×10^{-7}	2378
20	21.3	-0.004	-0.010	0.037	1.34×10^{-7}	2384
21	23.6	-0.028	-0.014	-0.016	2.08×10^{-7}	2426
22	28.3	0.003	0.022	0.016	5.13×10^{-7}	2482
23	27.4	0.006	0.025	-0.014	5.36×10^{-7}	2433
24	22.0	-0.035	-0.008	-0.008	1.28×10^{-7}	2425
25	24.3	-0.001	-0.024	-0.024	2.00×10^{-7}	2465

negligible.

Using these parameters, a cluster of 1736 stars was generated, with 25 stars meeting the criteria of $20\,M_\odot \leq M_* \leq 40\,M_\odot$. The details of these stars can be

found in Table 5.1. The three most massive stars are IDs 03, 06 and 16 at 36.0, 39.5 and 39.0 $M_\odot$ respectively. These are more massive than those assumed in Chapter 2, which used 35, 32 and 28 $M_\odot$ stars. The mass-loss rates are generally higher as well. For example, the 32 $M_\odot$ star was assigned a MS mass-loss rate of $2.5\times10^{-7}\,M_\odot\,yr^{-1}$ (see Table 2.1 for the stellar parameters used in Chapter 2). However, a 31.3 $M_\odot$ star in the generated cluster (star ID 17) has a mass-loss rate of $8.3\times10^{-7}\,M_\odot\,yr^{-1}$, which is approximately three times greater. This difference roughly reflects the current level of uncertainty in massive star mass-loss rates.

The total energy input of the 25 stars listed in Table 5.1 is $\dot{E}_{cl} = 2.46 \times 10^{37}\,ergs\,s^{-1}$, the cluster mass-loss rate is $\dot{M}_{cl} = 1.21 \times 10^{-5}\,M_\odot\,yr^{-1}$ and the average cluster velocity is $v_{\infty,cl} = 2541.38\,km\,s^{-1}$. This compares with the energy input from the cluster in Chapter 2, which had a MS energy input of $\dot{E}_{cl} = 1.14\times 10^{36}\,ergs\,s^{-1}$, a mass-loss rate of $\dot{M}_{cl} = 9 \times 10^{-7}\,M_\odot\,yr^{-1}$ and a cluster velocity $v_\infty = 2000\,km\,s^{-1}$. This makes the IMF generated cluster approximately 20 times more powerful, it deposits approximately 10 times more mass and generates a cluster wind which is 1.3 times faster than the cluster values in Chapter 2. Whilst the contribution from lower mass stars was ignored in that Chapter, it is not surprising that the mass-loss and energy input from a cluster of 25 high mass stars will be greater than predicted from the input of just three. The three most massive stars from the cluster list (star IDs 03, 06 and 16) contribute approximately 37% of the total energy and mass imparted into the ISM, with $\dot{E}_{3*} = 9.10 \times 10^{36}\,ergs\,s^{-1}$ and $\dot{M}_{3*} = 4.04 \times 10^{-6}\,M_\odot\,yr^{-1}$.

The positions of the stars are plotted in Fig. 5.1. The colour scale is a simplistic representation of the mass of the stars, which are split into three ranges with red being the three highest mass stars. The limits between the colours are red

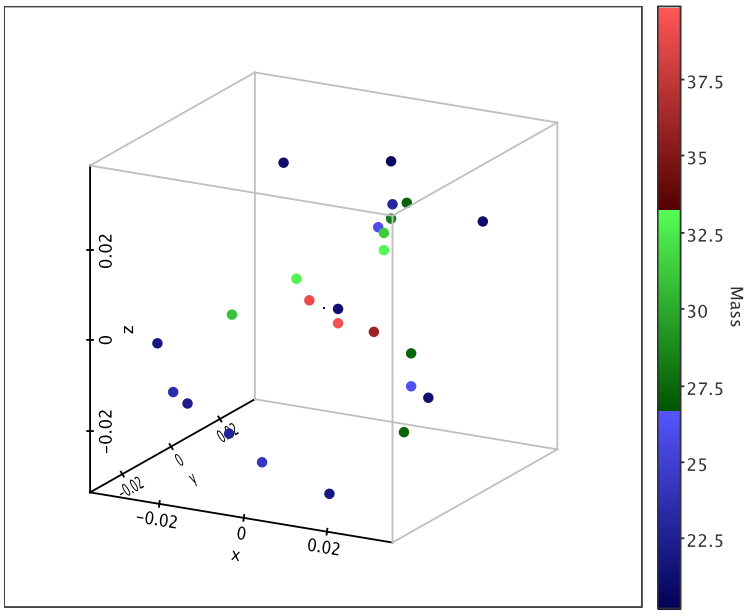

Figure 5.1: 3D representation of the positions of the 25 stars in the simulated cluster. The colour scale indicates the masses of the stars, with red being $34\,M_\odot \leq M_* \leq 40\,M_\odot$, green being $28\,M_\odot \leq M_* \leq 34\,M_\odot$ and blue being $20\,M_\odot \leq M_* \leq 28\,M_\odot$. The cluster radius is $R_{cl} = 0.04\,pc$.

between $34\,M_\odot \leq M_* \leq 40\,M_\odot$, green being between $28\,M_\odot \leq M_* \leq 34\,M_\odot$ and blue being between $20\,M_\odot \leq M_* \leq 28\,M_\odot$. There is, by design, mild mass-segregation present in the positioning of the stars, with the three most massive stars clearly located near the centre of the cluster, and the lower mass stars in a ring around the edge. The radius of this stellar cluster is $R_{cl} = 0.04\,pc$. This is consistent with stellar clusters of this size, and also with the simulations detailed in Chapter 2.

5.3 Results

The left panel of Fig. 5.2 shows the mass flux off the grid as a function of time during the first few thousand years, when all 25 of the stars are on the MS. The mass flux is initially zero until the cluster wind begins to sweep material off the edge of the grid, and then steadily increases up until $t \approx 110\,\mathrm{yrs}$, at which point the shell of swept-up material surrounding the cluster wind reaches the edge of the grid. Due to the small simulation volume, the shell does not take long to leave the grid, and despite expanding into an inhomogeneous environment it is not yet spherical as the individual wind-blown bubbles have not yet fully merged. The material behind the shell is less dense, and therefore the mass flux declines slightly as the shell leaves the grid. The mass flux stabilises at $t \approx 180\,\mathrm{yrs}$ at a value of $1.6\times10^{-6}\,\mathrm{M_\odot\,yr^{-1}}$ for the remainder of the initial expansion.

The right panel of Fig. 5.2 shows the total energy flux off the grid as a function of time. The energy flux increases from zero at the time when the first material begins to leave the grid to $\approx 5\times10^{36}\,\mathrm{ergs\,s^{-1}}$ at $t = 180\,\mathrm{yrs}$. This compares with the total kinetic power of the cluster wind of $2.46\times10^{37}\,\mathrm{ergs\,s^{-1}}$. This implies that approximately 80% of the kinetic energy is radiated away.

Fig. 5.3 shows density slices through the centre of the 3D simulation in each of the three planes at $t = 180\,\mathrm{yrs}$, once the wind has reached its steady state and whilst all of the stars are on the MS. With 25 stars in such a close cluster, there are many instabilities and shocks created by the colliding stellar winds. Although the density around the cluster centre is generally high, there are some regions which show much lower densities (see for example the right panel of Fig. 5.3). In each of the three planes the three highest mass stars are visible (see Fig. 5.1) at the

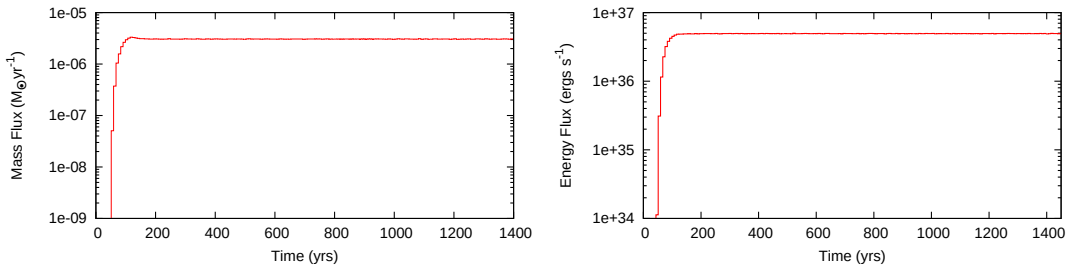

Figure 5.2: Total mass and energy fluxes off the grid as a function of time for the first few thousand years of the simulation. [Left]: shows the total mass flux off the grid and [Right]: shows the total energy flux off the grid.

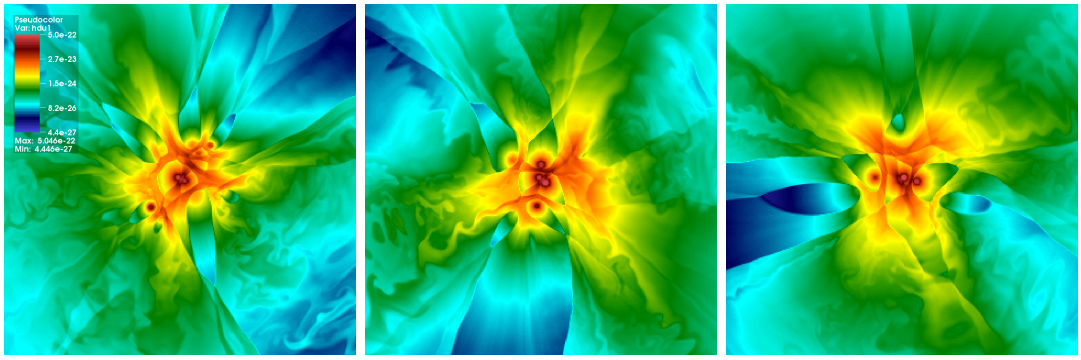

Figure 5.3: Density slice through the 3D simulation in three planes whilst all 25 stars are on the MS. The cluster radius is 0.04 pc, and each panel is 0.3 pc×0.3 pc. [Left]: xy [Middle]: xz and [Right]: yz.

centre due to the mass segregation incorporated into the simulations, although a few of the lower mass stars are also visible in these slices.

A 3D visualisation of the cluster at this time is shown in Fig. 5.4 using the software package VisIt visualisation. The cluster wind has clearly reached the edge of the grid. There appear to be regions through which material is streaming out from the central cluster, and other regions of lower density which are less affected by the colliding winds. The streams of colliding wind material demonstrate multiple instabilities, with their density decreasing the further from the stellar cluster they reach.

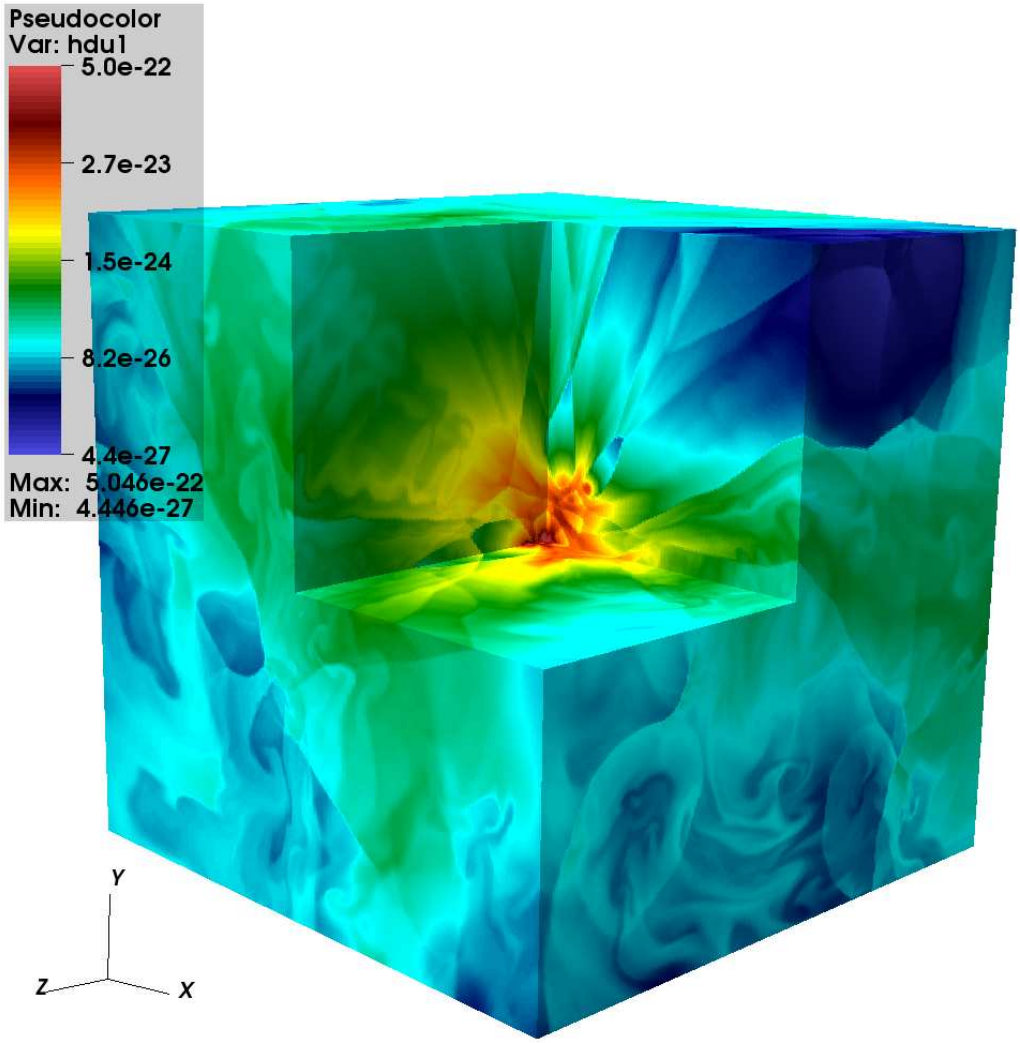

Figure 5.4: 3D density plot of the stellar cluster at t = 180 yrs, whilst all 25 stars are on the MS. An octant has been cut away to show the central cluster. The cluster radius is 0.04 pc and each side has length 0.3 pc. The orientation of the 3D cube is shown in the bottom left hand corner.

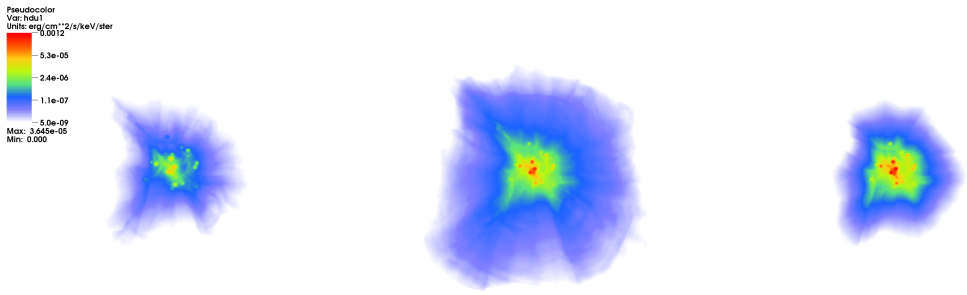

Figure 5.5: Synthetic X-ray emission for the cluster during the MS. [Left] shows the soft BB1 (0.1–0.5 keV) X-ray emission, [Middle] shows the medium BB2 (0.5–2.5 keV) emission and [Right] shows the hard BB3 (2.5–10.0 keV) emission.

5.4 X-ray and Radio Emission from the Cluster

The X-ray and radio emission from the stellar cluster will now be examined using the radiative transfer codes described in Chapters 3 and 4.

5.4.1 X-ray Emission

Synthetic images of the X-ray emission of the cluster at t = 180 yrs are shown in Fig. 5.5. It is immediately apparent that the soft 0.1–0.5 keV X-rays undergo extensive attenuation, as the luminosity in this energy band is visually much lower than observed in the medium 0.5–2.5 keV region (see left and middle panel). This is confirmed by the X-ray spectrum at this time, shown in Fig. 5.6. The spectrum shows substantial attenuation until approximately 0.7 keV, after which there are minor attenuation effects until about 1 keV. At these low energies the dominant source of the attenuation is the ISM column, with only minor contributions coming from within the cluster.

The hard 2.5–10 keV emission (right panel in Fig. 5.5) traces the emission

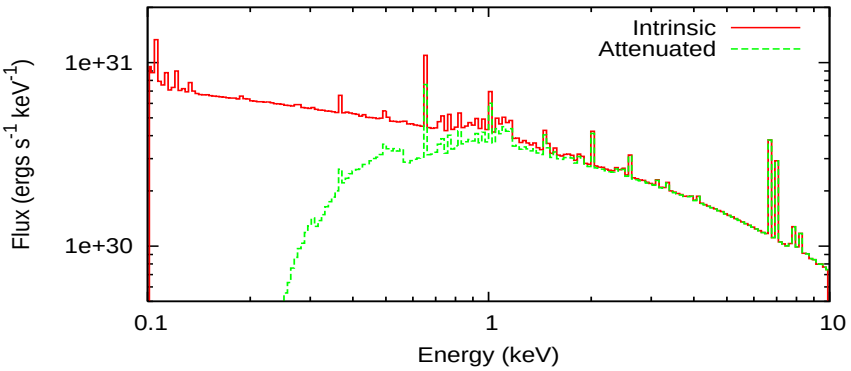

Figure 5.6: The X-ray spectrum for the cluster at t = 180 yrs, whilst all the stars are on the MS. The solid red line shows the total intrinsic emission produced by the cluster. The green dashed line shows the total observable emission after all attenuation effects are considered.

in the cluster centre, where multiple shocks are occuring. It also traces the individual stars, a feature seen in all three of the energy bands. However, this is probably due to the setup conditions where the winds are injected as thermal energy. Ideally the emission in the immediate vicinity of the stars should not be included. The soft and medium energy bands show the more diffuse, extended emission surrounding the cluster, although much of this is attenuated at the shortest wavelengths.

5.4.2 Radio Emission

A synthetic thermal radio image of the cluster at 1.4 GHz is shown in Fig. 5.7. Again, the individual cluster members are visible in this synthetic image, although this is again likely related to the way in which the winds are mapped. Multiple shocks are also visible at this wavelength and coincident with the results from the X-ray images. The visible shock towards the top left of the image coincides with one of the streams of material visible in Fig. 5.4. The spectrum of the cluster is

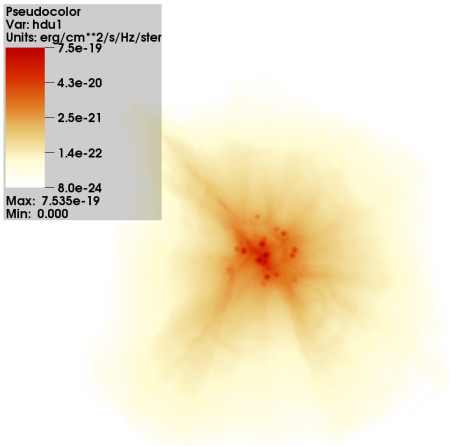

Figure 5.7: Synthetic thermal radio 1.4 GHz emission for the cluster at t = 180 yrs, whilst all 25 stars are on the MS.

optically thin at this time.

5.5 Conclusion

This Chapter takes a first look at investigating the energy and momentum imparted into the ISM by a massive young stellar cluster. Although the cluster size was chosen to mimic the cluster used as a basis for the simulations in Chapter 2, the increased number of 20 and 30 $M_{\odot}$ stars created a more powerful cluster wind. The cluster of 1736 stars, the 25 most massive of which were mapped and tracked, were placed within a cluster radius of 0.04 pc. Mild mass segregation was incorporated such that the three most massive stars were located at the centre of the cluster and the lower mass stars towards the edges.

The cluster wind reaches a steady state very early in its lifetime, approximately 180 yrs after the winds are switched on. Only approximately 20% of the

total kinetic power imparted by the cluster wind flows off the grid, with the remaining 80% radiated into the surrounding ISM. This value is very high and does not seem to be reflected in the X-ray emission.

The X-ray and thermal radio emission during the early MS phase of the cluster reveal the presence of shocks and instabilities where the winds from the massive stars are colliding. There is also substantial attenuation of the lowest energy X-rays occuring.

This Chapter contains only preliminary results, and much more work must be carried out in order to make true comparisons to existing models and observations of massive clusters.

Chapter 6

Conclusions

6.1 Summary

This thesis contains descriptions of simulations performed to determine the degree to which a massive young stellar cluster can affects its natal giant molecular cloud (GMC). These are the first 3D hydrodynamic simulations of stellar wind feedback into an inhomogeneous, clumpy environment. The initial conditions have been selected to make these simulations as realistic as possible by using results from the turbulent GMC simulations of Vázquez-Semadeni *et al.* (2008) to be representative of a clump within a GMC. This clump is in pressure equilibrium with the surrounding homogeneous medium, allowing the breakout of the cluster winds to be analysed. This effect is similar to champagne flows which have been observed in many star forming regions. Incorporating stellar evolution has also provided an opportunity to separate the effects of various stellar evolutionary phases on the surrounding material. Similarly, the SN explosion of each star has been analysed separately to determine the degree to which the thermal energy

produced can couple with the dense remnant clumps. Importantly, it was found that over 99% of the SN energy escaped. Using the outputs of these complex hydrodynamical simulations in radiative transfer codes allows realistic predictions of the X-ray and thermal radio emission to be made. A more realistic input model has allowed better comparisons to actual observations of massive young stellar clusters. This section summarizes the important findings that have been presented throughout this thesis.

The mechanical input from the winds and supernovae of a cluster with three massive O-stars into a giant molecular cloud (GMC) clump was investigated using a 3D hydrodynamical model in Chapter 2. The cluster wind blows out of the molecular clump, the remains of which confine and shape the initial structure and expansion of the wind-blown bubble. The cluster wind breaks free of the GMC clump along low density channels allowing hot, high speed gas to flow away from the cluster through the gaps in the shell opened up by these blow-outs. The dense clumps are ablated by the cluster wind as it flows out of the GMC, loading mass into them. Increasing the density of the GMC clump by a factor of two and the radius to 5 pc slows the break-out phase, but does not significantly affect the qualitative picture. This complex interaction of the cluster wind with its environment is far removed from the results of the simple spherically symmetric models proposed by Castor *et al.* (1975) and Chevalier & Clegg (1985).

The early confinement of the winds leads to a brightening in both the intrinsic X-ray and radio emission of the cluster, as shown in Chapters 3 and 4 where the outputs of the hydrodynamical model were run through radiative transfer ray tracing codes. In the case of the X-ray emission, this brightening is caused by the increased pressure created by the confinement of the cluster wind. As the clump

is ablated and destroyed by the action of the cluster wind the latter becomes increasingly less confined, leading to a reduction in pressure within the bubble and a subsequent decrease in the X-ray luminosity. This ties in with the leaky bubble model proposed by Harper-Clark & Murray (2009). Initially the dense parts of the clump decrease the observed X-ray emission due to attenuation, but once the cluster wind has cleared a large portion of this material the attenuation from the ISM is dominant. The radio flux density follows the same pattern, being initially high and decreasing as the pressure within the bubble decreases and the wind material leaks from the clump.

By about 1 Myrs only the densest clumps remain, although thse prove surprisingly resistant to ablation by the cluster wind. The covering fraction of the clump remains approximately constant for the rest of the cluster MS, and so, therefore, does the X-ray and radio emission. During this phase, mass-loading reaches factors of 200–300 as the cluster wind streams through the molecular material in the GMC clump. This factor reduces to approximately 35 times the mass-loss rate of the cluster during the later WR dominated phase. Despite this, the destruction and sweeping up of molecular material is relatively slow, and a substantial amount remains when the first star explodes as a SN.

The density, temperature, pressure and velocity of gas in the cluster environment all span many orders of magnitude. The hottest gas typically occurs at the reverse shock of the cluster wind, and cools as it expands away from the cluster and mixes in with denser surrounding material. A multitude of weaker shocks exist around dense inhomogeneities entrained into gas flowing at mildly supersonic speeds.

The most massive star evolves to become a red supergiant (RSG) at $t = 4.0$ Myrs,

and then further to become a Wolf-Rayet (WR) star at t = 4.1 Myrs. The other two stars remain in their MS phase during this time. The RSG-enriched cluster wind is slow and dense, causing an increase in the thermal radio emission. This increase is limited to a bright peak at the cluster centre, which indicates the extent of the RSG-enhanced cluster wind at this time. The radio spectrum also gains an optically thick component at this time. In contrast, the X-ray luminosity decreases during this phase, as the amount of material at X-ray emitting temperatures drops. This phase is very short-lived, and deposits a lot of material into the simulation. The slow, RSG-enhanced cluster wind is subsequently swept-up by the high momentum, powerful WR-enhanced wind, which heats it to high temperatures. Both the X-ray and radio emission are high during this phase, and 78% of the computational volume becomes filled with X-ray emitting gas. Whilst the radio flux density is still two orders of magnitude higher than in the MS phase of the cluster wind, it actually decreases slightly from the RSG-enhanced wind. The radio spectrum returns to being completely optically thin during this phase.

After 4.4 Myrs the most massive star in the simulation explodes as a supernova (SN). These simulations imply that the highly structured environment into which the SN energy is released and the high porosity of the GMC clump at this stage allows the SN blast wave to rip through the cluster largely unimpeded. The forward shock refracts around the remaining dense inhomogeneities. Although the SN shock destroys the molecular material through which it passes, the cooling times of the dense regions are short enough for the material to quickly reform. Despite injecting less energy into the cluster environment than the SN explosion, the winds are actually more efficient at removing the molecular material.

Due to the way in which the explosion is initialised, the emission from the SN

should only be analysed from the time at which the interaction of the blastwave with the surrounding material becomes dominant. This occurs approximately 900 yrs after the explosion at X-ray energies and approximately 500 yrs at radio energies. The ejecta begins to leave the grid 4600 yrs after the explosion. Comparisons with actual young core-collapse SNe have therefore only been made for remnants between the ages of $900 < t < 4600$ yrs. Four SNRs were identified within this age range. The simulated X-ray results are reasonably comparable to the observations of thsee four SNRs. However, only two of these SNRs have been studied at radio frequencies and they do not compare well to the simulated results. One possibility is that a large proportion of the surrounding molecular material has already been cleared, which will reduce the thermal radio emission, making the flux density lower than simulated. Comparing the observed SNRs with the SN of the $32\,M_{\odot}$ star, where more of the molecular material has been cleared, is a better match, supporting this theory.

A further 0.1 Myrs after the first SN explosion, the second most massive star begins its evolutionary sequence to become a RSG followed by a WR before exploding as a supernova. As before, the lowest mass star remains on its MS during this evolution. The final star evolves to the RSG branch 0.1 Myrs after the explosion of its brethren, at $t = 5.0$ Myrs, and explodes at $t = 5.4$ Myrs, signifying the death of the cluster. By $t = 6$ Myrs, almost all of the molecular material has been completely destroyed or dispersed.

The simulated emission from the cluster during the wind-dominated phases is substantially lower than predicted by 1D spherically symmetric bubble models. This is due to two of the assumptions made in these calculations, which are overly simplified compared to the models used in this thesis. Firstly, the

assumption that the hot wind material is completely confined by the shell of the wind-blown bubble is not true. The reduction in pressure within a leaky bubble results in a lower X-ray luminosity, as observed. Secondly, the surrounding density is inhomogeneous in contrast to most of the simple spherically symmetric models. However, comparisons between the simulated X-ray and radio emission and observations of young massive stellar clusters show promising compatibility.

Once the winds have broken out of the clump it is very porous. By examining the energy flux off the grid throughout the simulation it is apparent that between a quarter and half of the energy injected by the stellar winds is radiated away, leaving 50–75% of the energy from the cluster wind to escape into the wider environment. In comparison, more than 99% of the energy injected by each SN which escapes to the wider environment. Although these fractions are dependent on the initial conditions, especially the density and structure of the cluster environment, it is clear that the energy injected by both the winds and SN of massive stars couple poorly to the densest gas.

Although photoionization has not been treated in any of the simulations discussed in this thesis, the fraction of ionizing photons which are able to escape the cluster environment was estimated in Chapter 2. This increases from less than 1% at the start of the simulation, when the cluster is still enshrouded by the GMC clump, to 40% when the cluster is 1 Myrs old and only the densest of the clump material remains. This increases still further to approximately 60% after 4 Myrs. The escape fraction reduces briefly when the cluster wind is RSG dominated, as the mass-loss rate of the cluster wind increases dramatically, but overall the escape fraction increases as dense material is pushed away from the cluster.

The 3 O-stars which power the cluster wind in the simulations presented in this thesis are representative of a cluster of approximately $5000\,\mathrm{M}_{\odot}$, with a combined main sequence (MS) mass-loss rate of $9\times10^{-7}\,\mathrm{M}_{\odot}\,\mathrm{yr}^{-1}$ and energy input of $1.14\times10^{36}\,\mathrm{ergs\,s}^{-1}$. Such a cluster was actually compiled using a Saltpeter IMF in Chapter 5, where there were a total of 1736 cluster members, 25 of which have masses between 20 and $40\,\mathrm{M}_{\odot}$. The generated cluster is mass segregated, with the three most massive stars located at the cluster centre and the lower mass stars located towards the edges. The total kinetic energy input of such a cluster during the MS would be approximately 20 times greater than assumed in Chapter 2, and the mass-loss rate would be about 10 times greater. The three most massive stars in this cluster contribute approximately 37% of the total energy and mass imparted into the ISM.

Snapshots of the X-ray and thermal radio emission have been presented during the very early MS stage of the cluster. The density structure at this time indicates the presence of shocks and instabilities within the cluster wind, which is not unexpected. There is a great deal of attenuation present in the soft X-rays (0.1–0.5 keV), whilst the hard X-rays pick out the individual stars in the cluster. The thermal radio at 1.4 GHz also picks out the stars, and also some of the shocks present.

6.2 Future Work

The simulations presented in this thesis are a first look at the mechanical feedback from the winds and supernovae of massive stars. However, despite state of the art modelling, there is still much work to be done in this field. This section outlines

further steps that could be taken to develop and refine the work presented in this thesis.

In Section 2.2.4, the approximations and simplifications to the hydrodynamical models used in Chapter 2 were outlined. Amongst the processes which were neglected are gravity, magnetic fields, radiation pressure, photoionization, dust, cosmic rays and radiative losses from within the stellar cluster. Adding some, or all of these processes to the code would be a great way to begin building the complexity of the simulations. Including both photoionization and the effects of stellar winds would allow comparisons between the two feedback mechanisms to be made, where the contribution of each can be separated and analyzed. The neglect of direct radiation pressure and gravity will offset each other to some extent. Some of the dense clumps may be susceptible to self-gravity on the timescales considered here, with free-fall times of about 0.3 Myrs for the very densest clumps, and therefore including gravity in the simulations may be able to reproduce triggering of a new generation of stars, something that has not been considered in this work. Adding dust to the simulation may affect the cooling within the hot bubble. If the destruction of the dense clumps of material can continuously replenish the dust, then this could have a significant effect on the cooling (Everett & Churchwell, 2010) and contribute to the mass-loading of the wind-blown bubble. This would be another interesting avenue that warrants further work.

The evolution of the stars are by design treated very simplistically, with three pre-determined phases each with a single value for the mass-loss rates and wind velocities of the stars. The simulations detailed in Chapter 5 use a more sophisticated method, using evolutionary stellar tracks to constantly update the mass-loss rates of the stars. Adding this finer evolution to the stars would make

the model more realistic. The evolutionary stages of the three O-stars used in the simulation were manufactured so that they did not overlap - the two lower mass stars remain on the MS until the most massive star has exploded. It would be interesting, now that this control has been performed, to see the effect of multiple evolutionary phases occurring at once. Introducing more stars into the cluster would be one way to do this, and would also add more complexity to the simulation.

It should be noted that adding to the simulations presented in this thesis will increase the time and processing power required for them to run. This should be considered carefully when deciding how to refine or increase the complexity of the simulations.

The outputs from the hydrodynamical model were used at the basis for the simulated X-ray and radio observations presented in Chapters 3 and 4. However, emission at many more wavelengths can be looked at. I am currently collaborating with colleagues at the University of Exeter to examine the infrared emission at $22\,\mu$m and Hα emission from the simulations in Chapter 2. The results of this should prove a very interesting comparison to the X-ray and radio results presented in this thesis, and should help to build a comprehensive comparison between the simulations and observations of massive young stellar clusters.

The intracluster simulations detailed in Chapter 5 are recent additions to this thesis, and as such there is a lot of work which can be done to further the initial investigations presented here.

For instance, while the energy and momentum input from the cluster during the very early evolution of the cluster has been presented, this work needs to be extended such that these values can be analyzed over the course of the cluster

lifetime. As the evolution of the stars is treated in a more sophisticated way than in the original simulations the cluster mass-loss rate should alter as the stars age. Tracking the input of energy and momentum into the ISM throughout the lifetime of a massive cluster will therefore be possible.

It will be interesting to examine how the degree of radiative cooling of the shocked gas changes as stars evolve, and whether the parts of the cluster wind can undergo significant radiative losses while other parts remain closer to adiabatic. It will also be interesting to investigate the transition of a cluster wind from the adiabatic to radiative regimes.

Chemical enrichment of the ISM by the stellar winds and supernovae is another process which has not been considered in this thesis, and is another avenue that could be explored.

Comparisons between a mass-segregated cluster and one with no segregation were briefly mentioned, but this could warrant further investigation. For example, with the higher mass stars at the centre of the cluster evolving and exploding before the surrounding lower mass stars, interesting morphologies within the cluster wind could develop. The cluster was set at $5000\,\mathrm{M}_{\odot}$ in order to justify the assumptions made about the cluster used in Chapter 2. However, running several simulations which vary and compare the cluster parameters could be another factor to consider. Setting the cluster parameters to mimic those of well studied, young, massive stellar clusters, such M 17 would also prove an interesting study. It is possible to take this one step further, and use a stellar cluster generated in this way as the central cluster within a feedback simulation, such as those carried out in Chapter 2. Again, a simulation of this sort would allow for detailed comparisons with actual observations of stellar clusters which would help

to understand the processes occuring within them.

6.3 Final Remarks

The highly complex nature of massive young star forming regions makes determining the processes occurring within them difficult to separate and evaluate. In order to duplicate and elucidate these processes, simulations must strive to be equally as complex. The hydrodynamical models presented in this thesis are the first 3D simulations of a cluster wind expanding into an inhomogeneous, turbulent environment, and have made a good start at unraveling some part of this complexity, with promising results. These should be a solid base from which future simulations can work in the hope of building a full view of the feedback processes occurring in such regions.

Appendix A

Notes on Individual Stellar Clusters

A.1 RCW 38

RCW 38 is a very young (< 1 Myr), highly embedded ($A_V \sim 10$), and close ($D = 1.7$ kpc) stellar cluster surrounding a central pair of O5.5 stars (IRS 2) (e.g. Winston *et al.*, 2011). The dominant IRS 2 stars have cleared a region completely free of dust out to a radius of 0.1 pc. The extinction is patchy, and the HII region appears to be breaking out of the surrounding molecular gas in some directions. Extended warm dust is found throughout a $2 - 3$ pc region and coincides with extended (1.25×1.75 pc) X-ray plasma which is predominantly non-thermal (Wolk *et al.*, 2002). The power-law index of the emission steepens toward the cluster core. Contamination of the diffuse emission by unresolved point-sources is not significant at distances of more than 0.15 pc (~ 15 arcseconds) from the cluster center, though may be responsible for the more thermal nature of the diffuse

emission measured in the core (Wolk *et al.*, 2006). The cause of the non-thermal emission remains unclear.

The diffuse emission is strongest in the central core near IRS 2, and is confined on the southeast along a ridge. Recent *Spitzer* observations reveal that winds from IRS 2 have caused outflows towards the northeast, northwest and southwest of the central cluster (see e.g. Fig. 4 in Winston *et al.*, 2012).

An excellent review of this cluster is given in the Handbook of Star Formation, where the luminosity of the diffuse X-ray emission is given as about $3 \times 10^{32}\,\mathrm{ergs\,s^{-1}}$ (Wolk *et al.*, 2008).

A.2 The Omega Nebula (M17)

M17 is a very young blister H II region located on the northeast edge of one of the largest giant molecular clouds in the Galaxy, with an extent of 4° ($\sim 110\,\mathrm{pc}$, Elmegreen *et al.*, 1979). The geometry of M17 is thought to resemble the Orion Nebula HII region except that it is seen edge-on rather than face-on (Meixner *et al.*, 1992; Pellegrini *et al.*, 2007). M17 is photoionized by the massive stellar cluster NGC 6618, which has 14 identified O stars (Broos *et al.*, 2007), and is estimated to be $\sim 0.5\,\mathrm{Myr}$ old (Chini & Hoffmeister, 2008; Hoffmeister *et al.*, 2008). The distance has recently been determined using trigonometric parallax to be 2.0 kpc (Xu *et al.*, 2011). Several obscured O4-O5 stars form a central 1 arcminute ring in NGC 6618, and are principally responsible for ionizing the nebula. Extinction is patchy ($A_V = 3 - 15$ with an average of 8 to the OB stars, though some parts of the cluster have $A_V > 20$, Hanson *et al.*, 1997). The earliest O stars are an O4+O4 visual binary known as Kleinmann's Anonymous

Star (Kleinmann, 1973), which may in fact be a pair of colliding wind binaries (Broos *et al.*, 2007; Hoffmeister *et al.*, 2008; Rodríguez *et al.*, 2012). Evidence for an older ($2-5\,$Myr) stellar population to the North is presented by Povich *et al.* (2009).

The diffuse X-ray emisison from M17 has previously been analyzed by Dunne *et al.* (2003), Townsley *et al.* (2003), Hyodo *et al.* (2008), and most recently by Townsley *et al.* (2011). It has relatively high surface brightness and blows out to the east of the cluster, extending nearly $10\,$pc from the cluster. The plasma appears to be channelled by the famous northern and southern ionization bars (Povich *et al.*, 2007), and maintains roughly constant temperature as it flows (Hyodo *et al.*, 2008; Townsley *et al.*, 2003). Although obscuration changes across the field, a global fit to the diffuse emission with a 3-temperature NEI model yields $kT_1 = 0.28$, $kT_2 = 0.29$ and $kT_3 = 0.57\,$keV, with the highest temperature component providing 56% of the intrinsic luminosity (Townsley *et al.*, 2011). The absorption to each of these emission components increases with the temperature of the component, so that the kT_3 component suffers 6 times as much obscuration as kT_1. There are indications that the shocked gas is not in complete ionization equilibrium, which is suggestive of it recently being shocked. Several gaussian lines are also needed - the cause is speculated to be charge exchange processes. The total X-ray luminosity is $2.0 \times 10^{34}\,\mathrm{erg\,s^{-1}}$.

Townsley *et al.* (2003) previously determined that the X-ray plasma had a mass of $0.15\,M_\odot$, which when rescaled to a distance of $2.1\,$kpc becomes $0.3\,M_\odot$ (for an assumed distance D, $V_\mathrm{x} \propto D^3$, $L_\mathrm{x} \propto D^2$, $n_\mathrm{e,x} \propto (L_\mathrm{x}/V_\mathrm{x})^{1/2} \propto D^{-1/2}$, and $M_\mathrm{x} \propto n_\mathrm{e,x} V_\mathrm{x} \propto D^{5/2}$). Townsley *et al.* (2003) determine that $n_\mathrm{e,x} \sim 0.3\,\mathrm{cm^{-3}}$. The analysis by Hyodo *et al.* (2008), which does not quite include the most

easterly extent of the plasma, is generally consistent with the earlier work of Townsley *et al.* (2003), except for the determination of a significantly lower plasma temperature of $\approx 0.25\,\mathrm{keV}$.

Rodríguez *et al.* (2012) observed M 17 at 4.96, 8.46 and 22.46 GHz using the *JVLA* (Jansky Very Large Array) in the highest angular resolution A configuration. They revealed the presence of 38 compact radio sources, 19 of which have stellar counterparts detected in infrared, optical or X-rays, in addition to the hyper-compact (HC) cometary HII region, M 17 UC1. This HC HII region was first discussed by Felli *et al.* (1980), who estimated a density $n_e{>}10^6\,\mathrm{cm}^{-3}$ and an electron temperature $T_e{>}25,000\,\mathrm{K}$. It is approximately spherical, with a diamter of $\sim$0.006 pc, and is embedded in the molecular cloud adjacent to the SW of the M 17 region (Johnson *et al.*, 1998). There is widespread evidence of massive star formation occuring within $\sim$0.4 pc of UC1 (Genzel & Downes, 1977; Harper *et al.*, 1976; Knowles *et al.*, 1976). This region is much mroe compact, and therefore denser, than the region simulated.

Rodríguez *et al.* (2012) measure the flux density of this HII region to be 44, 107 and 194 mJy at 4.96, 8.46 and 22.46 GHz respectively. At $\mathrm{t} = 0.44$ Myrs the simulated flux densities are $\mathrm{S}_{4.98} = 191.1$ mJy, $\mathrm{S}_{8.71} = 179.75$ mJy and $\mathrm{S}_{23.16} = 160.51$ mJy.

Rodríguez *et al.* (2012) also estimate the spectral index of the M 17 UC1, to range from values of $\sim$2 (optically thick emission) near the head of the cometary nebula to values of $\sim$-0.1 (optically thin emission) near the tail. This result suggests that at least in this HC HII region the intermediate values of $\sim$1 for the spectral index comes from a gradient in optical depth across the face of the nebula.

A.3 Westerlund 2 (RCW 49)

Westerlund 2 (hereafter W2) is a compact young open cluster embedded in and responsible for the luminous HII region RCW 49. W2 contains at least a dozen OB stars. Two WR stars, WR20a and (especially) WR20b, lie outside the cluster core (see references in Churchwell *et al.*, 2004). W2 is also located in the direction of one of the Galaxys strongest sources of γ-rays (Aharonian *et al.*, 2007; H.E.S.S. Collaboration *et al.*, 2011). The distance to W2 has been very difficult to pin down, with estimates ranging from 2 to more than 8 kpc in the literature, but a new study puts it at 2.85 ± 0.43 kpc, and determines an age of no more than 2 Myr (Carraro *et al.*, 2013).

Diffuse X-ray emission from W2 was identified in a *Chandra* observation (Townsley *et al.*, 2005). The emission is brightest at the core of W2, and extends preferentially towards the west. The emission can be fitted with a 3-temperature thermal plasma model with $kT_1 = 0.1$, $kT_2 = 0.8$ and $kT_3 = 3.1$ keV, with the highest temperature component providing 30% of the intrinsic luminosity (Townsley *et al.*, 2005). Assuming a distance of 2.3 kpc, the absorption corrected 0.5-8 keV luminosity is $L_{\rm x} = 3 \times 10^{33}\,{\rm ergs\,s^{-1}}$. At $D = 2.85$ kpc, this increases to $L_{\rm x} = 4.6 \times 10^{33}\,{\rm ergs\,s^{-1}}$. The absorbing column to kT_1 is less than the identical columns to kT_2 and kT_3. The hardest thermal component is not well constrained, and replacing it with a power-law component ($\Gamma = 2.3$) also gives an acceptable fit. The diffuse flux will be slightly underestimated due to the use of a 5 arcmin radius extraction region and a nearby on-chip background region.

More recently diffuse emission has also been analyzed from a *Suzaku* observation (Fujita *et al.*, 2009). The *Chandra* pointing was used to determine the point

source contamination to the *Suzaku*-derived diffuse emission, and the central region (r<2 arcmin) was masked out. The diffuse emission is found to extend to an 8 arcminute radius. The spectral analysis is broadly consistent with the earlier results of Townsley *et al.* (2005).

Benaglia *et al.* (2013) observed W 2 using *ATCA* and found the total flux density across RCW 49 to be 146±12 Jy and 103±30 Jy at 5.5 GHz and 9.0 GHz respectively. They detect 6 discrete radio sources, only one of which has a counterpart at other wavelengths. The bulk of the emission seen in RCW 49 has a spectral index of $\alpha \sim 0$, which is consistent with the optically thin plasma expected from such an HII region. However, some emission from the so-called "bridge" region show signs of non-thermal components from relativistic electrons.

A.4 The Orion Extended Nebula (M42)

The Orion Nebula Cluster (ONC), also known as the Trapezium cluster, contains the nearest rich and concentrated sample of pre-MS stars. The OB members of the ONC photoionize the Orion Nebula (M 42), a blister HII region at the near edge of Orion A, the nearest giant molecular cloud ($D \approx 450$ pc). Güdel *et al.* (2008) recently detected diffuse, soft ($0.3 - 1$ keV) X-ray emission in the Extended Orion Nebula (EON). The characteristic temperature of the plasma is $kT \approx 0.2$ keV. The intrinsic X-ray luminosity in the $0.1 - 10$ keV energy band is $L_{\rm x} = 5.5 \times 10^{31}$ ergs s^{-1}. Two regions of diffuse emission, a northern and a southern, are identified with respective emission measures of EM = $\rm n_e^2 V$ = 1.5×10^{54} and 1.9×10^{54} cm^{-3}. The attenuating column $N_{\rm H}$ is very low, being 4.1×10^{20} cm^{-2} for the northern, and $< 10^{20}$ cm^{-2} for the southern.

The total mass of the X-ray emitting gas is estimated to be $0.07\,M_{\odot}$, which is roughly 10^5 yrs of mass-loss of the dominant O5.5 star θ^1Ori C. The radiative cooling time is estimated to be $\approx 1.8-3.9\,\mathrm{Myr}$. The density of the X-ray plasma is determined to be $n_{\mathrm{e}} = 0.1-0.5\,\mathrm{cm}^{-3}$. The X-ray and ionized gas are in approximate pressure equilibrium ($n_{\mathrm{HII}} \approx 100\,\mathrm{cm}^{-3}$), and the hot gas is likely channeled by the cooler denser structures rather than disrupting them by expansion. Leakage of the hot plasma via an X-ray champagne flow into the nearby Eridanus superbubble is suggested.

Garay *et al.* (1987) detected 21 radio sources in the Orion Nebula using the *VLA* in a combination of A, B and C configurations, all but one of which having either an infrared or X-ray counterpart. 13 of these sources are likely to be relatively dense fragments remaining from a massive molecular cloud, and are surrounded by ionized envelops. Garay *et al.* (1987) attribute the destruction of this giant molecular cloud to the action of radiation and stellar winds from the young stellar population formed from within it. Dicker *et al.* (2009) measure $\alpha = 1.19 \pm 0.12$ using *GBT* (Robert C. Byrd Green Bank Telescope) and the *VLA*. Wilson & Pauls (1984) observe an integrated flux over Orion A of 400 Jy at 23 GHz using the Efflesberg 100m telescope.

A.5 The Rosette Nebula

The Rosette Nebula is a blister HII region at the tip of the giant Rosette molecular cloud. It has a distinct ringlike appearance in both radio and optical images, and is photoionized by the open cluster NGC 2244 whose stellar winds have cleared a hole in the Nebula's centre (Celnik, 1985; Townsley *et al.*, 2003). NGC 2244

contains 7 O-type stars, all of which have MS luminosity classes, with the earliest spectral type being O4V((f)). A recent analysis of 6 of these stars by Martins *et al.* (2012) determined an upper age limit of 2 Myr for the most massive stars, in excellent agreement with earlier determinations (e.g. Hensberge *et al.*, 2000; Park & Sung, 2002). Photometric distance estimates range between 1.4 and 1.7 kpc, and 1.55 kpc is adopted in this work. Wang *et al.* (2008) find an absence of mass segregation and conclude that the cluster is not dynamically evolved. The two dominant O stars (HD 46223, O4V((f)); HD 46150, O5V((f))z) are widely separated (by at least 3 pc). In contrast, the O stars in the Trapezium Group and M17 are concentrated within the inner 0.5 pc.

Townsley *et al.* (2003) find that soft diffuse X-ray plasma surrounds the OB association and fills the nebula cavity completely. It likely originates from the O-star winds and is later brought to thermalization by wind-wind interactions or by shocking against surrounding molecular material. The X-ray emission is brightest in the central 3 pc radius, corresponding roughly to the central cavity. The diffuse emission can be fit by a two-temperature thermal plasma model, with components $kT_1 = 0.06 \pm 0.02$ and $kT_2 = 0.8 \pm 0.1$ and a single absorbing column $N_{\rm H} = 2 \pm 1 \times 10^{21}\,{\rm cm}^{-2}$. The hotter component is dominant. The intrinsic $0.5 - 2$ keV luminosity (for $D = 1.55$ kpc) is $\approx 7 \times 10^{32}\,{\rm ergs\,s}^{-1}$. There is no significant emission above 2 keV. Correcting Townsley *et al.*'s values for a slightly greater assumed distance, the diffuse plasma number density and mass are estimated as $n_{\rm e,x} \sim 0.1\,{\rm cm}^{-3}$ and $M_{\rm x} \sim 0.05\,M_\odot$.

Celnik (1985) observed the Rosette Nebula using the 100 m Effelberg telescope, and found the total flux density to be 420±70 Jy and 350±30 Jy at 1.41 GHz and 4.75 GHz respectively. He also measured a mean spectral index $\alpha = -0.15 \pm$

0.11. He found that the spectral index at the centre of the nebula was systematically larger than in the surrounding regions, and attributed this to a shell-type density model.

A.6 The Quintuplet Cluster

The Quintuplet cluster is named after its five brightest stars (Nagata *et al.*, 1990). It is located near the Galactic Centre, is unusually dense, and is host to at least 10 massive, windy, WR stars and more than a dozen luminous OB supergiants (Figer *et al.*, 1999a,b). It is somewhat less massive and dense than the Arches cluster, however. Its age is estimated to be about $3.5-4\,\mathrm{Myr}$ (Figer *et al.*, 1999b; Liermann *et al.*, 2012).

Law & Yusef-Zadeh (2004) determine that the Quintuplet cluster shows thermal diffuse emission with a peak temperature $kT = 2.42 \pm 0.5\,\mathrm{keV}$ at the cluster centre, and with $L_\mathrm{x} \sim 10^{34}\,\mathrm{ergs\,s^{-1}}$. The diffuse emission is much fainter than that in the Arches and has a very low surface brightness. It also has essentially the same spectral shape as the integrated spectrum from the detected sources. Considering the distance to the cluster, contamination by unresolved point-sources may be an issue.

Wang *et al.* (2006) analyze a deeper *Chandra* exposure. They report the same concerns as Law & Yusef-Zadeh (2004) and in addition note that the extent of the diffuse emission from the Quintuplet cluster is uncertain. With an extraction radius of 1 arcmin, Wang *et al.* (2006) find that a single-temperature thermal plasma model yields $kT = 10^{+4.6}_{-2.7}\,\mathrm{keV}$ and $N_\mathrm{H} = 3.8^{+0.7}_{-0.5} \times 10^{22}\,\mathrm{cm^{-2}}$, giving an absorption-corrected $2-8\,\mathrm{keV}$ luminosity of $L_\mathrm{x} \sim 3 \times 10^{33}\,\mathrm{ergs\,s^{-1}}$. The ra-

dial diffuse X-ray intensity profile falls off more rapidly than SPH simulations (Rockefeller *et al.*, 2005) predict.

Lang *et al.* (2005) detected ten radio sources in the Quintuplet cluster using the *VLA*. They observed these souces at $\nu = 4.9$, 8.5, 22.5 and 43.4 GHz to determine the spectral indices. Three of the sources were found to have flat spectral indices, with $\alpha \sim$-0.3 to -0.1 with an average error of $\pm$0.4. A futher six sources were observed to have rising spectral indices, with $\alpha \sim +0.4$ to $+2.0$ with errors ranging from $\pm$0.2–0.8. The final source is the Pistol Star, which has a spectral index $\alpha = +0.1 \pm 0.4$. The three most compact of these sources were thought to be produced by stellar wind emission. The rest of the sources are likely to be a combination of stellar wind emission and free-free emission from the surrounding ionized gas. Three of the sources had no stellar counterpart, and are likely to be caused by emission arising from compact or ultra-compact HII regions.

Although the total integrated flux density over the entire region is not quoted, a lower limit can be set by summing the flux densities of each of the radio sources detected. These lower limits are 12.62, 13.72, 13.55 and 8.9 mJy at 4.9, 8.5, 22.5 and 43.4 GHz respectively. All ten of the sources were detected at 4.9 and 8.5 GHz, but only eight were detected at 22.5 GHz and five at 43.4 GHz.

A.7 Westerlund 1

Westerlund 1 (hereafter W 1) is the most massive stellar cluster known in the Galaxy (Brandner *et al.*, 2008; Clark *et al.*, 2005). It contains a rich population of massive stars which include more than 20 WR stars (Crowther *et al.*, 2006), more than 80 OB stars, and short-lived transitional objects including luminous

blue variables (LBVs), red supergiants (RSGs) and half the currently known population of yellow hypergiants (YHGs) in the Galaxy. Estimates for its age range from $3.6 \pm 0.7\,\mathrm{Myr}$ (Brandner *et al.*, 2008) to $5 \pm 1\,\mathrm{Myr}$ (Lim *et al.*, 2013). Its distance remains somewhat uncertain, but estimates appear to be converging on the range $4 - 5\,\mathrm{kpc}$ (see Brandner *et al.*, 2008, and references therein). It shows evidence of mass segregation (Lim *et al.*, 2013).

At an age of $\sim 4 - 5\,\mathrm{Myr}$, perhaps 100 SNe have already occured in W 1 (see, e.g., the discussion in Muno *et al.*, 2006). The presence of an isolated X-ray pulsar confirms that supernovae have occurred there. However, the likelihood of a recent SNR contributing to the diffuse emission depends on the recent occurrence of a SN event in or near the core, as discussed in Muno *et al.* (2006) and Kavanagh *et al.* (2011).

The X-ray point sources from a *Chandra* observation are analyzed and reported by Clark *et al.* (2008), while the diffuse emission is analyzed by Muno *et al.* (2006). The diffuse emission has an intrinsic $(2 - 8\,\mathrm{keV})$ luminosity of $L_\mathrm{x} \sim 3 \pm 1 \times 10^{34}\,\mathrm{ergs\,s^{-1}}$, and a Lorentzian spatial distribution with a HWHM along the major axis of 25 ± 1 arcseconds ($\sim 0.5\,\mathrm{pc}$), and a 5 arcmin halo. The emission (in the energy range $1.5-8\,\mathrm{keV}$) can be fitted with a soft thermal component ($kT_1 \sim 0.7\,\mathrm{keV}$), plus either a harder thermal component ($kT_2 \sim 3\,\mathrm{keV}$) with a low ($\lesssim 0.3\,\mathrm{solar}$) Fe abundance, or a nonthermal component with a power-law index $\Gamma \sim 2$. The absorbing column, $N_\mathrm{H} \sim 2 \times 10^{22}\,\mathrm{cm^{-2}}$. In the thermal model, kT_2 increases with distance from the cluster, while in the non-thermal model, Γ is significantly steeper in the centre-most region considered. There is no evidence for a recent SN explosion. Less than 10^{-5} of the mechanical luminosity is dissipated as $2-8\,\mathrm{keV}$ X-rays so it is conjectured that a large fraction escapes into the

ISM. However, the X-ray halo between $2-5$ arcmin ($3-7$ pc radius) is observed to attain a constant surface brightness of $\approx 7 \times 10^{-14}$ ergs cm^{-2} s^{-1} arcmin^{-2}, which is not consistent with a cluster wind where almost all of the diffuse X-ray emission is produced within the core radius $R_{\rm c}$ (Stevens & Hartwell, 2003). A thermal interpretation of the halo of diffuse emission is further challenged by the high temperature and lack of line emission.

More recently, Kavanagh *et al.* (2011) analyze an XMM-Newton pointing and determine that the hard component in an inner 2 arcmin radius region is actually thermal, with a clearly detected He-like Fe 6.4 keV line. No evidence of a non-thermal component was found. They report that the diffuse emission has a $2-8$ keV luminosity of $L_{\rm x} \sim 1.7 \times 10^{33}$ erg s^{-1}.

Dougherty *et al.* (2010) find 18 cluster members in W 1, with spectra containing both thermal and non-thermal components using *ATCA*. The brightest source in the cluster is W 9, which has a radio flux density of 55.4 mJy at 8.6 GHz, making it one of the most luminous radio stars. They also found the total radio flux from W 1 to be 699, 523, 461 and 422 mJy at 1.4, 2.2, 4.8 and 8.6 GHz respectively. The extended emission (with the fluxes of the radio stars subtracted from the total emission) is 426, 351 and 307 mJy at 2.2, 4.8 and 8.6 GHz respectively. At t = 4 Myrs, the most massive star in the simulation evolves to become a RSG. At this time the flux density drastically increases due to the high density, reaching 3436, 3313, 3046 and 2862 mJy at 1.4, 2.2, 5.0 and 8.7 GHz respectively. This is approximately 5–6 times higher than observed interferometrically in W 1. However, at t = 3.9 Myrs the flux densities are 35, 34, 31 and 29 mJy at 1.4, 2.2, 5.0 and 8.7 GHz respectively. Whilst this is now considerably lower than the values observed in W 1 this is not wholely unexpected due to the considerably larger

number of O-stars present.

A.8 The Lagoon Nebula (M8, NGC 6530)

The Lagoon Nebula is an HII region associated with the young (13 Myr) open cluster NGC 6530, which contains several O-stars and about 60 B-stars. It is about 1.3 kpc away (see Henderson & Stassun, 2012, and references therein). Ongoing star formation occurs in several places, notably the Hourglass Nebula (the brightest part of M8) and M8 E. The Hourglass Nebula is illuminated by an O7V star (Herschel 36). Henderson & Stassun (2012) argue that NGC 6530 is slightly younger than the Orion Nebula Cluster (ONC), being $\lesssim$ 1.65 Myr assuming the ONC is 2 Myr old. If the ONC is actually 3 Myr old, this would give the Hourglass Nebula an age of 2.5 Myr. The Lagoon Nebula is summarized in Tothill *et al.* (2008).

Rauw *et al.* (2002) claim that soft diffuse emission was "probably" detected from the southern lobe of the Hourglass nebula. The emission can be fitted with an absorbed MEKAL model with $N_{\rm H} = 1.11^{+0.15}_{-0.17} \times 10^{22}\,{\rm cm}^{-2}$, $kT = 0.63^{+0.07}_{-0.05}\,{\rm keV}$ and an intrinsic $(0.2-2.0\,{\rm keV})$ luminosity of $6.6 \times 10^{32}\,{\rm ergs\,s}^{-1}$. However, there is unboutedly some contamination from unresolved point sources. No diffuse emission is seen from a qualitative examination of a *Chandra* observation of M8 which did not cover the Hourglass Nebula (Townsley *et al.*, 2003) - see also Damiani *et al.* (2004).

Woodward *et al.* (1986) performed multiwavelength observations of the inner core of the M 8 Hourglass region, including *VLA* observations in the C configuration at 5 GHz. They detected the total flux density to be 4030 mJy at 5 GHz,

assuming a distance of 1.5 kpc from the Sun. The total integrated flux density was found to be 2.17 Jy in the western lobe and 1.86 Jy in the eastern lobe. The radio maxima is observed to be in the northern lobe of the Hourglass. They assume an optically thin thermal plasma and an electron temperature of 7100 K based on observations by Rodriguez & Lichten (1979). However, Goudis (1975) determined that M 8 had both an optically thick and optically thin component, implying some non-thermal components to the spectra. In a subsequent paper, Goudis (1976) determined the presence of 10 ionizing stars in the cluster.

A.9 The Arches Cluster

The Arches cluster, like the Quintuplet cluster, lies close to the Galactic Centre, being only 26 pc away in projection (see, e.g. Figer *et al.*, 1999b). It is slightly younger (2−2.5 Myrs, Martins *et al.*, 2008; Najarro *et al.*, 2004) and more massive (Figer *et al.*, 2002) than the Quintuplet cluster. Clarkson *et al.* (2012) have recently measured the kinematic mass of the cluster using *Keck*-LGS adaptive optics.

The deepest *Chandra* observation to date is by Wang *et al.* (2006). Diffuse thermal X-ray emission with a prominent Fe Kα 6.7 keV emission line is seen from the core of the Arches cluster. The surface intensity declines steeply with radius, consistent with a cluster wind origin. This central ($r < 0.6$ pc) "plume" region can be fitted with a single temperature NEI plasma model with $kT = 2.56$ keV, $\tau = 1.2 \times 10^{11}\,\mathrm{cm^{-3}\,s}$, $N_{\mathrm{H}} = 1.1 \times 10^{23}\,\mathrm{cm^{-2}}$ and an intrinsic (2-8keV) luminosity of $L_{\mathrm{x}} = 3.8 \times 10^{33}\,\mathrm{ergs\,s^{-1}}$.

In contrast, the emission in the outer regions of the cluster shows a prominent

line at 6.4 keV, a power-law continuum emission of non-thermal origin, and a non-axissymmetric spatial distribution with a bowshock morphology. This may result from an ongoing collision between the cluster and the adjacent molecular cloud, which has a relative velocity of $120\,\mathrm{km\,s^{-1}}$. The interpretation of the 6.4 keV Fe Kα flourescence emission from neutral Fe is still debated, with Wang *et al.* (2006) favouring a cosmic ray origin but Capelli *et al.* (2011) favouring photoionization of nearby molecular clouds by X-ray photons. Wang *et al.* (2006) find that the SE extension (which is where the 6.4 keV emission is) is best fitted with a PL+Gaussian spectral model with $\Gamma = 1.3^{+1.4}_{-1.1}$ and $N_{\rm H} = 6.2 \times 10^{22}\,\mathrm{cm^{-2}}$, and has an intrinsic $(2-8\,\mathrm{keV})$ luminosity $L_{\rm x} = 4.1 \times 10^{33}\,\mathrm{ergs\,s^{-1}}$. An even more extended "LSBXE" region is fitted with a MEKAL+PL+GAUSSIAN spectral model with $kT = 0.45\,\mathrm{keV}$, $\Gamma = 1.3$(fixed) and $N_{\rm H} = 9.2 \times 10^{22}\,\mathrm{cm^{-2}}$, with an intrinsic $(2-8\,\mathrm{keV})$ $L_{\rm x} = 1.2 \times 10^{34}\,\mathrm{ergs\,s^{-1}}$.

Fig. 15 in Wang *et al.* (2006) shows the radial diffuse X-ray intensity profiles around the Arches cluster. It falls off much less rapidly than simulations (Rockefeller *et al.*, 2005).

Lang *et al.* (2001) detected 8 radio sources in the Arches cluster at 4.9 and 8.5 GHz using the A configuration of the *VLA*. Seven of these sources had counterparts at other wavelengths. The spectral indices of these stars range from 0.3–0.6, although there is one star exhibiting a spectrum of -0.7. The bulk of the emission is consistent with stellar wind emission, whilst the star with the non-thermal spectrum is thought to be tracing a young, lower mass member of the cluster. Although the total integrated flux density over the entire region is not quoted, a lower limit can be set by summing the flux densities of each of the radio sources detected. These lower limits are 2.69 and 3.21 mJy at 4.9 and

8.5 GHz respectively.

A.10 NGC 3576 (RCW 57)

NGC 3576 is a giant HII region located at a distance of 2.8 ± 0.3 kpc (Figuerêdo *et al.*, 2002), and which is projected to within 30 arcminutes of the more distant region NGC 3603. Together these regions make up the RCW 57 complex. The ionizing cluster for NGC 3576 remains deeply embedded in the centre of an extended filamentary dust cloud, and not enough massive stars have yet been found to account for the radio luminosity (Barbosa *et al.*, 2003; Figuerêdo *et al.*, 2002). The evidence for sequential star formation in NGC 3576 remains controversial (see Purcell *et al.*, 2009, and references therein). These authors provide a schematic of the region (their Fig. 16).

Townsley *et al.* (2011) analyzed two *Chandra* pointings. A southern pointing was centered on NGC 3576, while a northern pointing was designed to search for a young stellar cluster associated with the O8V+O8V eclipsing binary HD 97484 (EM Car) and the O9.5Ib star HD 97319. Diffuse emission is seen to the SE of NGC 3576 (hereafter identified as NGC 3576S), while hard X-rays were seen in the northern pointing. Townsley *et al.* (2011) identified these sources as NGC 3576S and NGC 3576N, respectively. The northern pointing revealed a young cluster (termed NGC 3576OB) which appears older than NGC 3576 to the south.

NGC 3576S requires a 2-temperature spectral fit, with $kT_1 = 0.31^{+0.06}_{-0.07}$ and $kT_2 = 0.53$. The absorbing columns are $N_{\rm H} = 1.3 \times 10^{22}\,{\rm cm}^{-2}$ and $N_{\rm H} = 2.5 \times 10^{21}\,{\rm cm}^{-2}$, respectively. The softer component dominates the total emission which has an intrinsic $L_{\rm x} = 1.1 \times 10^{34}\,{\rm ergs\,s}^{-1}$. Townsley *et al.* (2011) suggests that the

hot plasma responsible for this emission has forced itself out through a low-density pathway, analogous to the outflow seen from M17, but seen more face-on and at a slightly earlier phase. A gaussian at 0.72 keV (which accounts for 16% of the total emission) is required for a good fit. This may represent charge exchange processes.

In contrast NGC 3576N requires the presence of a power-law component in spectral models. The intrinsic luminosity is $L_{\rm x} = 1.2 \times 10^{34}\,{\rm ergs\,s^{-1}}$, 24% of which is contributed by a power-law continuum. A 3-temperature model is also required for a good fit, with the hardest NEI component ($kT_3 = 0.7\,{\rm keV}$) accounting for 48% of the total emission. Townsley *et al.* (2011) speculate that the diffuse emission from this region has been enhanced by a recent cavity SN. There is no evidence for charge exchange.

de Pree *et al.* (1999) find the integrated flux density over the whole of NGC 3576 to be $S_{tot} = 71 \pm 1$ Jy at 8.8 GHz using *ATCA* in the B and D configurations. This is 73% of the single-dish, 14.7 GHz flux of 97.8 Jy observed by McGee & Newton (1981). Using *ATCA* has increased the spatial resolution of the observations of NGC 3576 by a factor of $\sim$10 over previous observations.

A.11 NGC 3603

The luminous giant HII region NGC 3603 contains the compact star cluster HD 97950, which is one of the most massive young star clusters in the Milky Way. It contains 3 core H-burning WN-stars and up to 50 O-stars (Drissen *et al.*, 1995). The most massive stars in the core appear to be coeval with an age of about 1 Myr, while less massive stars and stars in the cluster outskirts appear to be older (Me-

lena *et al.*, 2008; Pang *et al.*, 2013, and references therein). It shows clear mass segregation, despite its young age. Pang *et al.* (2013) suggest that dynamical processes may have been dominant for the high mass stars. Star formation appears to have occurred almost instantaneously, with Kudryavtseva *et al.* (2012) deriving an upper limit to the age spread of 0.1 Myr. The distance to NGC 3603 is thought to be 7 ± 1 kpc (Harayama *et al.*, 2008). Banerjee & Kroupa (2013) explore whether a phase of substantial gas-expulsion has occurred in NGC 3603.

A *Chandra* cycle 1 observation was presented by Moffat *et al.* (2002), who noted diffuse X-ray emission within a central region of 2 arcmin radius with an intrinsic luminosity $L_{\rm x} = 2 \times 10^{34}\,{\rm ergs\,s^{-1}}$. However, this is 20% of the integrated point source emission within this region and may be completely due to undetected point sources.

Townsley *et al.* (2011) recently re-analyzed this observation, finding 1328 point sources compared to the 348 sources found by Moffat *et al.* (2002). The diffuse X-ray emission is anti-coincident with the mid-IR emission which traces the surrounding heated dust. This is consistent with the hot plasma from the shocked stellar winds filling the cavities that they have carved. Excluding an area around the core of NGC 3603 (which is likely dominated by unresolved point sources) and a region to the west (which may contain foreground emission related to the NGC 3576 cluster), the diffuse X-ray emission is dominated by an NEI thermal plasma component with $kT_1 = 0.53\,{\rm keV}$, $\tau = 2 \times 10^{10}\,{\rm cm^{-3}\,s}$, $N_{\rm H} = 2 \times 10^{22}\,{\rm cm^{-2}}$, and which contributes 86% of the total intrinsic $L_{\rm x} = 2.6 \times 10^{35}\,{\rm ergs\,s^{-1}}$. No evidence for charge exchange processes was found though the exposure is quite short.

de Pree *et al.* (1999) estimate the flux density of 13 sources at 8.8 GHz to

be 25 Jy using *ATCA* in the B and D configurations. This is only 38% of the single-dish flux density of 65.9 Jy. Moffat *et al.* (2002) investigated the small-scale structure in the region using the longest possible baseline of *ATCA*. They detected two significant but faint radio sources in the central cluster region, the strongre of which is located right at the centre of the cluster. They find a flux density $S_\nu = 3.3 \pm 0.3$ mJy at 3 cm (10 GHz) for this source. This is a reasonable flux if arising from the winds of ∼10–20 hot O/WNL stars as a result of thermal bremsstrahlung emission.

A.12 NGC 2024 (The Flame Nebula)

The Flame Nebula, NGC 2024, is one of the nearest sites of massive star formation ($D = 415$ pc, Anthony-Twarog, 1982). It is part of the Orion B giant molecular cloud (e.g. Mitchell *et al.*, 2001) and is near the Horsehead Nebula. A 3D structure of the region was proposed by Barnes *et al.* (1989) (see also Emprechtinger *et al.*, 2009). (Bik *et al.*, 2003) suggested that the O8V-B2V star IRS 2b is the ionizing source of the HII region, but Burgh *et al.* (2012) note that it could be a supergiant. The age of NGC 2024 is unclear, with estimates ranging from 0.3 Myr (Meyer, 1996) to several Myr (Comeron *et al.*, 1996).

Diffuse X-ray emission with a radius of 0.5 pc from the centre of NGC 2024 was reported by Ezoe *et al.* (2006b). The emission has a very hard continuum ($kT > 8$ keV) and shows a He-like Fe Kα line. Fitting the data with a "leaky absorber" model (where emission from a single temperature plasma reaches the observer via two paths with different absorption) returns $kT \approx 11$ keV with $N_\mathrm{H} = 0.21 \times 10^{22}$ and 3.3×10^{22} cm^{-2}. The intrinsic X-ray luminosity in the $0.5 - 7$ keV

band is $L_{\rm x} = 2 \times 10^{31}\,{\rm ergs\,s^{-1}}$. Ezoe *et al.* (2006b) note that a single massive star with a wind comparable to, or stronger than, that of a typical B0.5V star has enough energetics to power the observed X-ray emission. This work shows that diffuse emission is present in a MSFR in which only late O to early B stars exist.

Rodríguez *et al.* (2003) found 25 compact radio sources in a region of 4'×4' in the Flame Nebula using the A configuration of the *VLA*, 21 of which have counterparts at other wavelengths. Earlier studies by Terzian *et al.* (1968) and Mezger & Ellis (1968) determined the flux density over NGC 2024 using the *NRAO* to be 64.9, 65.9, 63.0 and 58.6 Jy at 1.41, 2.695, 5.0 and 15.35 GHz respectively.

References

Abbott, D.C., Bieging, J.H., Churchwell, E. & Cassinelli, J.P. (1980). VLA radio continuum measurements of mass loss from early-type stars. *ApJ*, **238**, 196–202. 134

Abbott, D.C., Bieging, J.H. & Churchwell, E. (1981). Mass loss from very luminous OB stars and the Cygnus superbubble. *ApJ*, **250**, 645–659. 134

Adelberger, K.L., Steidel, C.C., Shapley, A.E. & Pettini, M. (2003). Galaxies and Intergalactic Matter at Redshift z˜3: Overview. *ApJ*, **584**, 45–75. 1

Aharonian, F., Akhperjanian, A.G., Bazer-Bachi, A.R., Beilicke, M., Benbow, W. *et al.* (2007). Detection of extended very-high-energy γ-ray emission towards the young stellar cluster Westerlund 2. *A&A*, **467**, 1075–1080. 203

Alūzas, R., Pittard, J.M., Hartquist, T.W., Falle, S.A.E.G. & Langton, R. (2012). Numerical simulations of shocks encountering clumpy regions. *MNRAS*, **425**, 2212–2227. 64

Anthony-Twarog, B.J. (1982). The H-beta distance scale for B stars - The Orion association. *AJ*, **87**, 1213–1222. 217

Ascenso, J., Alves, J. & Lago, M.T.V.T. (2009). No evidence of mass segregation in massive young clusters. *A&A*, **495**, 147–155. 11

Axon, D.J. & Taylor, K. (1978). M82 - The exploding galaxy. *Nature*, **274**, 37. 1

Banerjee, S. & Kroupa, P. (2013). Did the Infant R136 and NGC 3603 Clusters Undergo Residual Gas Expulsion? *ApJ*, **764**, 29. 216

Barbosa, C.L., Damineli, A., Blum, R.D. & Conti, P.S. (2003). Gemini Mid-Infrared Imaging of Massive Young Stellar Objects in NGC 3576. *AJ*, **126**, 2411–2420. 214

Barnes, P.J., Crutcher, R.M., Bieging, J.H., Storey, J.W.V. & Willner, S.P. (1989). Orion B (NGC 2024). I - VLA and IR observations of the H II region. *ApJ*, **342**, 883–907. 217

Becker, W., Prinz, T., Winkler, P.F. & Petre, R. (2012). The Proper Motion of the Central Compact Object RX J0822-4300 in the Supernova Remnant Puppis A. *ApJ*, **755**, 141. 128, 166

Beerer, I.M., Koenig, X.P., Hora, J.L., Gutermuth, R.A., Bontemps, S., Megeath, S.T., Schneider, N., Motte, F., Carey, S., Simon, R., Keto, E., Smith, H.A., Allen, L.E., Fazio, G.G., Kraemer, K.E., Price, S., Mizuno, D., Adams, J.D., Hernández, J. & Lucas, P.W. (2010). A Spitzer View of Star Formation in the Cygnus X North Complex. *ApJ*, **720**, 679–693. 30

Benaglia, P., Koribalski, B., Peri, C.S., Marti, J., Sanchez-Sutil, J.R., Dougherty, S.M. & Noriega-Crespo, A. (2013). High resolution radio emission from RCW 49/Westerlund 2. *ArXiv e-prints*. 204

Beuther, H., Linz, H. & Henning, T., eds. (2008). *Massive Star Formation: Observations Confront Theory*, vol. 387 of *Astronomical Society of the Pacific Conference Series*. 1

Bieging, J.H., Abbott, D.C. & Churchwell, E.B. (1982). Mass loss rates for Wolf-Rayet stars from radio continuum observations. *ApJ*, **263**, 207–214. 134

Bieging, J.H., Abbott, D.C. & Churchwell, E.B. (1989). A survey of radio emission from Galactic OB stars. *ApJ*, **340**, 518–536. 38, 134

Bik, A., Lenorzer, A., Kaper, L., Comerón, F., Waters, L.B.F.M., de Koter, A. & Hanson, M.M. (2003). Identification of the ionizing source of NGC 2024. *A&A*, **404**, 249–254. 217

Bik, A., Puga, E., Waters, L.B.F.M., Horrobin, M., Henning, T., Vasyunina, T., Beuther, H., Linz, H., Kaper, L., van den Ancker, M., Lenorzer, A., Churchwell, E., Kurtz, S., Kouwenhoven, M.B.N., Stolte, A., de Koter, A., Thi, W.F., Comerón, F. & Waelkens, C. (2010). Sequential Star Formation in RCW 34: A Spectroscopic Census of the Stellar Content of High-Mass Star-Forming Regions. *ApJ*, **713**, 883–899. 30

Blair, W.P., Morse, J.A., Raymond, J.C., Kirshner, R.P., Hughes, J.P., Dopita, M.A., Sutherland, R.S., Long, K.S. & Winkler, P.F.

(2000). Hubble Space Telescope Observations of Oxygen-rich Supernova Remnants in the Magellanic Clouds. II. Elemental Abundances in N132D and 1E 0102.2-7219. *ApJ*, **537**, 667–689. 127, 166

Bland, J. & Tully, B. (1988). Large-scale bipolar wind in M82. *Nature*, **334**, 43–45. 2

Blondin, J.M., Kallman, T.R., Fryxell, B.A. & Taam, R.E. (1990). Hydrodynamic simulations of stellar wind disruption by a compact X-ray source. *ApJ*, **356**, 591–608. 50

Bodenheimer, P., Tenorio-Tagle, G. & Yorke, H.W. (1979). The gas dynamics of H II regions. II - Two-dimensional axisymmetric calculations. *ApJ*, **233**, 85–96. 26

Bonatto, C., Santos, J.F.C., Jr. & Bica, E. (2006). Mass functions and structure of the young open cluster NGC 6611. *A&A*, **445**, 567–577. 11, 174

Bonnell, I.A. & Bate, M.R. (2005). Binary systems and stellar mergers in massive star formation. *MNRAS*, **362**, 915–920. 11

Bonnell, I.A. & Bate, M.R. (2006). Star formation through gravitational collapse and competitive accretion. *MNRAS*, **370**, 488–494. 9

Bonnell, I.A., Bate, M.R., Clarke, C.J. & Pringle, J.E. (1997). Accretion and the stellar mass spectrum in small clusters. *MNRAS*, **285**, 201–208. 10

Bonnell, I.A., Bate, M.R. & Zinnecker, H. (1998). On the formation of massive stars. *MNRAS*, **298**, 93–102. 11

Bowler, B.P., Waller, W.H., Megeath, S.T., Patten, B.M. & Tamura, M. (2009). An Infrared Census of Star Formation in the Horsehead Nebula. *AJ*, **137**, 3685–3699. 27

Bradamante, F., Matteucci, F. & D'Ercole, A. (1998). The influence of stellar energetics and dark matter on the chemical evolution of dwarf irregulars. *A&A*, **337**, 338–348. 18

Brandl, B.R. (2005). 30 Doradus - a Template for "Real Starbursts"? In R. de Grijs & R.M. González Delgado, eds., *Starbursts: From 30 Doradus to Lyman Break Galaxies*, vol. 329 of *Astrophysics and Space Science Library*, 49. 43

Brandner, W., Grebel, E.K., Barbá, R.H., Walborn, N.R. & Moneti, A. (2001). Hubble Space Telescope NICMOS Detection of a Partially Embedded, Intermediate-Mass, Pre-Main-Sequence Population in the 30 Doradus Nebula. *AJ*, **122**, 858–865. 43

Brandner, W., Clark, J.S., Stolte, A., Waters, R., Negueruela, I. & Goodwin, S.P. (2008). Intermediate to low-mass stellar content of Westerlund 1. *A&A*, **478**, 137–149. 163, 208, 209

Breysacher, J., Azzopardi, M. & Testor, G. (1999). The fourth catalogue of Population I Wolf-Rayet stars in the Large Magellanic Cloud. *A&AS*, **137**, 117–145. 43

Broos, P.S., Feigelson, E.D., Townsley, L.K., Getman, K.V., Wang, J., Garmire, G.P., Jiang, Z. & Tsuboi, Y. (2007). The Young Stellar Population in M17 Revealed by Chandra. *ApJS*, **169**, 353–385. 42, 121, 161, 200, 201

Bruhweiler, F.C., Freire Ferrero, R., Bourdin, M.O. & Gull, T.R. (2010). The Young Interstellar Bubble Within the Rosette Nebula. *ApJ*, **719**, 1872–1883. 75

Burgh, E.B., France, K. & Snow, T.P. (2012). Cosmic Origins Spectrograph Observations of NGC 2024: An Indirect View into the Heart of the Flame. *ApJL*, **756**, L6. 217

Canizares, C.R. & Winkler, P.F. (1981). Evidence for elemental enrichment of Puppis A by a Type II supernova. *ApJL*, **246**, L33–L36. 128, 166

Cantó, J., Raga, A.C. & Rodríguez, L.F. (2000). The Hot, Diffuse Gas in a Dense Cluster of Massive Stars. *ApJ*, **536**, 896–901. 16, 32

Capelli, R., Warwick, R.S., Porquet, D., Gillessen, S. & Predehl, P. (2011). Fe Kα line emission from the Arches cluster region - evidence for ongoing particle bombardment? *A&A*, **530**, A38. 213

Cappa, C.E., Barbá, R., Duronea, N.U., Vasquez, J., Arnal, E.M., Goss, W.M. & Fernández Lajús, E. (2011). A multifrequency study of the active star-forming complex NGC 6357 - I. Interstellar structures linked to the open cluster Pis 24. *MNRAS*, **415**, 2844–2858. 86

Carraro, G., Turner, D., Majaess, D. & Baume, G. (2013). The distance to the young open cluster Westerlund 2. *A&A*, **555**, A50. 203

Castelletti, G., Dubner, G., Golap, K. & Goss, W.M. (2006). New VLA observations of the SNR Puppis A: the radio properties and the correlation with the X-ray emission. *A&A*, **459**, 535–544. 166, 167

Castor, J., McCray, R. & Weaver, R. (1975). Interstellar bubbles. *ApJL*, **200**, L107–L110. xv, 12, 15, 18, 19, 20, 21, 32, 93, 188

Celnik, W.E. (1985). The Rosette nebula. II - Radio continuum and recombination line observations. *A&A*, **144**, 171–178. 205, 206

Chabrier, G. (2003). Galactic Stellar and Substellar Initial Mass Function. *PASP*, **115**, 763–795. 9

Chen, L., de Grijs, R. & Zhao, J.L. (2007). Mass Segregation in Very Young Open Clusters: A Case Study of NGC 2244 and NGC 6530. *AJ*, **134**, 1368–1379. 11, 174

Chevalier, R.A. (2005). Young Core-Collapse Supernova Remnants and Their Supernovae. *ApJ*, **619**, 839–855. 126

Chevalier, R.A. & Clegg, A.W. (1985). Wind from a starburst galaxy nucleus. *Nature*, **317**, 44–+. xv, 15, 16, 17, 18, 19, 20, 21, 32, 188

Chini, R. & Hoffmeister, V. (2008). *Star Formation in M17*, 625. 40, 121, 161, 200

Choudhury, R., Mookerjea, B. & Bhatt, H.C. (2010). Triggered Star Formation and Young Stellar Population in Bright-rimmed Cloud SFO 38. *ApJ*, **717**, 1067–1083. 30

Chu, Y.H. & Mac Low, M.M. (1990). X-rays from superbubbles in the Large Magellanic Cloud. *ApJ*, **365**, 510–521. 34

Chu, Y.H., Chang, H.W., Su, Y.L. & Mac Low, M.M. (1995). X-Rays from Superbubbles in the Large Magellanic Cloud. III. X-Ray–dim Superbubbles. *ApJ*, **450**, 157. 117

Churchwell, E., Whitney, B.A., Babler, B.L., Indebetouw, R., Meade, M.R., Watson, C., Wolff, M.J., Wolfire, M.G., Bania, T.M., Benjamin, R.A., Clemens, D.P., Cohen, M., Devine, K.E., Dickey, J.M., Heitsch, F., Jackson, J.M., Kobulnicky, H.A., Marston, A.P., Mathis, J.S., Mercer, E.P., Stauffer, J.R. & Stolovy, S.R. (2004). RCW 49 at Mid-Infrared Wavelengths: A GLIMPSE from the Spitzer Space Telescope. *ApJS*, **154**, 322–327. 203

Clark, J.S., Negueruela, I., Crowther, P.A. & Goodwin, S.P. (2005). On the massive stellar population of the super star cluster ¡ASTROBJ¿Westerlund 1¡/ASTROBJ¿. *A&A*, **434**, 949–969. 163, 208

Clark, P.C., Bonnell, I.A. & Klessen, R.S. (2008). The star formation efficiency and its relation to variations in the initial mass function. *MNRAS*, **386**, 3–10. 209

Clarkson, W.I., Ghez, A.M., Morris, M.R., Lu, J.R., Stolte, A., McCrady, N., Do, T. & Yelda, S. (2012). Proper Motions of the Arches Cluster with Keck Laser Guide Star Adaptive Optics: The First Kinematic Mass Measurement of the Arches. *ApJ*, **751**, 132. 212

Cole, S., Lacey, C.G., Baugh, C.M. & Frenk, C.S. (2000). Hierarchical galaxy formation. *MNRAS*, **319**, 168–204. 1

Comeron, F. (1997). Dynamical evolution of wind-driven HII regions in strong density gradients. *A&A*, **326**, 1195–1214. 26

Comerón, F. & Schneider, N. (2011). RCW 108: Star formation in a Nearby Troubled Environment. In M. Treyer, T. Wyder, J. Neill, M. Seibert & J. Lee, eds., *UP2010: Have Observations Revealed a Variable Upper End of the Initial Mass Function?*, vol. 440 of *Astronomical Society of the Pacific Conference Series*, 47. 30

Comeron, F., Rieke, G.H. & Rieke, M.J. (1996). Properties of Low-Mass Objects in NGC 2024. *ApJ*, **473**, 294. 217

Condon, J.J. (1992). Radio emission from normal galaxies. *Ann. Rev. Astron. Astrophys.*, **30**, 575–611. 133

Contreras, M.E., Rodriguez, L.F., Gomez, Y. & Velazquez, A. (1996). VLA Observations of Massive Stars at 7 Millimeters. *ApJ*, **469**, 329. 135

Crowther, P.A. (2012). Environments of massive stars and the upper mass limit. In *Death of Massive Stars: Supernovae and Gamma-Ray Bursts*, vol. 279 of *IAU Symposium*, 9–17. 9

Crowther, P.A., Hadfield, L.J., Clark, J.S., Negueruela, I. & Vacca, W.D. (2006). A census of the Wolf-Rayet content in Westerlund 1 from near-infrared imaging and spectroscopy. *MNRAS*, **372**, 1407–1424. 163, 208

Crowther, P.A., Schnurr, O., Hirschi, R., Yusof, N., Parker, R.J., Goodwin, S.P. & Kassim, H.A. (2010). The R136 star cluster hosts several

stars whose individual masses greatly exceed the accepted 150 solar mass stellar mass limit. *MNRAS*, 1103–+. 9, 43

Crutcher, R.M. (2010). Role of Magnetic Fields in Star Formation. *Highlights of Astronomy*, **15**, 438–439. 4

Dale, J.E. & Bonnell, I. (2011). Ionizing feedback from massive stars in massive clusters: fake bubbles and untriggered star formation. *MNRAS*, **414**, 321–328. 49

Dale, J.E. & Bonnell, I.A. (2012). Ionization-induced star formation - III. Effects of external triggering on the initial mass function in clusters. *MNRAS*, **422**, 1352–1362. 27

Dale, J.E., Ercolano, B. & Bonnell, I.A. (2012). Ionizing feedback from massive stars in massive clusters - II. Disruption of bound clusters by photoionization. *MNRAS*, **424**, 377–392. 27, 49

Damiani, F. (2010). X-rays from young star clusters: a complement to optical and infrared views. In R. de Grijs & J.R.D. Lépine, eds., *IAU Symposium*, vol. 266 of *IAU Symposium*, 190–202. 34

Damiani, F., Flaccomio, E., Micela, G., Sciortino, S., Harnden, F.R., Jr. & Murray, S.S. (2004). A Deep Chandra X-Ray Observation of the Rich Young Cluster NGC 6530. I. The X-Ray Source Catalog and the Cluster Population. *ApJ*, **608**, 781–796. 211

de Pree, C.G., Nysewander, M.C. & Goss, W.M. (1999). NGC 3576 and NGC 3603: Two Luminous Southern H II Regions Observed at High Resolution with the Australia Telescope Compact Array. *AJ*, **117**, 2902–2918. 215, 216

Deeg, H.J., Brinks, E., Duric, N., Klein, U. & Skillman, E. (1993). New 325 MHz observations of H II galaxies - The mechanisms that shape the unusual radio spectra. *ApJ*, **410**, 626–649.

Deharveng, L., Schuller, F., Anderson, L.D., Zavagno, A., Wyrowski, F., Menten, K.M., Bronfman, L., Testi, L., Walmsley, C.M. & Wienen, M. (2010). A gallery of bubbles. The nature of the bubbles observed by Spitzer and what ATLASGAL tells us about the surrounding neutral material. *A&A*, **523**, A6. 31

Dekel, A. & Silk, J. (1986). The origin of dwarf galaxies, cold dark matter, and biased galaxy formation. *ApJ*, **303**, 39–55. 11

Dickel, J.R. & Milne, D.K. (1991). Radio Imaging of the Supernova Remnant N132D in the Large Magellanic Cloud. In R. Haynes & D. Milne, eds., *The Magellanic Clouds*, vol. 148 of *IAU Symposium*, 349. 166

Dicker, S.R., Mason, B.S., Korngut, P.M., Cotton, W.D., Compiègne, M., Devlin, M.J., Martin, P.G., Ade, P.A.R., Benford, D.J., Irwin, K.D., Maddalena, R.J., McMullin, J.P., Shepherd, D.S., Sievers, A., Staguhn, J.G. & Tucker, C. (2009). 90 GHz and 150 GHz Observations of the Orion M42 Region. A Submillimeter to Radio Analysis. *ApJ*, **705**, 226–236. 205

Dorland, H. & Montmerle, T. (1987). Hollow H II regions. II - Mechanism for wind energy dissipation and diffuse X-ray emission. *A&A*, **177**, 243–257. 120

Dorland, H., Montmerle, T. & Doom, C. (1986). Hollow H II regions. I - Effects of stellar evolution and wind energy dissipation. *A&A*, **160**, 1–17. 120

Dougherty, S.M. & Williams, P.M. (2000). Non-thermal emission in Wolf-Rayet stars: are massive companions required? *MNRAS*, **319**, 1005–1010. 134

Dougherty, S.M., Clark, J.S., Negueruela, I., Johnson, T. & Chapman, J.M. (2010). Radio emission from the massive stars in the galactic super star cluster Westerlund 1. *A&A*, **511**, A58. 164, 165, 210

Draine, B.T. & Woods, D.T. (1991). Supernova remnants in dense clouds. I - Blast-wave dynamics and X-ray irradiation. *ApJ*, **383**, 621–638. 2, 12

Drissen, L., Moffat, A.F.J., Walborn, N.R. & Shara, M.M. (1995). The Dense Galactic Starburst NGC 3603. I. HST/FOS Spectroscopy of Individual Stars in the Core and the source of Ionization and Kinetic Energy. *AJ*, **110**, 2235. 215

Dubner, G., Loiseau, N., Rodríguez-Pascual, P., Smith, M.J.S., Giacani, E. & Castelletti, G. (2013). The most complete and detailed X-ray view of the SNR Puppis A. *A&A*, **555**, A9. 129

Dubner, G.M., Braun, R., Winkler, P.F. & Goss, W.M. (1991). VLA observations of the supernova remnant Puppus A at 327 and 1515 MHz. *AJ*, **101**, 1466–1471. 167

Dunne, B.C., Chu, Y.H., Chen, C.H.R., Lowry, J.D., Townsley, L., Gruendl, R.A., Guerrero, M.A. & Rosado, M. (2003). Diffuse X-Ray Emission from the Quiescent Superbubble M17, the Omega Nebula. *ApJ*, **590**, 306–313. 92, 120, 121, 201

Dyson, J.E. (1994). Massive stars and their interactions with their environment. In T.P. Ray & S.V.W. Beckwith, eds., *Star Formation and Techniques in Infrared and mm-Wave Astronomy*, vol. 431 of *Lecture Notes in Physics, Berlin Springer Verlag*, 93–124. 56

Dyson, J.E. & Williams, D.A. (1980). *Physics of the interstellar medium*. 13

Dyson, J.E., Arthur, S.J. & Hartquist, T.W. (2002). The evolution of mass loaded supernova remnants. I. Constant and Mach Number dependent mass injection rates. *A&A*, **390**, 1063–1074. 88

Edgar, R. & Clarke, C. (2004). The effect of radiative feedback on Bondi-Hoyle flow around a massive star. *MNRAS*, **349**, 678–686. 7

Efstathiou, G. (2000). A model of supernova feedback in galaxy formation. *MNRAS*, **317**, 697–719. 29

Eichler, D. & Usov, V. (1993). Particle acceleration and nonthermal radio emission in binaries of early-type stars. *ApJ*, **402**, 271–279. 38

Elmegreen, B.G. & Lada, C.J. (1977). Sequential formation of subgroups in OB associations. *ApJ*, **214**, 725–741. 31

Elmegreen, B.G., Lada, C.J. & Dickinson, D.F. (1979). The structure and extent of the giant molecular cloud near M17. *ApJ*, **230**, 415. 200

Elmegreen, B.G., Palouš, J. & Ehlerová, S. (2002). Environmental dependences for star formation triggered by expanding shell collapse. *MNRAS*, **334**, 693–698. 12

Emprechtinger, M., Wiedner, M.C., Simon, R., Wieching, G., Volgenau, N.H., Bielau, F., Graf, U.U., Güsten, R., Honingh, C.E., Jacobs, K., Rabanus, D., Stutzki, J. & Wyrowski, F. (2009). The molecular environment of the massive star forming region NGC 2024: Multi CO transition analysis. *A&A*, **496**, 731–739. 217

Er, X.Y., Jiang, Z.B. & Fu, Y.N. (2009). A Numerical Simulation Study of Mass Segregation in Embedded Stellar Clusters. *ChA&A*, **33**, 139–150. 11

Er, X.Y., Jiang, Z.B. & Fu, Y.N. (2013). Mass segregation of embedded clusters in the Milky Way. *Research in Astronomy and Astrophysics*, **13**, 277–289. 174

Eriksen, K.A., Morse, J.A., Kirshner, R.P. & Winkler, P.F. (2001). Fabry-Perot [O III] λ5007 Å observations of the SMC oxygen-rich SNR 1E 0102-72.9. In S.S. Holt & U. Hwang, eds., *Young Supernova Remnants*, vol. 565 of *American Institute of Physics Conference Series*, 193–196. 123, 125

Everett, J.E. & Churchwell, E. (2010). Dusty Wind-blown Bubbles. *ApJ*, **713**, 592–602. 56, 194

Ezoe, Y., Kokubun, M., Makishima, K., Sekimoto, Y. & Matsuzaki, K. (2006a). Investigation of Diffuse Hard X-Ray Emission from the Massive Star-forming Region NGC 6334. *ApJ*, **638**, 860–877. 34, 91

Ezoe, Y., Kokubun, M., Makishima, K., Sekimoto, Y. & Matsuzaki, K. (2006b). The Discovery of Diffuse X-Ray Emission in NGC 2024, One of the Nearest Massive Star-forming Regions. *ApJL*, **649**, L123–L128. 91, 92, 217, 218

Ezoe, Y., Hamaguchi, K., Gruendl, R.A., Chu, Y.H., Petre, R. & Corcoran, M.F. (2009). Suzaku and XMM-Newton Observations of Diffuse X-Ray Emission from the Eastern Tip Region of the Carina Nebula. *PASJ*, **61**, 123. 34

Fall, S.M., Krumholz, M.R. & Matzner, C.D. (2010). Stellar Feedback in Molecular Clouds and its Influence on the Mass Function of Young Star Clusters. *ApJL*, **710**, L142–L146. 49

Fan, X., Carilli, C.L. & Keating, B. (2006). Observational Constraints on Cosmic Reionization. *Ann. Rev. Astron. Astrophys.*, **44**, 415–462. 2

Feast, M.W., Thackeray, A.D. & Wesselink, A.J. (1960). The brightest stars in the Magellanic Clouds. *MNRAS*, **121**, 337. 43

Felli, M., Johnston, K.J. & Churchwell, E. (1980). An unusual radio point source in M17. *ApJL*, **242**, L157–L161. 161, 202

Figer, D.F. (2005). An upper limit to the masses of stars. *Nature*, **434**, 192–194. 9

Figer, D.F., Kim, S.S., Morris, M., Serabyn, E., Rich, R.M. & McLean, I.S. (1999a). Hubble Space Telescope/NICMOS Observations of Massive Stellar Clusters near the Galactic Center. *ApJ*, **525**, 750–758. 207

Figer, D.F., McLean, I.S. & Morris, M. (1999b). Massive Stars in the Quintuplet Cluster. *ApJ*, **514**, 202–220. 207, 212

Figer, D.F., Najarro, F., Gilmore, D., Morris, M., Kim, S.S., Serabyn, E., McLean, I.S., Gilbert, A.M., Graham, J.R., Larkin, J.E., Levenson, N.A. & Teplitz, H.I. (2002). Massive Stars in the Arches Cluster. *ApJ*, **581**, 258–275. 212

Figuerêdo, E., Blum, R.D., Damineli, A. & Conti, P.S. (2002). The Stellar Content of Obscured Galactic Giant H II Regions. IV. NGC 3576. *AJ*, **124**, 2739–2748. 214

Flanagan, K.A., Canizares, C.R., Dewey, D., Houck, J.C., Fredericks, A.C., Schattenburg, M.L., Markert, T.H. & Davis, D.S. (2004). Chandra High-Resolution X-Ray Spectrum of Supernova Remnant 1E 0102.2-7219. *ApJ*, **605**, 230–246. 125

Franco, J., Tenorio-Tagle, G. & Bodenheimer, P. (1990). On the formation and expansion of H II regions. *ApJ*, **349**, 126–140. 27

Freyer, T., Hensler, G. & Yorke, H.W. (2003). Massive Stars and the Energy Balance of the Interstellar Medium. I. The Impact of an Isolated 60 M_{solar} Star. *ApJ*, **594**, 888–910. 173

Freyer, T., Hensler, G. & Yorke, H.W. (2006). Massive Stars and the Energy Balance of the Interstellar Medium. II. The 35 Solar Mass Star and a Solution to the "Missing Wind Problem". *ApJ*, **638**, 262–280. 53, 173

Fujita, Y., Hayashida, K., Takahashi, H. & Takahara, F. (2009). Suzaku Observation of Diffuse X-Ray Emission from the Open Cluster Westerlund 2: a Hypernova Remnant? *PASJ*, **61**, 1229–. 203

Gaensler, B.M. & Wallace, B.J. (2003). A Multifrequency Radio Study of Supernova Remnant G292.0+1.8 and Its Pulsar Wind Nebula. *ApJ*, **594**, 326–339. 126

Gaetz, T.J., Butt, Y.M., Edgar, R.J., Eriksen, K.A., Plucinsky, P.P., Schlegel, E.M. & Smith, R.K. (2000). Chandra X-Ray Observatory Arcsecond Imaging of the Young, Oxygen-rich Supernova Remnant 1E 0102.2-7219. *ApJL*, **534**, L47–L50. 125

Garay, G., Moran, J.M. & Reid, M.J. (1987). Compact continuum radio sources in the Orion Nebula. *ApJ*, **314**, 535–550. 205

Garcia-Segura, G. & Franco, J. (1996). From Ultracompact to Extended H II Regions. *ApJ*, **469**, 171. 27

Genzel, R. & Downes, D. (1977). H_2O in the Galaxy: sites of newly formed OB stars. **30**, 145–168. 161, 202

Ghavamian, P., Long, K.S., Blair, W.P., Park, S., Fesen, R., Gaensler, B.M., Hughes, J.P., Rho, J. & Winkler, P.F. (2012). Spitzer Imaging and Spectral Mapping of the Oxygen-rich Supernova Remnant G292.0+1.8. *ApJ*, **750**, 39. 126

Gonzalez, M. & Safi-Harb, S. (2003). New Constraints on the Energetics, Progenitor Mass, and Age of the Supernova Remnant G292.0+1.8 Containing PSR J1124-5916. *ApJL*, **583**, L91–L94. 126

Goudis, C. (1975). The radio spectra of four H II regions /Orion B, M8, M16 and M17/. *Ap&SS*, **37**, 455–462. 212

Goudis, C. (1976). A classification of the available astrophysical data of particular H II regions. V - M8 and M20: Mapping and physical parameters of the objects. *Ap&SS*, **40**, 281–314. 212

Gray, W.J. & Scannapieco, E. (2011). Formation of Compact Stellar Clusters by High-redshift Galaxy Outflows. II. Effect of Turbulence and Metal-line Cooling. *ApJ*, **733**, 88. 1

Grebel, E.K. & Chu, Y.H. (2000). Hubble Space Telescope Photometry of Hodge 301: An "Old" Star Cluster in 30 Doradus. *AJ*, **119**, 787–799. 43

Gritschneder, M., Naab, T., Walch, S., Burkert, A. & Heitsch, F. (2009). Driving Turbulence and Triggering Star Formation by Ionizing Radiation. *ApJL*, **694**, L26–L30. 27, 31

Güdel, M., Briggs, K.R., Montmerle, T., Audard, M., Rebull, L. & Skinner, S.L. (2008). Million-Degree Plasma Pervading the Extended Orion Nebula. *Science*, **319**, 309–. 33, 39, 41, 92, 204

Guo, Q., White, S., Li, C. & Boylan-Kolchin, M. (2010). How do galaxies populate dark matter haloes? *MNRAS*, **404**, 1111–1120. 2

Hanson, M.M., Howarth, I.D. & Conti, P.S. (1997). The Young Massive Stellar Objects of M17. *ApJ*, **489**, 698. 121, 200

Harayama, Y., Eisenhauer, F. & Martins, F. (2008). The Initial Mass Function of the Massive Star-forming Region NGC 3603 from Near-Infrared Adaptive Optics Observations. *ApJ*, **675**, 1319–1342. 216

Harper, D.A., Low, F.J., Rieke, G.H., Harley, A. & Thronson, A.J. (1976). The infrared emission of M17. *ApJ*, **205**, 136–143. 161, 202

Harper-Clark, E. & Murray, N. (2009). One-Dimensional Dynamical Models of the Carina Nebula Bubble. *ApJ*, **693**, 1696–1712. 15, 18, 19, 20, 21, 22, 23, 48, 63, 92, 96, 118, 119, 120, 189

Harper-Clark, E. & Murray, N. (2011). Simulations of Massive Star Cluster Formation and Feedback in Turbulent Giant Molecular Clouds. In J. Alves, B.G. Elmegreen, J.M. Girart & V. Trimble, eds., *Computational Star Formation*, vol. 270 of *IAU Symposium*, 235–238. 23

Heckman, T.M., Lehnert, M.D., Strickland, D.K. & Armus, L. (2000). Absorption-Line Probes of Gas and Dust in Galactic Superwinds. *ApJS*, **129**, 493–516. 2

Heiles, C. (1998). Whence the Local Bubble, Gum, Orion? GSH 238+00+09, A Nearby Major Superbubble toward Galactic Longitude 238 degrees. *ApJ*, **498**, 689. 39

Henderson, C.B. & Stassun, K.G. (2012). Time-series Photometry of Stars in and around the Lagoon Nebula. I. Rotation Periods of 290 Low-mass Pre-main-sequence Stars in NGC 6530. *ApJ*, **747**, 51. 211

Henize, K.G. (1956). Catalogues of Hα-Emission Stars and Nebulae in the Magellanic Clouds. *ApJS*, **2**, 315. 43

Hensberge, H., Pavlovski, K. & Verschueren, W. (2000). The eclipsing binary V578 Mon in the Rosette nebula: age and distance to NGC 2244 using Fourier disentangled component spectra. *A&A*, **358**, 553–571. 121, 206

H.E.S.S. Collaboration *et al.* (2011). Revisiting the Westerlund 2 field with the HESS telescope array. *A&A*, **525**, A46. 203

Hester, J.J., Scowen, P.A., Sankrit, R., Lauer, T.R., Ajhar, E.A., Baum, W.A., Code, A., Currie, D.G., Danielson, G.E., Ewald, S.P., Faber, S.M., Grillmair, C.J., Groth, E.J., Holtzman, J.A., Hunter, D.A., Kristian, J., Light, R.M., Lynds, C.R., Monet, D.G., O'Neil, E.J., Jr., Shaya, E.J., Seidelmann, P.K. & Westphal, J.A. (1996). Hubble Space Telescope WFPC2 Imaging of M16: Photoevaporation and Emerging Young Stellar Objects. *AJ*, **111**, 2349. 30

Hillenbrand, L.A. (1997). On the Stellar Population and Star-Forming History of the Orion Nebula Cluster. *AJ*, **113**, 1733–1768. 11, 174

Hillenbrand, L.A. & Hartmann, L.W. (1998). A Preliminary Study of the Orion Nebula Cluster Structure and Dynamics. *ApJ*, **492**, 540. 11, 174

Hoffmeister, V.H., Chini, R., Scheyda, C.M., Schulze, D., Watermann, R., Nürnberger, D. & Vogt, N. (2008). The Stellar Population of M17. *ApJ*, **686**, 310–324. 40, 121, 161, 200, 201

Hughes, J.P. (1987). X-ray studies of the supernova remnant N132D. I - Morphology. *ApJ*, **314**, 103–110. 127, 166

Hughes, J.P. (1988). X-Ray Observations of SNR EO102.2-72.2 in the SMC. In R.S. Roger & T.L. Landecker, eds., *IAU Colloq. 101: Supernova Remnants and the Interstellar Medium*, 125. 125

Hughes, J.P. & Singh, K.P. (1994). Elemental abundances of the supernova remnant G292.0+1.8: Evidence for a massive progenitor. *ApJ*, **422**, 126–135. 126

Hughes, J.P., Rakowski, C.E. & Decourchelle, A. (2000). Electron Heating and Cosmic Rays at a Supernova Shock from Chandra X-Ray Observations of 1E 0102.2-7219. *ApJL*, **543**, L61–L65. 125, 126

Hughes, J.P., Slane, P.O., Park, S., Roming, P.W.A. & Burrows, D.N. (2003). An X-Ray Pulsar in the Oxygen-rich Supernova Remnant G292.0+1.8. *ApJL*, **591**, L139–L142. 127

Hummer, D.G. (1988). A fast and accurate method for evaluating the nonrelativistic free-free Gaunt factor for hydrogenic ions. *ApJ*, **327**, 477–484. 138

Hwang, U., Canizares, C.R., Markert, T.H. & Hughes, J.P. (1992). High-Resolution X-Ray Spectroscopy of the Supernova Remnant N132D. In

American Astronomical Society Meeting Abstracts #180, vol. 24 of *Bulletin of the American Astronomical Society*, 790. 127

Hwang, U., Petre, R. & Flanagan, K.A. (2008). X-Ray-emitting Ejecta in Puppis A Observed with Suzaku. *ApJ*, **676**, 378–389. 129

Hyodo, Y., Tsujimoto, M., Hamaguchi, K., Koyama, K., Kitamoto, S., Maeda, Y., Tsuboi, Y. & Ezoe, Y. (2008). Suzaku Spectroscopy of Extended X-Ray Emission in M17. *PASJ*, **60**, 85. 121, 201

Jeans, J.H. (1902). The Stability of a Spherical Nebula. *Royal Society of London Philosophical Transactions Series A*, **199**, 1–53. 3

Jiang, Z., Yao, Y., Yang, J., Ando, M., Kato, D., Kawai, T., Kurita, M., Nagata, T., Nagayama, T., Nakajima, Y., Nagashima, C., Sato, S., Tamura, M., Nakaya, H. & Sugitani, K. (2002). Deep Near-Infrared Survey toward the M17 Region. *ApJ*, **577**, 245–259. 11, 174

Johnson, C.O., Depree, C.G. & Goss, W.M. (1998). A High-Resolution VLA Study of M17-UC1. *ApJ*, **500**, 302. 161, 202

Kahn, F.D. (1954). The acceleration of interstellar clouds. *Bull. Astron. Inst. Netherlands*, **12**, 187. 26

Kahn, F.D. (1974). Cocoons around early-type stars. *A&A*, **37**, 149–162. 7

Katsuda, S., Mori, K., Tsunemi, H., Park, S., Hwang, U., Burrows, D.N., Hughes, J.P. & Slane, P.O. (2008). Discovery of Fast-Moving X-Ray-Emitting Ejecta Knots in the Oxygen-Rich Supernova Remnant Puppis A. *ApJ*, **678**, 297–302. 128

Kavanagh, P.J., Norci, L. & Meurs, E.J.A. (2011). Diffuse thermal X-ray emission in the core of the young massive cluster Westerlund 1. *New Astr.*, **16**, 461–469. 34, 209, 210

Kennicutt, R.C., Jr. (1998). The Global Schmidt Law in Star-forming Galaxies. *ApJ*, **498**, 541. 4

Kereš, D., Katz, N., Davé, R., Fardal, M. & Weinberg, D.H. (2009). Galaxies in a simulated ΛCDM universe - II. Observable properties and constraints on feedback. *MNRAS*, **396**, 2332–2344. 1

Kim, S., Staveley-Smith, L., Dopita, M.A., Sault, R.J., Freeman, K.C., Lee, Y. & Chu, Y.H. (2003). A Neutral Hydrogen Survey of the Large Magellanic Cloud: Aperture Synthesis and Multibeam Data Combined. *ApJS*, **148**, 473–486. 128

Kleinmann, D.E. (1973). Bright Infrared Sources in M17. *Astrophys. Lett.*, **13**, 49. 201

Knowles, S.H., Caswell, J.L. & Goss, W.M. (1976). Excited OH radiation from the2113/2- J= 5/2 state in southern H II regions. *MNRAS*, **175**, 537–556. 161, 202

Koen, C. (2006). On the upper limit on stellar masses in the Large Magellanic Cloud cluster R136. *MNRAS*, **365**, 590–594. 9

Koenig, X.P., Leisawitz, D.T., Benford, D.J., Rebull, L.M., Padgett, D.L. & Assef, R.J. (2012). Wide-field Infrared Survey Explorer Ob-

servations of the Evolution of Massive Star-forming Regions. *ApJ*, **744**, 130. 1

Krumholz, M.R. & Matzner, C.D. (2009). The Dynamics of Radiation-pressure-dominated H II Regions. *ApJ*, **703**, 1352–1362. 25, 49, 55

Krumholz, M.R. & Thompson, T.A. (2012). Direct Numerical Simulation of Radiation Pressure-driven Turbulence and Winds in Star Clusters and Galactic Disks. *ApJ*, **760**, 155. 49

Krumholz, M.R., Matzner, C.D. & McKee, C.F. (2006). The Global Evolution of Giant Molecular Clouds. I. Model Formulation and Quasi-Equilibrium Behavior. *ApJ*, **653**, 361–382. 4

Krumholz, M.R., Klein, R.I. & McKee, C.F. (2007). Radiation-Hydrodynamic Simulations of Collapse and Fragmentation in Massive Protostellar Cores. *ApJ*, **656**, 959–979. 7, 8

Krumholz, M.R., Klein, R.I., McKee, C.F., Offner, S.S.R. & Cunningham, A.J. (2009). The Formation of Massive Star Systems by Accretion. *Science*, **323**, 754–. 7, 8

Kudryavtseva, N., Brandner, W., Gennaro, M., Rochau, B., Stolte, A., Andersen, M., Da Rio, N., Henning, T., Tognelli, E., Hogg, D., Clark, S. & Waters, R. (2012). Instantaneous Starburst of the Massive Clusters Westerlund 1 and NGC 3603 YC. *ApJL*, **750**, L44. 216

Kuiper, R., Klahr, H., Beuther, H. & Henning, T. (2010). Circumventing the Radiation Pressure Barrier in the Formation of Massive Stars via Disk Accretion. *ApJ*, **722**, 1556–1576. 7, 8

Kurtz, S., Churchwell, E. & Wood, D.O.S. (1994). Ultracompact H II regions. 2: New high-resolution radio images. *ApJS*, **91**, 659–712. 26

Lada, C.J., Alves, J. & Lada, E.A. (1996). Near-Infrared Imaging of Embedded Clusters: NGC 1333. *AJ*, **111**, 1964. 11, 174

Lang, C.C., Goss, W.M. & Rodríguez, L.F. (2001). Very Large Array Detection of the Ionized Stellar Winds Arising from Massive Stars in the Galactic Center Arches Cluster. *ApJL*, **551**, L143–L146. 135, 143, 213

Lang, C.C., Johnson, K.E., Goss, W.M. & Rodríguez, L.F. (2005). Stellar Winds and Embedded Star Formation in the Galactic Center Quintuplet and Arches Clusters: Multifrequency Radio Observations. *AJ*, **130**, 2185–2196. 135, 143, 208

Larson, R.B. (1982). Mass spectra of young stars. *MNRAS*, **200**, 159–174. 10

Larson, R.B. (1998). Early star formation and the evolution of the stellar initial mass function in galaxies. *MNRAS*, **301**, 569–581. 10

Larson, R.B. & Starrfield, S. (1971). On the formation of massive stars and the upper limit of stellar masses. *A&A*, **13**, 190–197. 7

Law, C. & Yusef-Zadeh, F. (2004). X-Ray Observations of Stellar Clusters Near the Galactic Center. *ApJ*, **611**, 858–870. 34, 207

Leitherer, C. & Robert, C. (1991). Observations of stellar winds from hot stars at 1.3 millimeters. *ApJ*, **377**, 629–638. 135

Leitherer, C., Drissen, L. & Robert, C. (1992). Injection of Mass and Energy Into the ISM by Massive Stars. In B. Barbuy & A. Renzini, eds., *The Stellar Populations of Galaxies*, vol. 149 of *IAU Symposium*, 447. 174

Leitherer, C., Chapman, J.M. & Koribalski, B. (1995). Radio Continuum Measurements of Southern Early-Type Stars. *ApJ*, **450**, 289. 134

Liermann, A., Hamann, W.R. & Oskinova, L.M. (2012). The Quintuplet cluster. III. Hertzsprung-Russell diagram and cluster age. *A&A*, **540**, A14. 207

Lim, B., Chun, M.Y., Sung, H., Park, B.G., Lee, J.J., Sohn, S.T., Hur, H. & Bessell, M.S. (2013). The Starburst Cluster Westerlund 1: The Initial Mass Function and Mass Segregation. *AJ*, **145**, 46. 11, 163, 174, 209

Linsky, J.L., Gagné, M., Mytyk, A., McCaughrean, M. & Andersen, M. (2007). Chandra Observations of the Eagle Nebula. I. Embedded Young Stellar Objects near the Pillars of Creation. *ApJ*, **654**, 347–360. 27

Lopez, L.A., Krumholz, M.R., Bolatto, A.D., Prochaska, J.X. & Ramirez-Ruiz, E. (2011). What Drives the Expansion of Giant H II Regions?: A Study of Stellar Feedback in 30 Doradus. *ApJ*, **731**, 91. 2, 12, 48

Mac Low, M.M. & Klessen, R.S. (2004). Control of star formation by supersonic turbulence. *Reviews of Modern Physics*, **76**, 125–194. 5

Mac Low, M.M., Toraskar, J., Oishi, J.S. & Abel, T. (2007). Dynamical Expansion of H II Regions from Ultracompact to Compact Sizes in Turbulent, Self-gravitating Molecular Clouds. *ApJ*, **668**, 980–992. 27

Martins, F., Hillier, D.J., Paumard, T., Eisenhauer, F., Ott, T. & Genzel, R. (2008). The most massive stars in the Arches cluster. *A&A*, **478**, 219–233. 212

Martins, F., Mahy, L., Hillier, D.J. & Rauw, G. (2012). A quantitative study of O stars in NGC 2244 and the Monoceros OB2 association. *A&A*, **538**, A39. 121, 206

Massey, P. & Hunter, D.A. (1998). Star Formation in R136: A Cluster of O3 Stars Revealed by Hubble Space Telescope Spectroscopy. *ApJ*, **493**, 180. 9

Mathewson, D.S., Healey, J.R. & Rome, J.M. (1962). A Radio Survey of the Southern Milky Way at a Frequency of 1440 Mc/s. I. The Isophotes and the Discrete Sources. *Australian Journal of Physics*, **15**, 354. 167

Matzner, C.D. (2002). On the Role of Massive Stars in the Support and Destruction of Giant Molecular Clouds. *ApJ*, **566**, 302–314. 2, 12

McGee, R.X. & Newton, L.M. (1981). Recombination lines /76 alpha/ of hydrogen, helium, carbon and one other element from high-emission-measure H II regions. *MNRAS*, **196**, 889–905. 215

McKee, C.F. & Ostriker, E.C. (2007). Theory of Star Formation. *Ann. Rev. Astron. Astrophys.*, **45**, 565–687. 5

McKee, C.F. & Ostriker, J.P. (1977). A theory of the interstellar medium - Three components regulated by supernova explosions in an inhomogeneous substrate. *ApJ*, **218**, 148–169. 11, 29

McMillan, S.L.W., Vesperini, E. & Portegies Zwart, S.F. (2007). A Dynamical Origin for Early Mass Segregation in Young Star Clusters. *ApJL*, **655**, L45–L49. 10

Meaburn, J., Dyson, J.E. & Hartquist, T.W. (1988). The sealing of fragmenting shells - evidence from optical studies of the VELA remnant. *MNRAS*, **230**, 243–247. 58

Meixner, M., Haas, M.R., Tielens, A.G.G.M., Erickson, E.F. & Werner, M. (1992). Far-infrared observations of M17SW - The clumpy structure of the photodissociation region. *ApJ*, **390**, 499–513. 200

Melena, N.W., Massey, P., Morrell, N.I. & Zangari, A.M. (2008). The Massive Star Content of NGC 3603. *AJ*, **135**, 878–891. 215

Melnick, J. (1985). The 30 Doradus nebula. I - Spectral classification of 69 stars in the central cluster. *A&A*, **153**, 235–244. 43

Menten, K.M., Reid, M.J., Forbrich, J. & Brunthaler, A. (2007). The distance to the Orion Nebula. *A&A*, **474**, 515–520. 38

Meyer, M.R. (1996). The Stellar Populations of Deeply Embedded Young Clusters: Near-Infrared Spectroscopy and Emergent Mass Distributions. *PASP*, **108**, 380. 217

Mezger, P.G. & Ellis, S.A. (1968). On the Electron Temperatures of the Orion Nebula and NGC 2024 (II): Observations of the Radio Recombination Lines. *Astrophys. Lett.*, **1**, 159–165. 218

Mezger, P.G. & Henderson, A.P. (1967). Galactic H II Regions. I. Observations of Their Continuum Radiation at the Frequency 5 GHz. *ApJ*, **147**, 471. 36

Milne, D.K. (1971). Radio observations of the supernova remnants IC443 and Puppis A. *Australian Journal of Physics*, **24**, 429. 167

Milne, D.K. & Hill, E.R. (1969). Radio emission from 16 possible supernova remnants. *Australian Journal of Physics*, **22**, 211. 167

Milne, D.K., Goss, W.M. & Danziger, I.J. (1983). Radio observations of the SNR Puppis A. *MNRAS*, **204**, 237–239. 167

Milne, D.K., Stewart, R.T. & Haynes, R.F. (1993). Radio polarization in the supernova remnant Puppis A (G 260.4 - 3.4). *MNRAS*, **261**, 366–370. 166, 167

Mitchell, G.F., Johnstone, D., Moriarty-Schieven, G., Fich, M. & Tothill, N.F.H. (2001). A Submillimeter Dust and Gas Study of the Orion B Molecular Cloud. *ApJ*, **556**, 215–229. 217

Moffat, A.F.J., Shara, M.M. & Potter, M. (1991). New Wolf-Rayet stars in Galactic open clusters - Sher 1 and the giant H II region core Westerlund 2. *AJ*, **102**, 642–653. 23

Moffat, A.F.J., Corcoran, M.F., Stevens, I.R., Skalkowski, G., Marchenko, S.V., Mücke, A., Ptak, A., Koribalski, B.S., Brenneman, L., Mushotzky, R., Pittard, J.M., Pollock, A.M.T. & Brandner, W. (2002). Galactic Starburst NGC 3603 from X-Rays to Radio. *ApJ*, **573**, 191–198. 33, 216, 217

Morse, J.A., Winkler, P.F. & Kirshner, R.P. (1995). Spatially Resolved Kinematics and Longslit Spectroscopy of the Young, Oxygen-Rich Supernova Remnant N132D in the Large Magellanic Cloud. *AJ*, **109**, 2104. 127, 166

Mouschovias, T.C. (1991). Magnetic braking, ambipolar diffusion, cloud cores, and star formation - Natural length scales and protostellar masses. *ApJ*, **373**, 169–186. 4

Muno, M.P., Law, C., Clark, J.S., Dougherty, S.M., de Grijs, R., Portegies Zwart, S. & Yusef-Zadeh, F. (2006). Diffuse, Nonthermal X-Ray Emission from the Galactic Star Cluster Westerlund 1. *ApJ*, **650**, 203–211. 92, 209

Murray, N., Quataert, E. & Thompson, T.A. (2010). The Disruption of Giant Molecular Clouds by Radiation Pressure and the Efficiency of Star Formation in Galaxies. *ApJ*, **709**, 191–209. 23, 49

Murray, S.D. & Lin, D.N.C. (1996). Coalescence, Star Formation, and the Cluster Initial Mass Function. *ApJ*, **467**, 728. 10

Nagata, T., Woodward, C.E., Shure, M., Pipher, J.L. & Okuda, H. (1990). AFGL 2004 - an infrared quintuplet near the Galactic center. *ApJ*, **351**, 83–88. 207

Najarro, F., Figer, D.F., Hillier, D.J. & Kudritzki, R.P. (2004). Metallicity in the Galactic Center: The Arches Cluster. *ApJL*, **611**, L105–L108. 212

O'dell, C.R. (2001). The Orion Nebula and its Associated Population. *Ann. Rev. Astron. Astrophys.*, **39**, 99–136. 39

Oey, M.S. (1996). The Dynamics of Superbubbles in the Large Magellanic Cloud. *ApJ*, **467**, 666. 120

Oskinova, L.M., Gruendl, R.A., Ignace, R., Chu, Y.H., Hamann, W.R. & Feldmeier, A. (2010). Hard X-Ray Emission in the Star-Forming Region ON 2: Discovery with XMM-Newton. *ApJ*, **712**, 763–777. 34

Padoan, P., Nordlund, Å., Kritsuk, A.G., Norman, M.L. & Li, P.S. (2007). Two Regimes of Turbulent Fragmentation and the Stellar Initial Mass Function from Primordial to Present-Day Star Formation. *ApJ*, **661**, 972–981. 9

Pang, X., Grebel, E.K., Allison, R.J., Goodwin, S.P., Altmann, M., Harbeck, D., Moffat, A.F.J. & Drissen, L. (2013). On the Origin of Mass Segregation in NGC 3603. *ApJ*, **764**, 73. 216

Park, B.G. & Sung, H. (2002). UBVI and Hα Photometry of the Young Open Cluster NGC 2244. *AJ*, **123**, 892–904. 206

Park, S., Hughes, J.P., Slane, P.O., Burrows, D.N., Gaensler, B.M. & Ghavamian, P. (2007). A Half-Megasecond Chandra Observation of the Oxygen-rich Supernova Remnant G292.0+1.8. *ApJL*, **670**, L121–L124. 126

Parker, J.W. (1993). The OB associations of 30 Doradus in the Large Magellanic Cloud. I - Stellar observations and data reductions. *AJ*, **106**, 560–577. 43

Pellegrini, E.W., Baldwin, J.A., Brogan, C.L., Hanson, M.M., Abel, N.P., Ferland, G.J., Nemala, H.B., Shaw, G. & Troland, T.H. (2007). A Magnetically Supported Photodissociation Region in M17. *ApJ*, **658**, 1119–1135. 200

Pellegrini, E.W., Baldwin, J.A. & Ferland, G.J. (2011). Structure and Feedback in 30 Doradus. II. Structure and Chemical Abundances. *ApJ*, **738**, 34. 2, 12, 48

Pellegrini, E.W., Oey, M.S., Winkler, P.F., Points, S.D., Smith, R.C., Jaskot, A.E. & Zastrow, J. (2012). The Optical Depth of H II Regions in the Magellanic Clouds. *ApJ*, **755**, 40. 83

Pelupessy, F.I. & Portegies Zwart, S. (2011). The evolution of embedded star clusters. *MNRAS*, 2133. 1

Pfalzner, S. (2011). Formation and dissolution of leaky clusters. *A&A*, **536**, A90. 1

Piatti, A.E., Bica, E. & Claria, J.J. (1998). Fundamental parameters of the highly reddened young open clusters Westerlund 1 and 2. *A&AS*, **127**, 423–432. 23

Pittard, J.M. (2007). *Mass-Loaded Flows*, 245. 56, 93

Pittard, J.M. (2009). 3D models of radiatively driven colliding winds in massive O+O star binaries - I. Hydrodynamics. *MNRAS*, **396**, 1743–1763. 60

Pittard, J.M. (2011). Tails of the unexpected: the interaction of an isothermal shell with a cloud. *MNRAS*, **411**, L41–L45. 51

Pittard, J.M., Dyson, J.E. & Hartquist, T.W. (2001a). Self-similar evolution of wind-blown bubbles with mass-loading by conductive evaporation. *A&A*, **367**, 1000–1010. 56

Pittard, J.M., Hartquist, T.W. & Dyson, J.E. (2001b). Self-similar evolution of wind-blown bubbles with mass loading by hydrodynamic ablation. *A&A*, **373**, 1043–1055. 56

Pittard, J.M., Arthur, S.J., Dyson, J.E., Falle, S.A.E.G., Hartquist, T.W., Knight, M.I. & Pexton, M. (2003). The evolution of mass loaded supernova remnants. II. Temperature dependent mass injection rates. *A&A*, **401**, 1027–1038. 88

Pittard, J.M., Dougherty, S.M., Coker, R.F. & Corcoran, M.F. (2005). X-ray and Radio Emission from Colliding Stellar Winds. In L.O. Sjouwerman & K.K. Dyer, eds., *X-Ray and Radio Connections*. 64, 135

Pittard, J.M., Hartquist, T.W. & Falle, S.A.E.G. (2010). The turbulent destruction of clouds - II. Mach number dependence, mass-loss rates and tail formation. *MNRAS*, **405**, 821–838. 60

Portegies Zwart, S.F., McMillan, S.L.W. & Gieles, M. (2010). Young Massive Star Clusters. *Ann. Rev. Astron. Astrophys.*, **48**, 431–493. 1

Povich, M.S. (2012). Beyond Str\"omgren Spheres and Wind-Blown Bubbles: An Observational Perspective on H II Region Feedback. *ArXiv e-prints*. 48

Povich, M.S., Stone, J.M., Churchwell, E., Zweibel, E.G., Wolfire, M.G., Babler, B.L., Indebetouw, R., Meade, M.R. & Whitney, B.A. (2007). A Multiwavelength Study of M17: The Spectral Energy Distribution and PAH Emission Morphology of a Massive Star Formation Region. *ApJ*, **660**, 346–362. 42, 201

Povich, M.S., Benjamin, R.A., Whitney, B.A., Babler, B.L., Indebetouw, R., Meade, M.R. & Churchwell, E. (2008). Interstellar Weather Vanes: GLIMPSE Mid-Infrared Stellar Wind Bow Shocks in M17 and RCW 49. *ApJ*, **689**, 242–248. 24, 25, 48

Povich, M.S., Churchwell, E., Bieging, J.H., Kang, M., Whitney, B.A., Brogan, C.L., Kulesa, C.A., Cohen, M., Babler, B.L., Indebetouw, R., Meade, M.R. & Robitaille, T.P. (2009). The Extended Environment of M17: A Star Formation History. *ApJ*, **696**, 1278–1306. 201

Purcell, C.R., Minier, V., Longmore, S.N., André, P., Walsh, A.J., Jones, P., Herpin, F., Hill, T., Cunningham, M.R. & Burton, M.G. (2009). Multi-generation massive star-formation in NGC 3576. *A&A*, **504**, 139–159. 214

Rauw, G., Nazé, Y., Gosset, E., Stevens, I.R., Blomme, R., Corcoran, M.F., Pittard, J.M. & Runacres, M.C. (2002). An XMM-Newton observation of the Lagoon Nebula and the very young open cluster NGC 6530. *A&A*, **395**, 499–513. 91, 92, 120, 211

Raymond, J.C. & Smith, B.W. (1977). Soft X-ray spectrum of a hot plasma. *ApJS*, **35**, 419–439. 127

Reines, A.E., Johnson, K.E. & Goss, W.M. (2008). Emerging Massive Star Clusters Revealed: High-Resolution Imaging of NGC 4449 from the Radio to the Ultraviolet. *AJ*, **135**, 2222–2239. 83

Reynolds, R.J. (1984). A measurement of the hydrogen recombination rate in the diffuse interstellar medium. *ApJ*, **282**, 191–196. 2

Reynolds, S.P. (1986). Continuum spectra of collimated, ionized stellar winds. *ApJ*, **304**, 713–720. 134

Reynoso, E.M., Green, A.J., Johnston, S., Dubner, G.M., Giacani, E.B. & Goss, W.M. (2003). Observations of the neutral hydrogen surrounding the radio-quiet neutron star RX J0822-4300 in Puppis A. *MNRAS*, **345**, 671–677. 128, 166

Rockefeller, G., Fryer, C.L., Melia, F. & Wang, Q.D. (2005). Diffuse X-Rays from the Arches and Quintuplet Clusters. *ApJ*, **623**, 171–180. 208, 213

Rodriguez, L.F. & Lichten, S.M. (1979). Radio recombination line observations of M8 at 5 and 10 GHz. *Astrophys. Lett.*, **20**, 37–41. 212

Rodríguez, L.F., Gómez, Y. & Reipurth, B. (2003). A Cluster of Compact Radio Sources in NGC 2024 (Orion B). *ApJ*, **598**, 1100–1106. 218

Rodríguez, L.F., González, R.F., Montes, G., Asiri, H.M., Raga, A.C. & Cantó, J. (2012). Compact Radio Sources in M17. *ApJ*, **755**, 152. 161, 163, 201, 202

Rogers, H. & Pittard, J.M. (2013). Feedback from winds and supernovae in massive stellar clusters - I. Hydrodynamics. *MNRAS*, **431**, 1337–1351. 93, 94, 136

Rybicki, G.B. & Lightman, A.P. (1979). *Radiative processes in astrophysics*. 138

Salpeter, E.E. (1955). The Luminosity Function and Stellar Evolution. *ApJ*, **121**, 161–+. 9

Schild, H. & Testor, G. (1992). Spectral types and UBV magnitudes of stars in the 30 Doradus complex. *A&AS*, **92**, 729–748. 43

Schmid-Burgk, J. (1982). Nonspherical stellar envelopes and winds - Effects of structure on radiative fluxes and apparent mass loss rates. *A&A*, **108**, 169–175. 134

Schnerr, R.S., Rygl, K.L.J., van der Horst, A.J., Oosterloo, T.A., Miller-Jones, J.C.A., Henrichs, H.F., Spoelstra, T.A.T. & Foley, A.R. (2007). Radio observations of candidate magnetic O stars. *A&A*, **470**, 1105–1109. 134

Scuderi, S., Panagia, N., Stanghellini, C., Trigilio, C. & Umana, G. (1998). Radio observations of stellar winds from early type stars. *A&A*, **332**, 251–267. 134

Sedov, L.I. (1959). *Similarity and Dimensional Methods in Mechanics*. 29

Seward, F.D., Forman, W.R., Giacconi, R., Griffiths, R.E., Harnden, F.R., Jr., Jones, C. & Pye, J.P. (1979). X-rays from Eta Carinae and the surrounding nebula. *ApJL*, **234**, L55–L58. 21

Shu, F.H., Adams, F.C. & Lizano, S. (1987). Star formation in molecular clouds - Observation and theory. *Ann. Rev. Astron. Astrophys.*, **25**, 23–81. 4

Silich, S., Tenorio-Tagle, G. & Rodríguez-González, A. (2004). Winds Driven by Super Star Clusters: The Self-Consistent Radiative Solution. *ApJ*, **610**, 226–232. 18, 57

Silich, S., Tenorio-Tagle, G., Torres-Campos, A., Muñoz-Tuñón, C., Monreal-Ibero, A. & Melo, V. (2009). On the Heating Efficiency Derived from Observations of Young Super Star Clusters in M82. *ApJ*, **700**, 931–936. 18

Silk, J. (2003). A new prescription for protogalactic feedback and outflows: where have all the baryons gone? *MNRAS*, **343**, 249–254. 29

Smith, B.J., Struck, C. & Nowak, M.A. (2005). Chandra X-Ray Imaging of the Interacting Starburst Galaxy System NGC 7714/7715: Tidal Ultraluminous X-Ray Sources, Emergent Wind, and Resolved H II Regions. *AJ*, **129**, 1350–1368. 120

Smith, L.J. (2004). The Return of Mass and Energy from Clusters to the Interstellar Medium. In H.J.G.L.M. Lamers, L.J. Smith & A. Nota, eds., *The Formation and Evolution of Massive Young Star Clusters*, vol. 322 of *Astronomical Society of the Pacific Conference Series*, 159. 174

Smith, N. & Brooks, K.J. (2007). A census of the Carina Nebula - II. Energy budget and global properties of the nebulosity. *MNRAS*, **379**, 1279–1292. 22

Snider, K.D., Hester, J.J., Desch, S.J., Healy, K.R. & Bally, J. (2009). Spitzer Observations of The H II Region NGC 2467: An Analysis of Triggered Star Formation. *ApJ*, **700**, 506–522. 30

Stevens, I.R. & Hartwell, J.M. (2003). The cluster wind from local massive star clusters. *MNRAS*, **339**, 280–288. 15, 16, 17, 32, 120, 123, 210

Strickland, D.K. & Stevens, I.R. (2000). Starburst-driven galactic winds - I. Energetics and intrinsic X-ray emission. *MNRAS*, **314**, 511–545. 16

Strömgren, B. (1939). The Physical State of Interstellar Hydrogen. *ApJ*, **89**, 526. 26

Sutherland, R.S. (2010). A new computational fluid dynamics code I: Fyris Alpha. *Ap&SS*, **327**, 173–206. 51

Tan, J.C. & McKee, C.F. (2001). The Genesis of Super Star Clusters as Self-Gravitating HII Regions. In L. Tacconi & D. Lutz, eds., *Starburst Galaxies: Near and Far*, 188. 48

Tanaka, S.J. & Takahara, F. (2013). Properties of young pulsar wind nebulae: TeV detectability and pulsar properties. *MNRAS*, **429**, 2945–2952. 126

Taylor, G. (1950). The Formation of a Blast Wave by a Very Intense Explosion. I. Theoretical Discussion. *Royal Society of London Proceedings Series A*, **201**, 159–174. 29

Tenorio-Tagle, G. (1979). The gas dynamics of H II regions. I - The champagne model. *A&A*, **71**, 59–65. 26

Tenorio-Tagle, G., Bodenheimer, P., Lin, D.N.C. & Noriega-Crespo, A. (1986). On star formation in stellar systems. I - Photoionization effects in protoglobular clusters. *MNRAS*, **221**, 635–658. 11

Tenorio-Tagle, G., Silich, S.A., Kunth, D., Terlevich, E. & Terlevich, R. (1999). The evolution of superbubbles and the detection of Lyα in star-forming galaxies. *MNRAS*, **309**, 332–342. 12

Tenorio-Tagle, G., Palouš, J., Silich, S., Medina-Tanco, G.A. & Muñoz-Tuñón, C. (2003). On the formation of massive stellar clusters. *A&A*, **411**, 397–404. 12

Terzian, Y., Mezger, P.G. & Schraml, J. (1968). On the Electron Temperatures of the Orion Nebula and NGC 2024 (I): Radio Observations of the Free-Free Continuum. *Astrophys. Lett.*, **1**, 153–158. 218

Tothill, N.F.H., Gagné, M., Stecklum, B. & Kenworthy, M.A. (2008). *The Lagoon Nebula and its Vicinity*, 533. 211

Townsley, L., Feigelson, E., Montmerle, T., Broos, P., Chu, Y.H., Garmire, G. & Getman, K. (2005). Parsec-Scale X-ray Flows in High-Mass Star-Forming Regions. In L.O. Sjouwerman & K.K. Dyer, eds., *X-Ray and Radio Connections*. 24, 203, 204

Townsley, L.K., Feigelson, E.D., Montmerle, T., Broos, P.S., Chu, Y.H. & Garmire, G.P. (2003). 10 MK Gas in M17 and the Rosette Nebula:

X-Ray Flows in Galactic H II Regions. *ApJ*, **593**, 874–905. 33, 48, 91, 92, 121, 123, 201, 202, 205, 206, 211

Townsley, L.K., Broos, P.S., Feigelson, E.D., Brandl, B.R., Chu, Y.H., Garmire, G.P. & Pavlov, G.G. (2006a). A Chandra ACIS Study of 30 Doradus. I. Superbubbles and Supernova Remnants. *AJ*, **131**, 2140–2163. 43, 44

Townsley, L.K., Broos, P.S., Feigelson, E.D., Garmire, G.P. & Getman, K.V. (2006b). A Chandra ACIS Study of 30 Doradus. II. X-Ray Point Sources in the Massive Star Cluster R136 and Beyond. *AJ*, **131**, 2164–2184. 47

Townsley, L.K., Broos, P.S., Chu, Y.H., Gagné, M., Garmire, G.P., Gruendl, R.A., Hamaguchi, K., Mac Low, M.M., Montmerle, T., Nazé, Y., Oey, M.S., Park, S., Petre, R. & Pittard, J.M. (2011). The Chandra Carina Complex Project: Deciphering the Enigma of Carina's Diffuse X-ray Emission. *ApJS*, **194**, 15. 34, 93, 121, 201, 214, 215, 216

Usov, V.V. (1992). Stellar wind collision and X-ray generation in massive binaries. *ApJ*, **389**, 635–648. 38

van Buren, D. (1985). The initial mass function and global rates of mass, momentum, and energy input to the interstellar medium via stellar winds. *ApJ*, **294**, 567–577. 174

van Loo, S. (2010). Non-Thermal Radio Emission from â??Presumablyâ?? Single O Stars. In J. Martí, P.L. Luque-Escamilla & J.A. Combi, eds., *High Energy*

Phenomena in Massive Stars, vol. 422 of *Astronomical Society of the Pacific Conference Series*, 157. 134

van Loo, S., Runacres, M.C. & Blomme, R. (2005). A layered model for non-thermal radio emission from single O stars. *A&A*, **433**, 313–322. 134

van Marle, A.J., Meliani, Z. & Marcowith, A. (2012). A hydrodynamical model of the circumstellar bubble created by two massive stars. *A&A*, **541**, L8. 15

Vázquez-Semadeni, E., González, R.F., Ballesteros-Paredes, J., Gazol, A. & Kim, J. (2008). The nature of the velocity field in molecular clouds - I. The non-magnetic case. *MNRAS*, **390**, 769–780. 53, 187

Vink, J.S., de Koter, A. & Lamers, H.J.G.L.M. (2000). New theoretical mass-loss rates of O and B stars. *A&A*, **362**, 295–309. 13, 53, 175

Vink, J.S., de Koter, A. & Lamers, H.J.G.L.M. (2001). Mass-loss predictions for O and B stars as a function of metallicity. *A&A*, **369**, 574–588. 13, 53, 175

Wada, Q., Tsujimoto, M., Ebisawa, K. & Miller, E.D. (2013). Detection of a 522 s Pulsation from the Transient X-Ray Source Suzaku J0102.8-7204 (SXP 523) in the Small Magellanic Cloud. *PASJ*, **65**, L2. 125

Walborn, N.R. & Blades, J.C. (1997). Spectral Classification of the 30 Doradus Stellar Populations. *ApJS*, **112**, 457. 43

Walborn, N.R., Barbá, R.H. & Sewiło, M.M. (2013). The Top 10 Spitzer Young Stellar Objects in 30 Doradus. *AJ*, **145**, 98. 43

Walch, S.K., Whitworth, A.P., Bisbas, T., Wünsch, R. & Hubber, D. (2012). Dispersal of molecular clouds by ionizing radiation. *MNRAS*, **427**, 625–636. 49

Wang, J., Townsley, L.K., Feigelson, E.D., Broos, P.S., Getman, K.V., Román-Zúñiga, C.G. & Lada, E. (2008). A Chandra Study of the Rosette Star-forming Complex. I. The Stellar Population and Structure of the Young Open Cluster NGC 2244. *ApJ*, **675**, 464–490. 11, 206

Wang, P., Li, Z.Y., Abel, T. & Nakamura, F. (2010). Outflow Feedback Regulated Massive Star Formation in Parsec-Scale Cluster-Forming Clumps. *ApJ*, **709**, 27–41. 2, 12

Wang, Q.D., Dong, H. & Lang, C. (2006). The interplay between star formation and the nuclear environment of our Galaxy: deep X-ray observations of the Galactic centre Arches and Quintuplet clusters. *MNRAS*, **371**, 38–54. 34, 92, 207, 212, 213

Weaver, R., McCray, R., Castor, J., Shapiro, P. & Moore, R. (1977). Interstellar bubbles. II - Structure and evolution. *ApJ*, **218**, 377–395. 15, 32, 63, 117, 118, 119

White, R.L. (1985). Synchrotron emission from chaotic stellar winds. *ApJ*, **289**, 698–708. 38, 134

White, R.L. & Long, K.S. (1991). Supernova remnant evolution in an interstellar medium with evaporating clouds. *ApJ*, **373**, 543–555. 88

Whiteoak, J.B.Z. & Uchida, K.I. (1997). High-resolution radio observations of RCW 49. *A&A*, **317**, 563–568. 23

Whitworth, A. (1979). The erosion and dispersal of massive molecular clouds by young stars. *MNRAS*, **186**, 59–67. 26

Whitworth, A.P. & Francis, N. (2002). A threshold for sequentially self-propagating star formation. *MNRAS*, **329**, 641–646. 12

Wilson, T.L. & Pauls, T. (1984). Radio continuum and recombination line observations of Orion A. *A&A*, **138**, 225–230. 205

Winkler, P.F. & Kirshner, R.P. (1985). Discovery of fast-moving oxygen filaments in Puppis A. *ApJ*, **299**, 981–986. 128, 166

Winkler, P.F., Twelker, K., Reith, C.N. & Long, K.S. (2009). Expanding Ejecta in the Oxygen-Rich Supernova Remnant G292.0+1.8: Direct Measurement Through Proper Motions. *ApJ*, **692**, 1489–1499. 126

Winston, E., Wolk, S.J., Bourke, T.L., Megeath, S.T., Gutermuth, R. & Spitzbart, B. (2011). The Structure of the Star-forming Cluster RCW 38. *ApJ*, **743**, 166. 199

Winston, E., Wolk, S.J., Bourke, T.L., Megeath, S.T., Gutermuth, R. & Spitzbart, B. (2012). Spitzer Observations of Bow Shocks and Outflows in RCW 38. *ApJ*, **744**, 126. 200

Woermann, B., Gaylard, M.J. & Otrupcek, R. (2000). Hydroxyl lines towards Puppis A. *MNRAS*, **317**, 421–428. 128, 166

Wolfire, M.G. & Cassinelli, J.P. (1987). Conditions for the formation of massive stars. *ApJ*, **319**, 850–867. 6, 7

Wolk, S.J., Bourke, T.L., Smith, R.K., Spitzbart, B. & Alves, J. (2002). Discovery of Nonthermal X-Ray Emission from the Embedded Massive Star-forming Region RCW 38. *ApJL*, **580**, L161–L165. 34, 199

Wolk, S.J., Spitzbart, B.D., Bourke, T.L. & Alves, J. (2006). X-Ray and Infrared Point Source Identification and Characteristics in the Embedded, Massive Star-Forming Region RCW 38. *AJ*, **132**, 1100–1125. 200

Wolk, S.J., Bourke, T.L. & Vigil, M. (2008). *The Embedded Massive Star Forming Region RCW 38*, 124. 92, 200

Wolk, S.J., Broos, P.S., Getman, K.V., Feigelson, E.D., Preibisch, T., Townsley, L.K., Wang, J., Stassun, K.G., King, R.R., McCaughrean, M.J., Moffat, A.F.J. & Zinnecker, H. (2011). The Chandra Carina Complex Project View of Trumpler 16. *ApJS*, **194**, 12. 91

Wood, D.O.S. & Churchwell, E. (1989). The morphologies and physical properties of ultracompact H II regions. *ApJS*, **69**, 831–895. 26

Woodward, C.E., Pipher, J.L., Helfer, H.L., Sharpless, S., Moneti, A., Kozikowski, D., Oliveri, M., Willner, S.P., Lacasse, M.G. & Herter, T. (1986). Optical, radio, and infrared observations of compact H II regions. V - The Hourglass in M8. *AJ*, **91**, 870–889. 211

Wright, A.E. & Barlow, M.J. (1975). The radio and infrared spectrum of early-type stars undergoing mass loss. *MNRAS*, **170**, 41–51. 35, 133, 135

Xu, Y., Moscadelli, L., Reid, M.J., Menten, K.M., Zhang, B., Zheng, X.W. & Brunthaler, A. (2011). Trigonometric Parallaxes of Massive Star-forming Regions. VIII. G12.89+0.49, G15.03-0.68 (M17), and G27.36-0.16. *ApJ*, **733**, 25. 200

Yorke, H.W. & Kruegel, E. (1977). The dynamical evolution of massive protostellar clouds. *A&A*, **54**, 183–194. 7

Yorke, H.W. & Sonnhalter, C. (2002). On the Formation of Massive Stars. *ApJ*, **569**, 846–862. 8

Yorke, H.W., Tenorio-Tagle, G. & Bodenheimer, P. (1983). Theoretical radio continuum maps of H II regions in the champagne phase. *A&A*, **127**, 313–319. 26

Yorke, H.W., Tenorio-Tagle, G., Bodenheimer, P. & Rozyczka, M. (1989). The combined role of ionization and supernova explosions in the destruction of molecular clouds. *A&A*, **216**, 207–214. 2, 12, 27

Yu, J., de Grijs, R. & Chen, L. (2011). Rapid Dynamical Mass Segregation and Properties of Fractal Star Clusters. *ApJ*, **732**, 16. 10

Yusef-Zadeh, F., Law, C., Wardle, M., Wang, Q.D., Fruscione, A., Lang, C.C. & Cotera, A. (2002). Detection of X-Ray Emission from the Arches Cluster near the Galactic Center. *ApJ*, **570**, 665–670. 34

Zinnecker, H. & Yorke, H.W. (2007). Toward Understanding Massive Star Formation. *Ann. Rev. Astron. Astrophys.*, **45**, 481–563. 10